The Effects of Climate Change on Renewable Energy Resources in New York State

Final Report | Report Number 22-34 | August 2021

NEW YORK STATE
NYSERDA
New York State Energy Research and Development Authority

NYSERDA's Mission:

NYSERDA catalyzes New York's clean energy transition.

Our Vision:

Clean energy that supports a healthier and thriving future for all New Yorkers.

Our Promise to New Yorkers:

NYSERDA serves New York State as a trusted and credible resource for energy information, policies, and programs, through objective analysis and planning, innovative solutions, and impactful investments that are valued by New York residents and businesses.

The Effects of Climate Change on Renewable Energy Resources in New York State

Final Report

Prepared for:

New York State Energy Research and Development Authority

Albany, NY

Amanda Stevens
Project Manager

Prepared by:

University at Albany
Atmospheric Sciences Research Center

Albany, NY

Dr. Jeffrey M. Freedman
Research Faculty

Dan Kirk-Davidoff
UL Renewables, Lead Research Scientist

John Manobianco
Mano Nanotechnologies

NYSERDA Report 22-34 NYSERDA Contract 105161 January 2022

Notice

This report was prepared by the University at Albany (UAlbany) Atmospheric Sciences Research Center (ASRC) in the course of performing work contracted for and sponsored by the New York State Energy Research and Development Authority (NYSERDA). The opinions expressed in this report do not necessarily reflect those of NYSERDA or the State of New York, and reference to any specific product, service, process, or method does not constitute an implied or expressed recommendation or endorsement of it. Further, NYSERDA, the State of New York, and the contractor make no warranties or representations, expressed or implied, as to the fitness for particular purpose or merchantability of any product, apparatus, service, or the usefulness, completeness, or accuracy of any processes, methods, or other information contained, described, disclosed, or referred to in this report. NYSERDA, the State of New York, and the contractor make no representation that the use of any product, apparatus, process, method, or other information will not infringe privately owned rights and will assume no liability for any loss, injury, or damage resulting from, or occurring in connection with, the use of information contained, described, disclosed, or referred to in this report.

NYSERDA makes every effort to provide accurate information about copyright owners and related matters in the reports we publish. Contractors are responsible for determining and satisfying copyright or other use restrictions regarding the content of reports that they write, in compliance with NYSERDA's policies and federal law. If you are the copyright owner and believe a NYSERDA report has not properly attributed your work to you or has used it without permission, please email print@nyserda.ny.gov

Information contained in this document, such as web page addresses, are current at the time of publication.

Preferred Citation

New York State Energy Research and Development Authority (NYSERDA). 2022. "The Effects of Climate Change on Renewable Energy Resources in New York State," NYSERDA Report Number 22-34. Prepared by Dr. Jeffrey M. Freedman, Atmospheric Sciences Research Center, University at Albany, State University of New York. nyserda.ny.gov/publications

Abstract

With support from New York State Energy Research and Development Authority (NYSERDA), a public-private research partnership has completed a comprehensive study of climate change and its potential effects on the New York State's renewable energy resources.

We used the Weather Research and Forecasting (WRF model version 3.9.1) system to dynamically downscale climate projections from three model members of the Coupled Model Inter-comparison Project 5 (CMIP5) ensemble for two different climate change scenarios, Representative Concentration Pathway (RCP) 4.5 and RCP 8.5, for the near-future (2018–2037) and mid-future (2038–2057) periods. These future scenarios are compared with historical climate (1998–2017) simulations forced by runs of the CMIP5 models and a simulation forced by the European Center for Medium-Range Weather Forecasting (ECMWF) ERA-Interim reanalysis (ERA-I). Two inner nests covering the State and adjacent offshore waters were run at 6 kilometers (km) horizontal resolution (with 40 levels in the vertical, including 10 in the planetary boundary layer) to capture terrain effects and land-lake and land-sea interactions. The fine-scale resolution downscaling provides insight into how future climate change may influence New York State's weather and climate regimes and hence the distribution of renewable energy resources. Results show modest changes in the wind (±1%–2%) and solar (up to +5%) resource availability (within the observed historical interannual variability), with a general statewide increase (2%–4%) in precipitation during the near-future and mid-future scenarios, leading to little change or a modest increase in the State's hydropower resources.

Keywords

Climate change, renewable energy, wind, solar, hydropower, dynamic downscaling, CMIP5.

Acknowledgments

We would like to acknowledge the steadfast support and patience of NYSERDA, particularly Amanda Stevens, the NYSERDA project manager for this work. This was a team effort, a collaborative work between the academic (UAlbany's Atmospheric Sciences Research Center and the Department of Atmospheric and Environmental Sciences) and private sector (AWS Truepower and Mano Nanotechnologies). Special thanks to Philippe Beaucage, Dan Kirk-Davidoff, and Akila Gothandaraman of UL Renewables (AWS Truepower), and John Manobianco of Mano Nanotechnologies for the hard work they put into making a daunting modeling task possible and successful. Thanks also to Jason Covert and Shengzhe Chen, my two graduate students, who provided early support for the analysis and selection of the eventual CMIP5 models used in the modeling experiments. And to Geng Xia for his work on the bias-correction algorithm and other support during the postmodeling phase of the project.

Table of Contents

List of Figures

List of Tables

Acronyms and Abbreviations

~	approximately
-	minus
+	plus
<	less than
>	greater than
±	plus or minus
ΔSD	change or difference in standard deviation
ºC	degrees Celsius
ABL	atmospheric boundary layer
AGL	above ground level
ALB	Albany International Airport, Albany, NY
ASL	above sea level
ASOS	Automated Surface Observation System
ASRC	Atmospheric Sciences Research Center
BOEM	Bureau of Ocean Energy Management
BUF	Buffalo, NY
CEDA	Center for Environmental Data Analysis
Climate Act	Climate Leadership and Community Protection Act
CO_2	carbon dioxide
CSV	comma-separated values
DNI	direct normal irradiance
ECMWF	European Center for Medium-Range Weather Forecasting
ERA-I	ECMWF Interim Reanalysis
FRG	Farmingdale, NY
GB	gigabyte
GEC	Garnet Energy Center
GFDL	Geophysical Fluid Dynamics Laboratory
GHG	greenhouse gas
GHI	global horizontal irradiance
g/kg	grams per kilogram
GW	gigawatt
hPa	hectopascal
in/yr	inches per year
IPCC	Intergovernmental Panel on Climate Change
ISD	integrated surface data
IT	information technology
JFK	John F. Kennedy International Airport, Jamaica, NY

km	kilometers
kWh	kilowatt hours
LiDAR	Light Detection and Ranging
LISF	Long Island Solar Farm
LLNL	Lawrence Livermore National Laboratory
m	meters
m/s	meters per second
MAWS	mean annual wind speed
MGJ	Montgomery, NY, ASOS station
mm	millimeters
mm/h	millimeters per hour
mm/yr	millimeters/year
MP	microphysics scheme
MW	megawatts
NARCCAP	North American Regional Climate Change Assessment Program
NASA	National Aeronautics and Space Administration
NCAR	National Center for Atmospheric Research
NCEI	National Centers for Environmental Information
NEC	North Side Energy Center
NOAA	National Oceanographic and Atmospheric Administration
NYISO	New York Independent System Operator
NYS	New York State
NYSERDA	New York State Energy Research and Development Authority
NYSM	New York State Mesonet
PBL	planetary boundary layer (used interchangeably with ABL)
POR	period of record
R2	coefficient of determination
RAOB	Radiosonde Observation
RCP	Representative Concentration Pathway
RGGI	Regional Greenhouse Gas Initiative
RMSE	root mean square error
SLP	sea level pressure
SOW	scope of work
SRSP	South Ripley Solar Project
SST	sea surface temperatures
SYR	Syracuse, NY
TB	terabytes
UAlbany	University at Albany
USGS	U.S. Geological Survey

W/m^2	watts per square meter
WS	wind speed
WSM6	WRF Single-Moment 6-class

Models, Model Archives, and Reanalysis Datasets

BNU-ESM	Beijing Normal University Earth System Model
CNRM-CM5	Centre National de Recherches Météorologiques Climate Model, version 5
CSIRO-Mk3.6.0	Commonwealth Scientific and Industrial Research Organisation Mark 3.6.0 Climate Model
CMIP5	Coupled Model Intercomparison Project Phase 5
ESMs	Earth System Models
GFDL-CM3	Geophysical Fluid Dynamics Laboratory Climate Model, version 3
GFDL-ESM2G	Geophysical Fluid Dynamics Laboratory Earth System Model, version 2G
GFDL-ESM2M	Geophysical Fluid Dynamics Laboratory Earth System Model, version 2M
IPSL-CM5B-LR	Institut Pierre-Simon Laplace Climate Model 5B, Low Resolution
MIROC5	Model for Interdisciplinary Research on Climate, version 5
MPI-ESM-LR	Max Planck Institute Earth System Model, Low Resolution
MPI-ESM-MR	Max Planck Institute Earth System Model, Medium Resolution
MRI-CGCM3	Meteorological Research Institute Coupled Global Climate Model, version 3
MERRA	Modern-Era Retrospective Analysis for Research and Applications
MERRA-2	Modern-Era Retrospective Analysis for Research and Applications, version 2
PRISM	Parameter-elevation Regressions on Independent Slopes Model
PCMDI	Program for Climate Model Diagnosis and Intercomparison
WRF	Weather Research and Forecasting model

Summary

With support from NYSERDA, a public-private research partnership has completed a comprehensive study of climate change and its potential effects on the State's renewable energy resources.

We used the Weather Research and Forecasting (WRF, model version 3.9.1) system to dynamically downscale climate projections from three models in the International Panel on Climate Change (IPCC) Coupled Model Inter-comparison Project 5 (CMIP5) ensemble for two different climate change scenarios, Representative Concentration Pathway (RCP) 4.5 and RCP8.5, for near-future (2018–2037) and mid-future (2038–2057) periods. These future scenarios are compared with historical climate (1998–2017) simulations forced by runs of the CMIP5 models and a simulation forced by the European Centre for Medium-Range Weather Forecasting (ECMWF) ERA-Interim reanalysis (ERA-I). Two inner nests covering the State and adjacent offshore waters were run at 6 kilometers (km) resolution to capture terrain effects and land-lake and land-sea interactions, providing insight into how future climate change may influence New York State's (NYS) weather and climate regimes and, hence, the distribution of renewable energy resources.

The work involved multiple tasks, including:

1. Creating an inventory of historical data sets to be used for development of an observational historical data base, and validation and verification of a dynamically downscaled historical baseline
2. Developing a downscaled historical baseline (1998–2017) used to bias-correct model output
3. Selecting three CMIP5 model members for use in the dynamical downscaling experiments.
4. Analyzing the results (annual, seasonal, and diurnal) from the downscaling experiments, including future changes in precipitation, hub-height wind speed (e.g., 100 meters [m] above ground or sea level), and surface irradiance (global horizontal irradiance, or GHI) under the two scenarios (RCP4.5 and RCP8.5) and two future periods (near-future, 2018–2037, and mid-future, 2038–2057). The analysis also considered changes in power production, particularly for wind power, given its nonlinear relationship with wind speed.

S.1 Future Trends in Precipitation

As summarized in Table S-1, for the RCP4.5 scenario all three models show a consistent precipitation increase over the d03 grid (13–52 mm/yr [0.4–1.9 in/yr], or a 1%–5% increase over a historical baseline average of 772–932 mm/yr) during the near-future period with an acceleration of the increase in annual precipitation during the mid-future period (37–95 mm/yr [1.2–3.1 in/yr], a 5%–10% increase) over the domain. In contrast, for the RCP8.5 scenario, two of the three models, Geophysical Fluid Dynamics

Laboratory (GFDL) and National Center for Atmospheric Research (NCAR), show a decrease in precipitation during the near-future period (-18 to -67 mm/yr [-0.6 to -2.2 in/yr], a 2%–7% decrease) in annual precipitation over the domain, while the Model for Interdisciplinary Research on Climate, version 5 (MIROC5) run shows a positive trend of 57-61 mm/yr (4.6–4.8 in/yr) in domain-wide annual precipitation. For the mid-future RCP8.5 scenario, only the NCAR model shows a decrease in annual precipitation (-5.1 mm/yr trend or a decrease of 4.0 in/yr in annual precipitation); the GFDL and MIROC5 models show positive trends (2.2 and 6.2 mm/yr). If we consider the model ensemble average (both scenarios), regional changes show an overall increase in mean annual precipitation for both periods (15–37 mm/yr) of 1.3%–4.0% over the historical mean yearly average, well within the interannual variability of 131–195 mm/yr. Note that regional changes vary above and below the domain averages, reflecting local effects of topography and proximity to large bodies of water (e.g., the Great Lakes and Atlantic Ocean).

Table S-1. Precipitation Change in the d03 Domain

Expressed in mm/yr and percent change.

Model	Scenario	mm/yr (%change)	
		2018–2037	2038–2057
GFDL-CM3	RCP4.5	13 (1)	95 (11)
	RCP8.5	-18 (-2)	22 (2)
NCAR-CCSM4	RCP4.5	52 (7)	58 (7)
	RCP8.5	-67 (-9)	-51 (-7)
MIROC5	RCP4.5	50 (5)	37 (4)
	RCP8.5	57 (6)	61 (7)
Mean		**14.5 (+1.3)**	**37 (+4.0)**

S.2 Future Trends in Wind Speeds

For the d03 domain, both scenarios show a very slight increase in 100m above ground level (AGL) wind speeds (-0.02 to +0.06 m/s, or +0.02%–+0.06%) during the near-future and mid-future periods for the GFDL and MIROC5 runs (Table S-2; note the mean historical average 100-m wind speed for all models within the d03 domain is 7.8 m/s). The same is true for the d04 domain (partially offshore; mean domain wind speed of 8.0 m/s) with a range of +0.01 to -0.21 m/s. The NCAR runs, however, show a more robust increase in wind speeds for both future periods: 0.46 m/s (near-future) and 0.35 m/s (mid-future) for the d03 domain, and 0.19 m/s (near-future) and 0.20 m/s (mid-future) for the d04 domain. As with precipitation, these values fall within the region's historical and projected future interannual variability (0.2 to 0.4 m/s for both domains).

We note, however, that the NCAR d03 near-future increase could result in a 10% increase in capacity factor, depending on the turbine and local mean wind speed. The largest decrease shown in Table S-2 (-0.21 m/s for d04, mid-future period) could result in approximately a 5% decrease in the regional capacity factor. If we consider the model ensemble average (both scenarios), regional changes in wind speed are quite small (<0.05 m/s), or less than 1% of the domain-averaged 100-m wind speeds. Again, local effects of topography (e.g., surface roughness) will lead to regionally larger or smaller changes in hub-height wind speeds.

Table S-2. Change in Annual Wind Speed at 100 meters

Expressed in m/s and percent change from base period (1998–2017) for the d03 and d04 domains.

Model	Scenario	D03 m/s per yr (% change)		D04 m/s per yr (% change)	
		2018–2037	2038–2057	2018–2037	2038–2057
GFDL-CM3	RCP4.5	-0.10 (-1)	0.00 (0)	-0.09 (-1)	0.01 (0)
	RCP8.5	-0.16 (-2)	-0.16 (-2)	-0.16 (-2)	-0.21 (-3)
NCAR-CCSM4	RCP4.5	0.07 (1)	0.03 (0)	0.00 (0)	-0.02 (0)
	RCP8.5	0.46 (6)	0.35 (4)	0.19 (2)	0.20 (3)
MIROC5	RCP4.5	0.00 (0)	-0.02 (0)	-0.04 (-1)	-0.09 (-1)
	RCP8.5	0.00 (0)	-0.11 (-1)	0.00 (0)	-0.16 (-2)
Mean		**0.05 (0.6%)**	**0.02 (0.2%)**	**-0.02 (0.2%)**	**-0.05 (-0.6%)**

S.3 Future Trends in Surface Irradiance

Baseline historical annual mean surface irradiance for the three models ranges from 257 to 277 watts per square meter (W/m^2) for the d03 domain and 292 to 311 W/m^2 for the d04 domain. Interannual variability is approximately 10–15 W/m^2, or 4%–5%. As Table S-3 shows, the GFDL and MIROC5 models show modest changes of <2.5% for both RCP scenarios and the near-future and mid-future periods under RCP4.5 and RCP8.5. All three models show modest decreases under the near-future RCP4.5 for both domains, with reductions of <7 W/m^2or <2.3%.

For the mid-future period and RCP4.5 scenario (noting the absence of output from the GFDL), the NCAR and MIROC5 models also indicate little change or a modest decrease in surface irradiance (the largest decrease of 4.59 W/m^2 for the NCAR model over the d03 domain, or < 1.5%). The NCAR-CCSM4 RCP8.5 model runs, however, show an increase of approximately 22–23 W/m^2 in GHI for both periods, about 8% of the annual available mean solar energy and greater than the model's interannual variability (15 W/m^2).

We note that the downscaled NCAR-CCSM4 RCP8.5 also exhibit larger annual changes from the historical baseline averages for precipitation (Table S-1) and 100 m wind speeds (Table S-2). However, the NCAR RCP8.5 2-m temperature changes (not shown) are comparable with the GFDL and MIROC5 model runs, therefore we have no reason to suspect any errors in the downscaling process.

We intend to further explore the reasons for the projected larger changes in surface irradiance for the NCAR-CCSM4 RCP8.5 runs (e.g., changes in cloudiness or atmospheric aerosols). In general, however, if we consider the model ensemble average (both scenarios), domain-wide changes range from near zero for the near-future period up to +15 W/m^2 (5%–8% of the mean) for the d03 domain, around the interannual variability (12 to 15 W/m^2) of the solar energy resource.

Table S-3. Change in Annual Mean Solar Irradiance

Expressed in W/m^2 and percent change from base period (1998–2017) for the d03 and d04 domains.

Model	Scenario	D03 GHI (Wm^{-2})		D04 GHI (W/m^2)	
		2018–2037	2038–2057	2018–2037	2038–2057
GFDL-CM3	RCP4.5	-3.84 (-1)	NA (NA)	-5.16 (-2)	NA (NA)
	RCP8.5	-5.20 (-2)	6.40 (2)	-5.43 (-2)	7.72 (3)
NCAR-CCSM4	RCP4.5	-7.02 (-2)	-4.59 (-2)	-2.43 (-1)	-0.36 (0_
	RCP8.5	22.26 (8)	22.97 (8)	21.31 (8)	21.97 (8)
MIROC5	RCP4.5	-7.12 (-2)	-3.28 (-1)	-5.62 (-2)	0.52 (0)
	RCP8.5	-6.09 (-2)	-8.61 (-3)	-6.14 (-2)	-2.43 (-1)
Mean		**-0.18 (0)**	**14.69 (5)**	**-0.58 (0)**	**5.48 (2)**

1 Introduction

New York State (NYS) is aggressively integrating greater amounts of renewable energy (i.e., wind, solar, and hydropower) into the power grid. However, very little is known about the potential effects of climate change on the future distribution of renewable energy resources on a spectrum of temporal (diurnal to decadal) and spatial (local to regional) scales. Any redistribution of renewable energy potential may be disruptive to New York State's current plans, policies, and goals under the Climate Leadership and Community Protection Act[1] (Climate Act) program (NYSERDA 2021) and participation in the Regional Greenhouse Gas Initiative. As of 2021, New York State generated approximately 29% of its energy from renewable sources, with 83% of that share coming from hydropower (EIA 2021, NYISO 2021).

The University at Albany (UAlbany) Atmospheric Sciences Research Center (ASRC) and project partners conducted a comprehensive study to assess the potential influence of climate change on New York States's wind, solar, and hydropower resources. Specifically, the team:

1. Developed an inventory of solar, wind, and hydro (precipitation) datasets to establish a current climatology (1998–2017) of renewable energy resources.
2. Conducted high-resolution model sensitivity studies using downscaled output from a diverse subset of Earth System Models (ESMs) to project the near-future renewable energy resource distribution in New York State.
3. Analyzed the near-future (2018–2037) and mid-future (2038–2057) results to identify changes in the State's potential renewable energy distribution and variability.
4. Communicated preliminary and final project results to interested government, academia, utility groups, and industry stakeholders.

1.1 Previous Studies

Climate model outputs from the International Panel on Climate Change (IPCC) Coupled Model Inter-comparison Project 5 (CMIP5) suite and its predecessors have been widely used to project regional changes in temperature and hydrological cycles (e.g., Baker and Huang 2014), but comparatively few studies have used the datasets to project future changes in surface layer or hub-height (approximately 80–120 meters above ground level [m AGL]) wind, and even fewer have investigated the potential effects on the solar power resource (although some have examined future changes in gross cloudiness (e.g., Lin and Qian 2014)). One caveat is the large uncertainty in quantifying the historical baseline resource or trends (e.g., Torralba et al. 2017).

Notably, Chen (2020) examined the impact of climate change on the wind resource over North America using medium-resolution (25–50 km) simulations in the North America downscaling project (NA-CORDEX). He found a general (~5%) decrease in wind power availability over the northeastern U.S. during the second half of the 21st century. Pryor et al. (2012) analyzed the regional model simulations in the North American Regional Climate Change Assessment Program (NARCCAP; Mearns et al. 2012), constrained by the global model projections from CMIP3 (Meehl et al. 2007), to conclude that greenhouse gas (GHG)-induced climate change will not significantly affect wind power potential in the U.S. in the coming decades. Kulkarni and Huang (2014), using a subset of five CMIP5 models, found an overall increase in wind power potential during the winter season over the Eastern U.S., with a concomitant decrease in wind energy during the warmer months under the Representative Concentration Pathways (RCP) 8.5 scenario. Few studies have examined regional effects of climate change on hydropower resources in New York State (e.g., Hayhoe et al. 2006), no studies have examined potential impacts of climate change on the State's integrated wind, solar, and hydropower resources.

There have been recent efforts investigating the effects of climate change on New York State (e.g., water supply and urban heat effects in the New York Metropolitan Area; Solecki and Rosenzweig 2019), with some brief mention of renewables (e.g., Rosenzweig et al. 2011). But no studies have employed dynamical downscaling to analyze the potential impacts of climate change on New York State's three principal renewable energy resources: wind, solar, and hydropower.

We used the Weather Research and Forecasting (WRF model version 3.9.1) system to dynamically downscale climate projections from three models in the Coupled Model Intercomparison Project 5 (CMIP5) ensemble for two different climate change scenarios, RCP4.5 and RCP8.5, for near-future (2018–2037) and mid-future (2038–2057) periods. These future scenarios are compared with historical climate (1998–2017) simulations forced by runs of the CMIP5 models and a simulation forced by the ERA-I reanalysis. Two inner nests, covering the State and adjacent offshore waters, were run at 6 km resolution, to capture terrain effects and land-lake and land-sea interactions, providing insight into how future climate change may influence New York State's weather and climate regimes and hence the distribution of renewable energy resources.

The work involved multiple tasks, including:

1. Creating an inventory of historical datasets to be used for development of an observational historical database, and validation and verification of a dynamically downscaled historical baseline.
2. Developing a downscaled historical baseline (1998–2017) to bias-correct model output.
3. Selecting three CMIP5 model members for use in the dynamical downscaling experiments.
4. Analyzing the results annual, seasonal, and diurnal from the downscaling experiments, including future changes in precipitation, hub height wind speed (e.g., 100 m above ground or sea level), and surface irradiance (global horizontal irradiance, or GHI) under two scenarios (RCP4.5 and RCP8.5) and two future periods (near-future, 2018–2037, and mid-future, 2038–2057). The analysis also considered changes in power production, particularly for wind power given its nonlinear relationship with wind speed.

This report is organized as follows:

- Section 2 summarizes work performed under Task 1: Inventory Long-term Solar, Wind, and Precipitation Datasets.
- Section 3 highlights Task 2 work Selection of CMIP5 Subset.
- Section 4 details the downscaling (Task 3) work performed Downscaling of CMIP5").
- Section 5 presents the Task 4 analyses detailing future changes in the renewable energy resources ("Analyze Future Scenario Changes in Renewable Energy Power Distribution").
- Section 6 provides conclusions based upon the findings of the downscaling work and analyses.

2 Inventory Long-Term Solar, Wind, and Precipitation Datasets(Task 1)

This task developed validation data sets (Table 1) for the historical climatology of solar, wind, and precipitation: 1) surface irradiance or global horizontal irradiance (GHI), typically measured in watts per square meter (W/m^2); 2) wind speed in meters per second (m/s) and direction; and 3) precipitation in millimeters. All relevant data sets were downloaded, quality controlled, and archived on ASRC servers. Historical solar irradiance data (highlighted in yellow in Table 1) including GHI, direct normal irradiance (DNI), and diffuse radiance were acquired by ASRC; ERA-I data were downloaded and quality controlled by UL-AWS Truepower.[2] Historical time series extend through 2017, with the exceptions of the TD6421 dataset, (the National Center for Environmental Information's [NCEI] "Enhanced Hourly Wind Station Data"), which is only available through 2000 (see Figure 1). These datasets formed the basis for validating the model's historical climatology. We used the period 1998–2017 as the historical climatology baseline.

Table 1. Task 1: Summary of Historical Datasets

Dataset	Type	Spatial Extent	Date Range	Raw Data Storage Requirement (GB)
TD_6421	Station	U.S.	1942–2000	19
NCDC DS3505 (ISD-LITE)	Station	Global	1901–2017	600
USHCN (Monthly)	Station	U.S.	~1820–2017	0.2
USGS	Station	NYS	1995–2017	6.4
PRISM	Gridded (station and radar)	CONUS	1995–2017	34
SUNY-NSRDB	Gridded (satellite)	U.S.	1991–2010	63
SolarAnywhere	Gridded (satellite)	NYS	1998–2017	1,429
ERA-I	Reanalysis	Global	1979–2017	—

Datasets listed in Table 1 were stored on Dr. Freedman's server (Seabreeze) in their original format. Processed data were converted from their original format to an appropriate comma-separated values (CSV) format (example in Figure 2) to enable efficient analysis and cross-platform sharing. All datasets have some degree of quality control performed by their respective data provider (e.g., NCEI, the U.S. Geological Survey), prior to being downloaded. When available, quality control codes were stored with the processed CSV files alongside the corresponding data records. This enabled efficient filtering of the data based on their data provider's quality control standards, which are documented online and in metadata files stored on Seabreeze. All scripts used to process the raw data are written in Python (Van Rossum and Drake 2009) and are retained for future use. Most code used for graphical plots and statistical analysis shown in this report are written in R (R Core Team 2018). Figures 1 and 2 summarize the datasets and parameters used. The following sections describe the individual datasets used for the historical solar, wind, and precipitation analysis.

Figure 1. Summary of Datasets Used, Parameters, and Period of Record

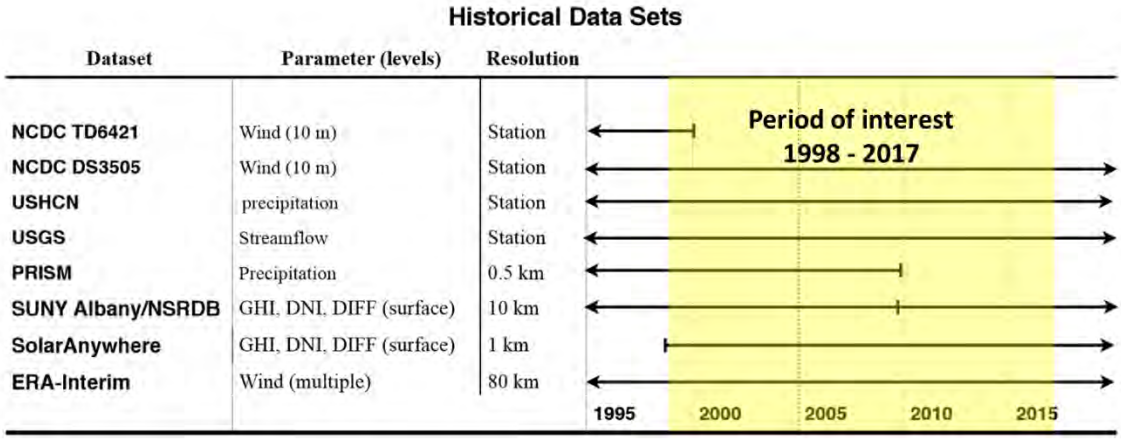

Figure 2. Example of Parameters Format

```
#year,month,day,hour,WSpd_ms-1,WDir_deg,WSpd_10m_ms-1,Z_m,Sp_surf_m,Src_flg,QC_flg
1999,01,01,00,7.7,240,7.7,10.12,7.7,-9999,-9999
1999,01,01,01,6.6,250,6.6,10.12,6.6,-9999,-9999
1999,01,01,02,7.7,280,7.7,10.12,7.7,-9999,-9999
1999,01,01,03,6.1,280,6.1,10.12,6.1,-9999,-9999
1999,01,01,04,5.1,280,5.1,10.12,5.1,-9999,-9999
```

2.1 Solar

Development of a consistent, gridded, baseline solar irradiance (including the global horizontal, direct normal, and diffuse components) was based exclusively upon the satellite-derived 1 km resolution U Albany/SolarAnywhere hourly gridded data encompassing all of New York State (Clean Power Research 2013). Hourly irradiances span from 40.355º to 43.555º in latitude, from -71.655º to -80.555º in longitude, and temporally from 1 January 1998–31 December 2017. Data resolution is approximately 0.01º in latitude and longitude (~1 km × 1 km). This amounts to over 450,000 individual locations in the geographic window, and over 40 billion individual data points.

2.2 Wind

As with the solar irradiance historical climatology, we used a 1998–2017 baseline extracted from the NCEI simplified Integrated Surface Data ("ISD-Lite") using 17 long-term observation sites in New York State that are also the source of the TD6421 and U.S. Historical Climate Network data (Table 1 and Figure 1).

An original Task 1 deliverable required downscaling a reanalysis dataset, such as the Modern-Era Retrospective Analysis for Research and Applications (MERRA), to 9 km using the WRF modeling system to create a gridded dataset for 80, 100, and 120 m AGL winds. However, we found a high resolution (0.125º × 0.125º, or 14 km × 10 km) ERA-I dataset for 10 m AGL winds, and after a careful comparative analysis, we used a modified (by UL-AWS Truepower) 0.75º × 0.75º (60 km × 83 km) ERA-I Reanalysis product for 100 m winds. These datasets were sufficient for the baseline observational climatology and were augmented by the downscaling (to 6 km) of the ERA-I Reanalysis that UL-AWS Truepower performed as part of Task 3.1.

2.3 Precipitation and Streamflow

A continuous station-based time series of observational precipitation (ISD-Lite and USGS) streamflow data, augmented by the extracted gridded Parameter-elevation Regressions on Independent Slopes Model (PRISM 2014 data; see Daly et al. 1994) output was created and quality controlled. This data set was used to validate the model output of the ERA-I historical baseline precipitation climatology.

3 Selection of CMIP5 Subset (Task 2)

The purpose of Task 2 was to select a subset of CMIP5 climate models to use for Task 3 work, producing the downscaled historical and future scenarios model runs. More specifically, the objective was to identify three models that best maximize differences in model climates and biases, are representative of the inter-seasonal and inter-annual climate variability over New York State, and maximize overall model quality. One tool initially proposed to be used in the selection process was the analysis package from the Program for Climate Model Diagnosis and Inter-comparison (PCMDI) at Lawrence Livermore National Laboratory (LLNL) to examine the statistical spread of the CMIP5 model output over New York State.

Figure 3. Map of Original Grid Domains for Historical and Future Modeling Runs

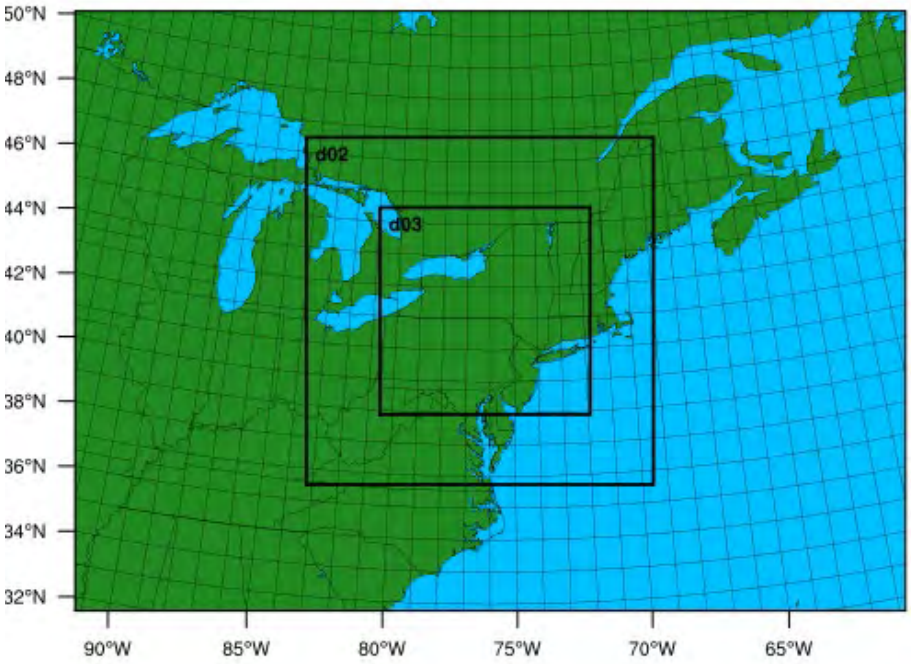

We compiled an initial list of 50 candidate models (Table 2) and developed additional metrics used in choosing the final three models to be selected from the CMIP5 model suite.[3] To perform the CMIP5 selection, historical data from sources encompassing the proposed middle grid (the 18 km "d02"; see Figure 3) for the dynamic downscaling exercises Task 3was analyzed. CMIP5 output was downloaded from the Center for Environmental Data Analysis (CEDA) overseen by the National Centres for Atmospheric Science and Earth Observation in the UK, one of four repositories for CMIP5 output.

Table 2. List of CMIP5 Models and Organizations Used for Task 2

Organization	CMIP5 Model	Resolution (lat × lon degrees)
CSIRO-BOM	ACCESS1-0	1.25 × 1.875
CSIRO-BOM	ACCESS1-3	1.25 × 1.875
BCC	bcc-csm1^{-1}	2.8 × 2.8
BCC	bcc-csm1^{-1}-m	1.12 × 1.12
BNU	BNU-ESM	2.79 × 2.79
CCCma	CanCM4	2.8 × 2.8
CCCma	CanESM2	2.8 × 2.8
NCAR	CCSM4	0.94 × 1.25
NSF-DOE-NCAR	CESM1-BGC	0.9 × 1.25
NSF-DOE-NCAR	CESM1-CAM5	1.4 × 1.4
NSF-DOE-NCAR	CESM1-FASTCHEM	1.4 × 1.4
NSF-DOE-NCAR	CESM1-WACCM	1.4 × 1.4
CMCC	CMCC-CESM	3.75 × 3.75
CMCC	CMCC-CM	0.75 × 0.75
CMCC	CMCC-CMS	1.88 × 1.88
CNRM-CERFACS	CNRM-CM5	1.4 × 1.4
CNRM-CERFACS	CNRM-CM5-2	1.4 × 1.4
CSIRO-QCCCE	CSIRO-Mk3.6.0	1.8 × 1.8
ICHEC	EC-EARTH	1.12 × 1.125
LASG-CESS	FGOALS-g2	1.6 × 2.8
FIO	FIO-ESM	—
NOAA-GFDL	GFDL-CM2p1	—
NOAA-GFDL	GFDL-CM3	2.0 × 2.5
NOAA-GFDL	GFDL-ESM2G	2 × 2.5
NOAA-GFDL	GFDL-ESM2M	2 × 2.5
NASA-GISS	GISS-E2-H	2 × 2.5
NASA-GISS	GISS-E2-H-CC	2 × 2.5
NASA-GISS	GISS-E2-R	2 × 2.5
NASA-GISS	GISS-E2-R-CC	2 × 2.5
MOHC	HadCM3	2.5 × 3.75
MOHC	HadGEM2-AO	2.5 × 3.75
MOHC	HadGEM2-CC	1.25 × 1.875
MOHC	HadGEM2-ES	1.25 × 1.875
INM	inmcm4	1.5 × 2.0
IPSL	IPSL-CM5A-LR	1.8 × 3.75
IPSL	IPSL-CM5A-MR	1.25 × 2.5
IPSL	IPSL-CM5B-LR	1.875 × 1.875
MIROC	MIROC4h	0.5625 × 0.5625

Table 2. (continued)

Organization	CMIP5 Model	Resolution (lat × lon degrees)
MIROC	MIROC5	1.40625 × 1.40625
MIROC	MIROC-ESM	2.8125 × 2.8125
MIROC	MIROC-ESM-CHEM	2.8125 × 2.8125
MPI-M	MPI-ESM-LR	1.9 × 1.9
MPI-M	MPI-ESM-MR	1.8 × 1.8
MPI-M	MPI-ESM-P	1.8 × 1.8
MRI	MRI-CGCM3	1.1 × 1.1
MRI	MRI-ESM1	1.1 × 1.1
NCC	NorESM1-M	1.9 × 2.5
NCC	NorESM1-ME	1.9 × 2.5

During the initial analysis, we discovered some software issues within the PCMDI modules. After an extended troubleshooting effort and communication with the developers at LLNL, we concluded that an alternative quantitative method to compute the model output statistics was required. (According to the PCMDI developers, problems we identified during the installation and troubleshooting of PCMDI were not resolvable by their research group and would require time to fix and would delay our progress to begin WRF downscaling.) Our group at ASRC then developed alternative Python code to duplicate PCMDI applications to be used for identifying likely CMIP5 candidates according to metrics as referenced in the SOW. These include agreement of:

1. Standard deviation of surface irradiance, 10-m wind speed and direction, and precipitation on monthly and daily timescales
2. Root mean square error (RMSE) for the same variables and timescales
3. Coefficient of determination (R^2) for the same variables on monthly and seasonal timescales

We compared the gridded observational dataset for all metrics, averaged to the CMIP5 historical coarser grids, ranging from 1^o to 2.5^o resolution.

A list was then compiled of all CMIP5 model member temporal and spatial attributes (e.g., resolution, number of verticSal levels; see Table 3). Overall CMIP5 model performance was then ranked according to monthly statistics of RMSE and standard deviation as compared with historical observations over New York State (Table 4). Focusing on RMSE for wind speed and GHI, initial rankings were compiled (Table 4). Solid or dashed lines around particular models indicate best performance for the column metric. This preliminary ranking favored the GFDL-CM3 (Geophysical Fluid Dynamics Laboratory Climate Model, version 3), CNRM-CM5 (Centre National de Recherches Météorologiques Climate

Model, version 5), and BNU-ESM (Beijing Normal University Earth System Model) models. However, issues arose with the BNU-ESM model (as discussed below), which resulted in replacement with the MIROC5-ESM. Finally, the CMRN-CM5 model did not have the requisite wind fields to confidently perform the downscaling work; after consulting with Aiguo Dai (one of the collaborators on this project) and the climate modeling community, it was replaced with the National Center for Atmospheric Research (NCAR)-CCSM4 model.

Table 3. All Candidate CMIP5 Members for Downscaling Tasks

					3hr Historical				3hr RCP4.5				3hr RCP8.5				6hr Historical				6hr RCP4.5				6hr RCP8.5				Day Historical					Day RCP4.5					Day RCP8.5					Monthly Historical inter comparison initial conditions				
Organization	CMIP5 Model	<2.5 deg	Number of levels	Resolution (lat x lon degrees)	rsds	pr	ua	va	rsds	pr	ua	va	rsds	pr	ua	va	rsds	pr	ua	va	rsds	pr	ua	va	rsds	pr	ua	va	rsds	pr	ua	va	sfcWind	rsds	pr	ua	va	sfcWind	rsds	pr	ua	va	sfcWind	vas	uas	rsds	pr	sfcWind
CSIRO-BOM	ACCESS1-0	Yes	38	1.25 x 1.875	Yes	Yes	Yes	Yes	Yes	Yes	Yes	Yes	Yes	Yes	Yes	Yes	No	No	Yes	Yes	No	No	Yes	Yes	No	No	Yes	Yes	Yes	Yes	Yes	Yes	Yes	Yes	Yes	Yes	Yes	Yes	Yes	Yes	Yes	Yes	Yes	Yes	Yes	Yes	Yes
CSIRO-BOM	ACCESS1-3	Yes		1.25 x 1.875	Yes	Yes	Yes	Yes	Yes	Yes	Yes	Yes	No	No	No	No	No	No	Yes	Yes	No	No	Yes	Yes	No	No	Yes	Yes	Yes	Yes	Yes	Yes	Yes	Yes	Yes	Yes	Yes	Yes	Yes	Yes	Yes	Yes	Yes	Yes	Yes	Yes	Yes	Yes
BCC	bcc-csm1-1	No	26	2.8 x 2.8	Yes	Yes	Yes	Yes	Yes	Yes	Yes	Yes	Yes	Yes	Yes	Yes	No	No	Yes	Yes	No	No	Yes	Yes	No	No	Yes	Yes	Yes	Yes	Yes	Yes	Yes	Yes	Yes	Yes	Yes	Yes	Yes	Yes	Yes	Yes	Yes	Yes	Yes	Yes	Yes	No
BCC	bcc-csm1-1-m	Yes	NA	1.12 x 1.12	Yes	Yes	Yes	Yes	Yes	Yes	Yes	Yes	Yes	Yes	Yes	Yes	No	No	Yes	Yes	No	No	Yes	Yes	No	No	Yes	Yes	Yes	Yes	Yes	No	Yes	Yes	Yes	Yes	Yes	No	Yes	Yes	Yes	Yes	No	Yes	Yes	Yes	Yes	No
BNU	BNU-ESM	No	NA	2.79 x 2.79	Yes	Yes	Yes	Yes	Yes	Yes	Yes	Yes	Yes	Yes	Yes	Yes	No	No	Yes	Yes	No	No	Yes	Yes	No	No	Yes	Yes	Yes	Yes	Yes	Yes	Yes	Yes	Yes	Yes	Yes	Yes	Yes	Yes	Yes	Yes	Yes	Yes	Yes	Yes	Yes	Yes
CCCma	CanCM4	No	35	2.8 x 2.8	No	No	No	No	No	No	No	No	No	No	No	No	No	No	No	No	No	No	No	No	No	No	No	No	No	Yes	No	No	No	No	Yes	No	No	No	No	No	No	No	No	No	No	No	No
CCCma	CanESM2	No	35	2.8 x 2.8	No	No	No	No	No	No	No	No	No	No	No	No	No	No	Yes	Yes	No	No	Yes	Yes	No	No	Yes	Yes	Yes	Yes	Yes	Yes	Yes	Yes	Yes	Yes	Yes	No	Yes	Yes	Yes	Yes	Yes	Yes	Yes	Yes	Yes	Yes
NCAR	CCSM4	Yes	26	0.94 x 1.25	Yes	Yes	No	No	Yes	Yes	No	No	Yes	Yes	No	No	No	No	Yes	Yes	No	No	Yes	Yes	No	No	Yes	Yes	Yes	Yes	Yes	No	Yes	Yes	Yes	Yes	Yes	No	Yes	Yes	Yes	Yes	No	No	No	No	No	No
NSF-DOE-NCAR	CESM1-BGC	Yes		0.9 x 1.25	No	No	No	No	No	No	No	No	No	No	No	No	No	No	No	No	No	No	No	No	No	No	No	No	No	Yes	No	No	No	No	Yes	No	No	No	No	No	Yes	No	No	No	No	No	No
NSF-DOE-NCAR	CESM1-CAM5	Yes	26	1.4 x 1.4	No	No	No	No	No	No	No	No	No	No	No	No	No	No	No	No	No	No	No	No	No	No	No	No	No	Yes	No	No	No	No	Yes	No	No	No	No	No	Yes	No	No	No	No	No	Yes
NSF-DOE-NCAR	CESM1-FASTCHEM	NA		NA	No	No	No	No	No	No	No	No	No	No	No	No	No	No	No	No	No	No	No	No	No	No	No	No	No	No	No	No	No	No	No	No	No	No	No	No	No	No	No	No	No	No	No	No
NSF-DOE-NCAR	CESM1-WACCM	NA		NA	No	No	No	No	No	No	No	No	No	No	No	No	No	No	No	No	No	No	No	No	No	No	No	No	No	No	No	No	No	No	No	No	No	No	No	No	No	No	No	No	No	No	No	No
CMCC	CMCC-CESM	No		3.75 x 3.75	No	No	No	No	No	No	No	No	No	No	No	No	No	No	No	No	No	No	No	No	No	No	No	No	No	Yes	Yes	Yes	Yes	Yes	No	No	No	No	No	Yes	Yes	Yes	Yes	Yes	Yes	Yes	Yes	Yes	Yes
CMCC	CMCC-CM	Yes		0.75 x 0.75	Yes	Yes	Yes	Yes	Yes	Yes	Yes	Yes	Yes	Yes	Yes	Yes	No	No	Yes	Yes	No	No	Yes	Yes	No	No	Yes	Yes	Yes	Yes	Yes	No	Yes	Yes	Yes	Yes	No	Yes	Yes	Yes	Yes	No	Yes	Yes	Yes	Yes	Yes	No
CMCC	CMCC-CMS	Yes		1.88 × 1.88	No	No	No	No	No	No	No	No	No	No	No	No	No	No	No	No	No	No	No	No	No	No	No	No	Yes	Yes	Yes	Yes	Yes	Yes	Yes	Yes	Yes	Yes	Yes	Yes	Yes	Yes	Yes	Yes	Yes	Yes	Yes	Yes
CNRM-CERFACS	CNRM-CM5	Yes	31	1.4 x 1.4	Yes	Yes	Yes	Yes	Yes	Yes	Yes	Yes	Yes	Yes	Yes	Yes	No	No	Yes	Yes	No	No	Yes	Yes	No	No	Yes	Yes	Yes	Yes	Yes	Yes	Yes	Yes	Yes	Yes	Yes	Yes	No	No	No	No	Yes	Yes	Yes	Yes	Yes	Yes
CNRM-CERFACS	CNRM-CM5-2	NA		NA	No	No	No	No	No	No	No	No	No	No	No	No	No	No	No	No	No	No	No	No	No	No	No	No	No	No	No	No	No	No	No	No	No	No	No	No	No	No	No	No	Yes	Yes	Yes	Yes
CSIRO-QCCCE	CSIRO-Mk3-6-0	Yes	18	1.8 x 1.8	No	No	No	No	No	No	No	No	No	No	No	No	No	No	Yes	Yes	No	No	Yes	Yes	No	No	Yes	Yes	Yes	Yes	Yes	Yes	Yes	Yes	Yes	Yes	Yes	Yes	Yes	Yes	Yes	Yes	Yes	Yes	Yes	Yes	Yes	Yes
ICHEC	EC-EARTH	Yes	62	1.12 x 1.125	Yes	Yes	Yes	Yes	Yes	Yes	Yes	Yes	No	Yes	No	No	No	No	Yes	Yes	No	No	Yes	Yes	No	No	Yes	Yes	Yes	Yes	Yes	Yes	Yes	Yes	Yes	Yes	Yes	Yes	Yes	Yes	Yes	Yes	Yes	Yes	Yes	No	Yes	Yes
LASG-CESS	FGOALS-g2	No	26	1.6 x 2.8	Yes	Yes	No	No	Yes	Yes	No	No	Yes	Yes	No	No	No	No	Yes	Yes	No	No	Yes	Yes	No	No	Yes	Yes	Yes	Yes	Yes	No	Yes	Yes	Yes	Yes	No	Yes	Yes	Yes	Yes	No	No	No	No	Yes	No
FIO	FIO-ESM	NA	NA	NA	No	No	No	No	No	No	No	No	No	No	No	No	No	No	No	No	No	No	No	No	No	No	No	No	No	No	No	No	No	No	No	No	No	No	No	No	No	No	No	No	No	No	No	No
NOAA-GFDL	GFDL-CM2p1	NA	NA	NA	No	No	No	No	No	No	No	No	No	No	No	No	No	No	No	No	No	No	No	No	No	No	No	No	No	No	No	No	No	No	No	No	No	No	No	No	No	No	No	No	Yes	Yes	Yes	No
NOAA-GFDL	GFDL-CM3	Yes	48	2.0 x 2.5	Yes	Yes	Yes	Yes	Yes	Yes	Yes	Yes	Yes	Yes	Yes	Yes	No	No	Yes	Yes	No	No	Yes	Yes	No	No	Yes	Yes	Yes	Yes	Yes	Yes	Yes	Yes	Yes	Yes	Yes	Yes	Yes	Yes	Yes	Yes	Yes	Yes	Yes	Yes	Yes	Yes
NOAA-GFDL	GFDL-ESM2G	No	48	2 x 2.5	Yes	Yes	Yes	Yes	Yes	Yes	No	No	Yes	Yes	Yes	Yes	No	No	Yes	Yes	No	No	Yes	Yes	No	No	Yes	Yes	Yes	Yes	Yes	Yes	Yes	Yes	Yes	Yes	Yes	Yes	Yes	Yes	Yes	Yes	Yes	Yes	Yes	Yes	Yes	Yes
NOAA-GFDL	GFDL-ESM2M	No	48	2 x 2.5	Yes	Yes	Yes	Yes	Yes	Yes	Yes	Yes	Yes	Yes	Yes	Yes	No	No	Yes	Yes	No	No	Yes	Yes	No	No	Yes	Yes	Yes	Yes	Yes	Yes	Yes	Yes	Yes	Yes	Yes	Yes	Yes	Yes	Yes	Yes	Yes	Yes	Yes	Yes	Yes	Yes
NASA-GISS	GISS-E2-H	No	40	2 x 2.5	Yes	Yes	Yes	Yes	No	No	No	No	No	No	No	No	No	No	No	No	No	No	No	No	No	No	No	No	No	Yes	No	No	No	No	Yes	No	No	No	No	No	No	No	No	No	No	No	No	No
NASA-GISS	GISS-E2-H-CC	NA	NA	NA	No	No	No	No	No	No	No	No	No	No	No	No	No	No	No	No	No	No	No	No	No	No	No	No	No	No	No	No	No	No	No	No	No	No	No	No	No	No	No	No	Yes	Yes	Yes	Yes
NASA-GISS	GISS-E2-R	No	40	2 x 2.5	Yes	Yes	Yes	Yes	Yes	Yes	Yes	Yes	No	No	No	No	No	No	No	No	No	No	No	No	No	No	No	No	No	Yes	No	No	Yes	No	Yes	No	No	Yes	No	No	No	No	No	Yes	Yes	Yes	Yes
NASA-GISS	GISS-E2-R-CC	NA	NA	NA	No	No	No	No	No	No	No	No	No	No	No	No	No	No	No	No	No	No	No	No	No	No	No	No	No	No	No	No	No	No	No	No	No	No	No	No	No	No	No	No	Yes	Yes	Yes	Yes
MOHC	HadCM3	No	19	2.5 x 3.75	No	No	No	No	No	No	No	No	No	No	No	No	No	No	No	No	No	No	No	No	No	No	No	No	No	Yes	Yes	Yes	Yes	No	Yes	Yes	Yes	Yes	No	No	No	No	No	Yes	Yes	Yes	Yes
MOHC	HadGEM2-AO	NA	NA	NA	No	No	No	No	No	No	No	No	No	No	No	No	No	No	No	No	No	No	No	No	No	No	No	No	No	No	No	No	No	No	No	No	No	No	No	No	No	No	No	No	Yes	Yes	Yes	Yes
MOHC	HadGEM2-CC	Yes	60	1.25 x 1.875	No	No	No	No	No	No	No	No	No	No	No	No	No	No	Yes	Yes	No	No	Yes	Yes	No	No	Yes	Yes	Yes	Yes	Yes	Yes	Yes	Yes	Yes	Yes	Yes	Yes	Yes	Yes	Yes	Yes	Yes	Yes	Yes	Yes	Yes	Yes
MOHC	HadGEM2-ES	Yes	60	1.25 x 1.875	Yes	Yes	Yes	Yes	Yes	Yes	Yes	Yes	Yes	Yes	Yes	Yes	No	No	Yes	Yes	No	No	Yes	Yes	No	No	Yes	Yes	Yes	Yes	No	No	Yes	Yes	Yes	Yes	Yes	Yes	Yes	Yes	Yes	Yes	Yes	Yes	Yes	Yes	Yes	Yes
INM	inmcm4	Yes	21	1.5 x 2.0	Yes	Yes	Yes	Yes	Yes	Yes	Yes	Yes	Yes	Yes	Yes	Yes	No	No	Yes	Yes	No	No	Yes	Yes	No	No	Yes	Yes	Yes	Yes	No	No	Yes	Yes	Yes	Yes	No	Yes	Yes	Yes	Yes	No	Yes	Yes	Yes	Yes	Yes	No
IPSL	IPSL-CM5A-LR	Yes	39	1.8 x 3.75	Yes	Yes	Yes	Yes	Yes	Yes	No	No	Yes	Yes	Yes	Yes	No	No	Yes	Yes	No	No	Yes	Yes	No	No	Yes	Yes	Yes	Yes	Yes	Yes	Yes	Yes	Yes	Yes	Yes	Yes	Yes	Yes	Yes	Yes	Yes	Yes	Yes	Yes	Yes	Yes
IPSL	IPSL-CM5A-MR	Yes	39	1.25 x 2.5	Yes	Yes	Yes	Yes	Yes	Yes	Yes	Yes	Yes	Yes	Yes	Yes	No	No	Yes	Yes	No	No	Yes	Yes	No	No	Yes	Yes	Yes	Yes	Yes	Yes	Yes	Yes	Yes	Yes	Yes	Yes	Yes	Yes	Yes	Yes	Yes	Yes	Yes	Yes	Yes	Yes
IPSL	IPSL-CM5B-LR	Yes		1.875 × 1.875	No	No	No	No	No	No	No	No	No	No	No	No	No	No	Yes	Yes	No	No	Yes	Yes	No	No	Yes	Yes	Yes	Yes	Yes	Yes	Yes	Yes	Yes	Yes	Yes	Yes	Yes	Yes	Yes	Yes	Yes	Yes	Yes	Yes	Yes	Yes
MIROC	MIROC4h	Yes	56	0.5625 × 0.5625	Yes	Yes	Yes	Yes	Yes	Yes	Yes	Yes	No	No	No	No	No	No	Yes	Yes	No	No	Yes	Yes	No	No	No	No	Yes	Yes	Yes	Yes	Yes	Yes	Yes	Yes	Yes	Yes	Yes	Yes	Yes	Yes	Yes	Yes	No	No	No	No	No
MIROC	MIROC5	Yes	40	1.40625 × 1.40625	Yes	Yes	Yes	Yes	Yes	Yes	Yes	Yes	Yes	Yes	Yes	Yes	No	No	Yes	Yes	No	No	Yes	Yes	No	No	Yes	Yes	Yes	Yes	Yes	Yes	Yes	Yes	Yes	Yes	Yes	Yes	Yes	Yes	Yes	Yes	Yes	Yes	Yes	Yes	Yes	Yes
MIROC	MIROC-ESM	No	80	2.8125 × 2.8125	Yes	Yes	Yes	Yes	Yes	Yes	Yes	Yes	Yes	Yes	Yes	Yes	No	No	Yes	Yes	No	No	Yes	Yes	No	No	Yes	Yes	Yes	Yes	Yes	Yes	Yes	Yes	Yes	Yes	Yes	Yes	Yes	Yes	Yes	Yes	Yes	Yes	Yes	Yes	Yes	Yes
MIROC	MIROC-ESM-CHEM	No	80	2.8125 × 2.8125	Yes	Yes	Yes	Yes	Yes	Yes	Yes	Yes	Yes	Yes	Yes	Yes	No	No	Yes	Yes	No	No	Yes	Yes	No	No	Yes	Yes	Yes	Yes	Yes	Yes	Yes	Yes	Yes	Yes	Yes	Yes	Yes	Yes	Yes	Yes	Yes	Yes	Yes	Yes	Yes	Yes
MPI-M	MPI-ESM-LR	Yes	47	1.9 x 1.9	No	No	No	No	No	No	No	No	No	No	No	No	No	No	Yes	Yes	No	No	Yes	Yes	No	No	Yes	Yes	Yes	Yes	Yes	Yes	Yes	Yes	Yes	Yes	Yes	Yes	Yes	Yes	Yes	Yes	Yes	Yes	Yes	Yes	Yes	Yes
MPI-M	MPI-ESM-MR	Yes		1.8 x 1.8	No	No	No	No	No	No	No	No	No	No	No	No	No	No	Yes	Yes	No	No	Yes	Yes	No	No	Yes	Yes	Yes	Yes	Yes	Yes	Yes	Yes	Yes	Yes	Yes	Yes	Yes	Yes	Yes	Yes	Yes	Yes	Yes	Yes	Yes	Yes
MPI-M	MPI-ESM-P	Yes		1.8 x 1.8	No	No	No	No	No	No	No	No	No	No	No	No	No	No	Yes	Yes	No	No	No	No	No	No	Yes	Yes	Yes	Yes	Yes	No	No	No	No	No	No	No	No	No	No	No	No	Yes	Yes	Yes	Yes	Yes
MRI	MRI-CGCM3	Yes	48	1.1 x 1.1	Yes	Yes	Yes	Yes	Yes	Yes	Yes	Yes	Yes	Yes	Yes	Yes	No	No	Yes	Yes	No	No	Yes	Yes	No	No	Yes	Yes	Yes	Yes	Yes	Yes	Yes	Yes	Yes	Yes	Yes	Yes	Yes	Yes	Yes	Yes	Yes	Yes	Yes	Yes	Yes	Yes
MRI	MRI-ESM1	Yes		1.1 x 1.1	Yes	Yes	Yes	Yes	No	No	No	No	No	No	No	No	No	No	Yes	Yes	No	No	No	No	No	No	No	No	Yes	Yes	Yes	Yes	Yes	No	No	No	No	No	No	No	No	No	No	Yes	Yes	Yes	Yes	Yes
NCC	NorESM1-M	Yes	26	1.9 x 2.5	No	Yes	No	No	No	Yes	No	No	No	Yes	No	No	No	Yes	Yes	No	No	Yes	Yes	No	No	Yes	Yes	No	Yes	Yes	Yes	Yes	No	Yes	Yes	Yes	Yes	No	Yes	Yes	Yes	Yes	No	No	No	Yes	Yes	Yes	No
NCC	NorESM1-ME	NA	NA	NA	No	No	No	No	No	No	No	No	No	No	No	No	No	No	No	No	No	No	No	No	No	No	No	No	No	No	No	No	No	No	No	No	No	No	No	No	No	No	No	No	Yes	Yes	Yes	No

Table 3 (continued)

					3hr Historical				3hr RCP4.5				3hr RCP8.5				6hr Historical				6hr RCP4.5				6hr RCP8.5				Day Historical					Day RCP4.5					Day RCP8.5					Monthly Historical inter comparison initial conditions				
Organization	CMIP5 Model	<2.5 deg	Number of levels	Resolution (lat x lon degrees)	rsds	pr	ua	va	rsds	pr	ua	va	rsds	pr	ua	va	rsds	pr	ua	va	rsds	pr	ua	va	rsds	pr	ua	va	rsds	pr	ua	va	sfcWind	rsds	pr	ua	va	sfcWind	rsds	pr	ua	va	sfcWind	vas	uas	rsds	pr	sfcWind
CSIRO-BOM	ACCESS1-0	Yes	38	1.25 x 1.875	Yes	Yes	Yes	Yes	Yes	Yes	Yes	Yes	Yes	Yes	Yes	Yes	No	No	Yes	Yes	No	No	Yes	Yes	No	No	Yes	Yes	Yes	Yes	Yes	Yes	Yes	Yes	Yes	Yes	Yes	Yes	Yes	Yes	Yes	Yes	Yes	Yes	Yes	Yes	Yes	Yes
CSIRO-BOM	ACCESS1-3	Yes		1.25 x 1.875	Yes	Yes	Yes	Yes	Yes	Yes	Yes	Yes	No	No	No	No	No	No	Yes	Yes	No	No	Yes	Yes	No	No	Yes	Yes	Yes	Yes	Yes	Yes	Yes	Yes	Yes	Yes	Yes	Yes	Yes	Yes	Yes	Yes	Yes	Yes	Yes	Yes	Yes	Yes
BCC	bcc-csm1-1	No	26	2.8 x 2.8	Yes	Yes	Yes	Yes	Yes	Yes	Yes	Yes	Yes	Yes	Yes	Yes	No	No	Yes	Yes	No	No	Yes	Yes	No	No	Yes	Yes	Yes	Yes	Yes	Yes	Yes	Yes	Yes	Yes	Yes	Yes	Yes	Yes	Yes	Yes	Yes	Yes	Yes	Yes	Yes	No
BCC	bcc-csm1-1-m	Yes	NA	1.12 x 1.12	Yes	Yes	Yes	Yes	Yes	Yes	Yes	Yes	Yes	Yes	Yes	Yes	No	No	Yes	Yes	No	No	Yes	Yes	No	No	Yes	Yes	Yes	Yes	Yes	Yes	No	Yes	Yes	Yes	Yes	No	Yes	Yes	Yes	Yes	No	Yes	Yes	Yes	Yes	Yes	No
BNU	BNU-ESM	No	NA	2.79 x 2.79	Yes	Yes	Yes	Yes	Yes	Yes	Yes	Yes	Yes	Yes	Yes	Yes	No	No	Yes	Yes	No	No	Yes	Yes	No	No	Yes	Yes	Yes	Yes	Yes	Yes	Yes	Yes	Yes	Yes	Yes	Yes	Yes	Yes	Yes	Yes	Yes	Yes	Yes	Yes	Yes	Yes
CCCma	CanCM4	No	35	2.8 x 2.8	No	No	No	No	No	No	No	No	No	No	No	No	No	No	No	No	No	No	No	No	No	No	No	No	No	Yes	No	No	No	No	Yes	No	No	No	No	No	No	No	No	No	No	Yes	No
CCCma	CanESM2	No	35	2.8 x 2.8	No	No	No	No	No	No	No	No	No	No	No	No	No	No	Yes	Yes	No	No	Yes	Yes	No	No	Yes	Yes	Yes	Yes	Yes	Yes	No	Yes	Yes	Yes	Yes	Yes	Yes	Yes	Yes	Yes	Yes	Yes	Yes	Yes	Yes	Yes	Yes
NCAR	CCSM4	Yes	26	0.94 x 1.25	Yes	Yes	No	No	Yes	Yes	No	No	Yes	Yes	No	No	No	No	Yes	Yes	No	No	Yes	Yes	No	No	Yes	Yes	Yes	Yes	Yes	Yes	No	Yes	Yes	Yes	Yes	Yes	No	Yes	Yes	Yes	Yes	No	No	No	No	Yes	No
NSF-DOE-NCAR	CESM1-BGC	Yes		0.9 x 1.25	No	No	No	No	No	No	No	No	No	No	No	No	No	No	No	No	No	No	No	No	No	No	No	No	No	Yes	No	No	No	No	Yes	No	No	No	No	No	Yes	No	No	No	No	Yes	No
NSF-DOE-NCAR	CESM1-CAM5	Yes	26	1.4 x 1.4	No	No	No	No	No	No	No	No	No	No	No	No	No	No	No	No	No	No	No	No	No	No	No	No	No	Yes	No	No	No	No	Yes	No	No	No	No	No	Yes	No	No	No	No	Yes	Yes
NSF-DOE-NCAR	CESM1-FASTCHEM	NA		NA	No	No	No	No	No	No	No	No	No	No	No	No	No	No	No	No	No	No	No	No	No	No	No	No	No	No	No	No	No	No	No	No	No	No	No	No	No	No	No	No	No	No	No	No
NSF-DOE-NCAR	CESM1-WACCM	NA		NA	No	No	No	No	No	No	No	No	No	No	No	No	No	No	No	No	No	No	No	No	No	No	No	No	No	No	No	No	No	No	No	No	No	No	No	No	No	No	No	No	No	No	No	No
CMCC	CMCC-CESM	No		3.75 x 3.75	No	No	No	No	No	No	No	No	No	No	No	No	No	No	No	No	No	No	No	No	No	No	No	No	Yes	Yes	Yes	Yes	Yes	No	No	No	No	No	Yes	Yes	Yes	Yes	Yes	Yes	Yes	Yes	Yes	Yes
CMCC	CMCC-CM	Yes		0.75 x 0.75	Yes	Yes	Yes	Yes	Yes	Yes	Yes	Yes	Yes	Yes	Yes	Yes	No	No	Yes	Yes	No	No	Yes	Yes	No	No	Yes	Yes	Yes	Yes	Yes	Yes	No	Yes	Yes	Yes	Yes	No	Yes	Yes	Yes	Yes	No	Yes	Yes	Yes	Yes	Yes	No
CMCC	CMCC-CMS	Yes		1.88 × 1.88	No	No	No	No	No	No	No	No	No	No	No	No	No	No	No	No	No	No	No	No	No	No	No	No	Yes	Yes	Yes	Yes	Yes	Yes	Yes	Yes	Yes	Yes	Yes	Yes	Yes	Yes	Yes	Yes	Yes	Yes	Yes	Yes	Yes
CNRM-CERFACS	CNRM-CM5	Yes	31	1.4 x 1.4	Yes	Yes	Yes	Yes	Yes	Yes	Yes	Yes	Yes	Yes	Yes	Yes	No	No	Yes	Yes	No	No	Yes	Yes	No	No	Yes	Yes	Yes	Yes	Yes	Yes	Yes	No	No	No	No	Yes	Yes	Yes	Yes	Yes	Yes	Yes	Yes	Yes	Yes	Yes
CNRM-CERFACS	CNRM-CM5-2	NA		NA	No	No	No	No	No	No	No	No	No	No	No	No	No	No	No	No	No	No	No	No	No	No	No	No	No	No	No	No	No	No	No	No	No	No	No	No	No	No	No	No	No	Yes	Yes	Yes	Yes	Yes
CSIRO-QCCCE	CSIRO-Mk3-6-0	Yes	18	1.8 x 1.8	No	No	No	No	No	No	No	No	No	No	No	No	No	No	Yes	Yes	No	No	Yes	Yes	No	No	Yes	Yes	Yes	Yes	Yes	Yes	Yes	Yes	Yes	Yes	Yes	Yes	Yes	Yes	Yes	Yes	Yes	Yes	Yes	Yes	Yes	Yes
ICHEC	EC-EARTH	Yes	62	1.12 x 1.125	Yes	Yes	Yes	Yes	Yes	Yes	Yes	Yes	No	Yes	No	No	No	No	Yes	Yes	No	No	Yes	Yes	No	No	Yes	Yes	Yes	Yes	Yes	Yes	Yes	Yes	Yes	Yes	Yes	Yes	Yes	Yes	Yes	Yes	Yes	Yes	Yes	Yes	Yes	Yes
LASG-CESS	FGOALS-g2	No	26	1.6 x 2.8	Yes	Yes	No	No	Yes	Yes	No	No	Yes	Yes	No	No	No	No	Yes	Yes	No	No	Yes	Yes	No	No	Yes	Yes	Yes	Yes	Yes	Yes	No	Yes	Yes	Yes	Yes	No	Yes	Yes	Yes	Yes	No	No	No	No	Yes	No
FIO	FIO-ESM	NA	NA	NA	No	No	No	No	No	No	No	No	No	No	No	No	No	No	No	No	No	No	No	No	No	No	No	No	No	No	No	No	No	No	No	No	No	No	No	No	No	No	No	No	No	No	No	No
NOAA-GFDL	GFDL-CM2p1	NA	NA	NA	No	No	No	No	No	No	No	No	No	No	No	No	No	No	No	No	No	No	No	No	No	No	No	No	No	No	No	No	No	No	No	No	No	No	No	No	No	No	No	No	No	No	No	No
NOAA-GFDL	GFDL-CM3	Yes	48	2.0 x 2.5	Yes	Yes	Yes	Yes	Yes	Yes	Yes	Yes	Yes	Yes	Yes	Yes	No	No	Yes	Yes	No	No	Yes	Yes	No	No	Yes	Yes	Yes	Yes	Yes	Yes	Yes	Yes	Yes	Yes	Yes	Yes	Yes	Yes	Yes	Yes	Yes	Yes	Yes	Yes	Yes	Yes
NOAA-GFDL	GFDL-ESM2G	No	48	2 x 2.5	Yes	Yes	Yes	Yes	Yes	No	No	Yes	Yes	Yes	Yes	Yes	No	No	Yes	Yes	No	No	Yes	Yes	No	No	Yes	Yes	Yes	Yes	Yes	Yes	Yes	Yes	Yes	Yes	Yes	Yes	Yes	Yes	Yes	Yes	Yes	Yes	Yes	Yes	Yes	Yes
NOAA-GFDL	GFDL-ESM2M	No	48	2 x 2.5	Yes	Yes	Yes	Yes	Yes	Yes	Yes	Yes	Yes	Yes	Yes	Yes	No	No	Yes	Yes	No	No	Yes	Yes	No	No	Yes	Yes	Yes	Yes	Yes	Yes	Yes	Yes	Yes	Yes	Yes	Yes	Yes	Yes	Yes	Yes	Yes	Yes	Yes	Yes	Yes	Yes
NASA-GISS	GISS-E2-H	No	40	2 x 2.5	Yes	Yes	Yes	Yes	No	No	No	No	No	No	No	No	No	No	No	No	No	No	No	No	No	No	No	No	No	Yes	No	No	Yes	No	No	No	No	No	No	No	No	No	No	No	No	No	No	No
NASA-GISS	GISS-E2-H-CC	NA	NA	NA	No	No	No	No	No	No	No	No	No	No	No	No	No	No	No	No	No	No	No	No	No	No	No	No	No	No	No	No	No	No	No	No	No	No	No	No	No	No	No	No	No	No	No	No
NASA-GISS	GISS-E2-R	No	40	2 x 2.5	Yes	Yes	Yes	Yes	Yes	Yes	Yes	Yes	No	No	No	No	No	No	No	No	No	No	No	No	No	No	No	No	No	Yes	No	No	Yes	No	Yes	No	No	Yes	No	No	No	No	No	No	No	No	No	No
NASA-GISS	GISS-E2-R-CC	NA	NA	NA	No	No	No	No	No	No	No	No	No	No	No	No	No	No	No	No	No	No	No	No	No	No	No	No	No	No	No	No	No	No	No	No	No	No	No	No	No	No	No	No	No	No	No	No
MOHC	HadCM3	No	19	2.5 x 3.75	No	No	No	No	No	No	No	No	No	No	No	No	No	No	No	No	No	No	No	No	No	No	No	No	No	Yes	Yes	Yes	Yes	No	Yes	Yes	Yes	Yes	No	No	No	No	No	No	No	No	No	No
MOHC	HadGEM2-AO	NA	NA	NA	No	No	No	No	No	No	No	No	No	No	No	No	No	No	No	No	No	No	No	No	No	No	No	No	No	No	No	No	No	No	No	No	No	No	No	No	No	No	No	No	No	No	No	No
MOHC	HadGEM2-CC	Yes	60	1.25 x 1.875	No	No	No	No	No	No	No	No	No	No	No	No	No	No	Yes	Yes	No	No	Yes	Yes	No	No	Yes	Yes	Yes	Yes	Yes	Yes	Yes	Yes	Yes	Yes	Yes	Yes	Yes	Yes	Yes	Yes	Yes	Yes	Yes	Yes	Yes	Yes
MOHC	HadGEM2-ES	Yes	60	1.25 x 1.875	Yes	Yes	Yes	Yes	Yes	Yes	Yes	Yes	Yes	Yes	Yes	Yes	No	No	Yes	Yes	No	No	Yes	Yes	No	No	Yes	Yes	Yes	Yes	Yes	Yes	Yes	Yes	Yes	Yes	Yes	Yes	Yes	Yes	Yes	Yes	Yes	Yes	Yes	Yes	Yes	Yes
INM	inmcm4	Yes	21	1.5 x 2.0	Yes	Yes	Yes	Yes	Yes	Yes	Yes	Yes	Yes	Yes	Yes	Yes	No	No	Yes	Yes	No	No	Yes	Yes	No	No	Yes	Yes	Yes	Yes	Yes	Yes	No	Yes	Yes	Yes	Yes	No	Yes	Yes	Yes	Yes	No	Yes	Yes	Yes	Yes	Yes	No
IPSL	IPSL-CM5A-LR	Yes	39	1.8 x 3.75	Yes	Yes	Yes	Yes	Yes	Yes	No	No	Yes	Yes	Yes	Yes	No	No	Yes	Yes	No	No	Yes	Yes	No	No	Yes	Yes	Yes	Yes	Yes	Yes	Yes	Yes	Yes	Yes	Yes	Yes	Yes	Yes	Yes	Yes	Yes	Yes	Yes	Yes	Yes	Yes
IPSL	IPSL-CM5A-MR	Yes	39	1.25 x 2.5	Yes	Yes	Yes	Yes	Yes	Yes	Yes	Yes	Yes	Yes	Yes	Yes	No	No	Yes	Yes	No	No	Yes	Yes	No	No	Yes	Yes	Yes	Yes	Yes	Yes	Yes	Yes	Yes	Yes	Yes	Yes	Yes	Yes	Yes	Yes	Yes	Yes	Yes	Yes	Yes	Yes
IPSL	IPSL-CM5B-LR	Yes		1.875 × 1.875	No	No	No	No	No	No	No	No	No	No	No	No	No	No	Yes	Yes	No	No	Yes	Yes	No	No	Yes	Yes	Yes	Yes	Yes	Yes	Yes	Yes	Yes	Yes	Yes	Yes	Yes	Yes	Yes	Yes	Yes	Yes	Yes	Yes	Yes	Yes
MIROC	MIROC4h	Yes	56	0.5625 × 0.5625	Yes	Yes	Yes	Yes	Yes	Yes	Yes	Yes	No	No	No	No	No	No	Yes	Yes	No	No	Yes	Yes	No	No	No	No	Yes	Yes	Yes	Yes	Yes	No	No	No	No	No	Yes	Yes	Yes	Yes	Yes	Yes	Yes	Yes	Yes	Yes	Yes
MIROC	MIROC5	Yes	40	1.40625 × 1.40625	Yes	Yes	Yes	Yes	Yes	Yes	Yes	Yes	Yes	Yes	Yes	Yes	No	No	Yes	Yes	No	No	Yes	Yes	No	No	Yes	Yes	Yes	Yes	Yes	Yes	Yes	Yes	Yes	Yes	Yes	Yes	Yes	Yes	Yes	Yes	Yes	Yes	Yes	Yes	Yes	Yes
MIROC	MIROC-ESM	No	80	2.8125 × 2.8125	Yes	Yes	Yes	Yes	Yes	Yes	Yes	Yes	Yes	Yes	Yes	Yes	No	No	Yes	Yes	No	No	Yes	Yes	No	No	Yes	Yes	Yes	Yes	Yes	Yes	Yes	Yes	Yes	Yes	Yes	Yes	Yes	Yes	Yes	Yes	Yes	Yes	Yes	Yes	Yes	Yes
MIROC	MIROC-ESM-CHEM	No	80	2.8125 × 2.8125	Yes	Yes	Yes	Yes	Yes	Yes	Yes	Yes	Yes	Yes	Yes	Yes	No	No	Yes	Yes	No	No	Yes	Yes	No	No	Yes	Yes	Yes	Yes	Yes	Yes	Yes	Yes	Yes	Yes	Yes	Yes	Yes	Yes	Yes	Yes	Yes	Yes	Yes	Yes	Yes	Yes
MPI-M	MPI-ESM-LR	Yes	47	1.9 x 1.9	No	No	No	No	No	No	No	No	No	No	No	No	No	No	Yes	Yes	No	No	Yes	Yes	No	No	Yes	Yes	Yes	Yes	Yes	Yes	Yes	Yes	Yes	Yes	Yes	Yes	Yes	Yes	Yes	Yes	Yes	Yes	Yes	Yes	Yes	Yes
MPI-M	MPI-ESM-MR	Yes		1.8 x 1.8	No	No	No	No	No	No	No	No	No	No	No	No	No	No	Yes	Yes	No	No	Yes	Yes	No	No	Yes	Yes	Yes	Yes	Yes	Yes	Yes	Yes	Yes	Yes	Yes	Yes	Yes	Yes	Yes	Yes	Yes	Yes	Yes	Yes	Yes	Yes
MPI-M	MPI-ESM-P	Yes		1.8 x 1.8	No	No	No	No	No	No	No	No	No	No	No	No	No	No	Yes	Yes	No	No	No	No	No	No	No	No	Yes	Yes	Yes	Yes	Yes	No	No	No	No	No	No	No	No	No	No	No	No	Yes	Yes	Yes	Yes
MRI	MRI-CGCM3	Yes	48	1.1 x 1.1	Yes	Yes	Yes	Yes	Yes	Yes	Yes	Yes	Yes	Yes	Yes	Yes	No	No	Yes	Yes	No	No	Yes	Yes	No	No	Yes	Yes	Yes	Yes	Yes	Yes	Yes	Yes	Yes	Yes	Yes	Yes	Yes	Yes	Yes	Yes	Yes	Yes	Yes	Yes	Yes	Yes
MRI	MRI-ESM1	Yes		1.1 x 1.1	Yes	Yes	Yes	Yes	No	No	No	No	No	No	No	No	No	No	Yes	Yes	No	No	No	No	No	No	Yes	Yes	Yes	Yes	Yes	Yes	No	No	No	No	No	No	No	No	No	No	No	No	Yes	Yes	Yes	Yes
NCC	NorESM1-M	Yes	26	1.9 x 2.5	No	Yes	No	No	No	Yes	No	No	No	Yes	No	No	No	No	Yes	Yes	No	No	Yes	Yes	No	No	Yes	Yes	Yes	Yes	Yes	Yes	No	Yes	Yes	Yes	Yes	No	Yes	Yes	Yes	Yes	No	Yes	Yes	Yes	Yes	Yes	No
NCC	NorESM1-ME	NA	NA	NA	No	No	No	No	No	No	No	No	No	No	No	No	No	No	No	No	No	No	No	No	No	No	No	No	No	No	No	No	No	No	No	No	No	No	No	No	No	No	No	No	No	No	No	No

rsds: Surface irradiance

pr: precipitation

ua(s): u component of the wind (10 m)

va(s): v component of the wind (10 m)

sfcWind: scalar surface wind speed

The last column indicates whether each CMIP5 member's historical conditions can be compared with other models

Table 4. CMIP5 Model Ranking Based on Monthly Standard Deviation Difference (ΔSD)

Solid lines around particular models indicate best performance for the column metric; dashed lines indicate next-best performance.

Model	Wind (land) ΔSD m/s	Model	Wind (offshore) ΔSD m/s	Model	GHI ΔSD W/m^2
MRI-CGCM3	0.0018	ACCESS1-0	0.0413	CNRM-CM5	2.2324
MPI-ESM-LR	0.0028	GFDL-CM3	0.0422	inmcm4	2.8828
GFDL-ESM2G	0.0096	CNRM-CM5	0.0576	IPSL-CM5B-LR	3.1512
IPSL-CM5B-LR	0.0147	CanESM2	0.0707	ACCESS1-0	4.1844
MPI-ESM-MR	0.0154	GFDL-ESM2M	0.0933	GFDL-ESM2G	4.2479
GFDL-CM3	0.0286	BNU-ESM	0.1034	NorESM1-M	4.3753
CSIRO-Mk3.6.0	0.0320	MIROC5	0.1056	GFDL-CM3	4.4974
BNU-ESM	0.0602	MPI-ESM-LR	0.1255	HadGEM2-CC	4.5655
CNRM-CM5	0.0644	MIROC-ESM	0.1285	MRI-CGCM3	4.7435
GFDL-ESM2M	0.0723	GFDL-ESM2G	0.1481	HadGEM2-ES	6.0051

4 Downscaling of CMIP5 (Task 3)

This task included multiple subtasks and objectives:

- Execute ERA-I-forced WRF runs for the 20-year historical period (1998–2017) and calibrate the WRF model.
- Execute historical (1998–2017) CMIP5-forced WRF runs under RCP4.5 and RCP8.5 scenarios and adjust the modeling system by bias correcting the historical baseline using ERA-I output.
- Execute CMIP5 future-scenario runs in WRF (dynamic downscaling) for the near-future and mid-future periods.

4.1 WRF Model Set Up and Testing

The following discussion summarizes the WRF set up and testing protocols followed to develop the final model configuration used in the downscaling experiments.

4.1.1 Efficient Use of Kratos and the UL-AWS Truepower Clusters: Finding the Optimal WRF Model Grid Configuration

Benchmarking experiments were run to determine how many nodes would be necessary to perform the downscaling work on each cluster under different (1) horizontal resolutions, (2) vertical resolutions, and (3) physics schemes. At the time the modeling experiments were initiated, Kratos had 14 nodes (or 392 cores),[4] with the resources shared amongst several ASRC faculty. Tests showed that, for the Kratos cluster, wall clock time[5] showed little improvement beyond 150 cores (or about 5 out of the 14 nodes); for UL-AWS Truepower, results were similar. Arrangements were made with UAlbany IT services to partition Kratos to wall off 4 nodes used exclusively for this project; other individual nodes were used on an as needed basis.

4.1.2 Best Configuration of WRF for the Downscaling Climate Simulation—Horizontal and Vertical Spatial Resolution

The original SOW referenced three nested grids of 36, 12, and 4 km for all downscaling runs (Figure 3). For three CMIP5 members and the two RCP scenarios covering two 20-year periods plus three 20-year historical periods (one per CMIP5 member), including 1 year to spin up each model run, and one 21-year reanalysis (ERA-I) run, a total of 336 years of simulations would need to be performed. The team conducted tests to determine the wall clock time necessary to perform all downscaling tasks. At 4 km resolution, using the nested grid layout as shown in Figure 4, based upon numerical simulations of 1 month of CMIP5 model output, it was estimated that it would take approximately 1.4 years of wall

clock time, even after reducing the number of vertical levels in the model from 50 to 40.[6] Further testing indicated moving to a slightly more coarse resolution with two inner nests of 6 km, a middle nest of 18 km, and outer nest of 54 km (Figure 4) would considerably reduce the projected wall clock time and have little impact on WRF's ability to reproduce weather systems that affect the distribution and availability of renewable energy resources in the State.

Figure 4. Map of Revised Grid Domains for Historical and Future Modeling Runs

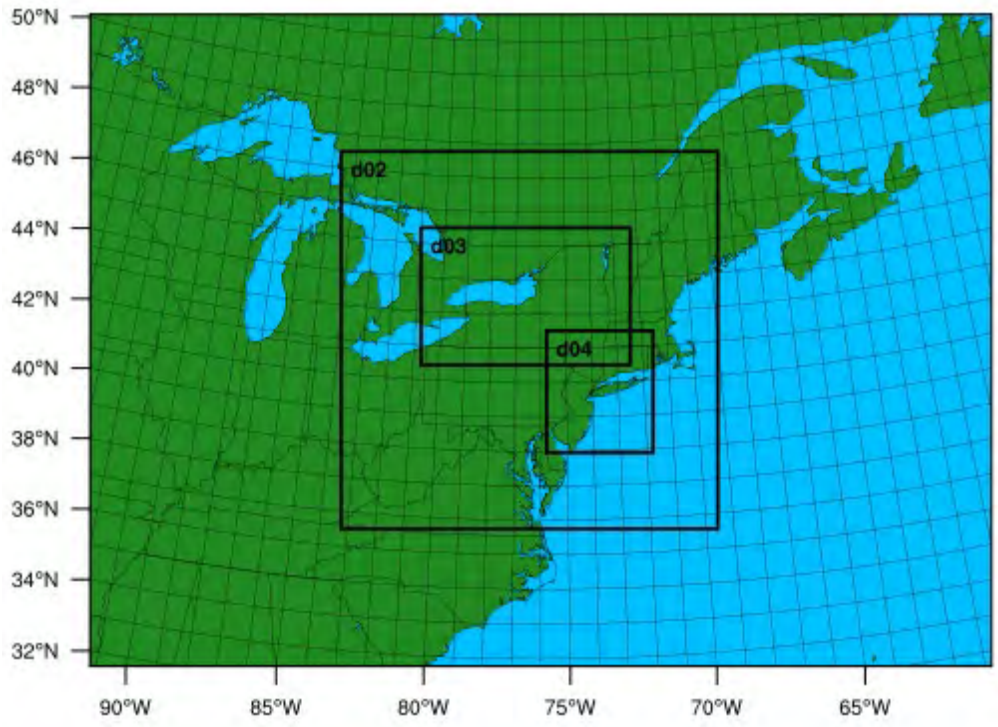

Table 5. Mesonet Observation Sites in New York State for Model Output Comparison

Division	NYSM Station	Longitude	Latitude	Elevation (m)
1. Western Plateau	Belmont, CA	-78.039583	42.242500	418
2. Eastern Plateau	Andes, NY	-74.80139	42.18227	518
3. Northern Plateau	Piseco, NY	-74.50432	43.46474	536
4. Coastal	Wantagh, NY[a]	-73.50616	40.6551	9
5. Hudson Valley	Red Hook, NY[b]	-73.88391	42.00168	65
6. Mohawk Valley	Herkimer, NY	-75.00957	43.03662	218
7. Champlain Valley	Chazy, NY[b]	-73.46461	44.89565	57
8. St. Lawrence Valley	Potsdam, NY	-74.974433	44.656867	129
9. Great Lakes	Ontario, NY/Webster, NY[b]	-77.37331	43.25941	100
10. Central Lakes	Jordan, MN[a]	-76.47006	43.0698	123

[a] Profiler (LiDAR/Radiometer) site.

[b] Profiler (LiDAR/Radiometer) and flux site.

Figure 5. Comparison of WRF Models at 4 km and 6 km Resolutions: Andes, NY (June 2017)

Panels display hourly 2 m air temperature in degrees Celsius (ºC; top left), specific humidity in grams per kilogram (g/kg; upper right), surface irradiance in W/m^2 (lower left), and 80 m wind speed in m/s (lower right).

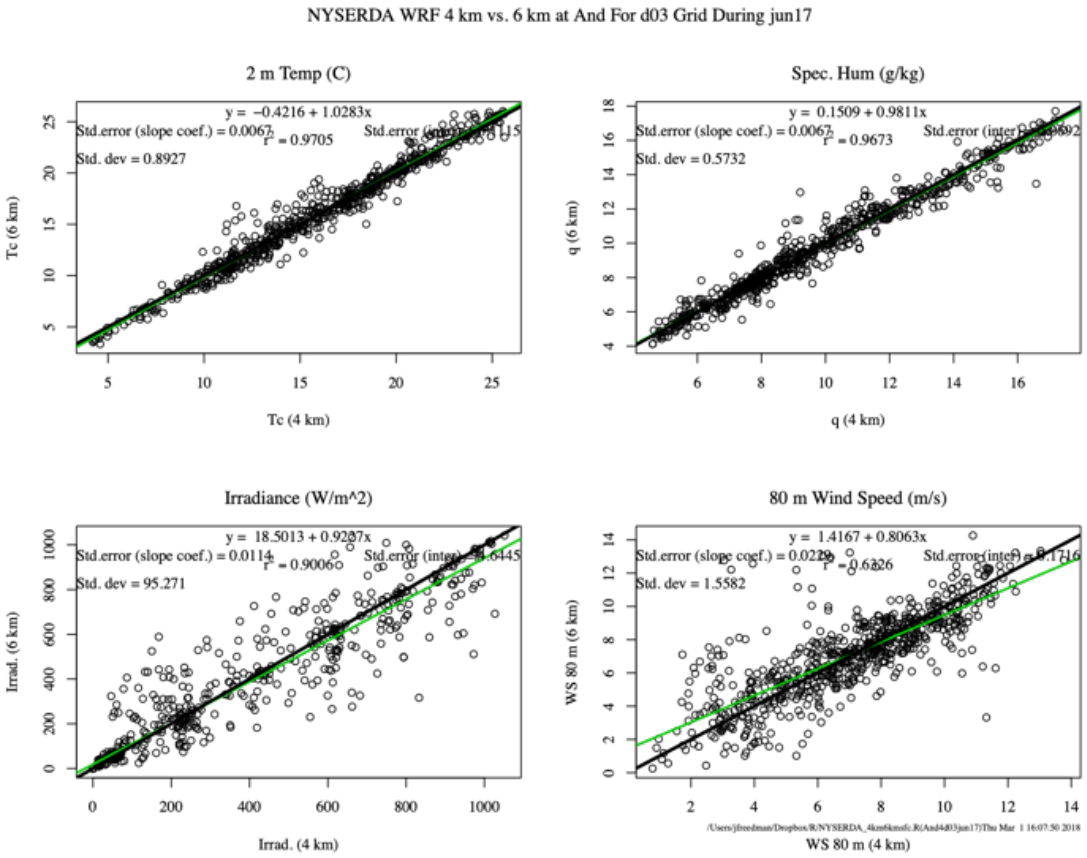

Figure 6. Comparison of WRF Models at 4 km and 6 km Resolutions: Andes, NY (December 2017)

Panels display hourly 2 m air temperature in ºC (top left), specific humidity in g/kg (upper right), surface irradiance in W/m^2 (lower left), and 80 m wind speed in m/s (lower right).

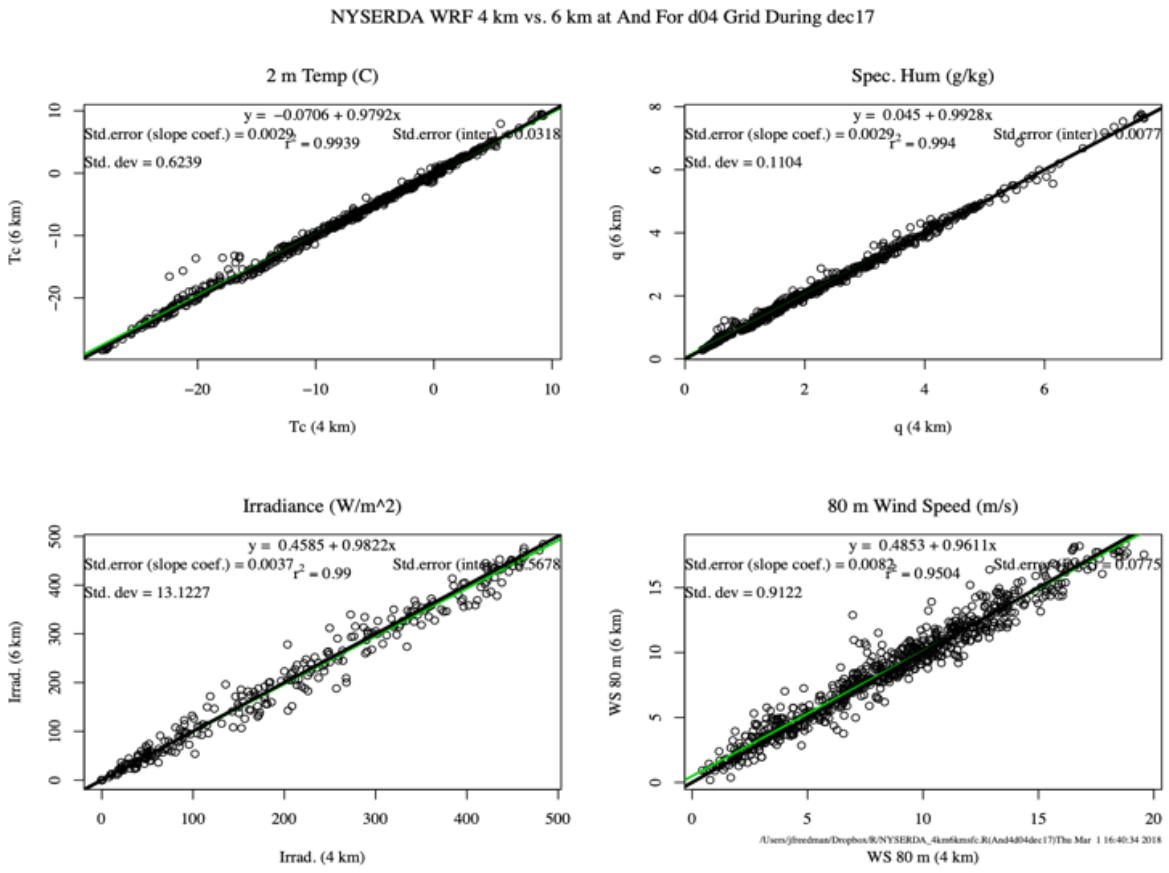

A series of sensitivity studies were performed comparing historical observations with WRF output at 4 and 6 km at selected points throughout the state. Two months were selected to represent the seasonal aspects of the atmospheric variability in the state: June 2017 (to capture convective systems,) and December 2017 (to sample cold season, larger scale weather system that typically affect New York). Model output was compared with New York State Mesonet (NYSM) observations at 10 sites (Table 5), one for each climatological region in New York. Model fields for the innermost grids (d03 and d04) were also examined. For December 2017, there was excellent agreement when comparing coefficient of determination (R^2) relationships for 4 and 6 km simulations for hourly precipitation, 2 m temperature and specific humidity, irradiance and wind speed (Figures 5 through 10), which show results for geographically and climatologically diverse regions (Figures 5 and 6, NYSM station Andes in the Catskills; Figures 7 and 8, NYSM station Ontario on Lake Ontario; and Figures 9 and 10, NYSM station

Wantagh on Long Island). We used monthly precipitation observations (Figure 11, June 2017, and Figure 12, December 2017) from all 10 NYSM stations. We note the very good agreement with little spread for all variables for day weather. Thus, the small change in the inner nest model resolution had a negligible effect on temperature, winds, irradiance, humidity, and precipitation. For June 2017, smaller-scale features (e.g., thunderstorms, PBL depth affecting winds) show more variation, especially for precipitation at Ontario and Andes as the convective nature of the rainfall will show more spatial and temporal variability for even minor changes in model resolution. However, total accumulated monthly precipitation (a much more important factor for climate variability/climate change studies) did not vary as much (Figure 11), for all sites for June and especially for December, indicating that it was model placement of convective precipitation cells that was determinative of agreement between the two test runs. For some sites (e.g., Piseco and Red Hook), the WRF 6 km performed better for accumulated precipitation than the 4 km runs. We note that for the winds at Wantagh (Figure 9), a coastal site influenced by maritime weather and sea breezes, there is little difference in wind speed correlation for the 4 and 6 km runs between June and December (Figures 9 and 10).

Figure 7. Comparison of WRF Models at 4 km and 6 km Resolutions: Ontario, NY (June 2017)

Panels display hourly 2 m air temperature in ºC (top left), specific humidity in g/kg (upper right), surface irradiance in W/m^2 (lower left), and 80 m wind speed in m/s (lower right).

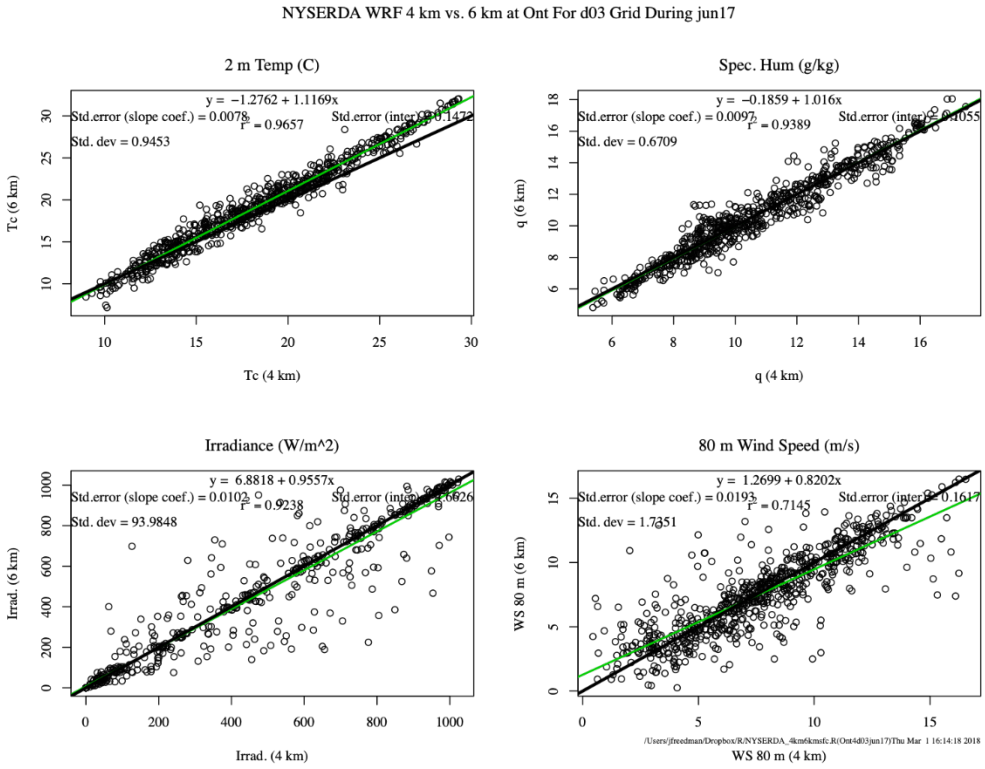

Figure 8. Comparison of WRF Models at 4 km and 6 km Resolutions: Ontario NY (December 2017)

Panels display hourly 2 m air temperature in ºC (top left), specific humidity in g/kg (upper right), surface irradiance in W/m^2 (lower left), and 80 m wind speed in m/s (lower right).

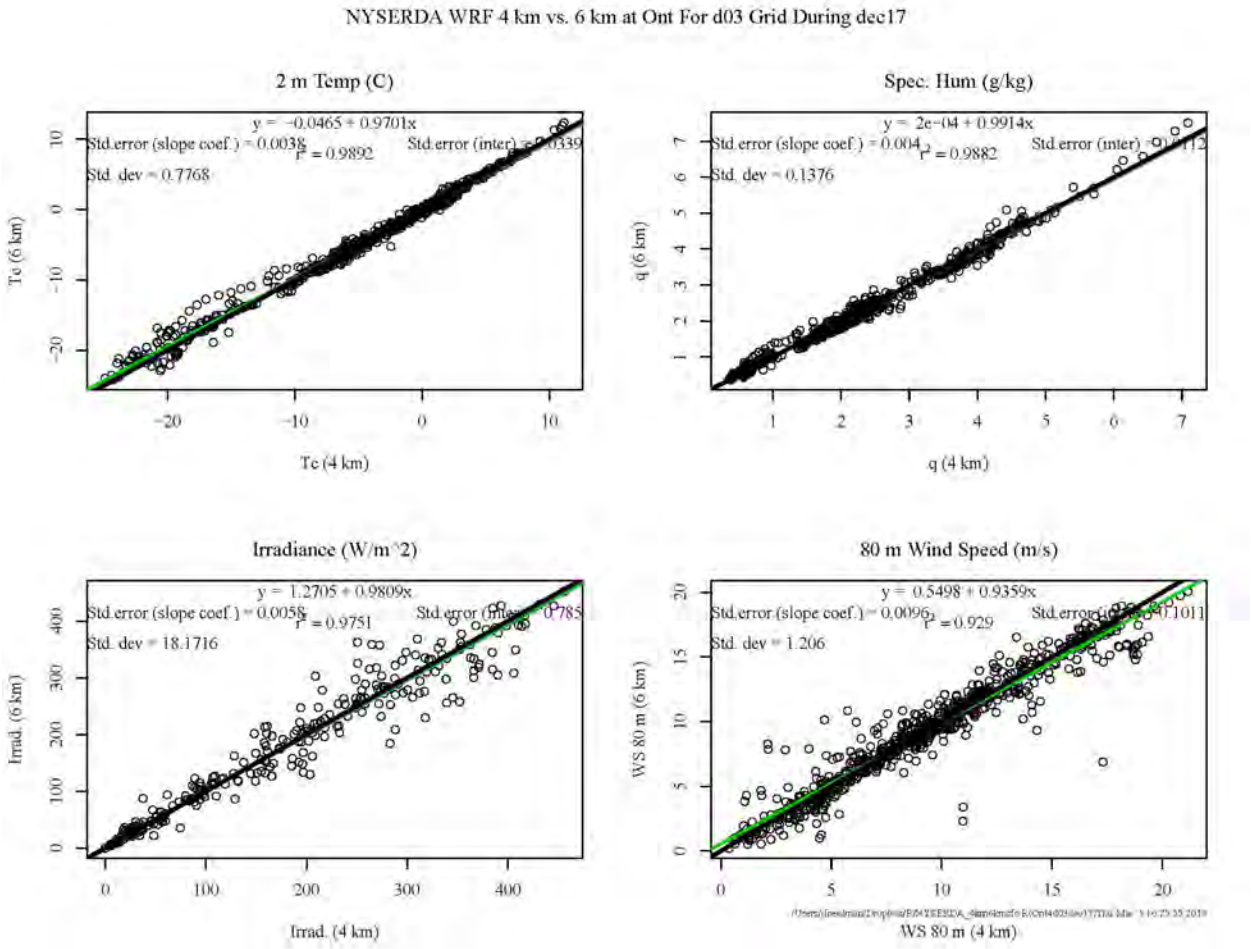

Figure 9. Comparison of WRF Models at 4 km and 6 km Resolutions: Wantagh, NY (June 2017)

Panels display hourly 2 m air temperature in ºC (top left), specific humidity in g/kg (upper right), surface irradiance in W/m^2 (lower left), and 80 m wind speed in m/s (lower right).

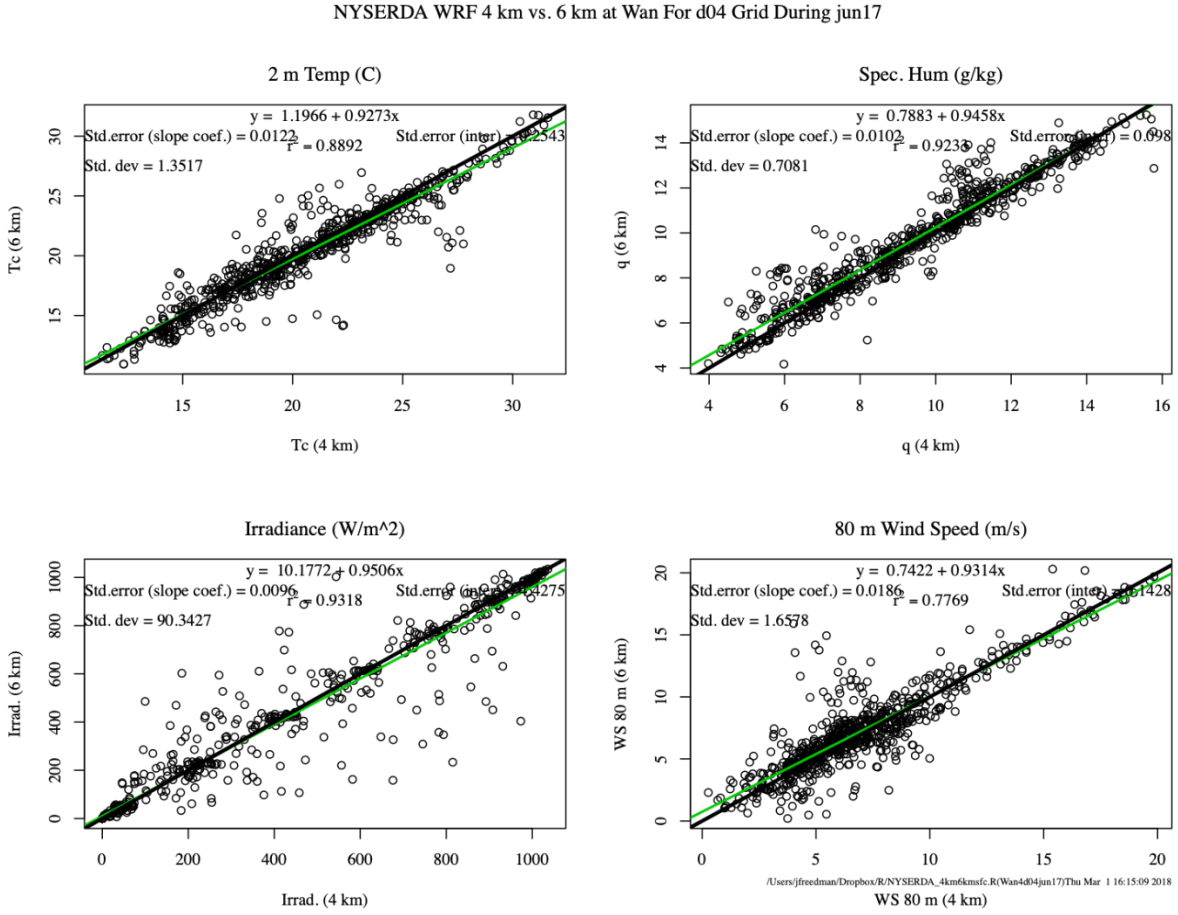

Figure 10. Comparison of WRF Models at 4 km and 6 km Resolutions: Wantagh, NY (December 2017)

Panels display hourly 2 m air temperature in ºC (top left), specific humidity in g/kg (upper right), surface irradiance in W/m^2 (lower left), and 80 m wind speed in m/s (lower right).

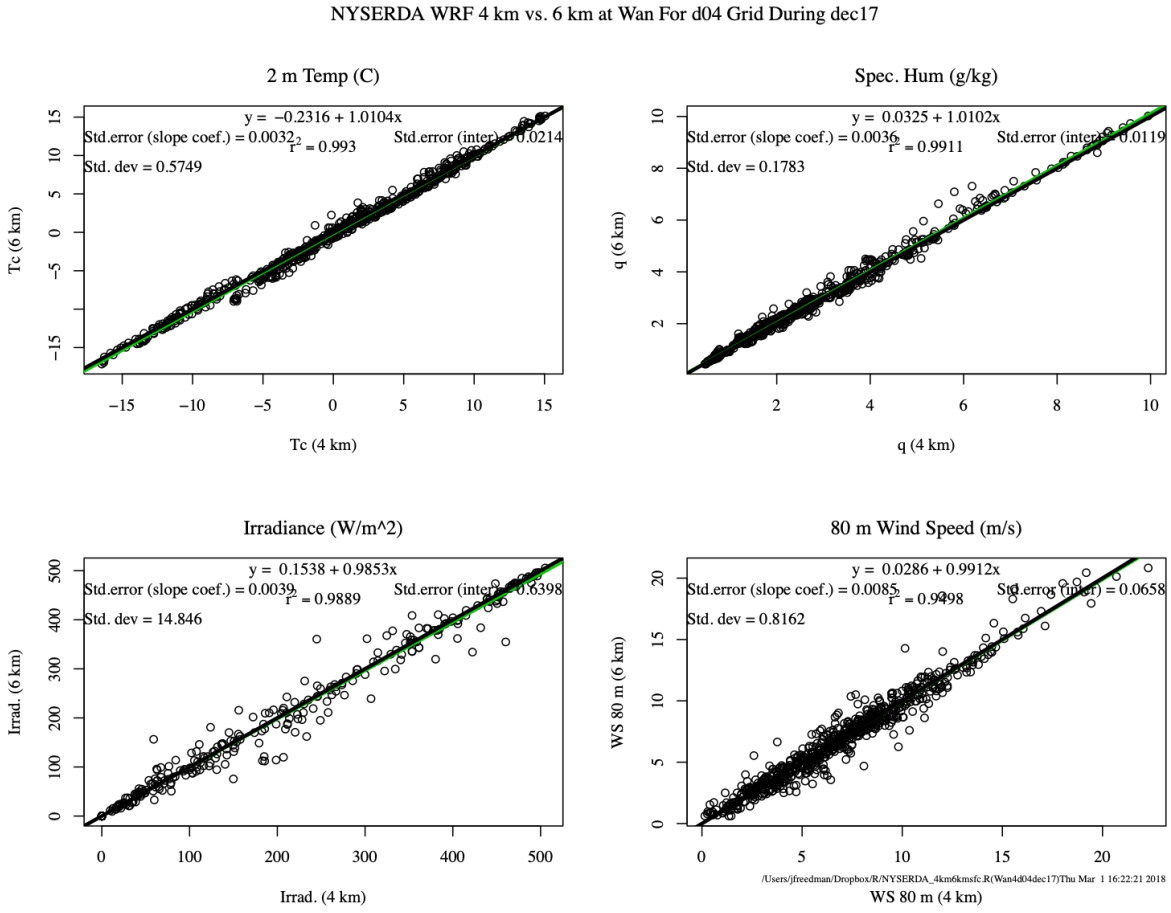

Figure 11. Accumulated Monthly Precipitation: June 2017

Accumulated precipitation for June 2017 is shown for WRF 4-km and 6-km runs at the NYSM stations listed in Table 5. Observational data from the NYSM for Andes were missing for June.

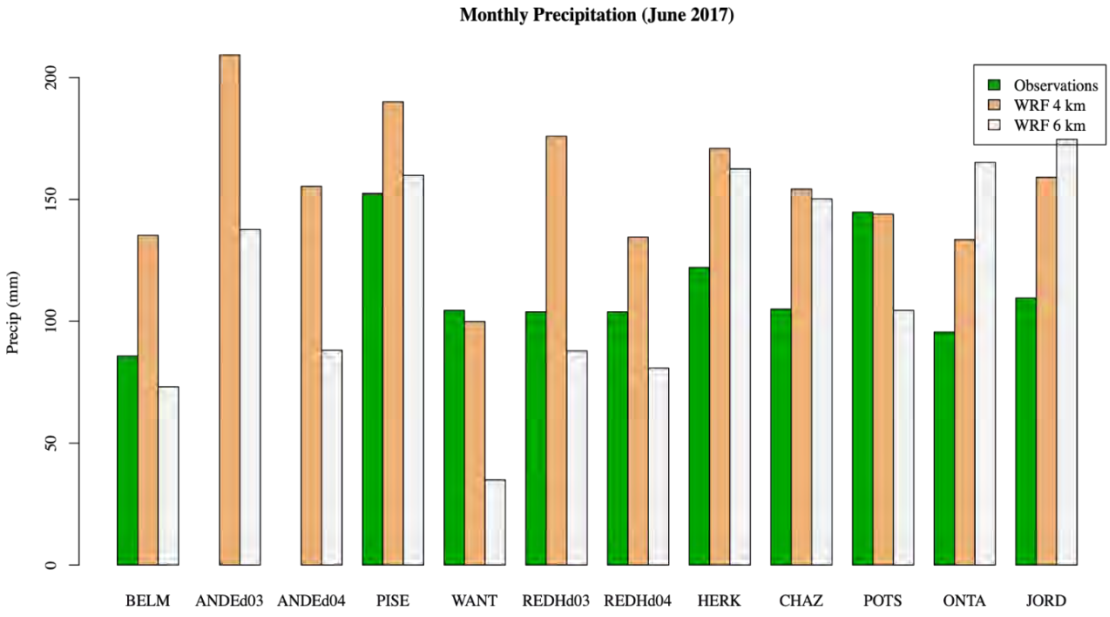

Figure 12. Accumulated Monthly Precipitation: December 2017

Accumulated precipitation for December 2017 is shown for WRF 4-km and 6-km runs at the NYSM stations listed in Table 5.

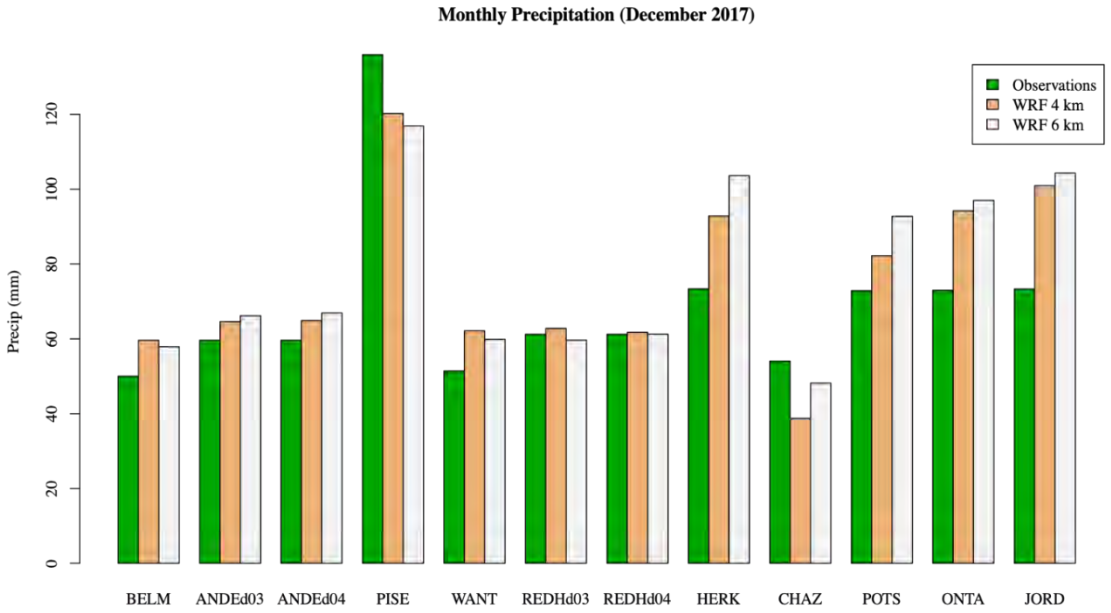

4.1.3 Determining the Relaxation Zone: Number of Grid Points as Buffer

Testing, consultation with other WRF user groups, and the current literature suggested using four grid points (24 km) as the relaxation zone configuration for the chosen nest grouping.

4.1.4 Surface Lake Physics

Two of the Great Lakes (Erie and Ontario) play a prominent role in the weather and climate of Western New York and Northern New York (e.g., lake effect snow, cloud suppression near the lakes during the warm season, and lake breezes). Therefore, sensitivity tests were performed on WRF's surface lake physics scheme to determine its efficacy in better reproducing the regional weather and climate attributes. Two six-month sensitivity studies—one with the lake physics scheme turned on and one without—were conducted. Results indicated that the lake model reasonably reproduced lake water temperature profiles and lake water skin temperature evolution (compared with observations) from the cold to warm seasons.

4.1.5 Dynamics: Whether to Turn on Adaptive Time Steps

Adaptive time stepping maximizes the model time step[7] while keeping the model numerically stable. The model time step is adjusted based on the domainwide horizontal and vertical stability criterion (Courant-Friedrichs-Lewy condition). Sensitivity tests showed that using adaptive time stepping shortens run times (i.e., wall clock time), providing a more efficient use of computational resources.

4.1.6 Model Spin Up: How Much Is Necessary to Equilibrate Soil Moisture

From the sensitivity studies performed above and feedback from the WRF User Community, we determined that one year of spin-up time per 20-year run would be sufficient for achieving model soil moisture equilibrium.

4.1.7 Output of Necessary Variables and Final WRF Configuration

We worked with UAlbany information technology services to confirm that all raw data, estimated at up to 300 terabytes (TB), remained accessible during the active phase of the project. With the above adjustments, the final model configuration is shown in Table 6. A complete 21-year run, including one year spin-up, took an average of about 17 days wall clock time.

Table 6. WRF Modeling System Setup

Configuration Element	Value
Domains	54, 18, 6 km (2)
Domain size (grid array)	(54 × 39), (67 × 67),(112 × 76,55 × 64)
Initialization	One-year spin-up
Vertical levels	40 (10 within PBL)
Time step	60 minutes
Microphysics	WSM6-class graupel scheme
Radiation	RRTMG Shortwave/Longwave
Planetary Boundary Layer (PBL)	MYNN 2.5 level TKE scheme
Cumulus	Kain-Fritsch
Land-surface	Noah Land-Surface Model
Soil levels	4

4.2 Execution of ERA-I-forced WRF Runs for the 20-year Historical Period (1998–2017) and Model Calibration

As part of the downscaling efforts, the SOW specified that the WRF model would use horizontal (i.e., east, west, north, and south) boundary conditions from the National Aeronautics and Space Administration's (NASA) MERRA reanalysis dataset for the 20-year historical period (1998–2017). However, UL-AWS Truepower's internal analysis found that the ERA-I reanalysis product performed better than MERRA, version 1 (MERRA1) in terms of hourly correlation of wind speeds to tall tower data (Brower et al. 2012). Another consideration involved the homogeneity of reanalysis products over long periods to avoid introducing false trends or spurious discontinuities. Studies have shown that the ERA-I dataset is more homogeneous (i.e., better continuity in time series and spatial fields) than other reanalysis products such as the National Oceanic and Atmospheric Administration's (NOAA) Climate Forecast System Reanalysis, MERRA1, and the National Centers for Environmental Prediction/NCAR datasets (Lileo and Petrik 2011, Decker et al. 2012, Brower et al. 2012). However, these studies did not involve dynamical downscaling with the WRF model. We also noted that MERRA1 and MERRA2 were not "WRF-ready" because they required considerable effort to ingest into the WRF model. Therefore, the team used the ERA-I to ensure a more robust historical baseline climatology and to conserve computational resources.

The initial ERA-I model runs encountered a few issues:

1. The model run stopped without explanation.
2. Sea surface temperature (SST) fields appeared questionable due to the missing diurnal cycle.
3. The initial microphysics scheme (MP) choice, Thompson aerosol-aware (MP28) (Thompson and Eidhammer 2014), produced spurious atmospheric fields.
4. Spectral nudging.

We resolved the WRF run stoppage with a modification of the use of adaptive time stepping. The SST issue stemmed from the way values of SST are output in the ERA-I dataset (once daily). We determined that the downscaled WRF runs do produce diurnal and day-to-day changes in skin temperature, which, over water, is equivalent to the SST.

After extended troubleshooting and discussion, including correspondence with Greg Thompson (NCAR project scientist and developer of the MP scheme), we determined that the Thompson MP scheme was incompatible with other necessary parameterizations, used in the WRF set up, which produced anomalous precipitation sea level pressure (SLP) and precipitation fields (Figure 13).

We then performed sensitivity experiments comparing the Thompson Aerosol Aware scheme with the WRF Single-Moment 6-class (WSM6) scheme (Hong and Lim 2006). These results confirmed realistic SLP and precipitation fields for the WSM6 scheme (see, e.g., Figure 14).

Figure 13. Thompson Aerosol Aware Scheme Simulation of Sea Level Pressure, Wind, and Precipitation

D01 grid ERA-I downscaled simulation using the Thompson Aerosol Aware scheme, 54-km resolution, January 2, 1997. Pressure in hectopascals (hPa) represented by contour lines, 10-m winds in millimeters per hour (mm/hr) by barbs, and precipitation in mm/hr by filled contours.

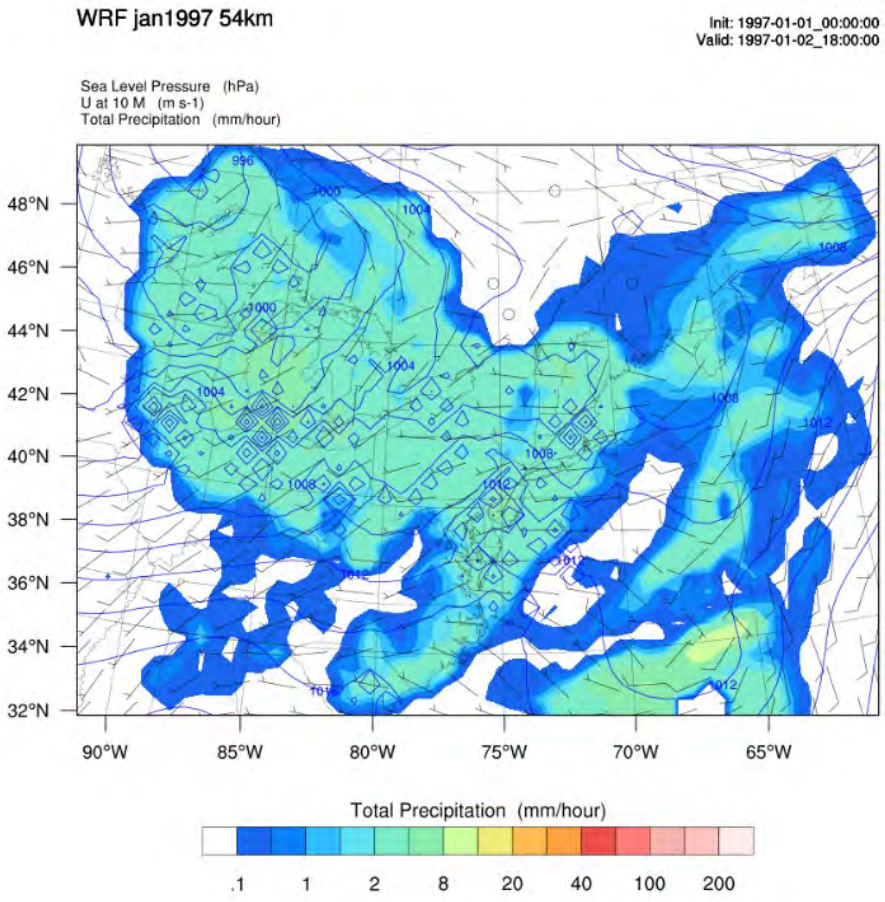

Figure 14. WSM6 Scheme Simulation of Sea Level Pressure, Wind, and Precipitation

D01 grid ERA-I downscaled simulation using the WSM6 microphysics scheme, 54-km resolution, January 2, 1997. Pressure in hectopascals (hPa) represented by contour lines, 10-m winds in mm/h by barbs, and precipitation in mm/h by filled contours.

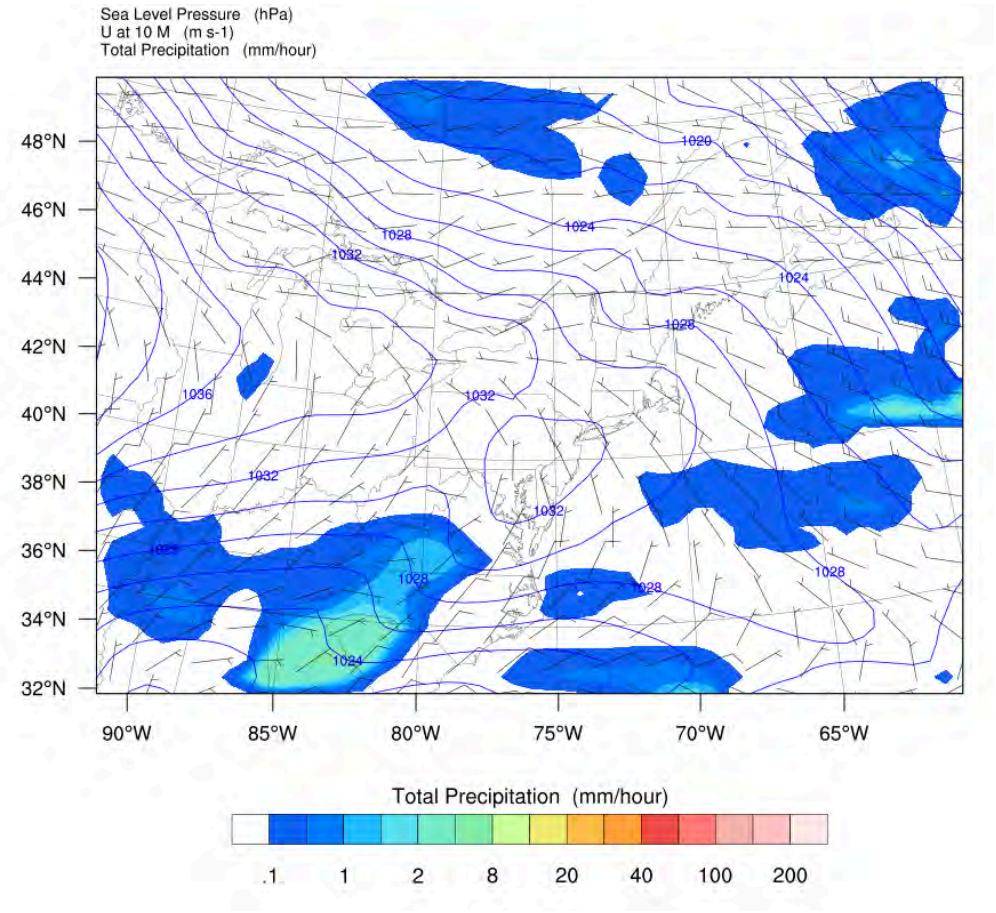

Regarding spectral nudging, sensitivity analysis showed that there was little difference in the 500 hPa temperature fields with or without this feature (Figure 15). This outcome gave us confidence that using the scheme would provide the proper constraints on model drift but not produce any spurious results on the inner high-resolution nests.

Figure 15. Comparison of 500 hPa Temperature Fields With and Without Spectral Nudging

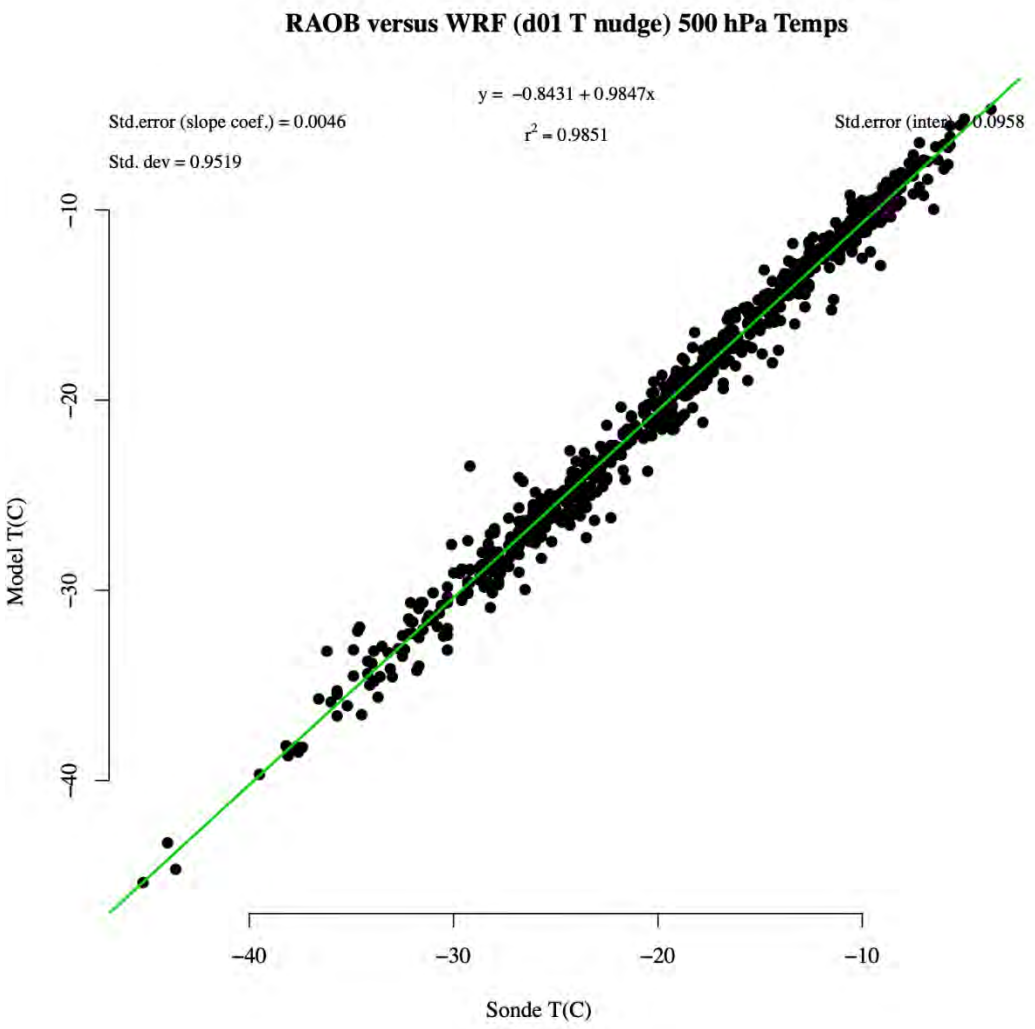

These WRF configuration modifications confirmed good agreement with ERA-I runs and observations. Figure 16 demonstrates this agreement through Weibull wind speed distribution plots, first described by Fréchet (1927), for a sample point in the d03 domain (6 km resolution) at Albany, NY. The Weibull wind speed distribution, a critical statistical analysis tool for wind energy industry, is used to directly estimate power output at a wind turbine. The Weibull probability density (that a speed will fall within a bin of unit width centered on speed V) is given by:

$$p(V) = \frac{k}{A}\frac{(V)^{k-1}}{(V)}e^{-\left(\frac{V}{A}\right)^{k}}$$

Equation 1

The Weibull function contains two parameters*: A*, the scale parameter, with a dimension of speed closely relates to wind speed, and *k*, the nondimensional shape parameter, which controls the width of the distribution. Figure 16 shows that the ERA-I downscaled 20-m wind speeds and the Albany Automated Surface Observation System (ASOS) observations have nearly identical *A* and *k* parameters, indicating model downscaling shows good fidelity to the observations.

Figure 16. Weibull Wind Speed Distribution: Albany, NY, ASOS Station (1997–2002)

The left panel shows the Weibull distribution of observed wind speeds at 10 m AGL at the Albany airport. The right panel shows the distribution of WRF ERA-I downscaled wind speeds at 20 m AGL.

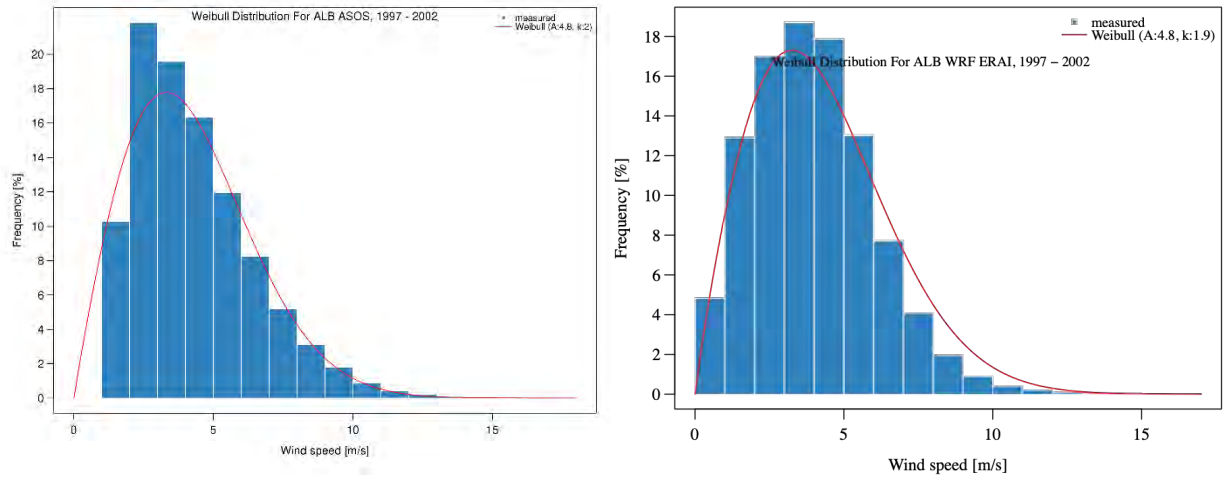

4.3 Execution of CMIP5-forced WRF Runs for the 20-Year Historical Period (1998–2017)

We first confirmed that the historical baseline to be used for the CMIP5 downscaling analysis is consistent with the ERA-I downscaled fields. We used the ERA-I fields to adjust the historical baseline outputs of the three CMIP5 model members to correct for any systematic biases (see section 4.3.2).

4.3.1 Initial Analysis of Model Fields

This section presents the initial comparison of model output fields from GFDL-CM3, NCAR-CCSM4, and BNU.[8] These data have not been bias corrected.

The historical baselines for the ERA-I and GFDL-CM3 compare quite well for wind, irradiance, and precipitation. For example, 100 m AGL wind roses for Albany, NY, showed strong agreement in direction, speed, and distribution (Figure 17), with negligible differences in average wind speed

(6.56 m/s for ERA-I versus 6.72 m/s for GFDL-CM3, or a <2.5% difference). Overall good agreement is also shown when examining regions that experience local and regional-scale circulations, such as the sea breeze. Figure 18 depicts 20-year (1998–2017) WRF 6-km downscaled June diurnal 100 m AGL wind speeds interpolated to John F. Kennedy International Airport (JFK), Jamaica, NY, on Long Island, with a nocturnal early morning positive speed bias (higher GFDL-CM3), but negligible differences during the afternoons. For irradiance (Figure 19), diurnal differences are also small, with, for example, maximum biases (~5%) during midday periods as interpolated to the Montgomery, NY, ASOS station (MGJ), about 10 km west of Newburgh.

Figure 17. Wind Roses for Averaged Wind Speed: Albany, NY

Wind speed at 100 m for the period 1998–2017. Wind speed frequency is shown in 4 m/s bins (up to 16 m/s), across 12 direction sectors (every 30 degrees). The left panel shows the ERA-I historical baseline; the right panel shows the CM3 historical baseline.

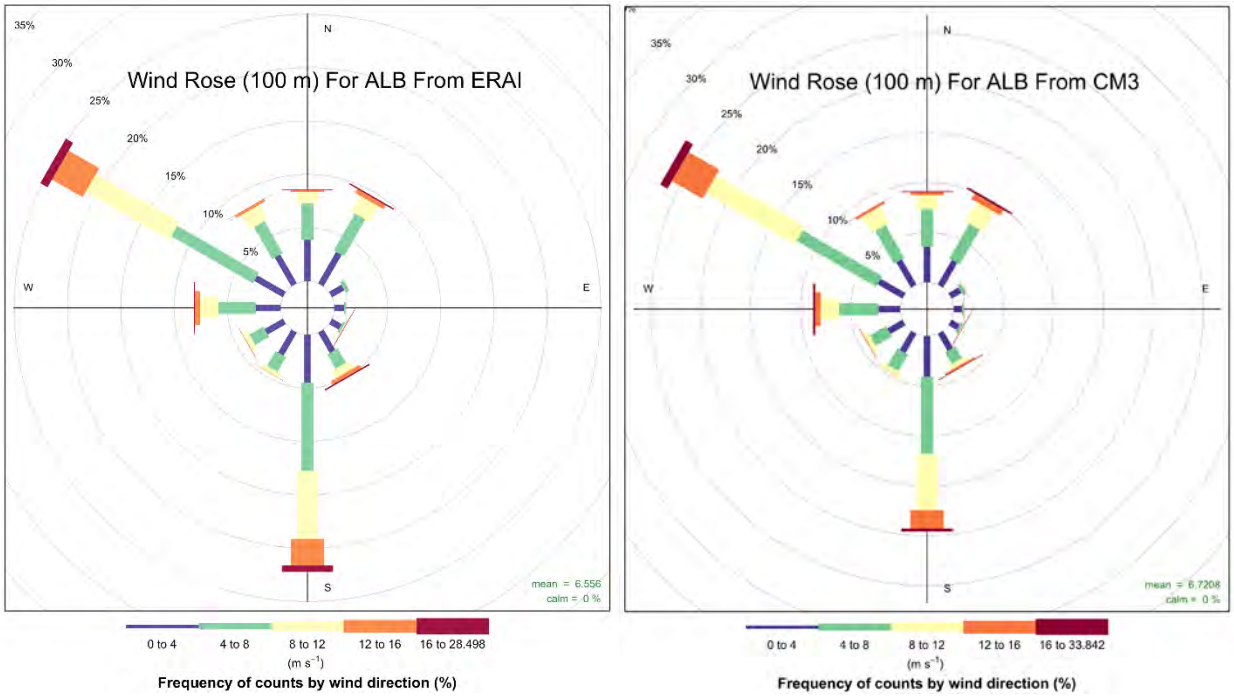

Figure 18. Diurnal Wind Speed: Jamaica, NY

Boxplots of 20-year (1998–2017) June wind speed (m/s) distributions at JFK for ERA-I (black median, green whiskers) and GFDL-CM3 (red median, blue whiskers). The box represents the span of the wind speed distribution within the first and third quartiles; upper and lower whiskers indicate maximum and minimum values; and open circles denote outliers.

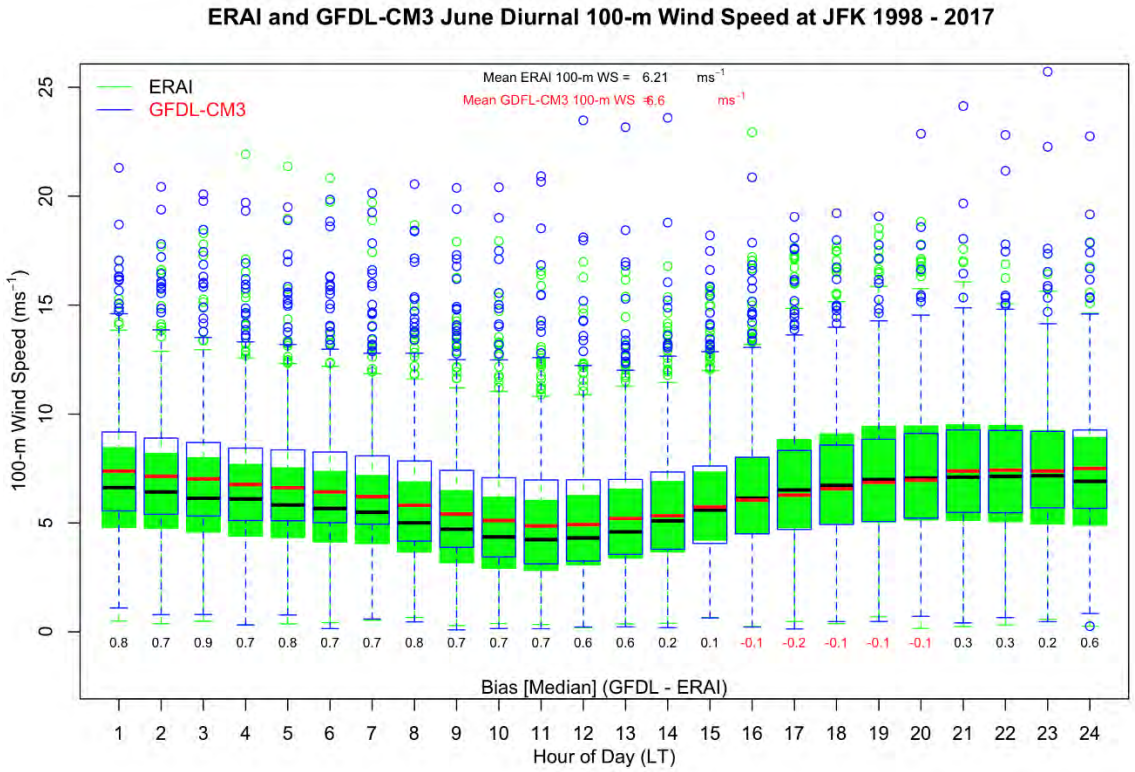

Figure 19. Global Horizontal Irradiance: Montgomery, NY

Boxplots of 20-year (1998–2017) June GHI distributions at MGJ for ERA-I (black median, green whiskers) and GFDL-CM3 (red median, blue whiskers). The box represents the span of the GHI distribution within the first and third quartiles; whiskers indicate maximum and minimum values; and open circles denote outliers.

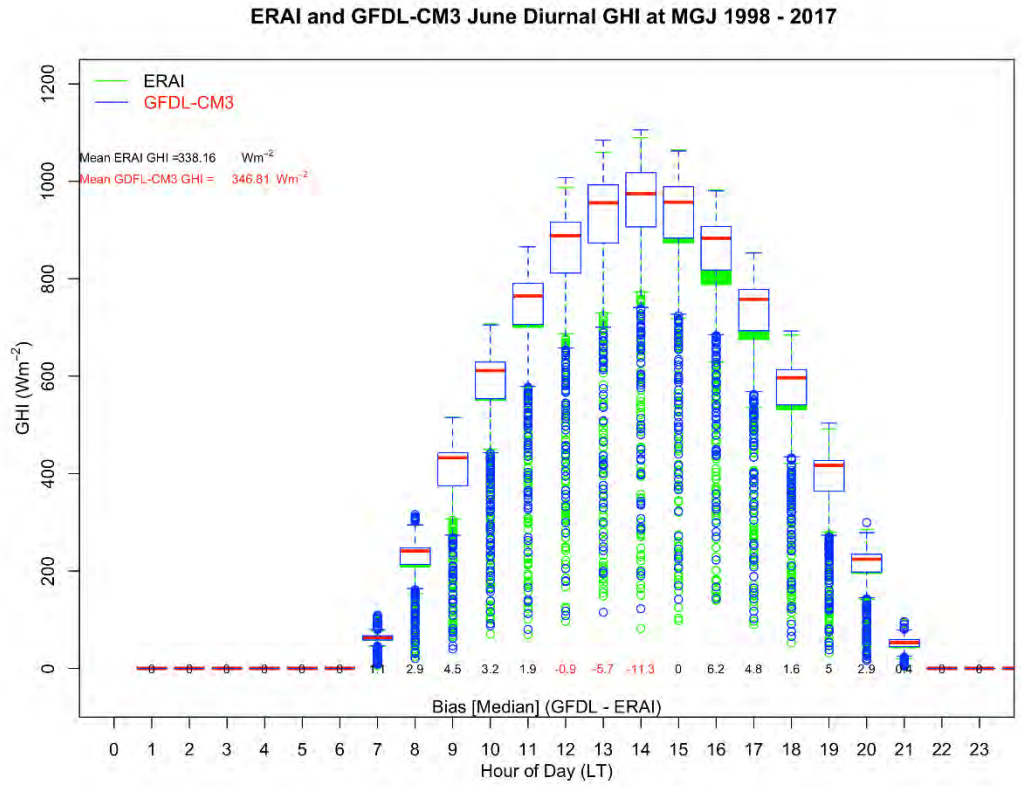

For precipitation, annual accumulation and daily distributions are good indicators of qualitative agreement. Daily accumulated precipitation at Syracuse, NY (SYR), showed good agreement between the ERA-I and GFDL-CM3 historical runs (Figure 20). Histograms of the daily precipitation frequency are also similar (Figure 21), indicating that the GFDL-CM3 historical runs capture not only he accumulated annual precipitation but also the distribution of the magnitude of daily precipitation events. The CMIP5 “historical” runs, unlike the reanalysis, do not depict actual historical weather. Because they are forced with atmospheric concentrations of carbon dioxide (CO_2) and other radiative gases, aerosols, and so forth, the simulations describe the state of the atmosphere in terms of expected weather and climate.

Figure 20. Modeled Historical Runs for Daily and Accumulated Precipitation: Syracuse, NY

Simulated year 2001. The top panel shows accumulated precipitation from ERA-I (solid black line) and GFDL-CM3 (dashed red line). The middle and bottom panels show daily precipitation for ERA-I and GFDL-CM3, respectively.

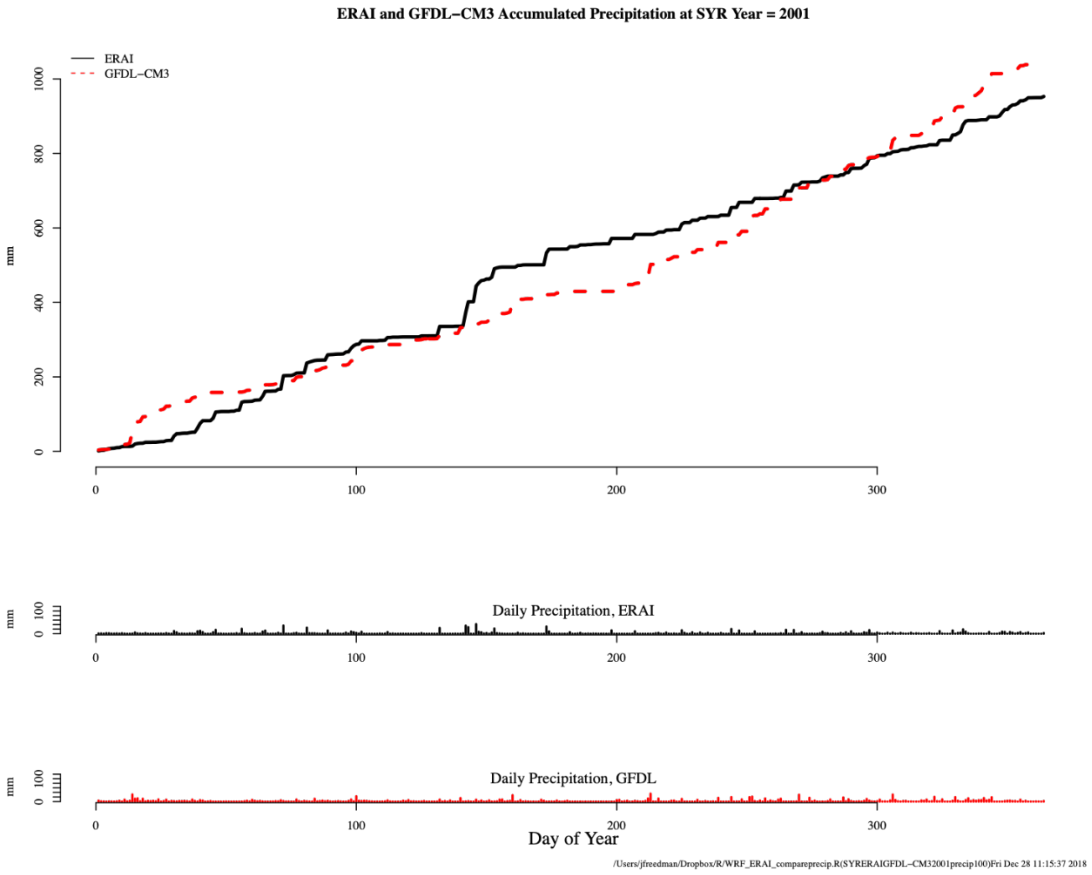

Figure 21. Daily Precipitation Frequency: Montgomery, NY (1998–2017)

Histograms show the frequency distribution of daily precipitation for the ERA-I (left) and GFDL-CM3 (right) historical simulations for the period 1998–2017.

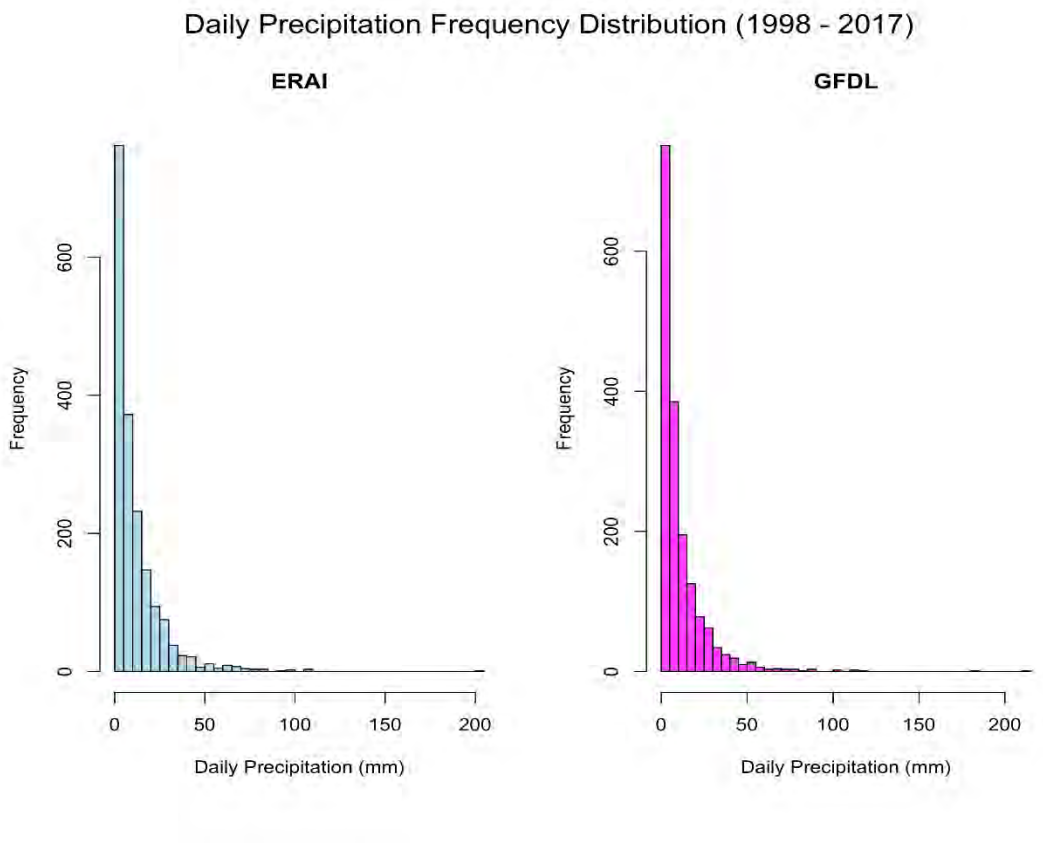

A comparison of the ERA-I and NCAR-CCSM4 global horizontal irradiance, surface (10-m) wind speeds, and precipitation shows good overall agreement on the 18 km (d02) grid (Figure 22). This includes generally increasing GHI with decreasing latitude (Figure 22, left), higher 10-m wind speeds over offshore waters and the Great Lakes (Figure 22, middle), and precipitation rate maxima over higher terrain (Figure 22, right). Figure 23 shows how the highest resolution model runs (6 km, d03 and d04) capture the fine-scale structure of the GHI, wind speed, and precipitation. Terrain effects are most apparent in the d03 (6 km) grid for GHI (Figure 23, top left), wind speed (Figure 23, top middle), and precipitation rate (Figure 23, right), where orographic in fluences from the Adirondack Mountains (Figure 23, top right) and Catskill Plateau (Figure 23, bottom right) appear.

Figure 22. Gridded Mean Fields for GHI, Winds, and Precipitation (18 km resolution)

18-km (d02) gridded mean fields for GHI, 10-m wind speed, and precipitation during the historical period (1998–2017). The left column shows GHI in W/m^2; middle, 10-m wind speeds in m/s; and right, precipitation in mm/day. The top row shows NCAR-CCSM4 modeled outputs; the bottom row, ERA-I.

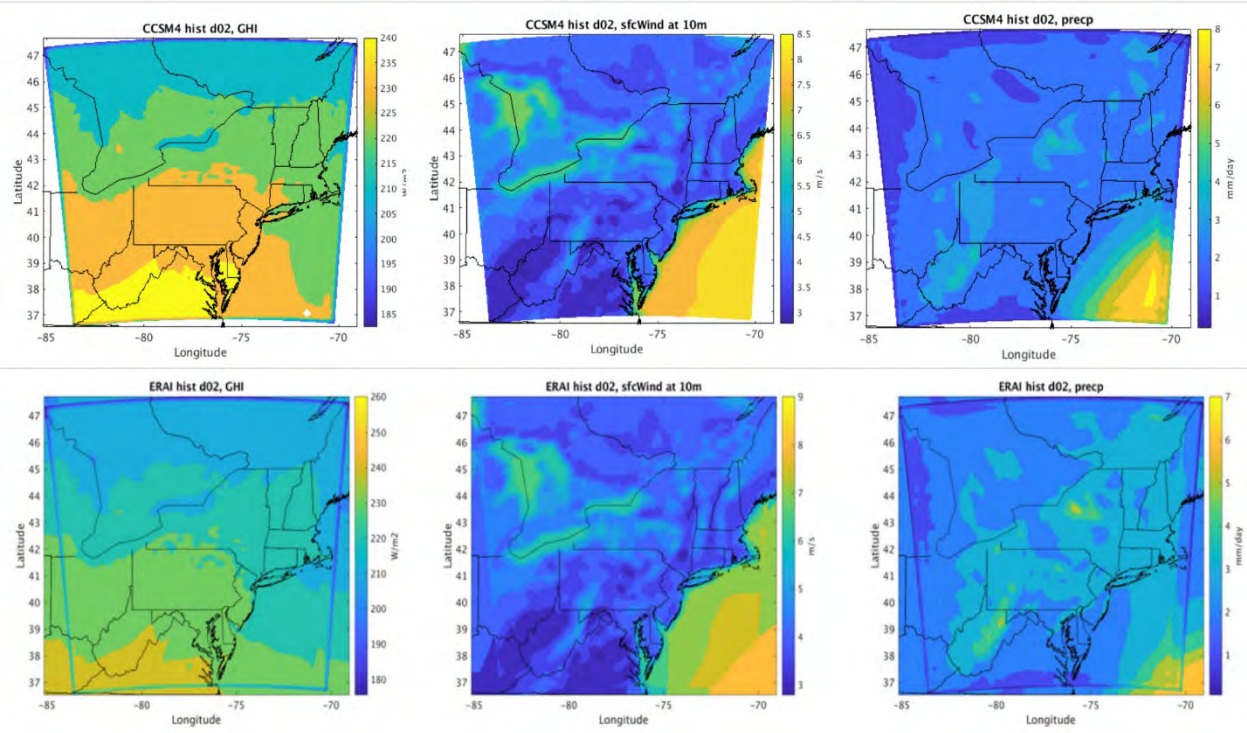

Figure 23. Gridded Mean Fields for GHI, Winds, and Precipitation (6 km resolution)

6-km (d03 and d04) gridded mean fields for GHI, 10-m wind speed, and precipitation during the historical period (1998–2017). The left column shows GHI (W/m^2); middle column, 10-m wind speeds (m/s); right column, precipitation (mm/day). The top row shows the d03 grid domain; the bottom row, d04.

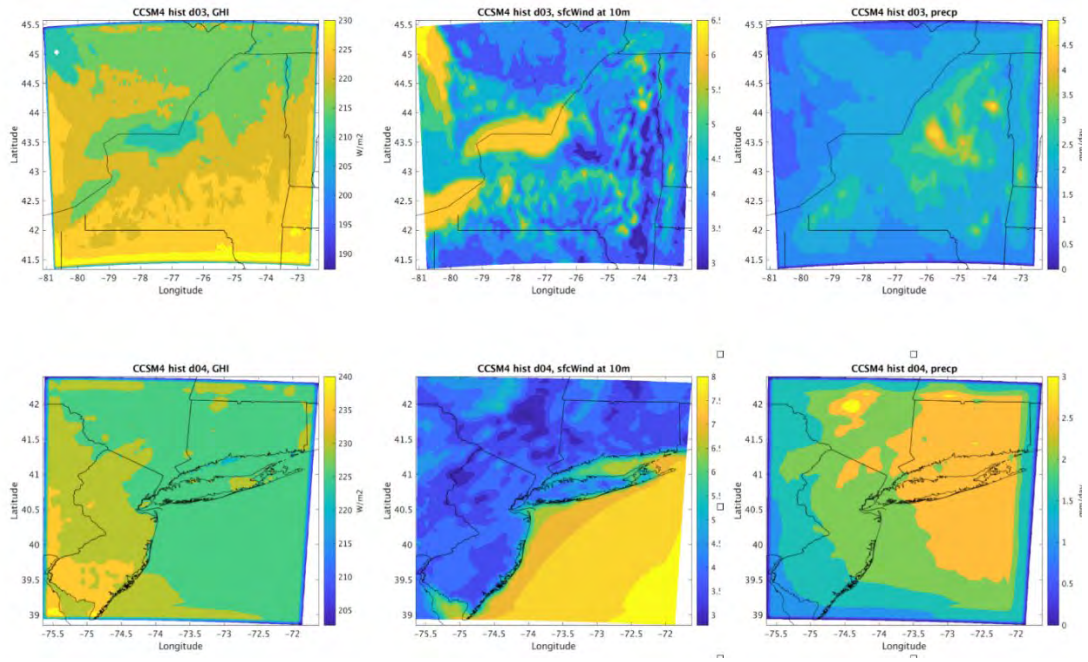

The historical runs (GFDL-CM3, NCAR-CCSM4, and BNU-ESM) showed good overall agreement on the 18 km (d02) and 6 km (d03) grids. Additional analysis of BNU-ESM historical output, however, found issues with discontinuities in the time series of several surface and surface-layer variables (especially in the outer d01 grid), including wind speed (at 10 m and 850 hPa; Figure 24) and surface irradiance (Figure 25). Further investigation found that other modeling groups identified similar issues, specifically the time series discontinuities and model forcing (Taylor 2012). Since the CMIP5 historical output covers the period through 2005, and the historical period for this work spans from 1998 to 2017, we combine historical and "future" (2006–2017) CMIP5 output to produce a continuous baseline time series for model downscaling runs. This led to the discovery of the time series discontinuities, which relate to using different atmospheric forcing attributes for the historical compared with future scenario runs, a characteristic of the BNU-ESM CMIP5 output (Taylor 2012). The discovery of the discontinuity and inconsistent forcing issues in the BNU-ESM historical runs led to substituting the MIROC5 CMIP5 member as the third model to ensure consistency and robustness in project results.

Figure 24. Time Series of 10-m Wind Speed

Annually averaged 10-m and 850-hPa wind speeds (m/s) for the historical baseline period (1998–2017) at the d01 grid cell nearest JFK. The top panel displays 10-m wind speeds; the bottom panel, 850-hPa wind speeds. Solid lines represent ERA-I (blue), BNU (green), NCAR-CCSM4 (red), and GFDL-CM3 (gold) model outputs. Dashed lines indicate trends over the 20-year period (m/s per decade).

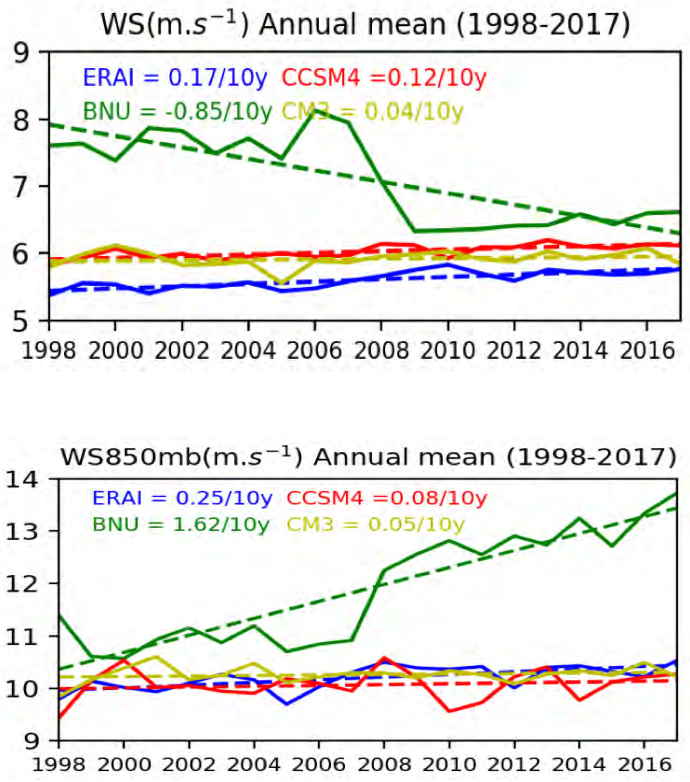

Figure 25. Time Series of Surface Irradiance

Surface irradiance (W/m²) for the historical baseline period (1998–2017) at the d01 grid cell nearest JFK. Solid lines represent ERA-I (blue), BNU (green), NCAR-CCSM4 (red), and GFDL-CM3 (gold) model outputs. Dashed lines indicate linear trends over the 20-year period (W/m2).

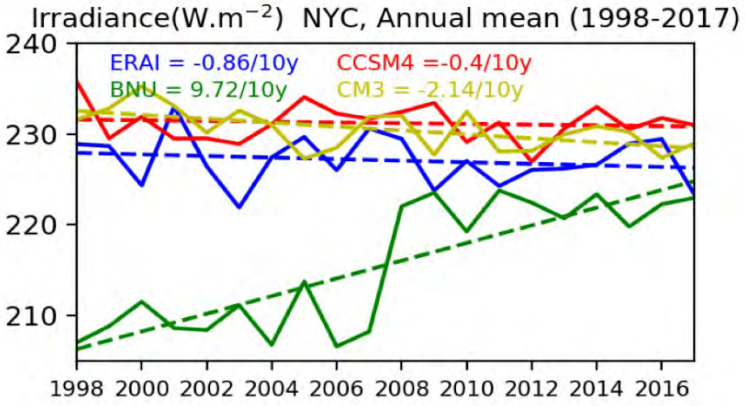

4.4 Execution of CMIP5 Future-Scenario Runs in WRF Through Performance of Dynamic Downscaling

4.4.1 Initial Results

Initial analysis was performed for several simulation months, along with analysis of the full 20-year runs to examine the downscaled output reasonableness (temporal and spatial continuity "sanity checks"). Figures 26 through 34 show initial results at selected locations comparing the GFDL-CM3 RCP4.5 historical (1998–2017) and near-future (2018–2037) periods. Figure 26 shows little change (~2% decrease) in the diurnal mean irradiance (GHI) at Farmingdale, NY (FRG), on Long Island, not far from the State's largest utility-scale solar generating facility (the Long Island Solar Farm at Brookhaven). The slight decrease is apparent during all daylight hours, except 9 a.m. and 4 p.m.

Figure 26. Historical and Mid-future Diurnal GHI Boxplot: Farmingdale, NY

Boxplot of 20-year historical period (1998–2017) and mid-future (2038–2057) diurnal GHI (W/m^2) at FRG for the GFDL-CM3 RCP4.5 scenario. The historical period is represented by the black median line and orange whiskers; the future period, by the red median line and blue whiskers.

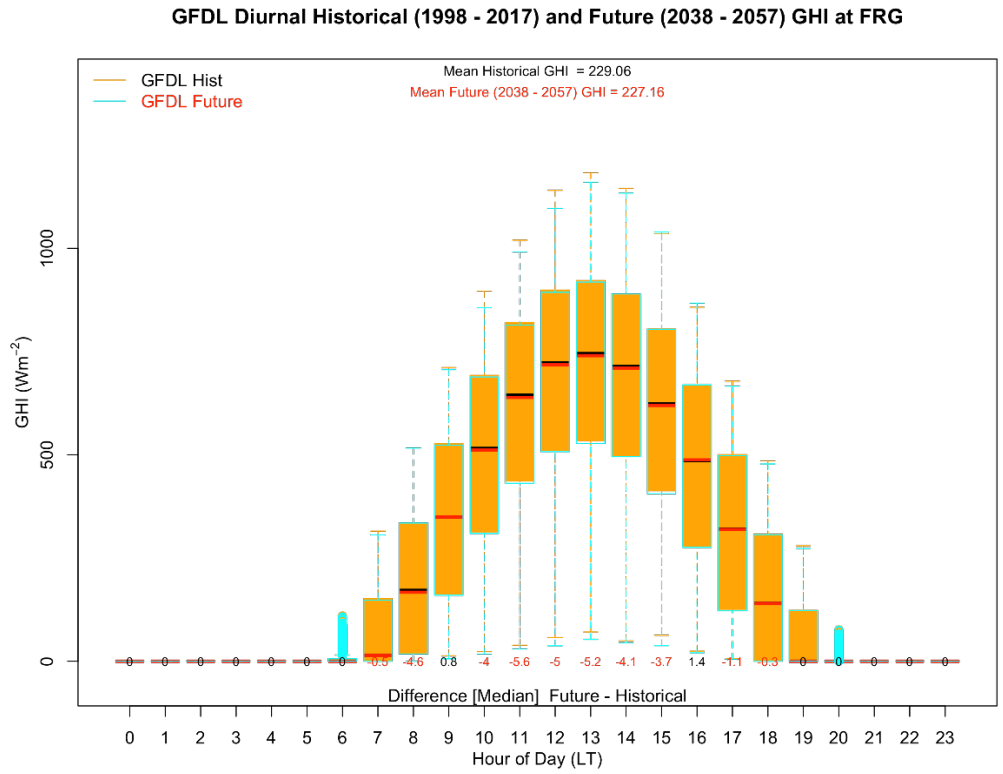

There is little change (~1% decrease) in mean 100-m wind speed at Buffalo, NY, (Figure 27) when comparing the historical GFDL climatology with the near-future period (2018–2037). This is balanced by nearly 5% decreases in the March–April and July–September periods, with corresponding increases in the late fall–winter and early summer periods.

RCP4.5 historical (1998–2017) and near-future (2018–2037) daily precipitation frequency histograms for MGJ show little change in the frequency of precipitation events or daily amounts, with a slight 3% increase in overall annual precipitation (Figure 28).

Figure 27. Historical and Near-future Monthly Wind Speed Boxplot: Buffalo, NY

Boxplot of monthly historical (1998–2017) and near-future (2018–2037) 100-m wind speeds (m/s) at BUF for GFDL RCP4.5 scenario.

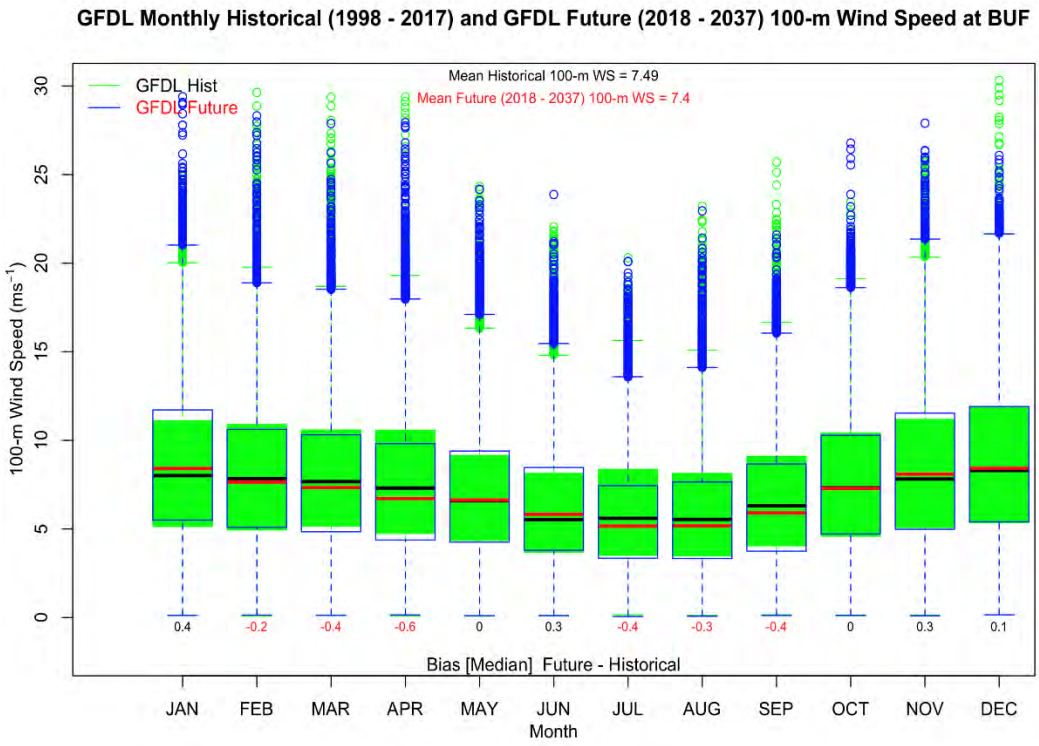

Figure 28. Historical and Near-Future Daily Precipitation Frequency: Montgomery, NY

Frequency histogram of daily precipitation for GFDL historical (1998–2017, left) and GFDL RCP4.5 near-future (2018–2037, right) scenario at MGJ.

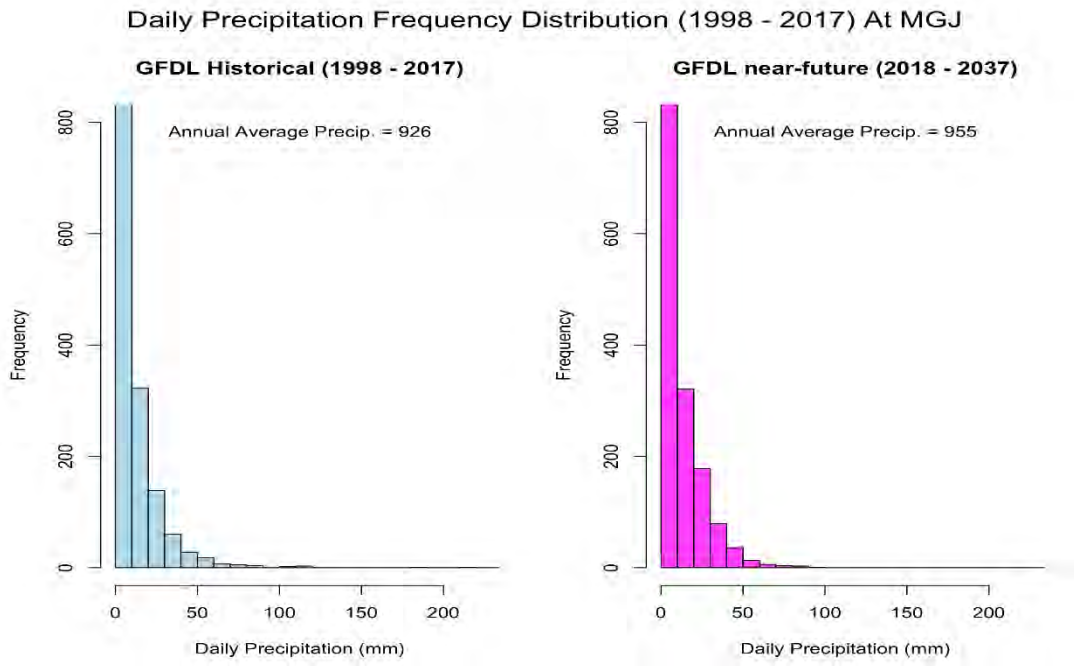

Initial analysis of mean 100-m wind speeds during the mid-future period under RCP4.5 indicates a slight increase in coastal regions. For example, at JFK, annual 100-m wind speeds increase about 1%, most occurring in the late spring and early summer (Figure 29). Larger increases are apparent during the warm season, however, perhaps a response to an enhanced sea breeze driven by increasing land-sea surface temperature differences. Wind speeds, for instance, increase nearly 4% in June for the mid-future period across the entire diurnal cycle (Figure 30), with median speed increases exceeding 10% during the afternoon, coinciding with the sea breeze maximum (see §5.1.4 for results). A comparison of the GFDL-CM3 RCP4.5 historical and mid-future daily precipitation frequency histograms for ALB shows a 24% increase in annual precipitation (from 925 to 1,156 mm), driven by increases in the frequency of moderate (>10 and <50 mm/day) and extreme (>50 mm/day) precipitation events (Figure 31). These results contrast with the near-future period summarized in Figure 28, which shows a modest increase in annual and daily precipitation.[9]

Figure 29. Historical and Near-Future Monthly Wind Speed Boxplot: JFK, Jamaica, NY

Boxplot of monthly historical (1998–2017) and near-future (2018–2037) 100-m wind speeds (m/s) at JFK for GFDL RCP4.5 scenario.

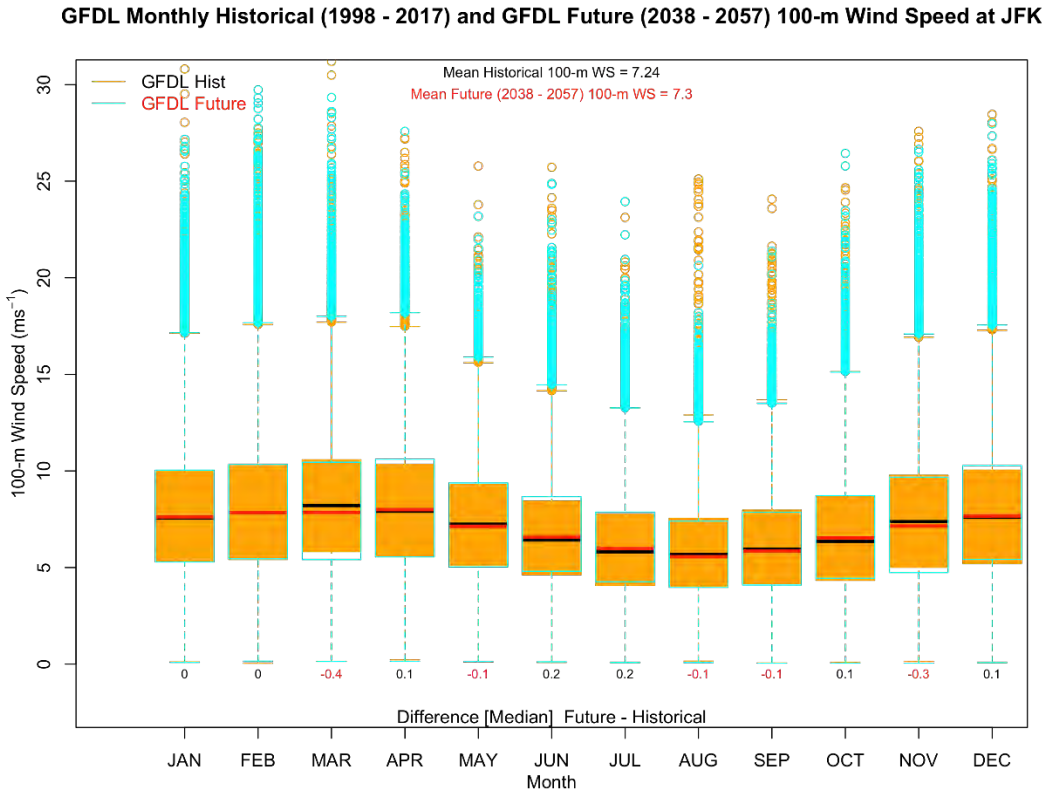

Figure 30. Historical and Mid-Future Diurnal Wind Speeds Boxplot: JFK, Jamaica, NY

Boxplot of 20-year historical (1998–2017) and mid-future (2038–2057) diurnal 100-m wind speeds (m/s) at JFK for GFDL-CM3 RCP4.5 scenario.

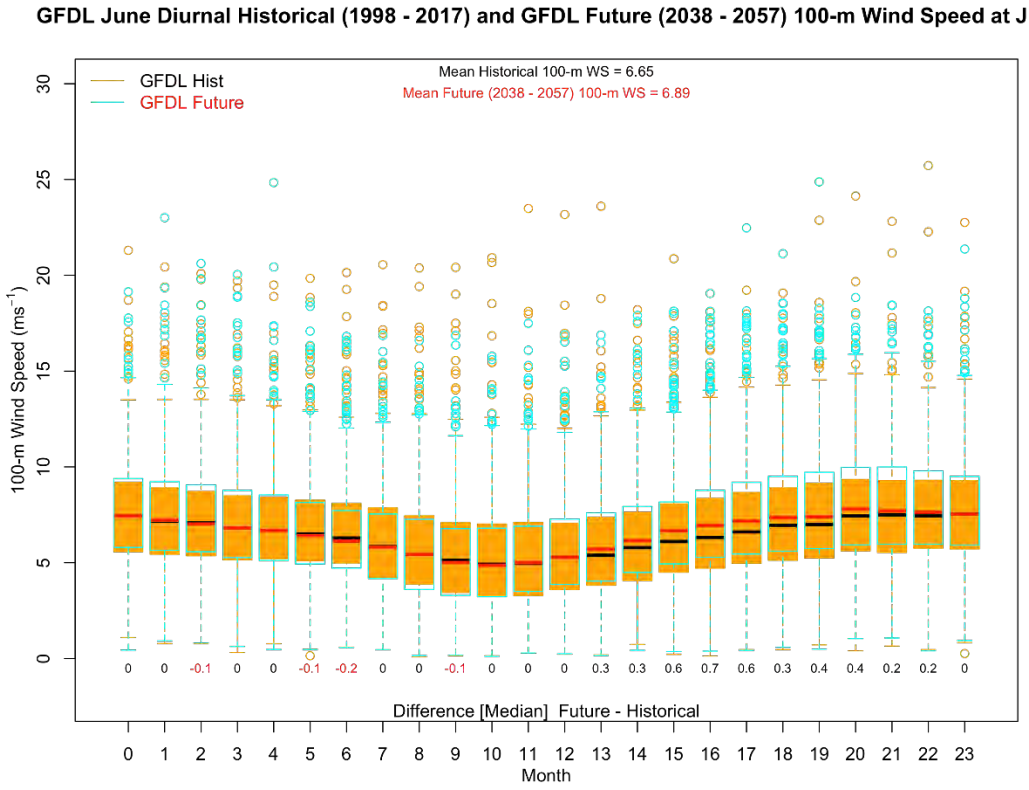

Figure 31. Historical and Mid-Future Daily Precipitation Frequency: Albany, NY

Daily precipitation (mm) frequency for GFDL historical (left) and mid-future (right) periods at ALB.

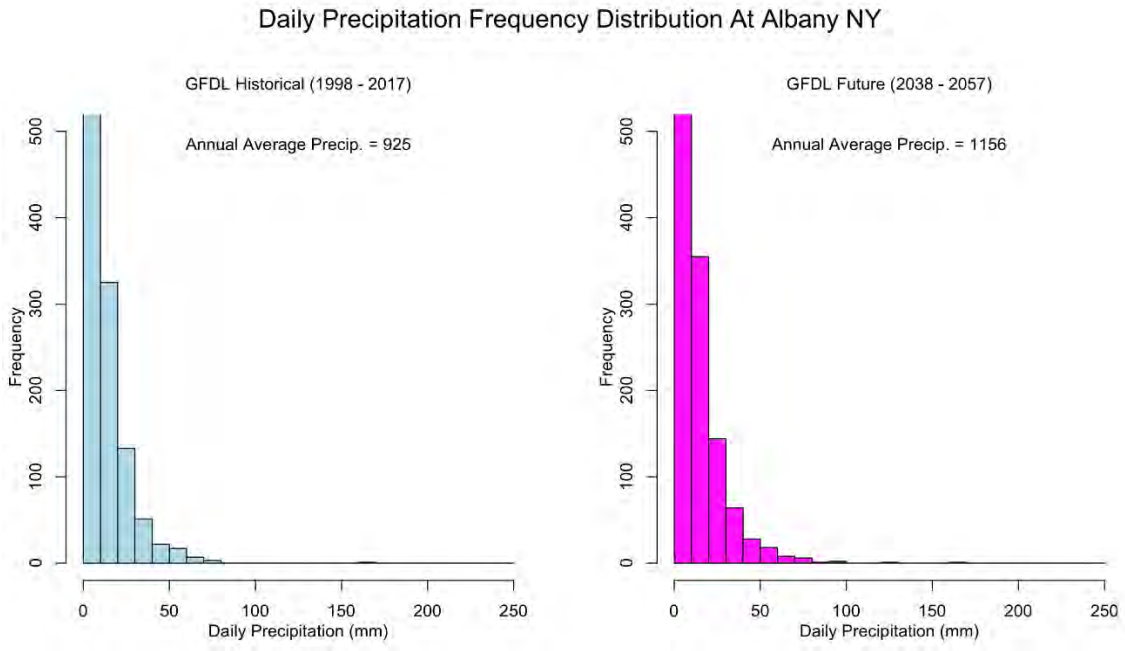

4.4.2 Bias correction of temperature, wind, irradiance, and precipitation fields

The SOW identifies the issue of CMIP5 model bias and the need to correct for non-climate-related differences between the historical baseline and the future model runs. The historical CMIP5 runs identify lateral boundary-forcing bias by comparing differences in solar, wind, and hydropower parameters, and other relevant variables, between WRF runs driven by ERA-I and those driven by CMIP5 models. In addition, differences between historical CMIP5 and WRF runs forced with CMIP5 data provide a measure of downscaling bias. These statistics reveal the potential improvements that higher-resolution WRF downscaling adds to a global ESM (i.e., one of the CMIP5 models) when compared with observations in the historical period. Furthermore, differences between WRF runs forced with a subset of three separate CMIP5 models highlight ESM biases in driving the RCM and quantify uncertainty in historical and future scenario assessments of solar and wind energy potential.

The CMIP5 historical runs provide the baseline for comparison with the future scenarios after accounting for various biases of the modeling framework that are not related to possible climate change.

To bias correct the downscaled CMIP5 historical runs, we applied the methodology specified by Bruyere et al. (2014) and Dai et al. (2017). For the historical simulation, for example, the GFDL-CM3 hourly wind speed bias correction is given by:

Equation 2.

$$U_{biascor_{CM3}} = U_{historical_{CM3}} - d\left(\bar{U}_{ERAI} - \bar{U}_{CM3}\right)$$
$$= \bar{U}_{CM3} + \acute{U}_{CM3} - \left(\bar{U}_{ERAI} - \bar{U}_{CM3}\right)$$
$$= \bar{U}_{ERAI} + \acute{U}_{CM3}$$

For the downscaling (RCP) simulations, the hourly GFDL-CM3 wind speed bias correction is given by:

Equation 3.

$$U_{biascor_{CM3}} = U_{CM3_{rcp}} - \left(\bar{U}_{ERAI} - \bar{U}_{CM3}\right)$$

where $\bar{U}_{ERAI}, \bar{U}_{CM3}, and \acute{U}_{CM3}$ represent the mean monthly climatologies and perturbation terms. For example, applying the bias correction terms to the wind speed profile for the downscaled GFDL-CM3 and NCAR-CCSM4 runs in the 10 lowest WRF levels (within the atmospheric boundary layer) results in a correction of -0.1 to -0.4 m/s (Figures 32 and 33).

Figure 32. Wind Speed Difference Before and After Bias Correction

Wind speed difference (U, m/s) before and after bias correction for the lowest 10 levels in the downscaled GFDL-CM3 (left) and NCAR-CCSM4 (right) historical runs.

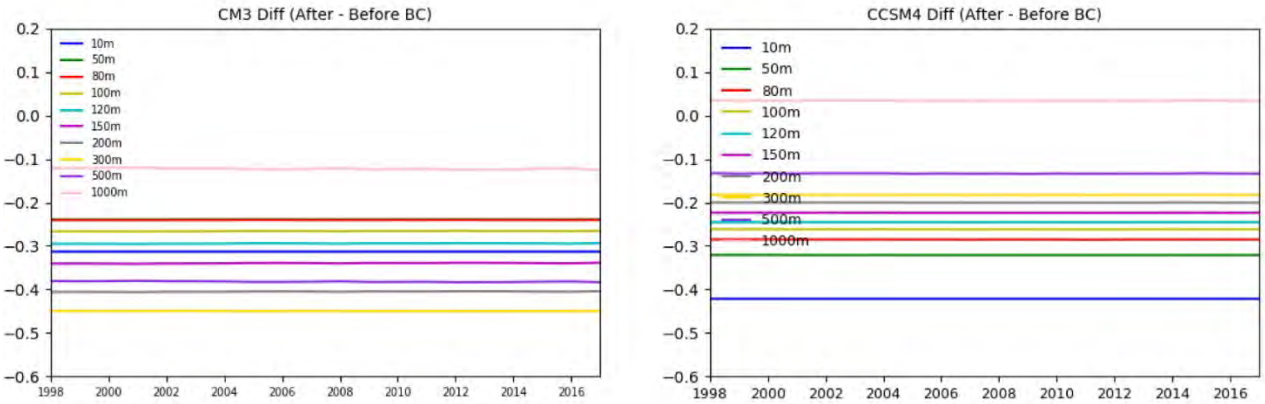

Figure 33. Wind Speed With and Without Bias Correction

Wind speed (U, m/s) before and after bias correction for the lowest 10 levels in the downscaled GFDL-CM3 (left) and NCAR-CCSM4 (right) historical runs. The top graphs show before bias correction; the bottom graphs, after bias correction.

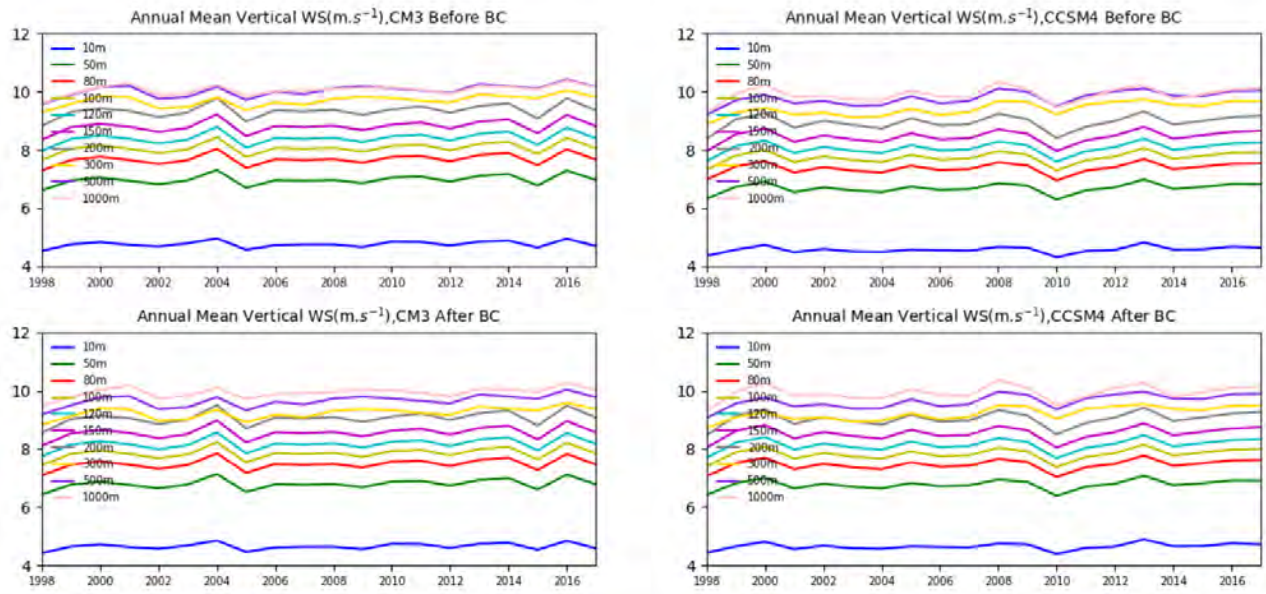

5 Evaluate Future Climate and Analyze Future Scenario Changes in Renewable Energy Power Distribution

We evaluated projected changes in New York State's climate and how those changes could potentially affect renewable energy resources and generation in the state.

5.1 Changes in Atmospheric Circulation Patterns That Can Be Linked With Regional-Scale Alterations

Using the 54 km (d01) and 18 km (d02) grids, we examined sea level pressure, 1,000 hPa and 500 hPa height patterns, and streamlines to identify changes in the large-scale and mesoscale circulation features that may be responsible for differences between historical and future scenario runs, and that might contribute to detectable changes in renewable energy generation in New York State. Analysis was performed on interannual variability, seasonal, and diurnal time frames. We found no significant changes in dominant large-scale circulation patterns affecting the distribution of wind and solar energy resources across New York State. (Note that all three downscaled models under both RCP scenarios project future temperature trends consistent with recent IPCC estimates and other regional studies for New York State. See Appendix D for monthly precipitation plots referencing temperature changes from the historical baseline.)

5.2 Changes in Atmospheric Circulations That Are Responsible for New York State's Local and Statewide Regions

We examined the 18 km and 6 km runs to detect changes in mesoscale circulations responsible for New York State's local and statewide regions that are currently favorable for renewables. These include the Southern Tier and Long Island for solar energy; the Tug Hill Plateau, offshore waters of Lake Erie and Lake Ontario, and the Atlantic coastal waters south of Long Island and New York City for wind; and the Niagara, St. Lawrence, Hudson, and Mohawk river basins for hydropower. We conducted this analysis on interannual variability and seasonal and diurnal time frames. We noted changes that include increased Great Lakes (Erie and Ontario) surface water temperatures and decreased ice coverage, which lead to monthly precipitation increases during the cold season in the snowbelt regions (especially downwind of Lake Ontario; see Appendix D). The sea breeze circulation also shows evidence of enhancement in the GFDL-CM3 model; however, results across the three downscaled models for both scenarios are mixed (see discussion below and Appendix B).

5.3 Future Trends in Precipitation

Annual precipitation in New York State ranges from less than 900 mm/yr (35 in/yr) in the Finger Lakes Region to more than 1,600 mm/yr (60 in/yr) in the higher peaks of the Catskills and Adirondacks and in the snowbelts downwind of Lake Ontario (Figure 34). Given its abundant water resources, New York State ranks third in the nation in hydropower (EIA 2021), generating nearly 6,000 megawatts (MW), or 22% of total generation capacity, of power from more than 200 hydroelectric facilities operating on rivers and streams throughout the State. Three large hydroelectric facilities—the New York Power Authority's (NYPA) St. Lawrence River Project (Robert Moses Power Dam), Niagara River Power Project, and the Blenheim-Gilboa Pumped Storage Project in Schoharie County—account for more than 75% of the hydropower generating capacity. The remaining approximately 1,500 MW comes from smaller facilities (<50 MW) scattered throughout the State (Figure 35). Because almost all hydropower generation in New York State occurs within the d03 domain, we focused our analysis on that region.

Figure 34. Map of Average Annual Precipitation in New York State (1981–2010)

Units in in/yr.

Source: PRISM 2014.

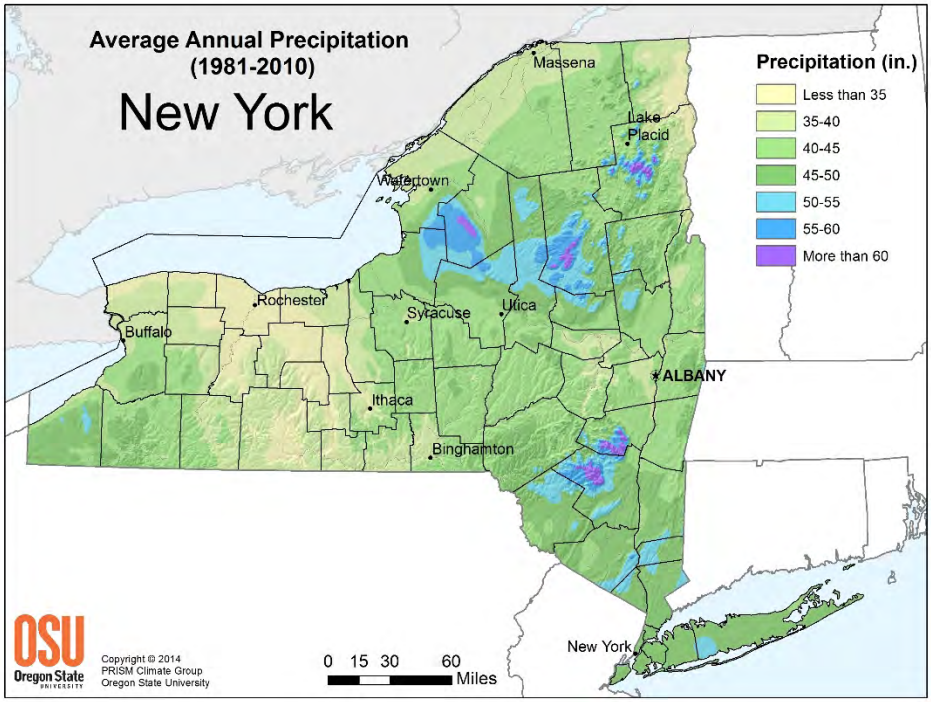

Table 7 summarizes model run results for annual precipitation changes (mm/yr) for the d03 domain (including regions outside of New York State) in near-future and mid-future periods compared with the historical baseline (1998–2017). For the near-future (2018–2037) RCP4.5 scenario, all three models show a consistent precipitation increase within the d03 grid (13–52 mm/yr [0.5–2.0 in/yr]) during the near-future period, with the increase in annual precipitation accelerating during the mid-future period (37–95 mm/yr [1.5–3.7 in/yr]), approximately a 5–10% increase over the domain.

Table 7. Modeled Future Annual Precipitation Changes (mm/yr): d03 Domain

Model	Scenario	d03 (mm/yr)	
		2018-2037	2038-2057
GFDL-CM3	RCP4.5	13 (1%)	95 (11%)
	RCP8.5	-18 (-2%)	22 (2%)
NCAR-CCSM4	RCP4.5	52 (7%)	58 (7%)
	RCP8.5	-67 (-9%)	-51 (-7%)
MIROC5	RCP4.5	50 (5%)	37 (4%)
	RCP8.5	57 (6%)	61 (7%)
	Mean	**14.5 (+1.3%)**	**37 (+4.0%)**

In contrast, for the near-future RCP8.5 scenario, two of the three models (GFDL and NCAR) show a precipitation decrease (-18 to -67 mm/yr [-0.7 to -2.6 in/yr]) over the domain (~2%–7% decrease), while the MIROC5 run shows an increase in annual precipitation of 57 mm/yr (2.4 in/yr). For the mid-future RCP8.5 scenario, only the NCAR model shows a decrease in annual precipitation (-51 mm/yr or 2.0 in/yr), while the GFDL and MIROC5 models show positive trends (22 and 62 mm/yr or 0.9 and 2.4 in/yr).

If we consider the ensemble means (the average of the three models for both scenarios for each period), we see a modest increase of 14.5 mm/yr (0.6 in/yr) for the near-future period, and a more pronounced increase of 37 mm/yr (1.5 in/yr) for the mid-future period.

Figure 35. Map of Hydroelectric Facilities in New York State

Source: EIA 2021.

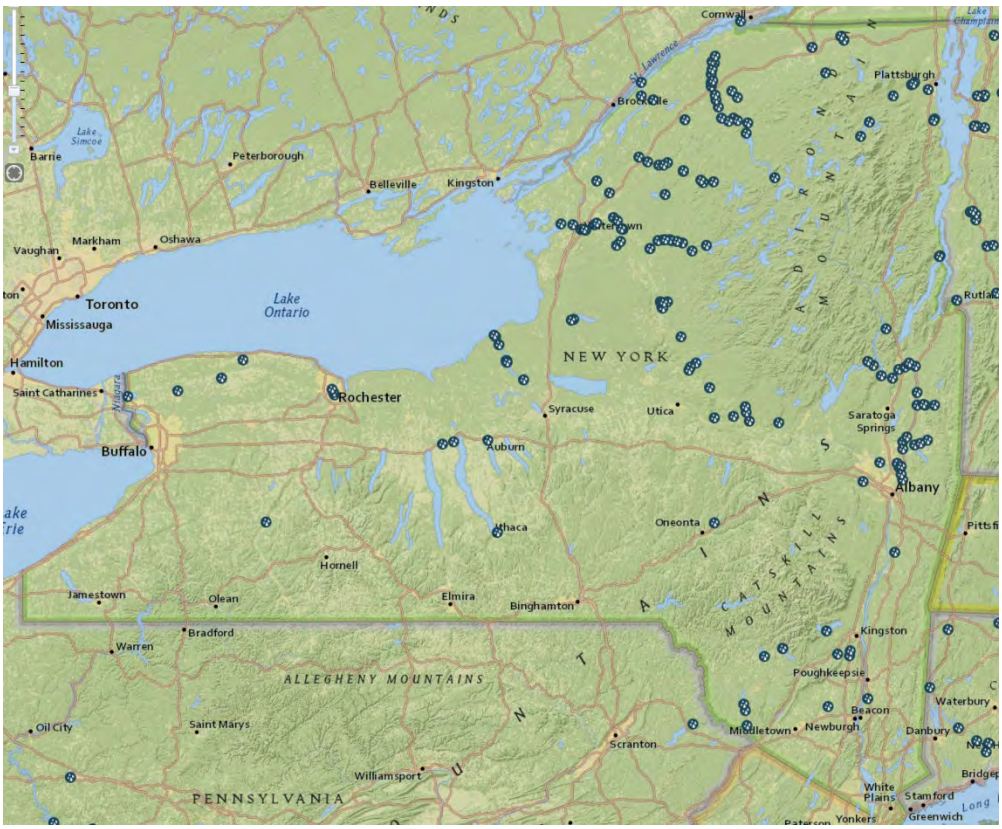

Table 7 results are presented in domain maps (Figures 36 and 37), highlighting local and regional mean annual precipitation distribution changes. For the RCP4.5 near-future period (Figure 36), the GFDL (Figure 36, top left) shows a small increase (13 mm/yr or 0.5 in/yr) across the entire d03 domain, with much higher increases over the Tug Hill Plateau (up to 100 mm/yr or nearly 4 in/yr) and the western part of the State. Most areas with existing hydroelectric generation are in regions with a greater-than-domain-average increase in precipitation.

We see similar results for the MIROC5 (Figure 36, middle left) and NCAR (Figure 36, bottom left) runs, which show the largest increases in the St. Lawrence Valley, on the Tug Hill Plateau (the Lake Ontario snowbelt), and downwind of Lake Erie. The mid-future runs (Figure 36, right) reveal a similar pattern, with the GFDL and NCAR models especially aggressive in increasing precipitation (>200 mm/yr or >8 in/yr) over much of the northern half of the State, particularly for the snowbelt region east of Lake Ontario. This may result from reduced lake ice during winter, which permits a longer lake-effect snow season (Appendix D).

A different pattern emerges under RCP8.5 (Figure 37). Model results are more mixed, with the GFDL showing a slight decrease in precipitation over Upstate New York in the near-future period (even in the snow belt regions), except at the higher elevations over the eastern part of the State (Figure 37, top left). For the mid-future period, however, average annual precipitation tends to increase over the State, especially over the higher terrain (Figure 37, top right). MIROC5 runs show a consistent increase in precipitation for both periods (Figure 37, middle), especially in the St. Lawrence Valley. The NCAR runs, in contrast, show larger decreases in precipitation in the western parts of the State (100–200 mm/yr or 4–8 in/yr). Exceptions to this pattern include the higher terrain in the southern Adirondacks, Lake Ontario snowbelt zones, and the St. Lawrence Valley.

New York State's hydropower regions can be defined by 14 major watersheds (Figure 38). Two watersheds, the St. Lawrence and Upper Hudson River (Sacandaga), account for a large fraction of the State's hydropower production, excluding the Niagara River facility. The third key region is the pump storage facility at Gilboa Dam. This analysis focuses on these three regions, examining trends and interannual variability.

Figure 36. Mean Precipitation Change for Domain d03 RCP4.5

Domain d03 RCP4.5 mean change in precipitation (mm/yr). Shown are the outputs for GFDL-CM3 near-future (top left) and mid-future (top right); MIROC5 near-future (middle left) and mid-future (middle right); and NCAR-CCSM4 near-future (bottom left) and mid-future (bottom right).

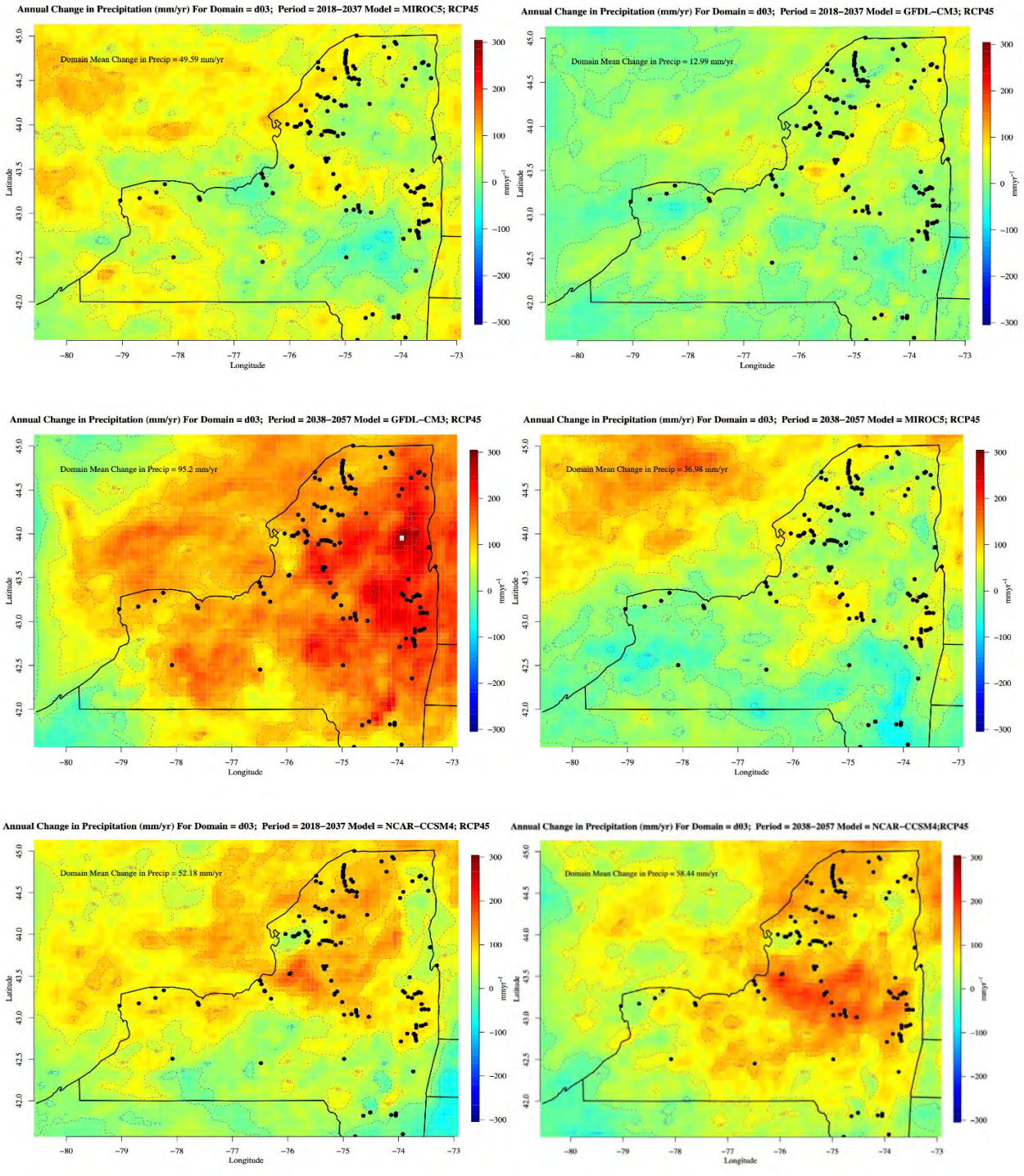

Figure 37. Mean Precipitation Change for Domain d03 RCP8.5

Domain d03 RCP8.5 mean change in precipitation (mm/yr). Shown are the outputs for GFDL-CM3 near-future (top left) and mid-future (top right); MIROC5 near-future (middle left) and mid-future (middle right); and NCAR-CCSM4 near-future (bottom left) and mid-future (bottom right).

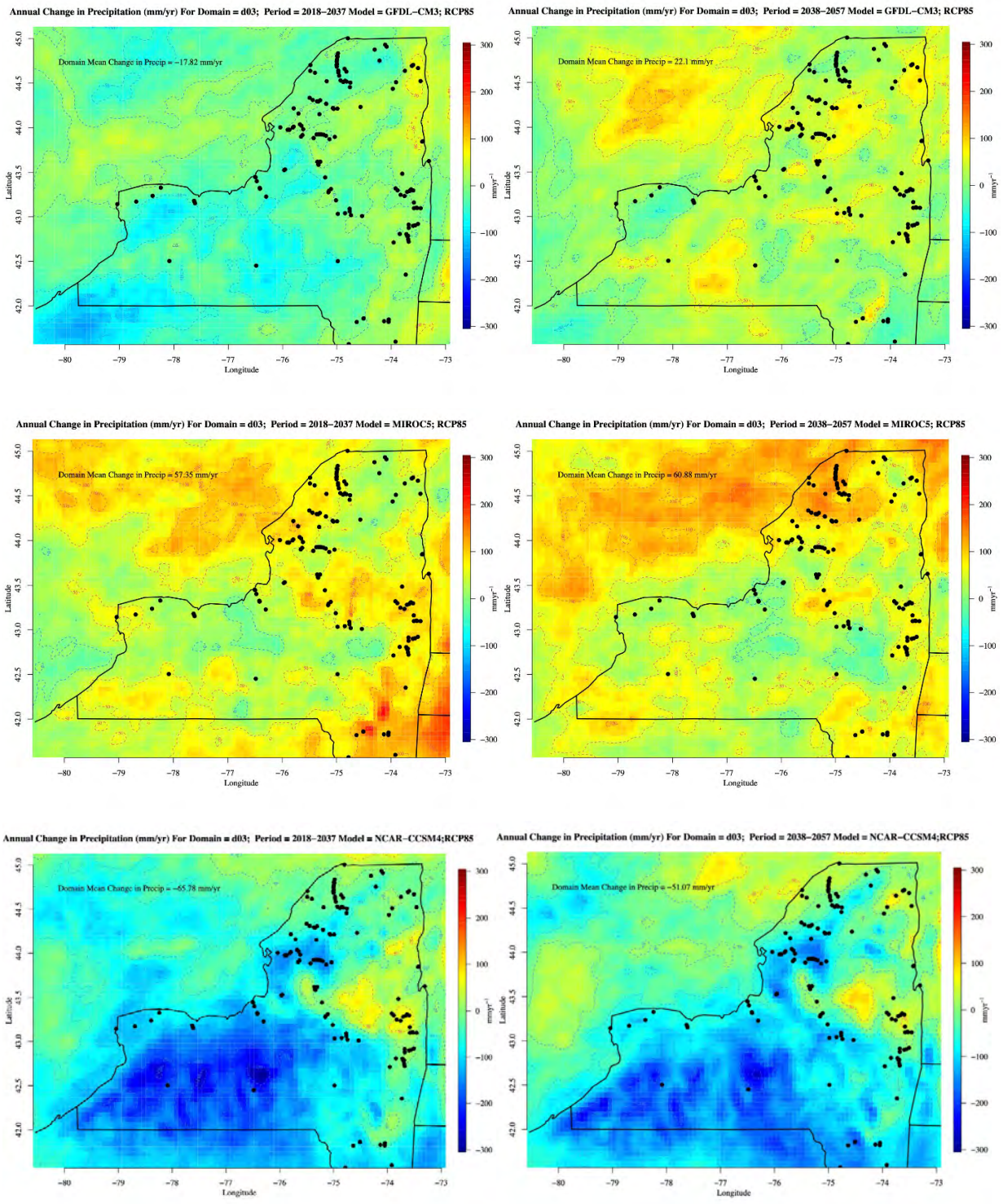

Figure 38. Map of Watersheds in New York State

Source: NYSDEC

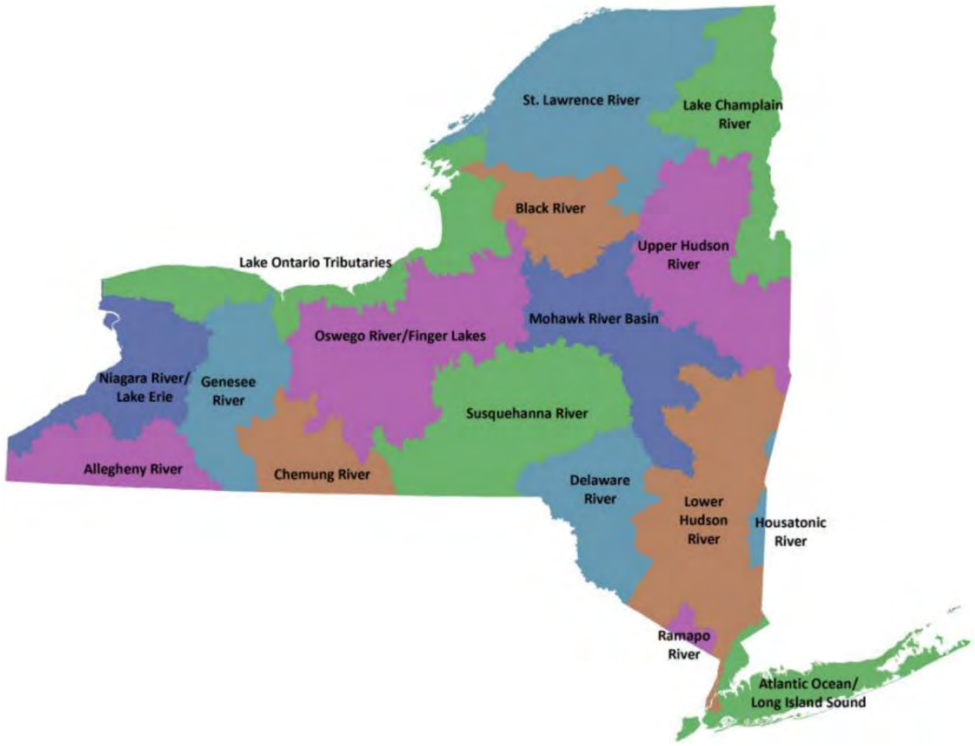

5.3.1 St. Lawrence Watershed

Most models project increased annual precipitation in the St. Lawrence watershed, with the exception of NCAR's RCP8.5 scenario, which shows decreases in both periods. Increases range from 12–138 mm/yr for the near-future, and 54–212 mm/yr for the mid-future (Table 8). Figure 39 shows this watershed's annual precipitation (mm), trends (mm/decade), and corresponding trend lines.

Table 8. Precipitation Change: St. Lawrence Watershed

Figures show in mm/yr.

Model	Scenario	2018–2037	2038–2057
GFDL-CM3	RCP4.5	138	212
	RCP8.5	88	54
NCAR-CCSM4	RCP4.5	12	92
	RCP8.5	-34	-58
MIROC5	RCP4.5	40	220
	RCP8.5	42	112
	Mean	**48**	**105**

Figure 39. Annual Precipitation Trends: St. Lawrence Watershed

Shown are the outputs for GFDL-CM3 RCP4.5 (top left); GFDL-CM3 RCP8.5 (top right); MIROC5 RCP4.5 (middle left); MIROC5 RCP8.5 (middle right); NCAR-CCSM4 RCP4.5 (bottom left); NCAR CCSM85 (bottom right).

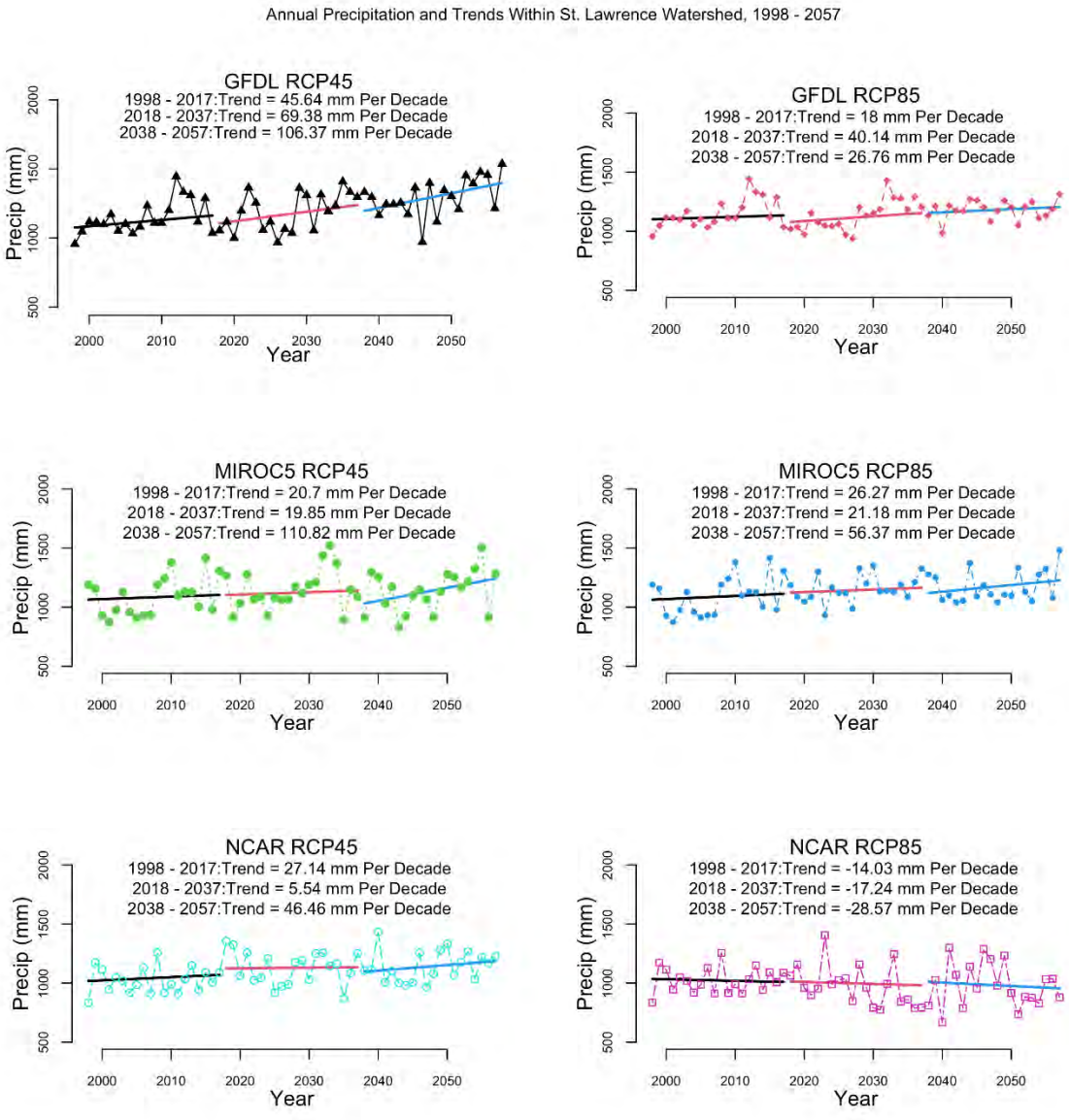

5.3.2 Upper Hudson River Watershed

Table 9 shows a similar picture for the Upper Hudson River watershed. All model runs except NCAR RCP8.5 show precipitation increases, with the near-future changes ranging from -34 to +138 mm/yr, and the mid-future changes from -68 to +168 mm/yr. Figure 40 shows annual precipitation (mm), trends (mm/decade), and corresponding trend lines for this watershed.

Table 9. Precipitation Change: Upper Hudson River Watershed

Figures show in mm/yr.

Model	Scenario	2018–2037	2038–2057
GFDL-CM3	RCP4.5	168	134
	RCP8.5	94	128
NCAR-CCSM4	RCP4.5	44	152
	RCP8.5	-48	-68
MIROC5	RCP4.5	30	150
	RCP8.5	28	168
	Mean	**53**	**111**

Figure 40. Annual Precipitation and Trends: Upper Hudson River Watershed

Shown are the outputs for GFDL-CM3 RCP4.5 (top left); GFDL-CM3 RCP8.5 (top right); MIROC5 RCP4.5 (middle left); MIROC5 RCP8.5 (middle right); NCAR-CCSM4 RCP4.5 (bottom left); NCAR CCSM85 (bottom right).

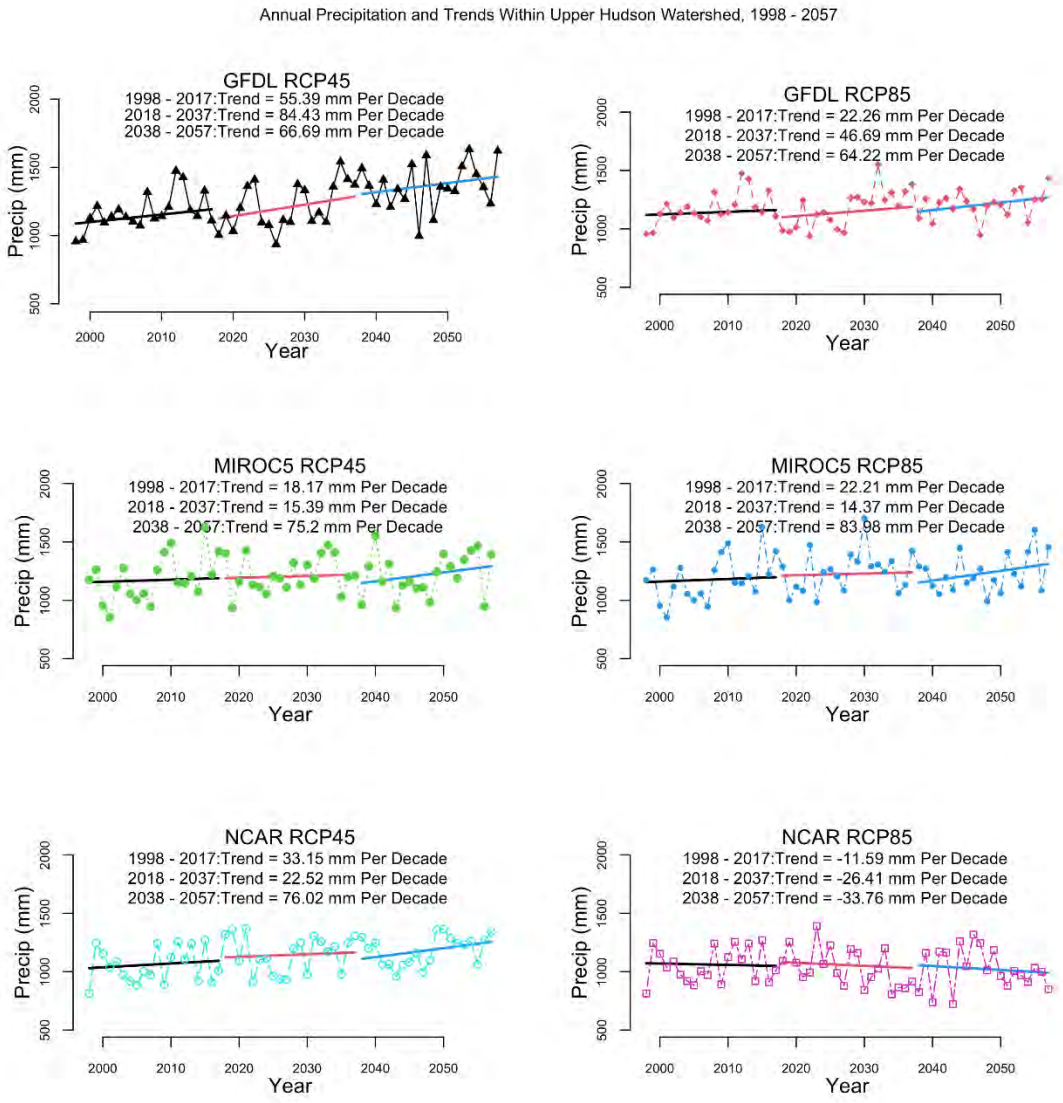

5.3.3 Gilboa Dam

Precipitation trends at Gilboa Dam are similar to those for the St. Lawrence and Upper Hudson River watersheds, with one notable exception: both NCAR RCP8.5 future periods show a modest decrease in precipitation. The GFDL shows a decline (-94 mm/yr) for the RCP4.5 mid-future period. Upon closer examination, however, the trend reflects a large increase in precipitation at the beginning of the mid-future period, followed by a gradual decrease accompanied by considerable interannual variability (Figure 41, top left). A key caveat to these model predictions is that trend analysis depends on the starting and ending dates. For example, the trend is positive when using 1998 as the start date and 2057 as the end date (roughly 20 mm/decade). Thus, the maps in Figures 36 and 37, showing the overall annual change in precipitation, may provide a more representative view of future precipitation predictions.

Table 10. Precipitation Change: Gilboa Dam

Units in mm/yr.

Model	Scenario	2018–2037	2038–2057
GFDL-CM3	RCP4.5	130	-94
	RCP8.5	96	218
NCAR-CCSM4	RCP4.5	48	76
	RCP8.5	-42	-2
MIROC5	RCP4.5	16	-82
	RCP8.5	-6	-30
	Mean	**40**	**-2**

Figure 41. Annual Precipitation Trends: Gilboa Dam

Shown are the outputs for GFDL-CM3 RCP4.5 (top left); GFDL-CM3 RCP8.5 (top right); MIROC5 RCP4.5 (middle left); MIROC5 RCP8.5 (middle right); NCAR-CCSM4 RCP4.5 (bottom left); NCAR CCSM85 (bottom right).

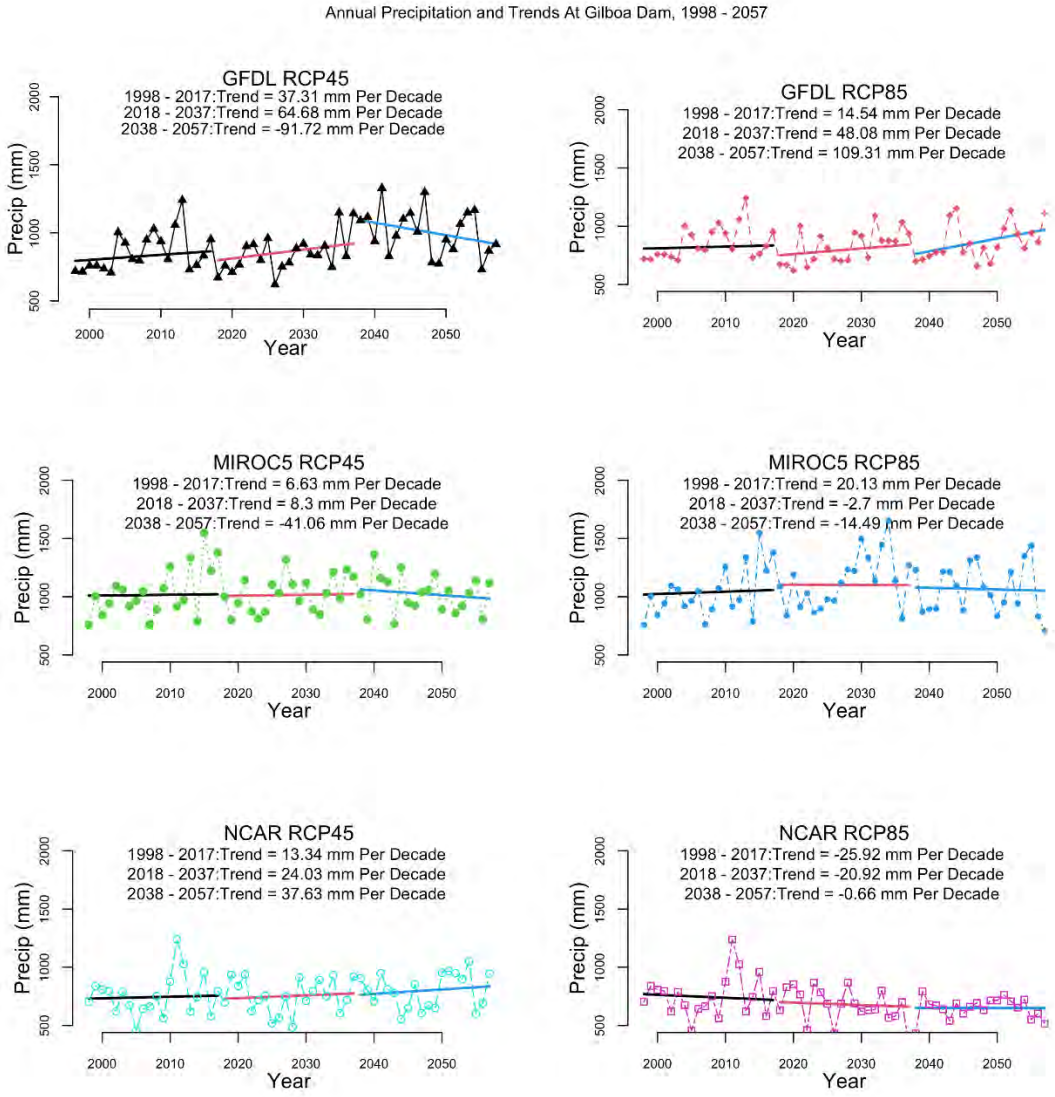

5.3.4 Seasonal Changes

Precipitation in New York State is generally evenly distributed throughout the year (Northeast Regional Climate Center 2021), so hydropower output does not experience large seasonal fluctuations as seen in the western U.S. This is especially true because the largest hydropower plants are located on rivers with substantial year-round flows (e.g., the Niagara and St. Lawrence). However, dozens of smaller hydropower plants located on smaller streams and rivers throughout the State depend on flows that exhibit seasonal characteristics (e.g., snowmelt) and on dam releases to maintain fisheries. Here, we summarize the changes in monthly precipitation characteristics over the d03 domain. Although the above analysis shows that most model runs indicate a general increase in precipitation across the domain, a seasonal aspect affects the distribution of the increase (or decrease). For the RCP4.5 near-future period, a noticeable reduction in precipitation occurs during summer, with the GFDL model showing the most significant decline (Figure 42), with up to a 0.4 mm/day (12 mm/month or about 0.4 in/month). During the winter and spring, average daily precipitation generally increases, with the NCAR model indicating an additional 0.75 mm/day in February (about 21 mm/month or 0.75 in/month).

Figure 42. Monthly Precipitation Change: D03 Grid RCP4.5, Near-Future Period

D03 grid RCP4.5 mean change in precipitation (mm/day) for the near-future period. Shown are the outputs for GFDL-CM3 (red bars), MIROC5 (green bars), and NCAR-CCSM4 (blue bars).

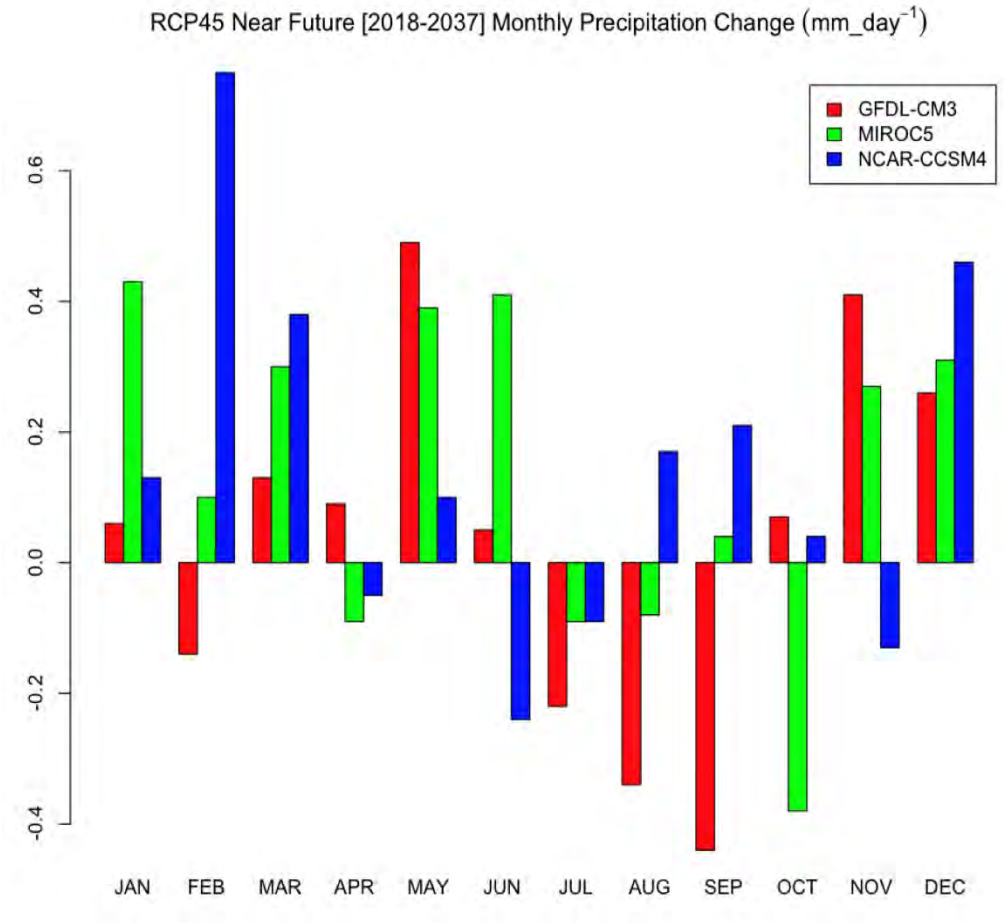

For the RCP4.5 mid-future period (Figure 43), a similar pattern emerges: generally more precipitation in winter (and shoulder months of November and March), with a slight decrease during summer. One notable exception is the NCAR model's January precipitation, which shows a relatively large decrease of 0.4 mm/day (12 mm/month or about 0.4 in/month). To demonstrate how much "noise" is inherent in the downscaling experiments, we note the large difference (magnitude and sign) in January precipitation for the NCAR runs between the near-future and mid-future periods. This is also the case for November. Additionally, the large difference in decreased summer season precipitation between the near-future and mid-periods for the GFDL is noteworthy.

Figure 43. Monthly Precipitation Change: D03 Grid RCP4.5, Mid-Future Period

D03 grid RCP4.5 mean change in precipitation (mm/day) for the mid-future period. Shown are the outputs for GFDL-CM3 (red bars), MIROC5 (green bars), and NCAR-CCSM4 (blue bars).

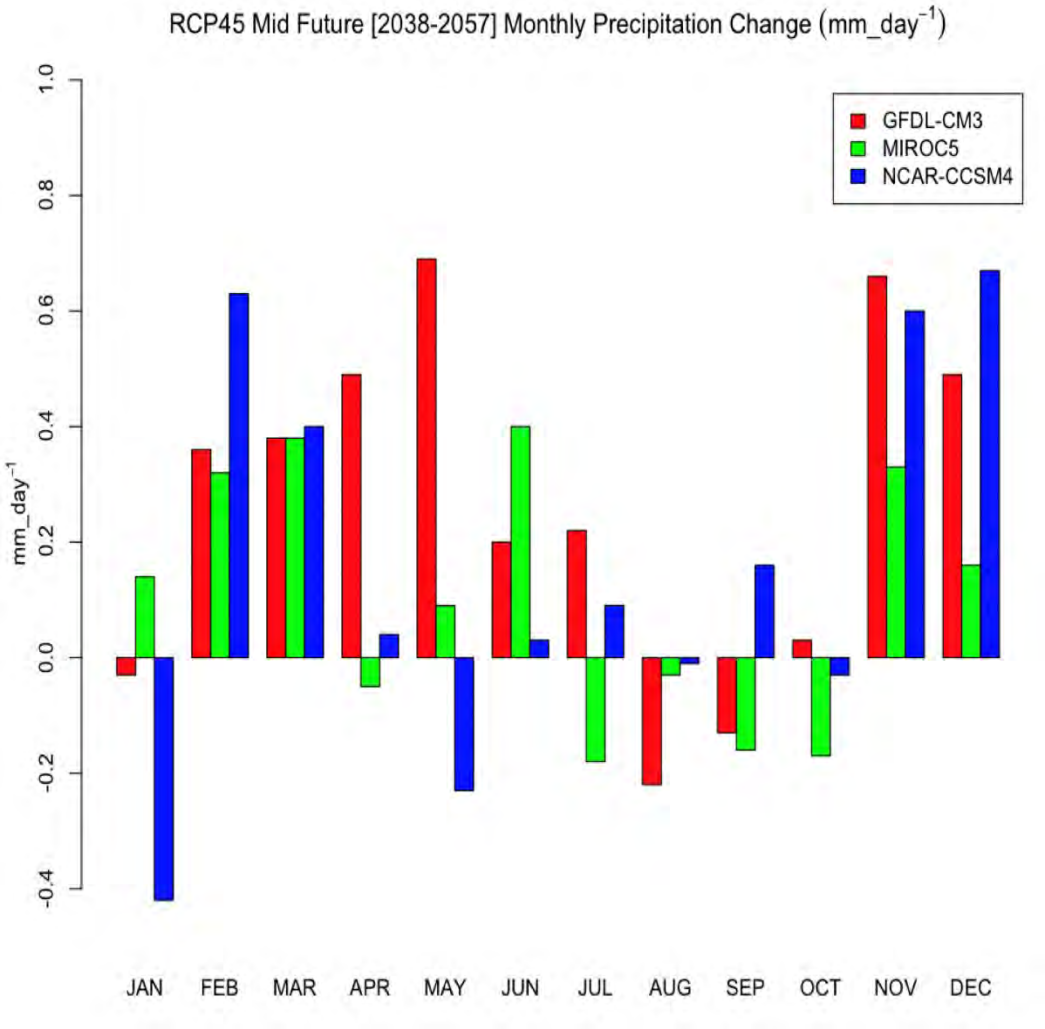

For the RCP8.5 runs, both the near-future and mid-future periods show strong consistency in the sign and magnitude of the change in monthly precipitation. Both periods feature a general increase in monthly precipitation from January to March, a slight decrease in late summer to early fall, and large decreases shown by the NCAR for April and December.

Figure 44. Monthly Precipitation Change: D03 Grid RCP8.5, Near-Future Period

D03 grid RCP8.5 mean change in precipitation (mm/day) for the near-future period. Shown are the outputs for GFDL-CM3 (red bars), MIROC5 (green bars), and NCAR-CCSM4 (blue bars).

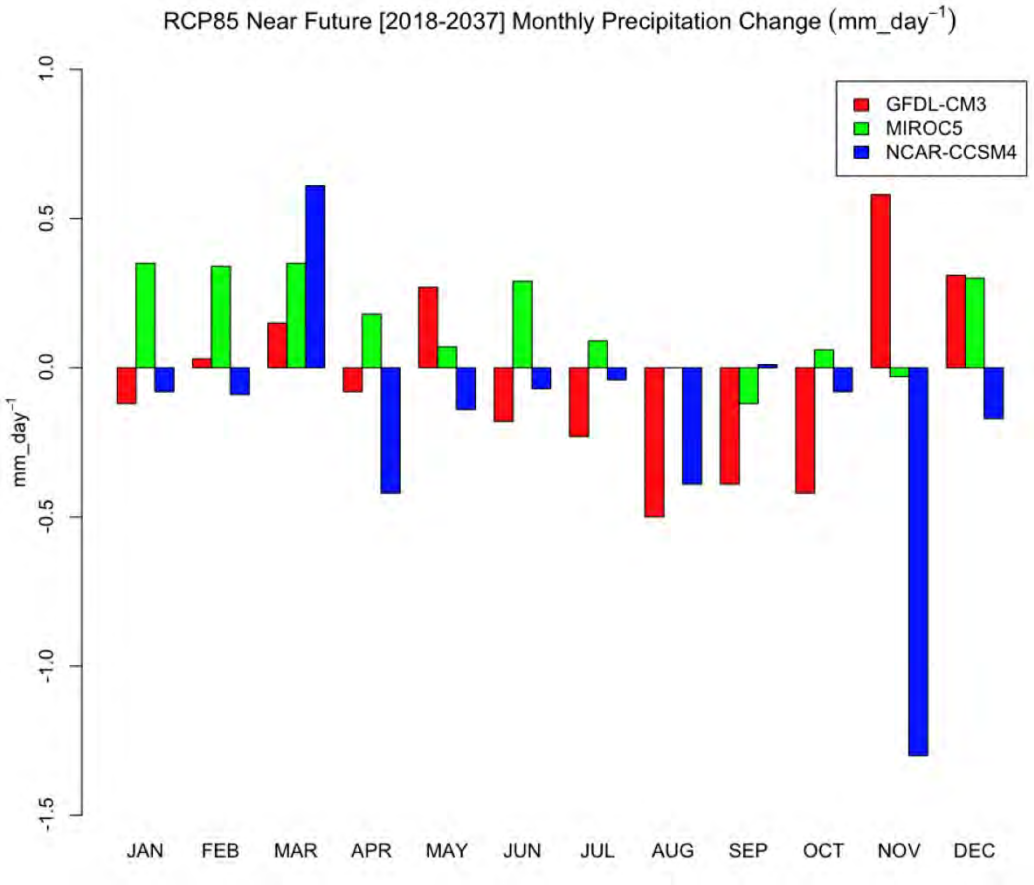

Since streamflow correlates linearly with precipitation (personal communication, P. Beaucage, UL-AWS Truepower), we infer that the changes in precipitation shown in the previous figures and accompanying discussion will lead to corresponding increases or decreases in streamflow, and hence, hydropower production at run-of-river dams, excluding the three major facilities at the Niagara and St. Lawrence rivers and the Gilboa pump station in the Catskills.

Figure 45. Monthly Precipitation Change: D03 Grid RCP8.5, Mid-Future Period

D03 grid RCP8.5 mean change in precipitation (mm/day) for the mid-future period. Shown are the outputs for GFDL-CM3 (red bars), MIROC5 (green bars), and NCAR-CCSM4 (blue bars).

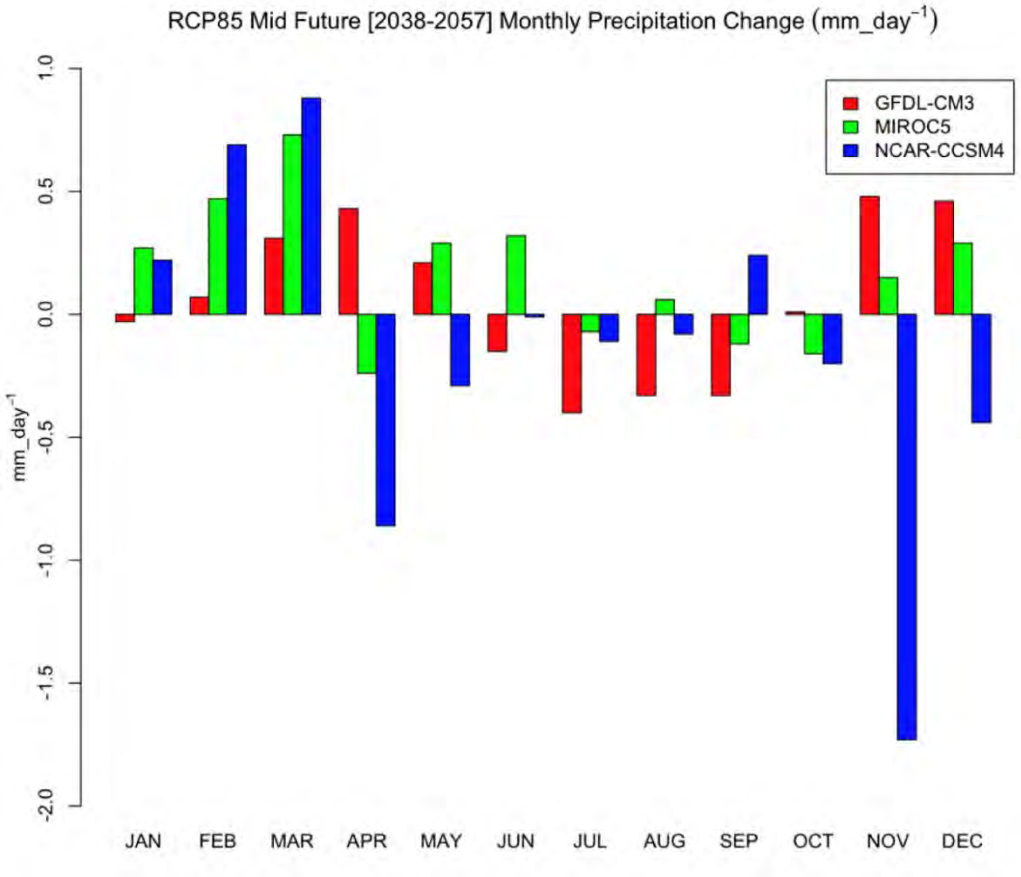

5.4 Future Trends in Wind

New York State, as of 2020, has in service nearly 2,000 MW (EIA 2021) of wind turbine generation (all onshore; see Figure 46). Much of this resource is located in the northwestern third of the State, from the Allegheny Plateau northeastward through the Tug Hill Plateau and the northeast corner of the State. Although new development is planned for inland locations, the State is more aggressively pursuing offshore wind, and, under the Climate Act, is committed to 9,000 MW of offshore wind energy by 2030. Much of the proposed offshore wind for New York State is in the New York Bight, a region bounded by the coastal waters east of New Jersey and south of Long Island (Figure 47). We present results for future trends in onshore (d03 domain) and offshore wind energy availability (part of d04 domain) in terms of wind speeds (m/s), with 100-m hub height considered typical for recent and future deployment of onshore and offshore wind turbines. In context, 100 m AGL or above sea level (ASL) represents a typical hub height.

Figure 46. Map of Wind Farms in New York State and Surrounding Area

Source: EIA 2021.

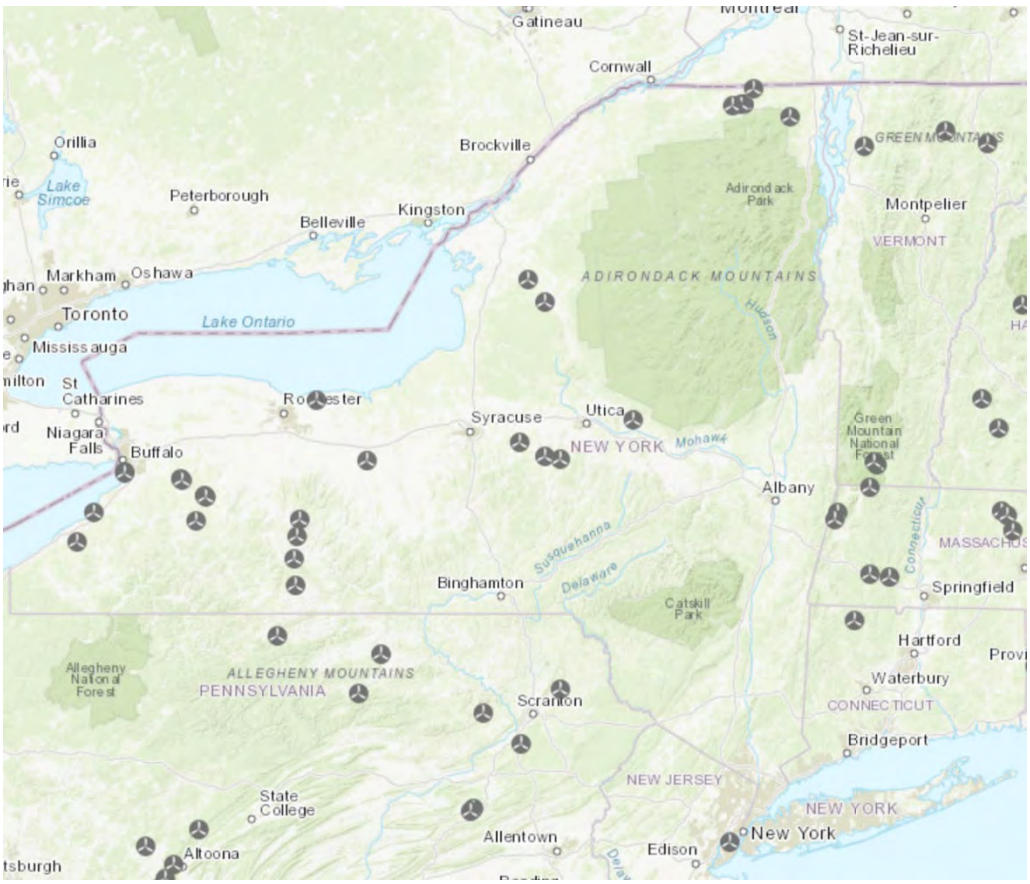

Figure 47. Map of Offshore Wind Energy Areas in the New York Bight

Coastal region appears in red square.

Source: Bureau of Ocean Energy Management

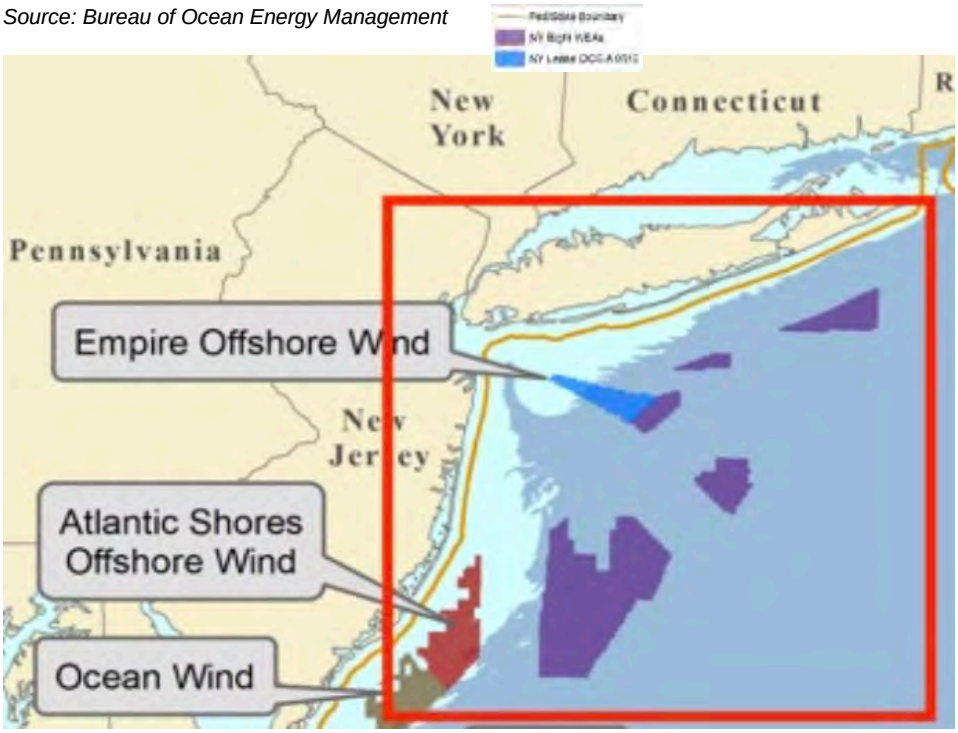

For the d03 domain, a very slight decrease (0 to -0.16 m/s) in 100-m wind speeds is apparent for both scenarios during the near-future and mid-future periods for the GFDL and MIROC5 runs (Table 11). The same applies to the d04 (mostly offshore) domain (+0.01 to -0.21 m/s). The NCAR runs, however, show a more robust increase in wind speeds, 0.46 m/s (near-future) and 0.35 m/s (mid-future) for the d03 domain, and 0.19–0.20 m/s for the d04 domain for both future periods. As with precipitation, this is within the interannual variability experienced in the region (0.5–1 m/s; see Figures 52 and 53). We note, however, that the NCAR d03 near-future increase could result in a 10% increase in capacity factor (depending on the turbine power curve and the mean local wind speed); the largest decrease shown in Table 11 (-0.21 m/s for d04, mid-future period), could result in approximately a 5% decrease in the regional capacity factor. Finally, if we consider the model ensemble average (both scenarios), regional changes in wind speed are quite small (<0.05 m/s), or less than 1% of the domain-averaged 100 m wind speeds. More local changes, however, do exhibit larger changes, as shown in the following figures.

Table 11. Change in Annual Wind Speed: D03 and D04 Grids

Change in 100-m wind speeds (m/s) from the base period (1998–2017) for the near-future (2018–2037) and mid-future (2038–2057) periods.

Model	Scenario	d03 (m/s per yr and %)		d04 (m/s per yr and %)	
		2018–2037	2038–2057	2018–2037	2038–2057
GFDL-CM3	RCP4.5	-0.10 (-1%)	0.00 (0%)	-0.09 (-1%)	0.01 (0%)
	RCP8.5	-0.16 (-2%)	-0.16 (-2%)	-0.16 (-2%)	-0.21 (-3%)
NCAR-CCSM4	RCP4.5	0.07 (1%)	0.03 (0%)	0.00 (0%)	-0.02 (0%)
	RCP8.5	0.46 (6%)	0.35 (4%)	0.19 (2%)	0.20 (3%)
MIROC5	RCP4.5	0.00 (0%)	-0.02 (0%)	-0.04 (-1%)	-0.09 (-1%)
	RCP8.5	0.00 (0%)	-0.11 (-1%)	0.00 (0%)	-0.16 (-2%)
Mean		**0.05 (0.6%)**	**0.02 (0.2%)**	**-0.02 (0.2%)**	**-0.05 (-0.6%)**

5.4.1 D03 Domain

For the domain d03 RCP4.5 near-future GFDL run (Figure 48, top left), the model predicts modest decreases in wind speeds across much of the region (average decline of 0.1 m/s). The largest decreases occur in the eastern part of the State, extending from the Lower Hudson Valley north through the Champlain Valley (where no wind farms operate). Other local minima appear along the shore of Lake Ontario and in the western part of the Southern Tier (near the Wethersfield and Bliss wind farms).

A similar pattern appears in the MIROC5 run (Figure 48, middle left), where the domain-average mean change in annual wind speed is zero. However, localized maximum increases (~+0.1 m/s) occur over the Finger Lakes Region, the Tug Hill Plateau, and Lake Champlain. The NCAR model run (Figure 48, bottom left) shows a larger variation in regional 100-m wind speed changes (from -0.1 to +0.2 m/s). The larger increases extend across most of the existing wind farm regions in New York State, from the Lake Erie shore south of Buffalo to the Clinton Wind Farm in the northeastern corner of the State.

Figure 48. Mean Change in Annual Wind Speed Change: Domain d03, RCP4.5

Domain d03 RCP4.5 mean change in annual wind speed (m/s). Shown are GFDL-CM3 near-future (top left) and mid-future (top right); MIROC5 near-future (middle left) and mid-future (middle right); and NCAR-CCSM4 near-future (bottom left) and mid-future (bottom right). Dashed red lines highlight regions with increased wind speeds over the baseline; dashed blue lines show decreasing regions. Black dots represent locations of existing wind turbines; purple dots depict hypothetical future wind farm locations based on UL-AWS Truepower analysis.

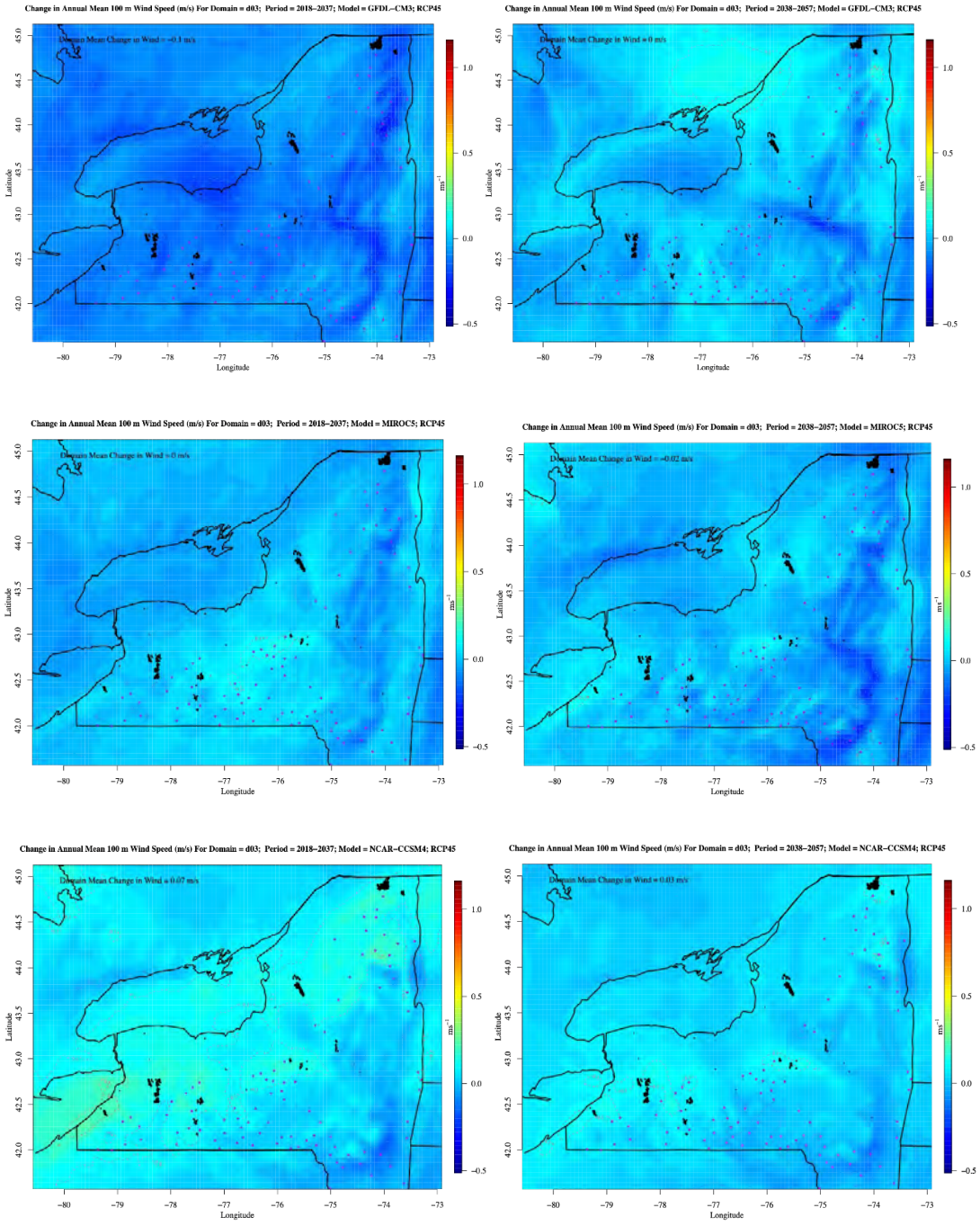

Similar patterns in 100-m wind speed changes are observed for the mid-future period (Figure 48, right), although the magnitude of change is generally smaller (domain change ±0.02 m/s and local changes ~±0.2 m/s).

For the RCP8.5 scenario, model differences are more pronounced. The GFDL (Figure 49, top) shows patterns similar to the RCP4.5 scenario, with a domain-average decrease of 0.16 m/s, and the largest decreases for the near-future period (Figure 49, top left) scattered across the State (up to 0.35 m/sin the Champlain Valley and Catskills), juxtaposed with areas of little change. The mid-future period shows similar patterns, but with more widespread negative values across the State, again adjacent to regions experiencing more modest decreases in 100-m winds. It is unclear what may be leading to these localized changes in wind speed, but the magnitude of the decreased winds stays within the interannual variability and model ensemble spread (uncertainty).

The MIROC5 RCP8.5 runs (Figure 49, middle) are similar to those of the RCP4.5, with a slight increase in 100-m wind speed near the Great Lakes and in Eastern New York. A positive trend is more widespread in the near-future period (Figure 49, middle left), while for the mid-future period, decreased wind speeds are more evident, with notable (but small) regions of larger decreases (up to 0.35 m/s) over the higher terrain of the Catskills and Adirondacks.

In contrast to the GFDL and MIROC models, the NCAR model shows widespread increases in wind speed for both periods, with a small area of the northeastern part of the State forecast to see 100-m wind speeds up to 1 m/s higher than the historical baseline period (1998–2017). This is the only region, scenario, and period where the departure from the historical baseline (in this case, positive), exceeds interannual variability and uncertainty. The NCAR and MIROC5 models handle changes in wind speed over the higher terrain differently: MIROC5 tends to show lower changes in 100 m winds, while the NCAR forecasts trend higher.

Figure 49. Mean Change in Annual Wind Speed: Domain d03, RCP8.5

Domain d03 RCP8.5 mean change in annual wind speed (m/s). Shown are GFDL-CM3 near-future (top left) and mid-future (top right); MIROC5 near-future (middle left) and mid-future (middle right); and NCAR-CCSM4 near-future (bottom left) and mid-future (bottom right). Dashed red lines highlight regions with increased wind speeds over the baseline; dashed blue lines show decreasing regions. Black dots represent locations of existing wind turbines; purple dots depict hypothetical future wind farm locations based on UL-AWS Truepower analysis.

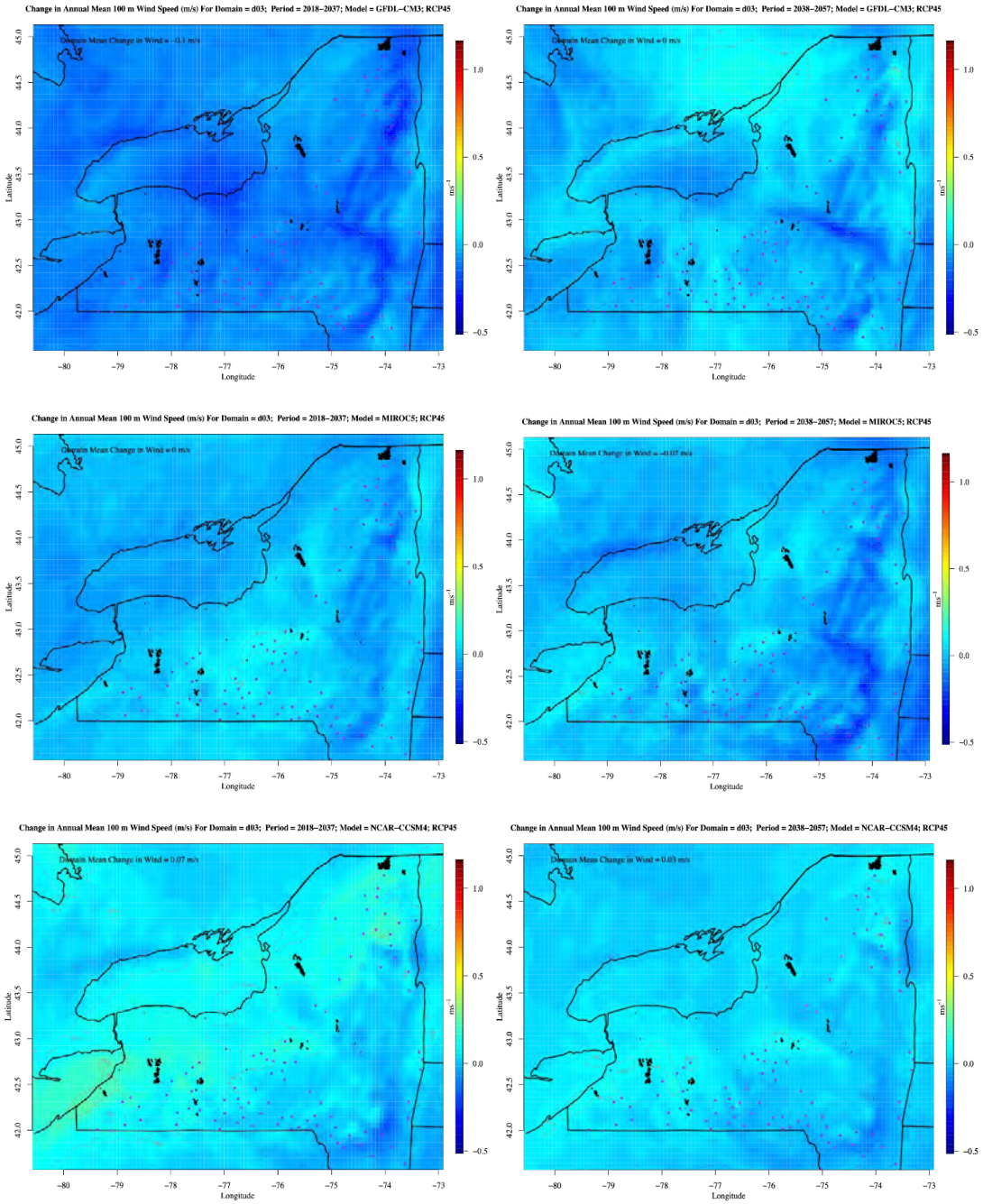

5.4.2 D04 Domain

The d04 domain does not include any utility-scale wind farms on land, nor are any planned for the near future. As a result, our analysis focuses on the offshore region, particularly two Bureau of Ocean Energy Management (BOEM) New York Bight wind development areas: Hudson North and Hudson South. These areas, outlined by black dots in the following figures, cover approximately two-thirds land and one-third coastal and offshore waters. The d04 domain provides valuable information for assessing future regional climate conditions because land-sea interactions play an important role in the weather and climate of the area.

As discussed earlier, for the RCP4.5 near-future period, d04 100-m wind speeds show little difference from the historical baseline (Table 11 and Figure 50). The GFDL and MIROC5 models show slight decreases, with the largest decreases (~0.2 m/s) occurring over the high terrain of the Catskills. Both models show small decreases over the offshore WEAs (0.07 to 0.14 m/s). At the steepest part of the power curve, this would represent a decrease of up to 3% in wind turbines, or about 10 gigawatts (GW) in total. Unlike the GFDL and MIROC5, the NCAR model shows a slight increase in the offshore waters, +0.05 m/s for each WEA, but no change over the entire domain.

For the RCP8.5 scenario (Figure 51), model differences emerge in the sign and magnitude of forecasted changes. The GFDL downscaling results (Figure 51, top) show a general, but slight, decrease in 100 m wind speed over the d04 domain for the near-future (-0.16 m/s) and mid-future (-0.21 m/s) periods, with somewhat larger decreases over the Hudson North (0.19 and 0.27 m/s) and Hudson South (0.20 and 0.31 m/s) WEAs. The decrease, from a baseline mean of about 9.1 m/s, would reduce power production by about 5% to 10%.

The MIROC5 downscaling runs (Figure 51, middle) show no change for domain-averaged 100-m wind speed for the near future period (Figure 51, middle left), with a slight reduction (-0.16 m/s) for the mid-future period (Figure 51, middle right). These changes are the same for the two BOEM WEAs, from near zero (near-future) to a decrease of 0.14 to 0.18 m/s (mid-future), indicating no change in power production for the near-future period and up to a 6% decrease in power production for the mid-future period.

The NCAR model (Figure 51, bottom) predicts comparable increases in 100-m wind speed and power production for the d04 domain and the offshore waters. Domain-averaged increase for the near-future period (Figure 51, bottom left) is 0.19 m/s, with the largest increases (~0.5 m/s) over the Catskills.

This translates to up to 10% power production gains, with larger increases occurring farther offshore. Results for the mid-future period (Figure 51, bottom right) are similar but slightly greater, with wind speed increases from the historical baseline ranging from 0.15 to 0.25 m/s, corresponding to a 3%–5% increase in power production over the Catskills region. In the offshore WEAs (Table 12), 100-m wind speeds increase by 0.15–0.25 m/s, with an equivalent (3%–5%) increase in power production over the offshore waters. Ensemble averages for the two WEAs (Table 12) show minimal changes (within ±0.03 to 0.05 m/s) in overall 100 m wind speeds, or ±1.5% for power production, with the mid-future period exhibiting the slightly higher values.

Figure 50. Mean Change in Annual Wind Speed: Domain d04, RCP4.5

Domain d04 RCP4.5 mean change in annual wind speed (m/s), Shown are GFDL-CM3 near-future (top left) and mid-future (top right); MIROC5 near-future (middle left) and mid-future (middle right); and NCAR-CCSM4 near-future (bottom left) and mid-future (bottom right). Dashed red lines highlight regions with increased wind speeds over the baseline; dashed blue lines show decreasing regions. Black dots represent theoretical 12 MW wind turbines located in parts of the Hudson North and Hudson South BOEM WEAs. MAWS change is given in m/s for each WEA.

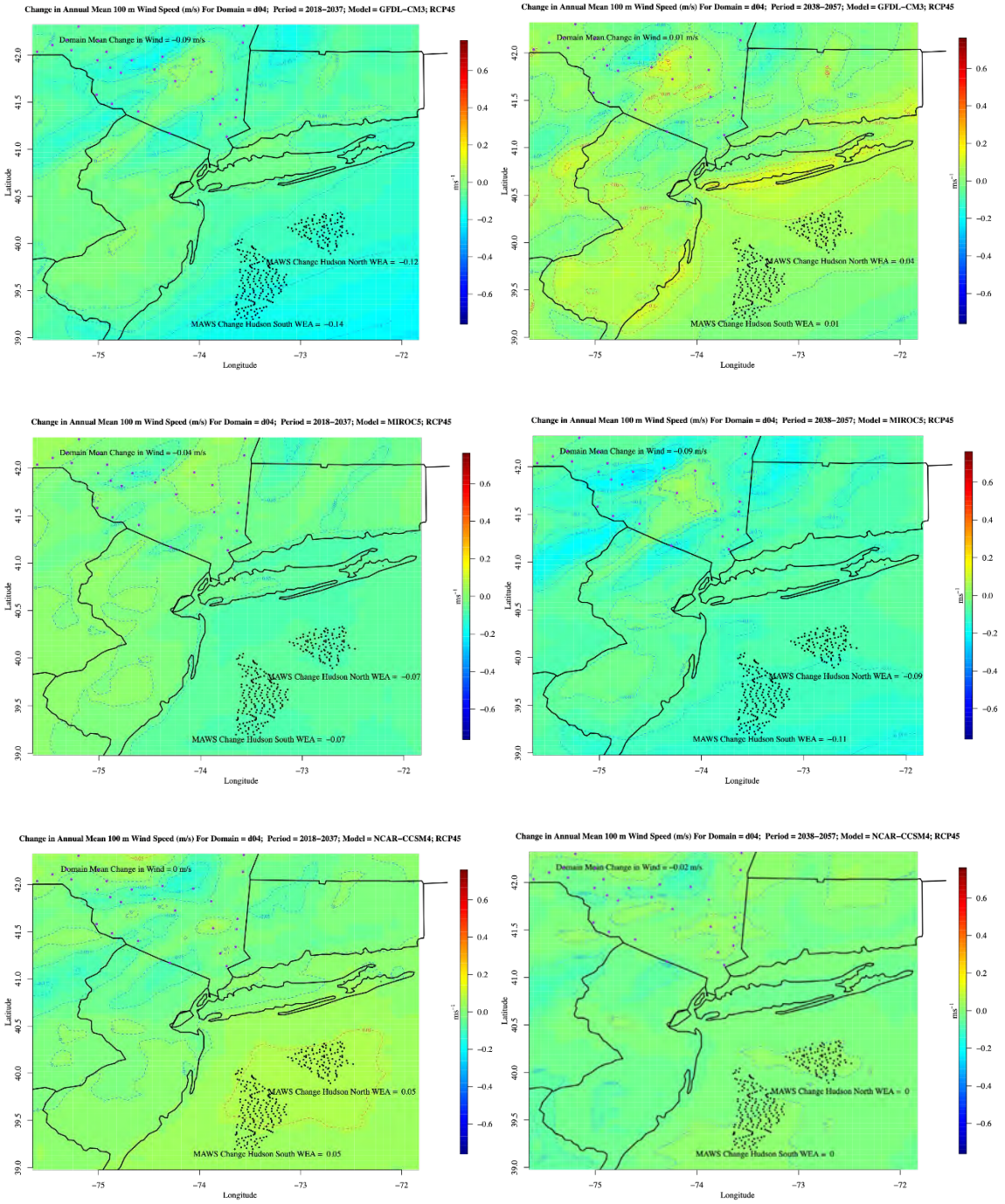

Figure 51. Mean Change in Annual Wind Speed: Domain d04, RCP8.5

Domain d04 RCP8.5 mean change in annual wind speed (m/s). Shown are GFDL-CM3 near-future (top left) and mid-future (top right); MIROC5 near-future (middle left) and mid-future (middle right); and NCAR-CCSM4 near-future (bottom left) and mid-future (bottom right). Dashed red lines highlight regions with increased wind speeds over the baseline; dashed blue lines show decreasing regions. Black dots represent theoretical 12 MW wind turbines located in parts of the Hudson North and Hudson South BOEM WEAs. MAWS change is given in m/s for each WEA.

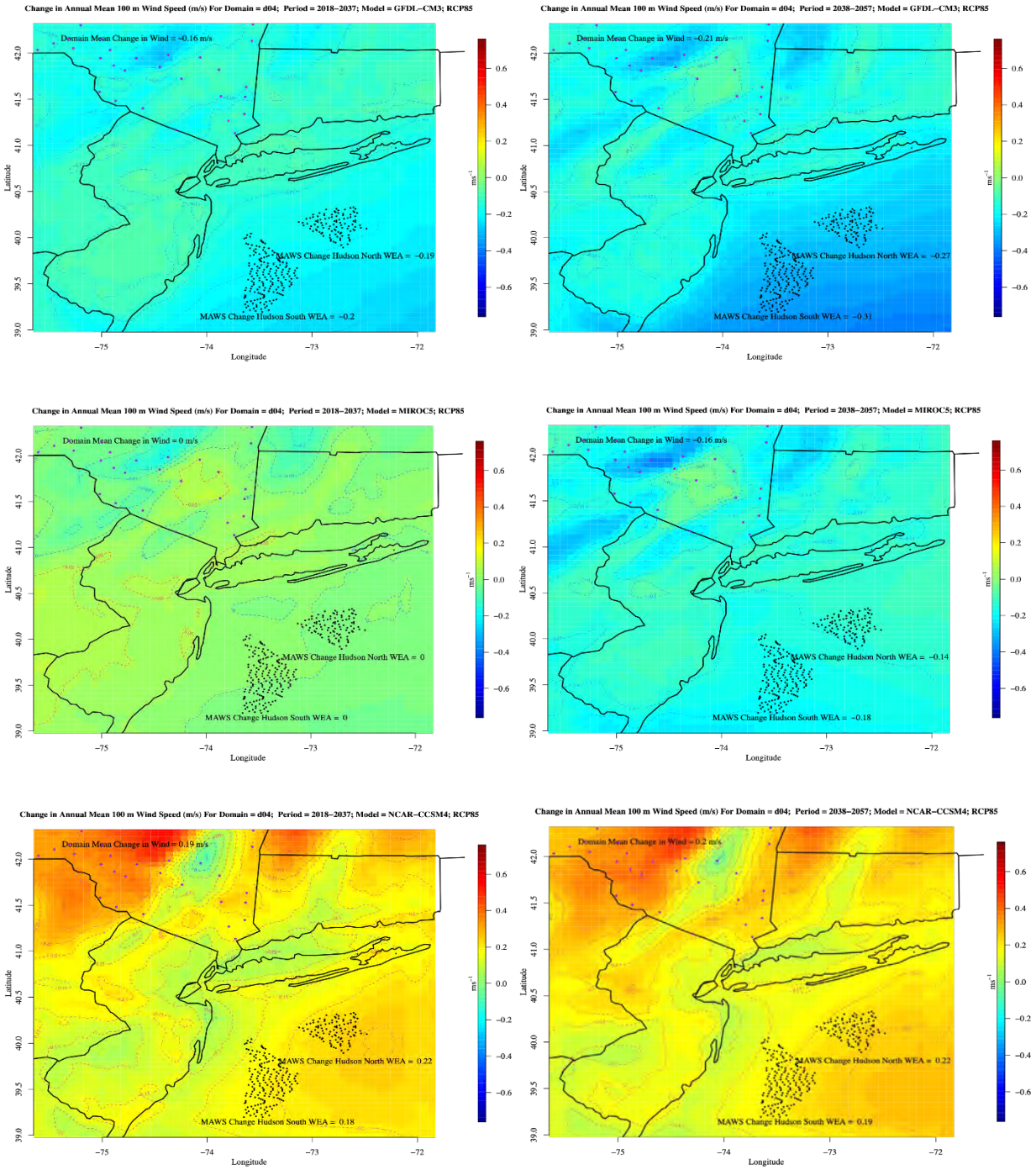

Table 12. Change in Annual Wind Speed: Hudson North and Hudson South Offshore WEAs

Annual changes in wind speed (m/s and %) at 100 m AGL for the Hudson North and Hudson South offshore WEAs.

Model	Scenario	Hudson North (m/s per year and %)		Hudson South (m/s per year and %)	
		2018–2037	2038–2057	2018–2037	2038–2057
GFDL-CM3	RCP4.5	-0.12 (-2%)	0.04 (1%)	-0.14 (-2%)	0.01 (0%)
	RCP8.5	-0.19 (-2%)	-0.27 (-3%)	-0.20 (-3%)	-0.31 (-4%)
NCAR-CCSM4	RCP4.5	0.05 (1%)	0.00 (0%)	0.05 (1%)	0.00 (0%)
	RCP8.5	0.22 (3%)	0.22 (3%)	0.18 (2%)	0.19 (2%)
MIROC5	RCP4.5	-0.07 (-1%)	-0.09 (-1%)	-0.07 (-1%)	-0.11 (-1%)
	RCP8.5	0.00 (0%)	-0.14 (-2%)	0.00 (0%)	-0.18 (-2%)
Mean		**-0.02 (0.0%)**	**-0.04 (-1%)**	**-0.03 (0%)**	**-0.07 (-1%)**

It must again be emphasized that the range of these increases and decreases is within the interannual variability and uncertainty (e.g., the range provided by the model predictions) based on the historical and future time series (see Figures 52–53).

5.4.3 Trends

Focusing on the two offshore WEAs (Table 12 and Figures 52 and 53), 100-m wind speeds change little during the first two periods (less than ±0.12 m/s decade^{-1}). In the mid-future period, the GFDL model, reflecting changes in Figures 50 and 51, and Table 12, presents more distinct trends, particularly with MIROC5 showing increases of up to 0.55 m/s per decade. As noted in the precipitation trends analysis, these values reflect the influence of start and end points more than a particular trend throughout the time series. Figures 52 and 53 demonstrate the interannual variability for all three models during the historical, near-future, and mid-future periods, with both scenarios reaching values up to 1 m/s and an ensemble mean of ±0.3 m/s (about 4%, consistent with observations). No apparent trend appears in interannual variability. This supports the conclusion that these model experiments indicate little change in 100-m wind speeds, wind energy potential, or interannual variability of the wind energy resource over the next 40 years.

Figure 52. Wind Speed Trends: Hudson North Wind Energy Area

100-m AGL wind speed trends (m/s per decade) for Hudson North offshore WEA from 1998 to 2057. Shown are RCP4.5 (right) and RCP8.5 (left); GFDL (top), MIROC5 (middle), and NCAR (bottom). Trend lines are as in Figure 39: historical period (black solid line, 1998–2017), near-future period (solid red line, 2018–2037), and mid-future period (solid blue line, 2038–2057).

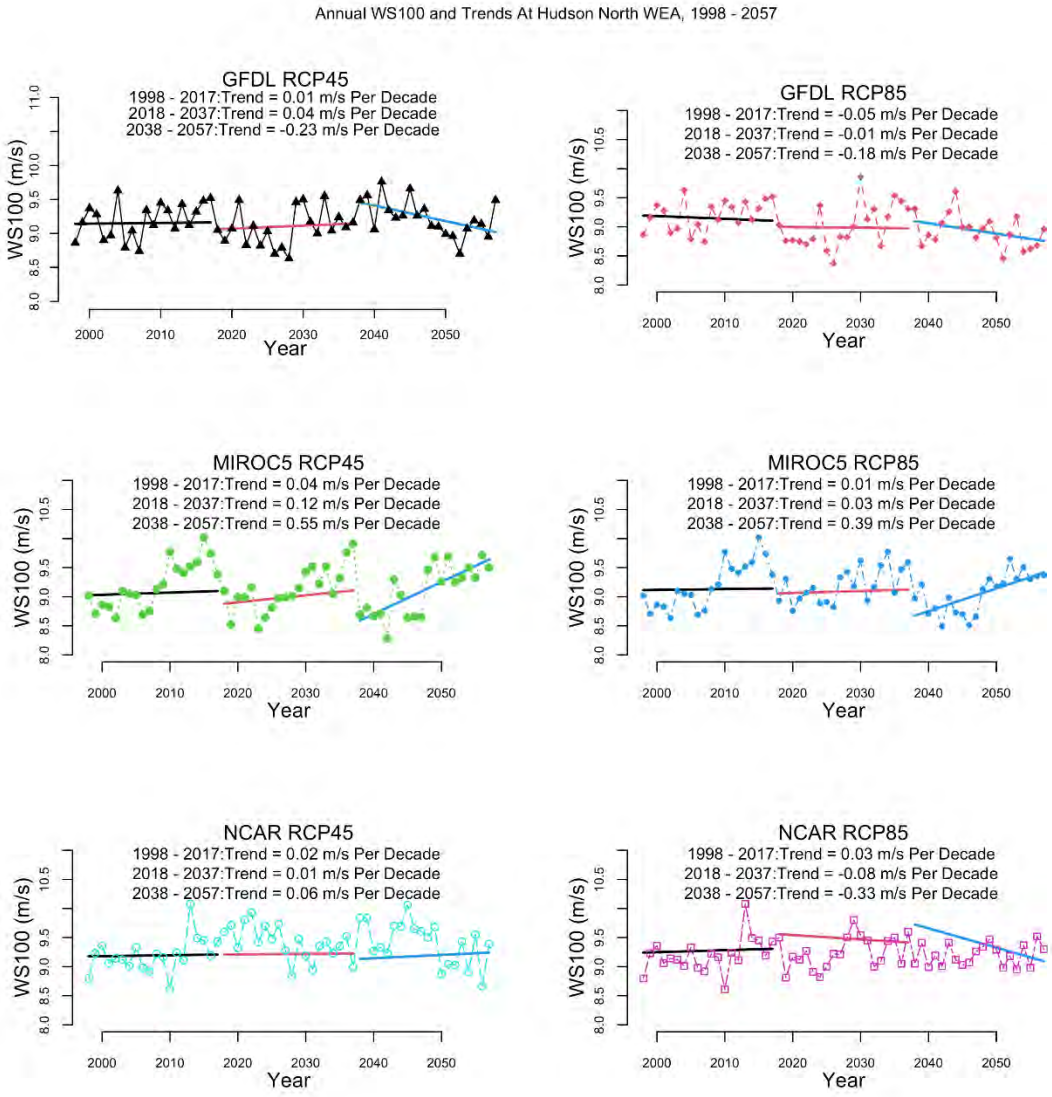

Figure 53. Wind Speed Trends: Hudson South Wind Energy Area

100-m AGL wind speed trends (m/s per decade) for Hudson North BOEM offshore WEA from 1998 to 2057. Shown are RCP4.5 (right) and RCP8.5 (left); GFDL (top), MIROC5 (middle), and NCAR (bottom). Trend lines are as in Figure 39: historical period (black solid line, 1998–2017), near-future period (solid red line, 2018–2037), and mid-future period (solid blue line, 2038–2057).

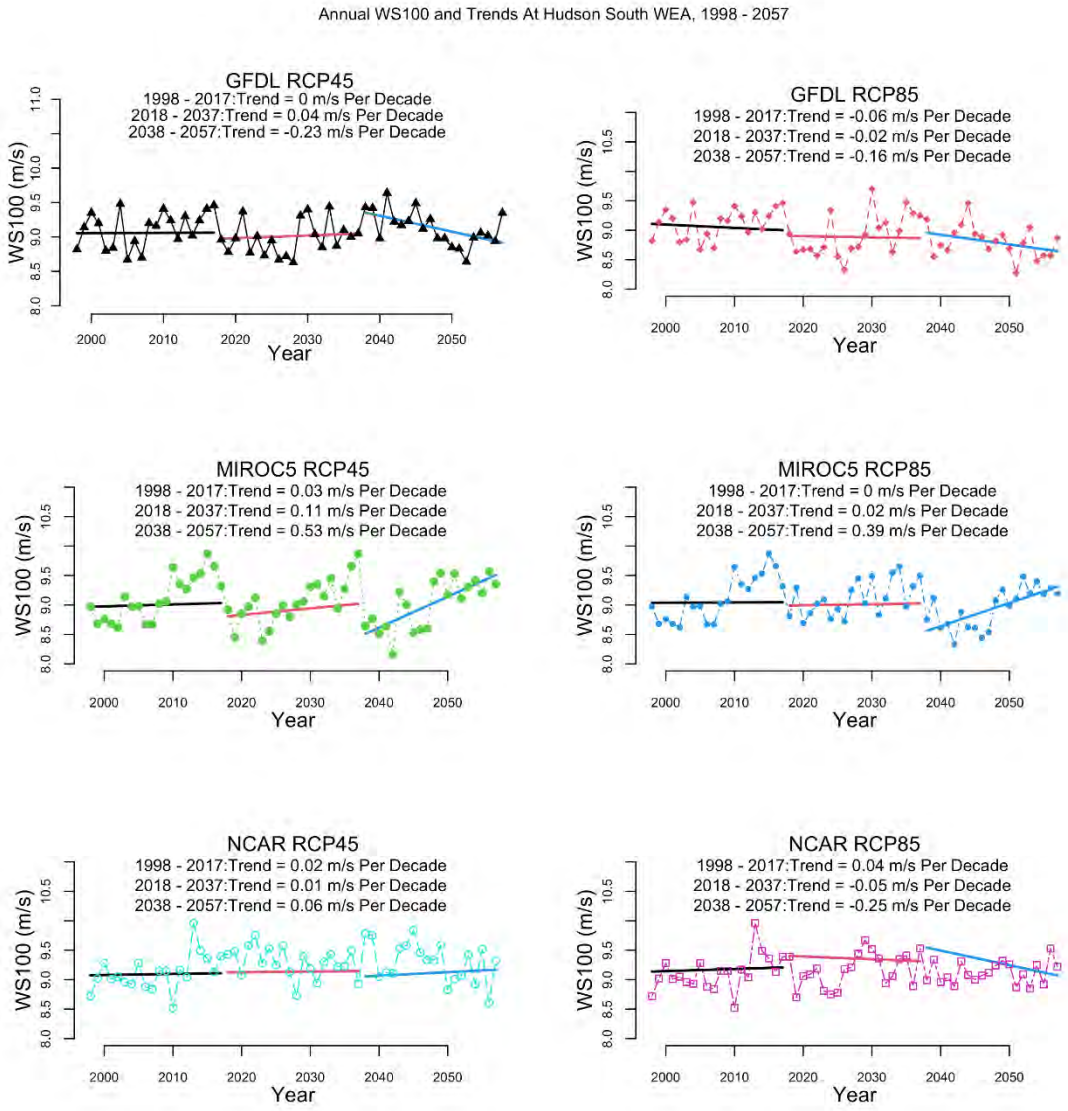

5.4.4 Monthly and Seasonal Changes

The monthly and seasonal changes in 100-m winds within the d03 and d04 domains appear in Figures 54 through 61. For the d03 domain, the RCP4.5 near-future period (Figure 54) shows a random distribution of monthly changes in wind speed. Only June displays agreement among all three models on the sign of the change, a small increase of ~+0.1 m/s. The GFDL model shows decreasing wind speeds from July through September, with July showing a decrease of nearly 0.6 m/s). No other monthly or seasonal trends are apparent. The NCAR-CCSM4 model shows the largest increase in February (~+0.45 m/s), while MIROC5 shows a similarly large increase in November. A similar pattern appears during the mid-future period (Figure 55), with the exception of the NCAR model producing large anomaly swings in January (~-0.6 m/s) and February (~+0.6 m/s). All three models show a slight decrease in wind speeds in July and a slight increase during November.

Figure 54. Monthly Wind Speed Change: D03 Grid, RCP4.5, Near-Future Period

Monthly 100-m wind speed change (m/s) for the d03 grid for the RCP4.5 near-future period. The outputs from GFDL-CM3 (red bars), MIROC5 (green bars), and NCAR-CCSM4 (blue bars) are shown.

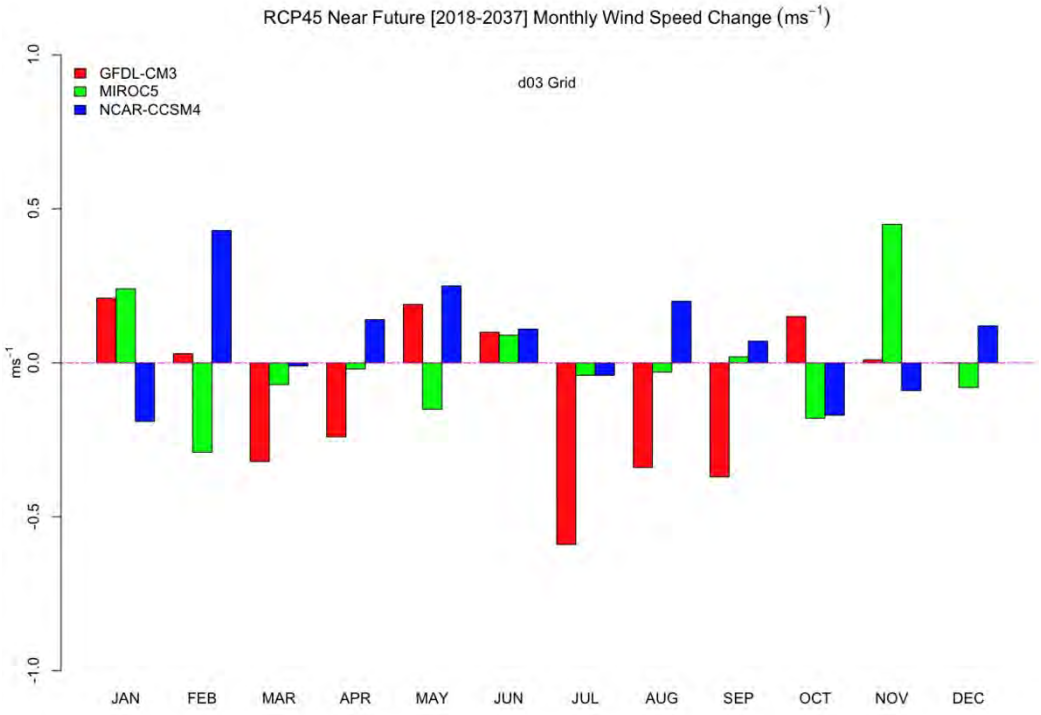

For the RCP8.5 scenario near-future period (Figure 56), the NCAR-CCSM4 model shows a more consistent pattern of increasing monthly wind speeds, with every month showing an increase in wind speeds (~+.2 m/s) to +0.75 m/s in March, consistent with the regional pattern shown in Figure 49. The GFDL-CM3 model shows decreasing winds during the warm season (June–October; >0.5 m/s for July and August). The MIROC5 runs show small changes (±0.3 or less m/s) for all months. Only two months, May and December, show model consistency in the sign of the change. A similar pattern is apparent for the mid-future period (Figure 57), but only October features sign consistency for the three model runs.

Figure 55. Monthly Wind Speed Change: D03, Grid RCP4.5, Mid-Future Period

Monthly 100-m wind speed change (m/s) for the d03 grid for the RCP4.5 mid-future period. The outputs from GFDL-CM3 (red bars), MIROC5 (green bars), and NCAR-CCSM4 (blue bars) are shown.

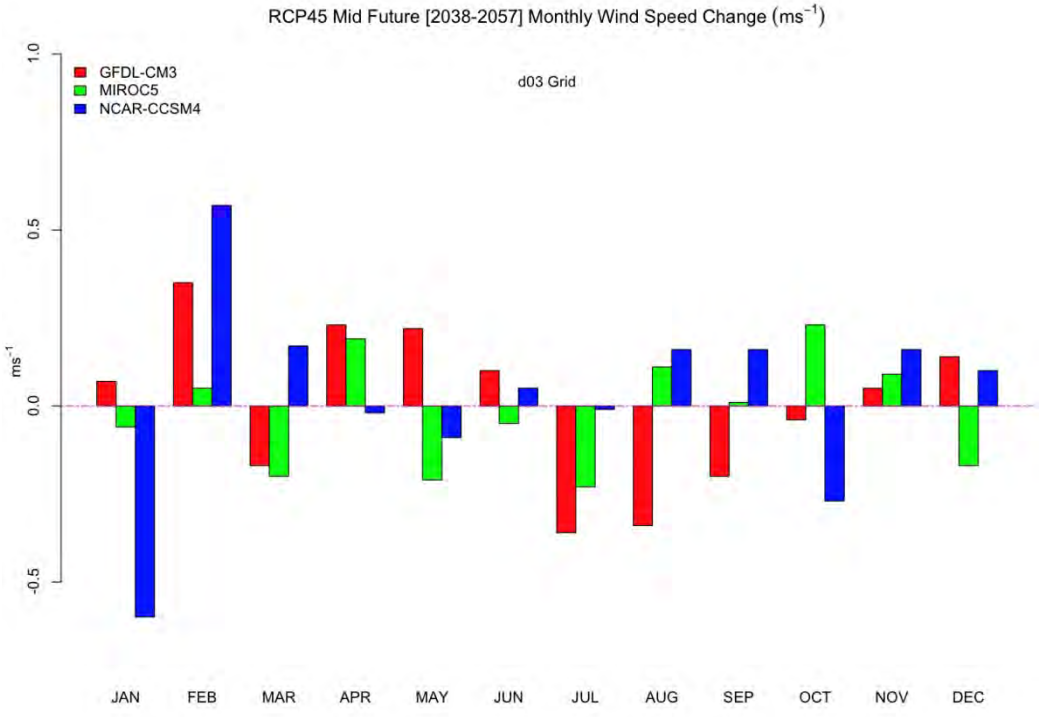

Figure 56. Monthly Wind Speed Change: D03 Grid, RCP8.5, Near-Future Period

Monthly 100-m wind speed change (m/s) for the d03 grid for the RCP8.5 near-future period. The outputs from GFDL-CM3 (red bars), MIROC5 (green bars), and NCAR-CCSM4 (blue bars) are shown.

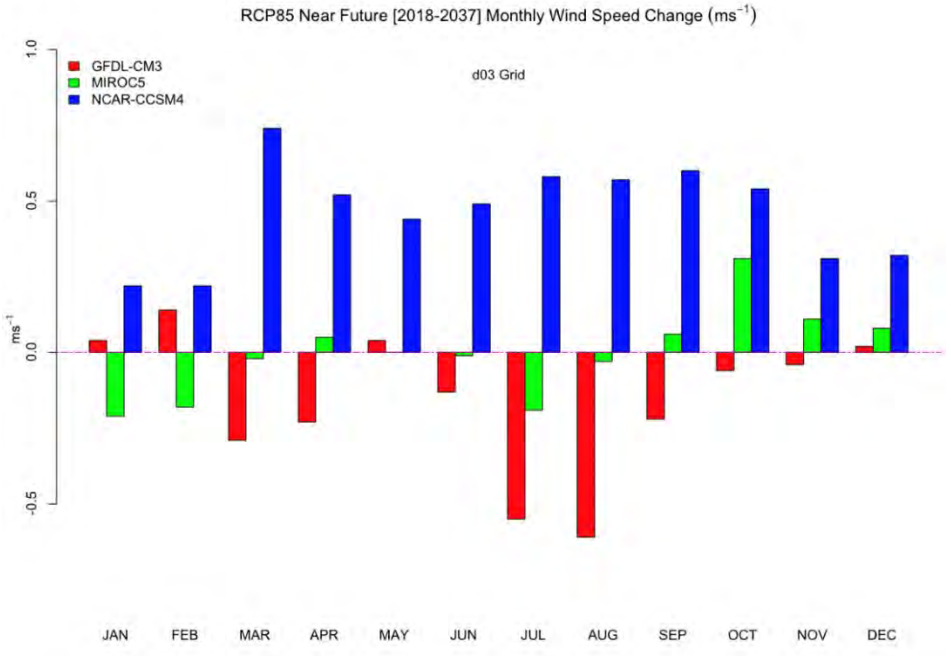

Figure 57. Monthly Wind Speed Change: D03 Grid RCP8.5, Mid-Future Period

Monthly 100-m wind speed change (m/s) for the d03 grid for the RCP8.5 mid-future period. The outputs from GFDL-CM3 (red bars), MIROC5 (green bars), and NCAR-CCSM4 (blue bars) are shown.

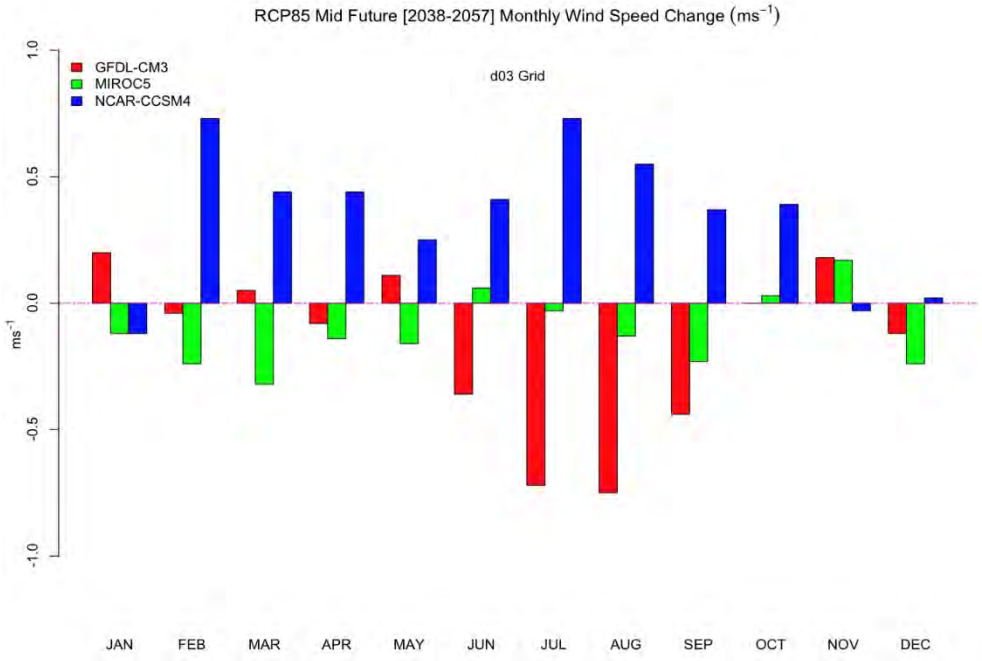

For the d04 domain RCP4.5 scenario, there is a bit more consistency regarding the sign of the change (Figures 58 and 59). For the near-future period, a weak signal of small decreases in 100-m wind speeds appears during the cold season (November–March). A similar pattern holds for the mid-future period. For the RCP8.5 scenario (Figures 60 and 61), the NCAR-CCSM4, which produced the most aggressive increases in 100-m winds over the d03 grid under RCP8.5, shows large increases during the warm season (~0.5 m/s). For the mid-future period (Figure 61), the NCAR model shows increases in 9 of 12 months.

Figure 58. Change in Monthly Wind Speed: D04 Grid, RCP4.5, Near-Future Period

Monthly 100-m wind speed change (m/s) for the d04 grid for the RCP4.5 near-future period. The outputs from GFDL-CM3 (red bars), MIROC5 (green bars), and NCAR-CCSM4 (blue bars) are shown.

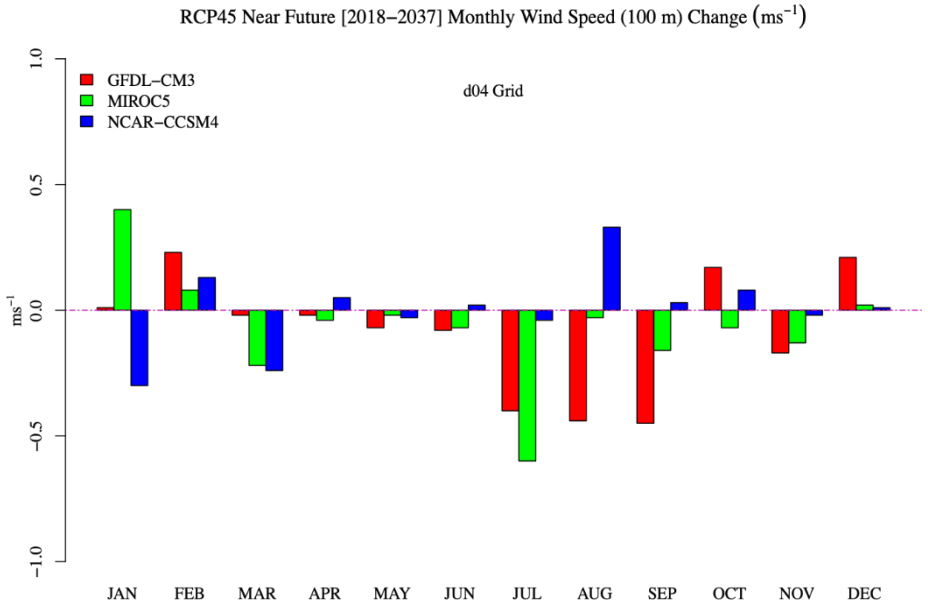

Figure 59. Change in Monthly Wind Speed: D04 Grid, RCP4.5, Mid-Future Period

Monthly 100-m wind speed change (m/s) for the d04 grid for the RCP4.5 mid-future period. The outputs from GFDL-CM3 (red bars), MIROC5 (green bars), and NCAR-CCSM4 (blue bars) are shown.

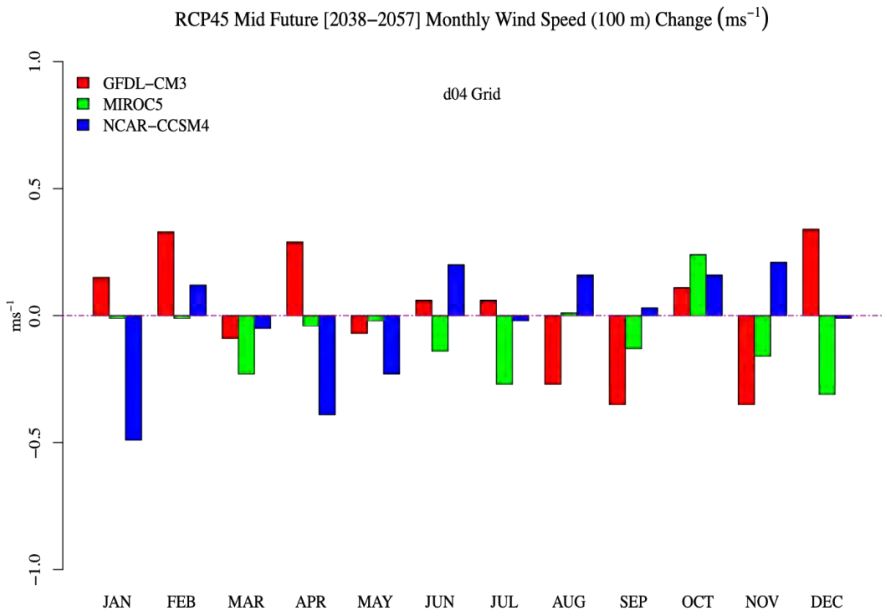

Figure 60. Change in Monthly Wind Speed: D04 Grid, RCP8.5, Near-Future Period

Monthly 100-m wind speed change (m/s) for the d04 grid for the RCP8.5 near-future period. The outputs from GFDL-CM3 (red bars), MIROC5 (green bars), and NCAR-CCSM4 (blue bars) are shown.

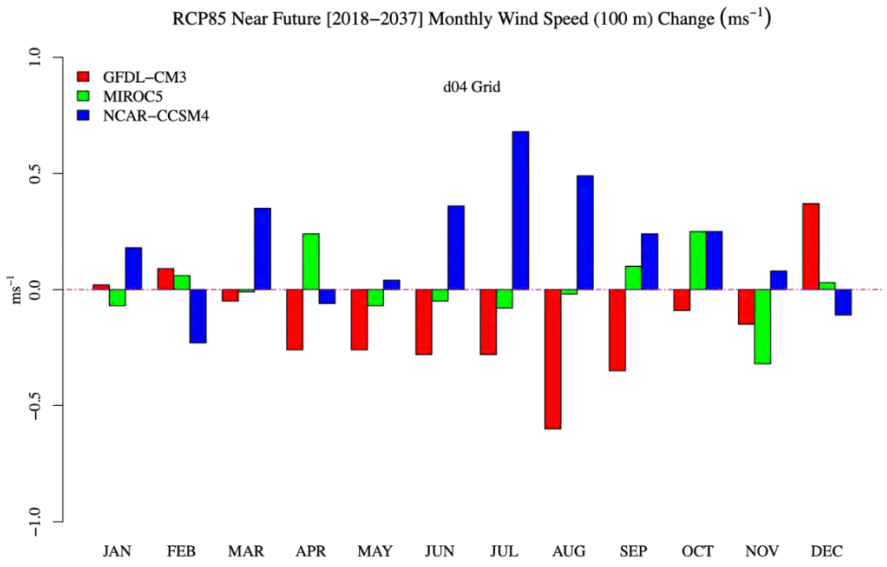

Figure 61. Change in Monthly Wind Speed Change: D04 Grid, RCP8.5, Mid-Future Period

Monthly 100-m wind speed change (m/s) for the d04 grid for the RCP8.5 mid-future period. The outputs from GFDL-CM3 (red bars), MIROC5 (green bars), and NCAR-CCSM4 (blue bars) are shown.

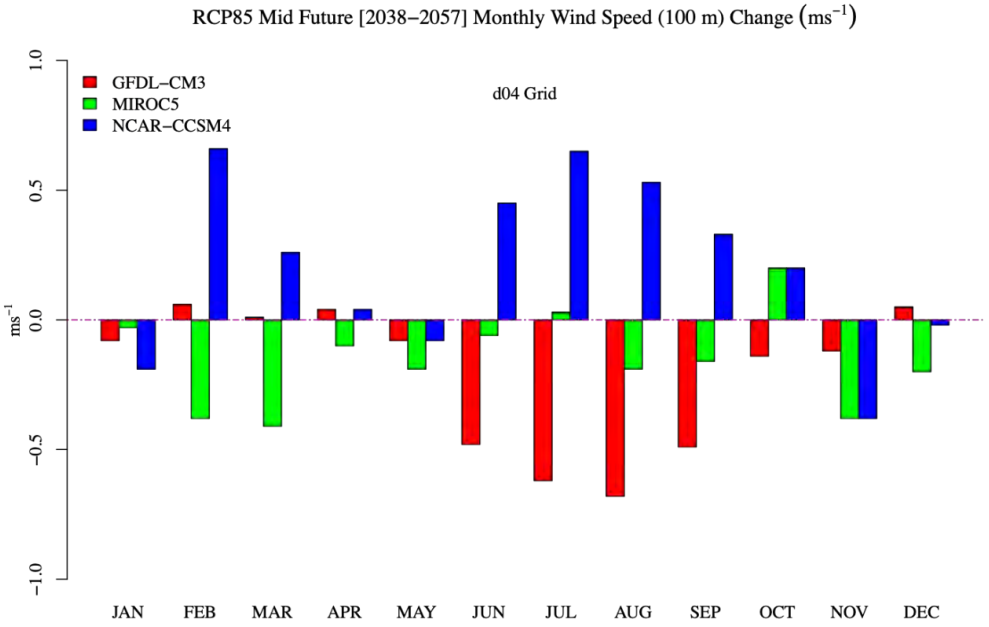

5.5 Future Trends in Solar (Surface Irradiance)

As of this writing, New York State ranks 10th in the nation in operational solar energy facilities, with more than 3,000 MW of installed capacity (See EIA 2021, NYSERDA 2021). Most utility-scale solar energy facilities are located in the populated regions of the State (Figure 62), which not surprisingly coincides with areas of stronger solar energy resources: specifically, the Hudson Valley, New York City and Long Island, the shores of Lakes Erie and Ontario,[10] and the Southern Tier (Figure 63). Distributed solar is also concentrated along population corridors, primarily in suburban regions in the southeast and near the Lake Erie (Buffalo) and Lake Ontario (Rochester) shorelines. This analysis focuses on two large-scale energy facilities in the d03 and d04 domains: the Garnet Energy Center (GEC), a proposed 200-MW photovoltaic solar energy generating facility with 20 MW of energy storage in the Town of Conquest, Cayuga County, and the Long Island Solar Farm (LISF), an operational 38 MW facilities in the Town of Brookhaven, Suffolk County, Long Island. Two other proposed facilities in the d03 domain are also referenced: the North Side Energy Center (NEC), 180-MW solar project located in the Towns of Massena, Brasher, and Norfolk in St. Lawrence County, and the 270-MW (with 20-MW storage) South Ripley Solar Project (SRSP) proposed for the Town of Ripley in Chautauqua County (see also Figure 64 and caption).

Figure 62. Map of Installed Solar Energy in New York State

Figures in MW installed by county.

Source: NYSERDA 2021.

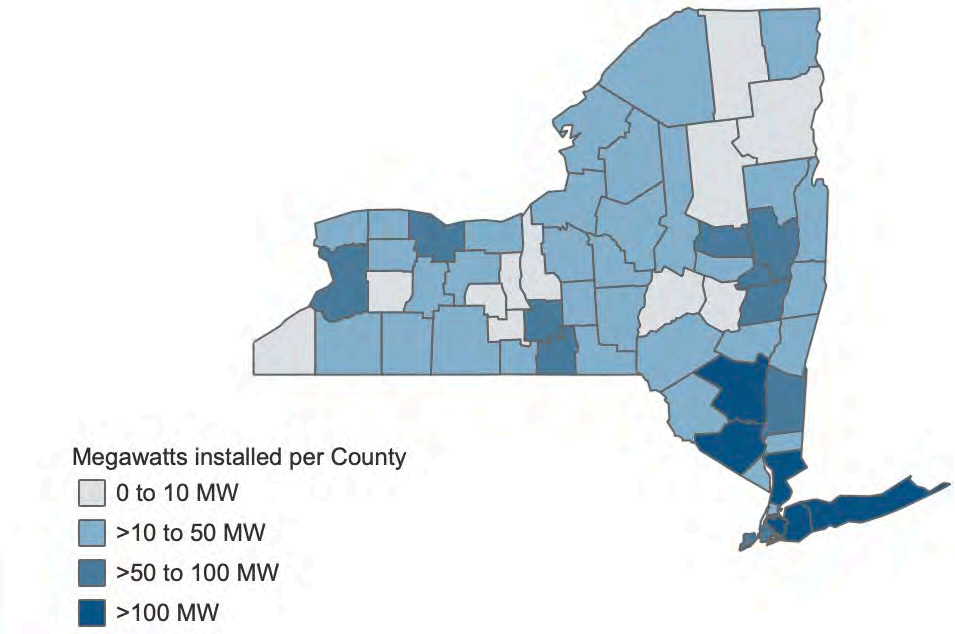

Figure 63. Map of Solar Resource in New York State

Solar resource (GHI), kilowatt-hours per square meter per day (kWh/m^2 per day) for New York State.

Source: National Renewable Energy Laboratory 2017

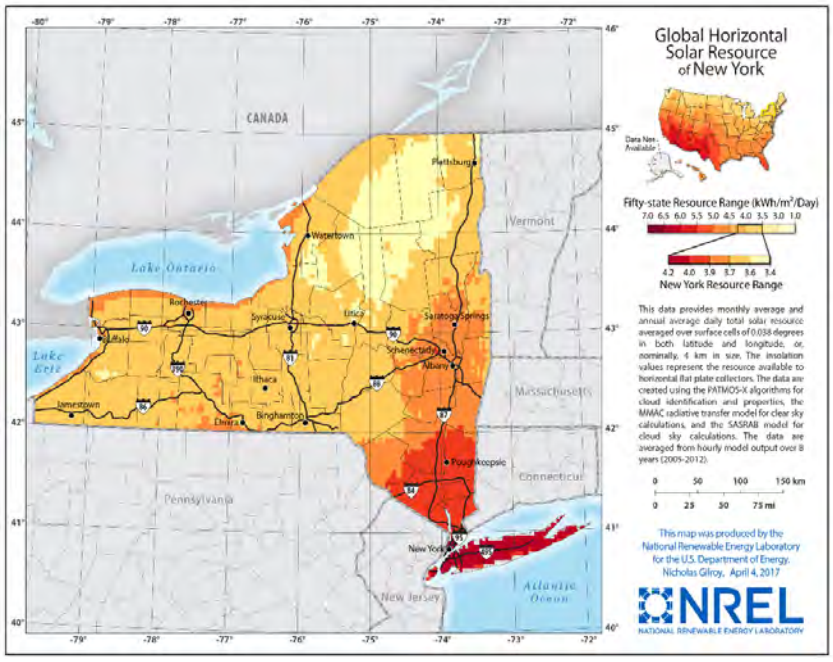

5.5.1 Issues with GFDL-CM3 RCP4.5 Mid-Future Period

Analysis identified an issue with the GFDL-CM3 RCP4.5 mid-future period. Ten years of the mid-future period run showed anomalously high values (>100 W/m^2 above the baseline historical output and corresponding years for the NCAR and MIROC5 models) in the downscaled output. We decided to remove this model run from this report; further analysis continues into the cause of these anomalous values.

5.5.2 Overview of the Mean Annual Change in Surface Irradiance

Baseline historical annual means in surface irradiance for the three models range from 257 to 277 W/m^2 for the d03 domain and 292 to 311 W/m^2 for the d04 domain. Interannual variability is around 20 W/m^2 or 6%–7%. Table 13 shows that the GFDL and MIROC5 models indicate modest changes for both scenarios and periods (<2.5%). All three models show modest decreases for both domains under RCP4.5 around the proposed GEC (see Table 14). For the mid-future period (noting the absence of GFDL output), the NCAR and MIROC5 models also indicate little change or a modest decrease in surface irradiance; the largest change is 4.59 W/m^2 for the NCAR model over the d03 domain, or <1.5%.

Table 13. Change in Annual Mean Solar Irradiance: D03 and D04 Grids

Annual mean 100 m solar irradiance change (W/m²) relative to the 1998–2017 base period for WRF grids d03 and d04.

Model	Scenario	D03 GHI (W/m^2)		D04 GHI (W/m^2)	
		2018–2037	2038–2057	2018–2037	2038–2057
GFDL-CM3	RCP4.5	-3.84	NA	-5.16	NA
	RCP8.5	-5.20	6.40	-5.43	7.72
NCAR-CCSM4	RCP4.5	-7.02	-4.59	-2.43	-0.36
	RCP8.5	22.26	22.97	21.31	21.97
MIROC5	RCP4.5	-7.12	-3.28	-5.62	0.52
	RCP8.5	-6.09	-8.61	-6.14	-2.43

For the RCP8.5 scenario, the GFDL model shows small decreases (-5.20 and -5.43 W/m^2) for the near-future period, followed by similar increases for the mid-future period. MIROC5 shows modest decreases for both periods and domains (-2.43 to -8.61 W/m^2). The NCAR model, however, shows increases across both domains and periods compared with the historical baseline. However, time series analysis of the annual mean values shows that the increase is largely confined to the near-future period, with the mid-future period featuring annual values declining from a 40-year positive trend, including the historical baseline (see Figure 68 and discussion following).

The ensemble average of all models for both scenarios shows little change in the near-future period, with slight or modest increases for the mid-future period (+5.48 W/m^2 for the d04 domain, or <2%, and +14.69 W/m^2 for the d03 domain, or about 5%). We next examine the spatial characteristics of the model-predicted changes.

For the RCP4.5 scenario, all three models are consistent in showing modest decreases in surface irradiance across the d03 domain (Figure 64). The largest decreases (>10 W/m^2) are located across the higher elevations of the State (particularly the Adirondacks). The smallest decreases occur over and along the immediate coasts of Lake Erie and Lake Ontario. The three proposed utility-scale facilities show values within ±2 W/m^2 of the domain averages shown in Table 13 and Figure 63. Tables 14 and 15 contain summaries of the irradiance changes at these facilities.

Table 14. Change in Surface Irradiance: Garnet Energy Center

Surface irradiance change (W/m²) relative to the GEC project site's 1998–2017 base period.

Model	Scenario	2018–2037	2038–2057
GFDL-CM3	RCP4.5	-3.73	NA
	RCP8.5	-5.82	6.16
NCAR-CCSM4	RCP4.5	-7.10	-3.54
	RCP8.5	26.27	26.65
MIROC5	RCP4.5	-7.76	-3.75
	RCP8.5	-6.65	-9.35

Table 15. Change in Surface Irradiance: Long Island Solar Farm

Surface irradiance change (W/m²) relative to the 1998–2017 base period for the LISF project site.

Model	Scenario	2018–2037	2038–2057
GFDL-CM3	RCP4.5	-7.26	NA
	RCP8.5	-7.73	3.74
NCAR-CCSM4	RCP4.5	-2.40	-0.61
	RCP8.5	20.70	21.37
MIROC5	RCP4.5	-6.52	-0.13
	RCP8.5	-6.05	-4.20

For the RCP8.5 scenario, greater model divergence appears (Table 13), which reflects Figure 65's spatial distribution. The GFDL runs show a small decrease in surface irradiance during the near-future period (Figure 65, top left), followed by a small (6.4 W/m^2) increase above the baseline during the mid-future period (Figure 65, top right). As in the RCP4.5 scenario, the larger decreases concentrate

over mountainous terrain, while smaller (to near zero) negative changes occur near the Great Lakes. The MIROC5 downscaling output shows a similar decrease (-6.09 W/m^2) during the near-future period (Figure 65, middle left), which slightly intensifies (to -8.61 W/m^2) during the mid-future period (Figure 65, middle right). Spatial patterns remain similar, although the MIROC5 runs depict a larger area of small declines in irradiance along the Southern Tier. In contrast, and consistent with Table 13, the NCAR model shows relatively large increases in surface irradiance across the entire State, with smaller increases near the Great Lakes and the largest enhancement in solar radiation over the Southern Tier and Finger Lakes regions (>30 W/m^2), or about a 10% increase over the historical baseline. As discussed below, this pattern primarily reflects a steady increase in irradiance during the near-future period, followed by a decline during the mid-future period (Figure 68).

A similar pattern is evident for the d04 domain (Figures 66 and 67), noting that one-third of the domain is over water. Under the RCP4.5 scenario, the GFDL near-future forecast (Figure 66, top left) shows a small decrease in surface irradiance (domain average of -5.16 W/m^2), with a slightly larger decrease of -7.26 W/m^2 at the LISF (see also Table 15). Larger reductions occur over Long Island and southeast of the Catskills. The MIROC5 near-future period (Figure 66, middle left), shows a similar pattern, although the area of minimum irradiance south of the Catskills shifts eastward toward the Mid-Hudson Valley and near the Connecticut border. During the mid-future period, however, the domainwide change trends back toward the historical baseline. The NCAR model runs for both future periods show minimal changes in irradiance across the domain, with the largest decreases (~ -4 to -6 W/m^2) inland and negligible changes over Long Island.

Under the RCP8.5 scenario (Figure 67), GFDL again projects a small decrease in surface irradiance during the near-future period (Figure 67, top left), with LISF showing a decrease of -7.73 W/m^2. This is followed by a compensating increase during the mid-future period (Figure 67, top right), with the largest increases occurring offshore and smaller increases over Long Island (where LISF increases by about 4 W/m^2) and the Lower Hudson Valley. MIROC5 shows a similar pattern, although both the near-future and mid-future periods show decreases of -6.14 and -2.43 W/m^2, respectively (Figure 67, middle).

Figure 64. Change in Global Horizontal Irradiance: Domain d03, RCP4.5

Domain d03 RCP4.5 mean change in annual global horizontal irradiance (W/m^2). Shown are GFDL-CM3 near-future (top), MIROC5 near-future (middle left), and mid-future (middle right); and NCAR-CCSM4 near-future (bottom left) and mid-future (bottom right). Local changes for three proposed utility-scale solar power generating facilities are shown: the 270 MW SRSP, the 200 MW GEC, and the 180-MW NEC. Dots represent 15 GW of assumed fixed (black) or tilted (red) utility-scale solar energy facilities.

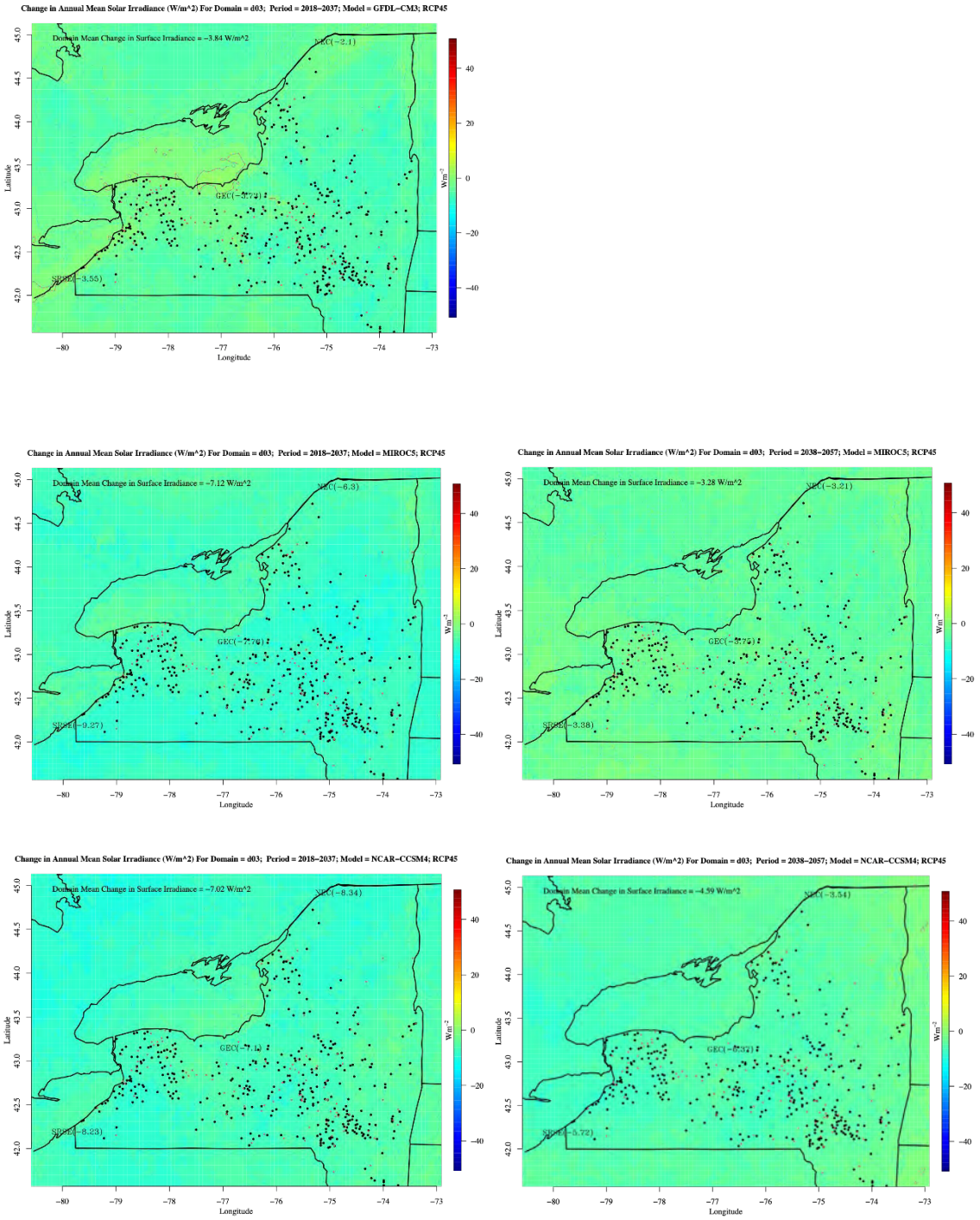

Figure 65. Change in Global Horizontal Irradiance: Domain d03, RCP8.5

Domain d03 RCP8.5 mean change in annual global horizontal irradiance (W/m^2). Shown are GFDL-CM3 near-future (top left) and mid-future (top right); MIROC5 near-future (middle left) and mid-future (middle right); and NCAR-CCSM4 near-future (bottom left) and mid-future (bottom right). Local changes for three proposed utility-scale solar power generating facilities are shown: the 270 MW SRSP, the 200 MW GEC, and the 180 MW NEC. Dots represent 15 GW of assumed fixed (black) or tilted (red) utility-scale solar energy facilities.

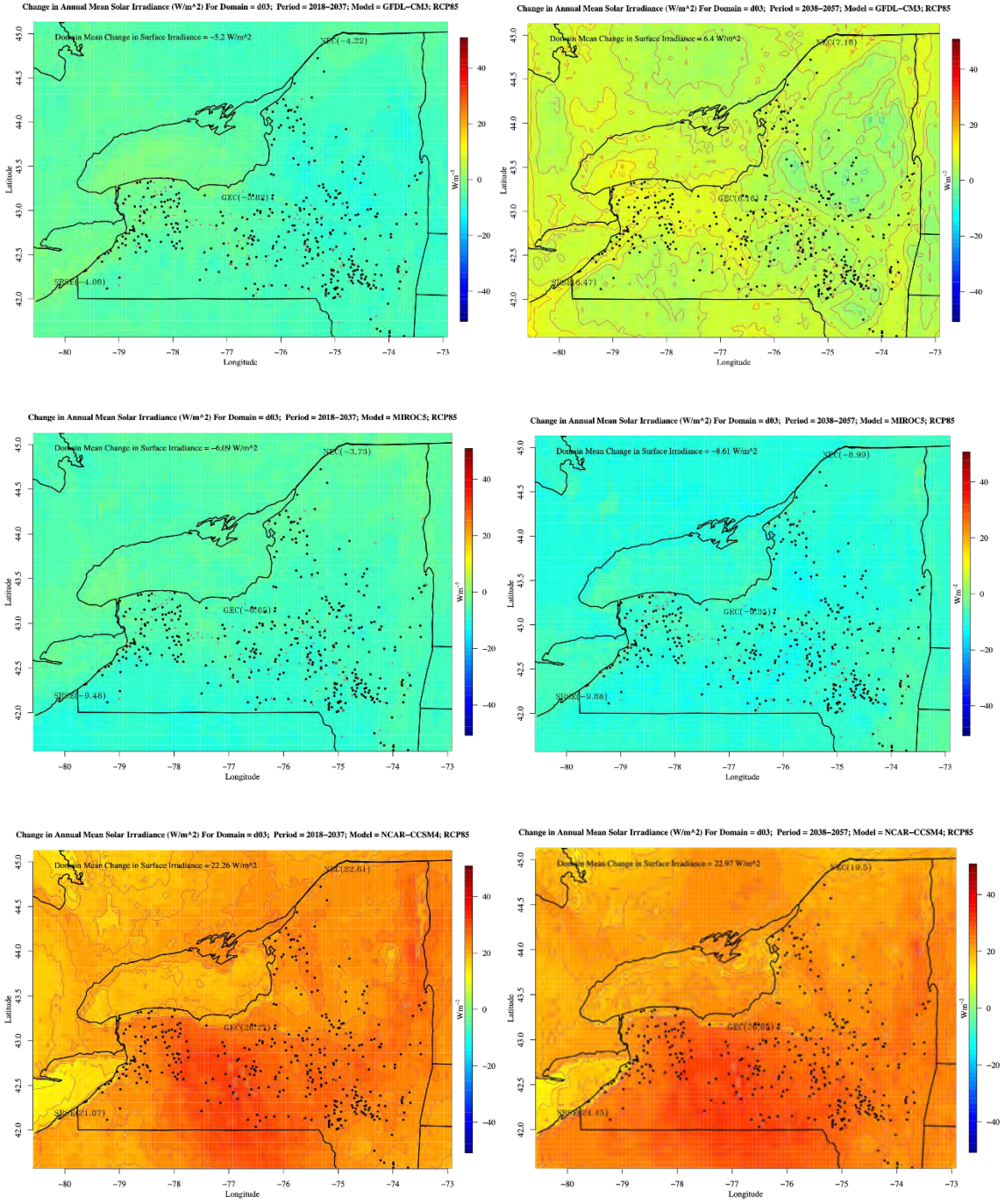

Figure 66. Change in Annual Global Horizontal Irradiance: Domain d04, RCP4.5

Domain d04 RCP4.5 mean change in annual global horizontal irradiance (W/m^2). Shown are GFDL-CM3 near-future (top); MIROC5 near-future (middle left), and mid-future (middle right); and NCAR-CCSM4 near-future (bottom left) and mid-future (bottom right). Changes in mean annual irradiance are shown for the operational 38 MW LISF power generating facility.

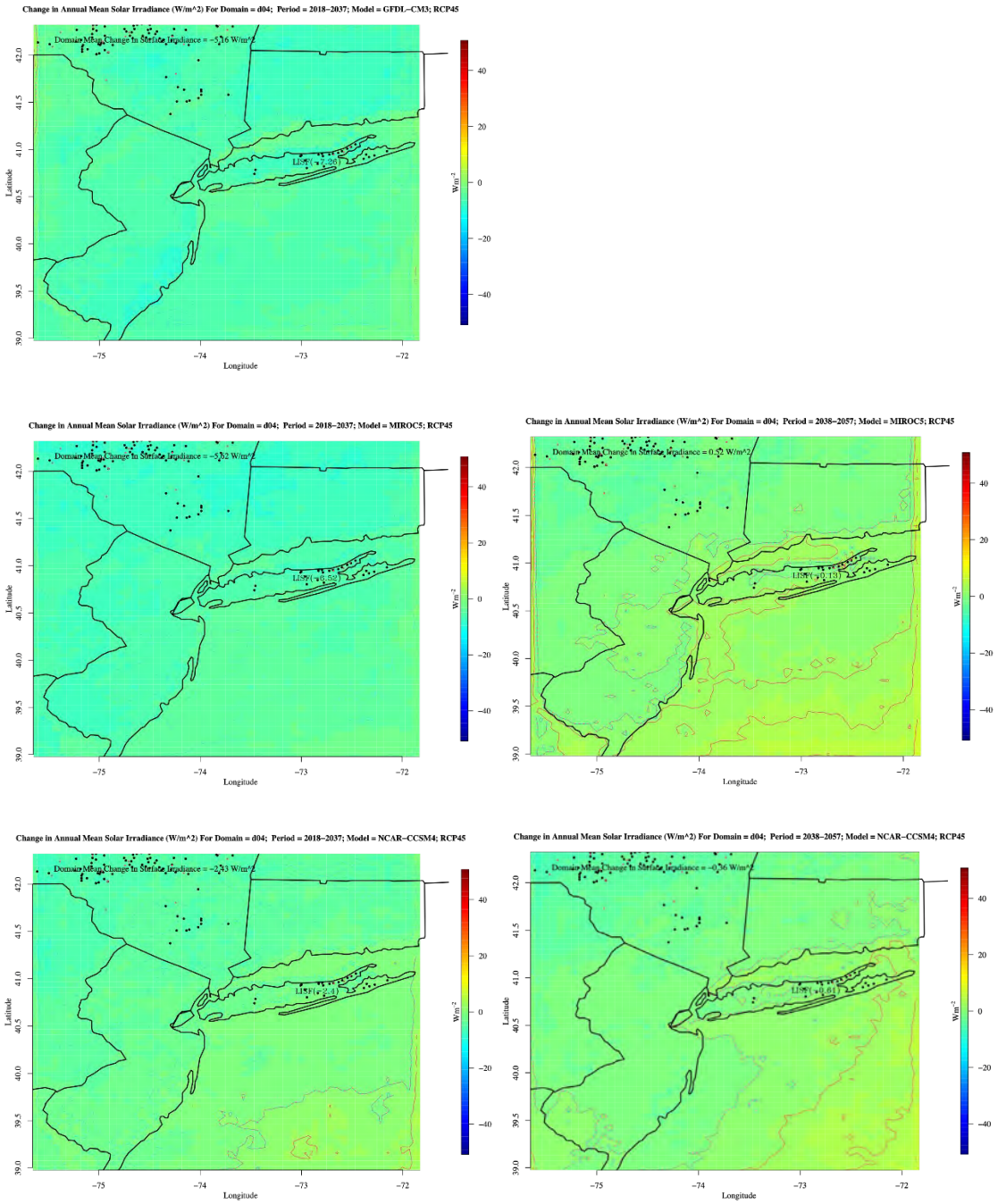

Figure 67. Change in Annual Global Horizontal Irradiance: Domain d04, RCP8.5

Domain d04 RCP8.5 mean change in annual global horizontal irradiance (W/m^2). Shown are GFDL-CM3 near-future (top left) and mid-future (top right); MIROC5 near-future (middle left) and mid-future (middle right); and NCAR-CCSM4 near-future (bottom left) and mid-future (bottom right). Changes in mean annual irradiance are shown for the operational 38 MW LISF power generating facility.

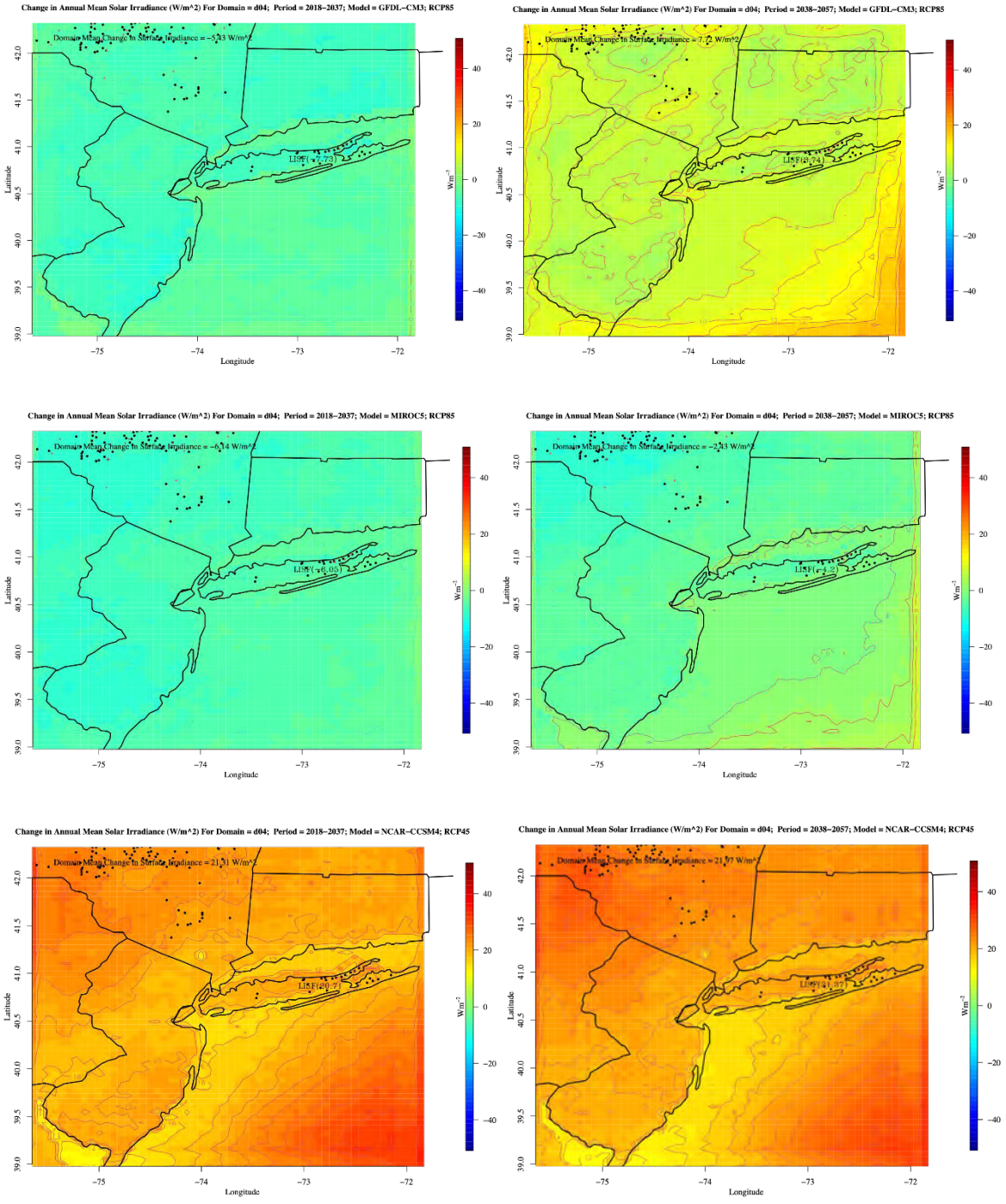

5.5.3 Period Trends

We repeat the caveat that period trends should not be confused with changes in the annual mean values. These are trends for a particular 20-year time series: 1998–2017, 2018–2037, or 2038–2057. Thus, for the trends represented in Figure 68 for both scenarios, the three models, and the three periods at GEC south of Lake Ontario, the "trend per decade" value can differ in sign and magnitude from the actual annual change in annual irradiance between the baseline and the two future periods. For example, for the NCAR RCP8.5 near-future period, the trend of -8.34 W/m^2 per decade is opposite in sign and more than twice the magnitude of the change in mean annual surface irradiance, which is +22.97 W/m^2.

The time series are more indicative of interannual variability, ranging from 20 to 40 W/m^2 across the three models. For RCP4.5, the GFDL model exhibits a consistently negative decadal trend (Figure 68, top left). Additionally, we include a trend estimate for the 2048–2057 period where the model output was determined to be reasonable. Interannual variability is greater than the trend or the change in annual irradiance (Figure 68, top left). Results for the mid-future period (Figure 68, top right) show qualitatively similar behavior.

MIROC5 shows minimal trends under both scenarios (Figure 68, middle panels), with similar interannual variability. Similarly, the NCAR RCP4.5 runs show little in the way of decadal trends, with a slight increase during the near-future and mid-future periods (2–4 W/m^2) and little change in interannual variability. For the mid-future period, however, we again emphasize that the trends reflect the 20-year period of record (POR) examined: the historical, near-future, and mid-future. This framing provides better insight into the near-equivalent increase in annual mean irradiance (~22 W/m^2), shown in Table 13 and Figure 67 (bottom panel).

Although trends within the near-future and mid-future periods either remain weak or show a distinct decrease within their respective 20-year PORs, their average annual irradiance values are elevated relative to the historical mean. The trend calculated for the 40-year period (1998–2037) captures the increase in the baseline annual mean irradiance, corresponding to an increase of ~10 W/m^2 per decade, as summarized in Table 13.

Figure 68. Annual mean surface irradiance and decadal trends: Garnet Energy Center (1998–2057)

Annual mean surface irradiance is shown in W/m², with decadal trends in W/m² per decade. Outputs are provided for RCP4.5 (left) and RCP8.5 (right), GFDL (top), MIROC5 (middle), and NCAR (bottom). Trend lines are (as in Figure 39) for the historical period (solid black line, 1998–2017), near-future period (solid red line, 2018–2037), and mid-future period (solid blue line, 2038–2057).

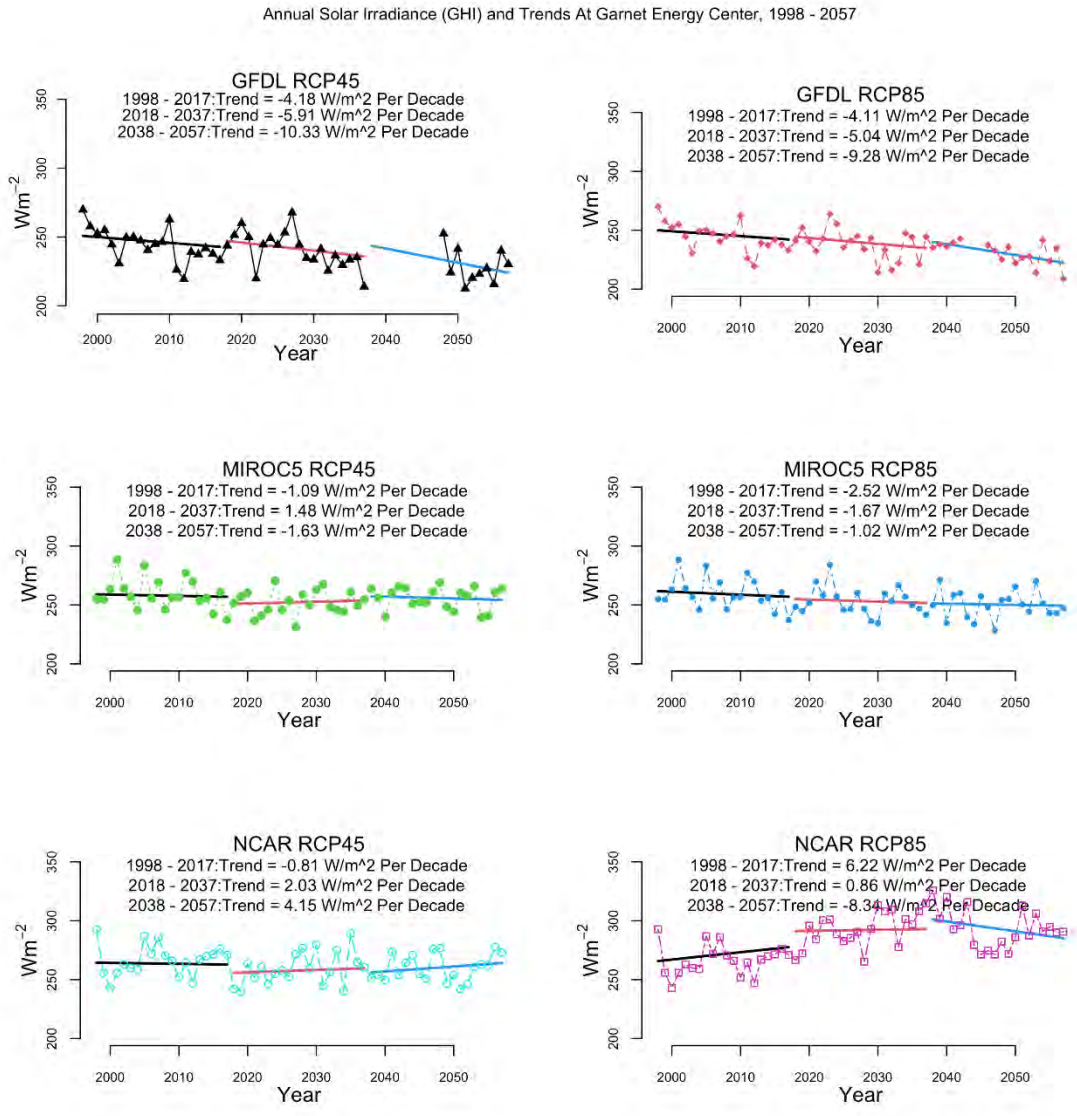

Figure 69. Change in Monthly Irradiance: D03 Grid, RCP4.5, Near-Future Period

Monthly changes in GHI are shown in W/m² for the d03 grid. Outputs are provided for GFDL-CM3 (red bars), MIROC5 (green bars), and NCAR-CCSM4 (blue bars).

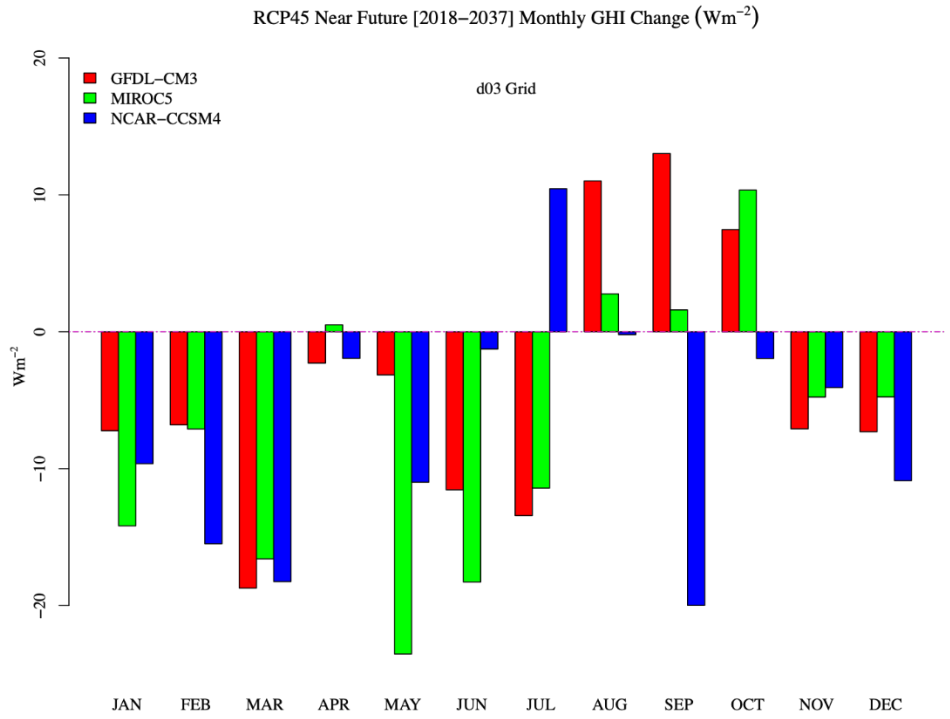

5.5.4 Monthly and Seasonal Changes

A distinct seasonal pattern appears during the near-future period for changes in monthly surface irradiance over the d03 domain for the RCP4.5 scenario (Figure 69). All three models show a decrease in surface irradiance (up to 25 W/m^2 for MIROC5 in May, and 12 W/m^2 in December, or about 7% for both months) from November through June (midfall through early summer), with a predominant increase in solar power availability during the midsummer through early fall (~13 W/m^2 in September, or about a 4% increase). During the mid-future period (Figure 70), the fall-winter season decrease is less distinct (with the caveat that the GFDL output is unavailable), with the NCAR model showing the largest decreases in March (>30 W/m^2, or 10%) and November (~20 W/m^2, or 12%). Again, summer (June through August) shows net increases in available irradiance, ranging up to 12 W/m^2 (around 3%) for the NCAR model.

For the RCP8.5 scenario (Figures 71 and 72), the near-future period shows distinct differences from those highlighted in the RCP4.5 near-future analysis (Figure 69). Only two months (March and October) show agreement among all three models, and the NCAR model forecasts monthly irradiance values above the historical baseline in all but one month. The increase during the warm season (April through September) exceeds 40 W/m^2 in April and August (or about 13% above the historical baseline). This is consistent with the relatively large annual average increase shown in Figure 65. However, the GFDL and MIROC5 models show a more modest decrease in irradiance during most months, with GFDL showing its greatest decrease for March (~30 W/m^2, or around 10%).

Figure 70. Change in Monthly Irradiance: D03 Grid, RCP4.5, Mid-Future Period

Monthly changes in GHI are shown in W/m² for the d03 grid. Outputs are provided for GFDL-CM3 (red bars), MIROC5 (green bars), and NCAR-CCSM4 (blue bars).

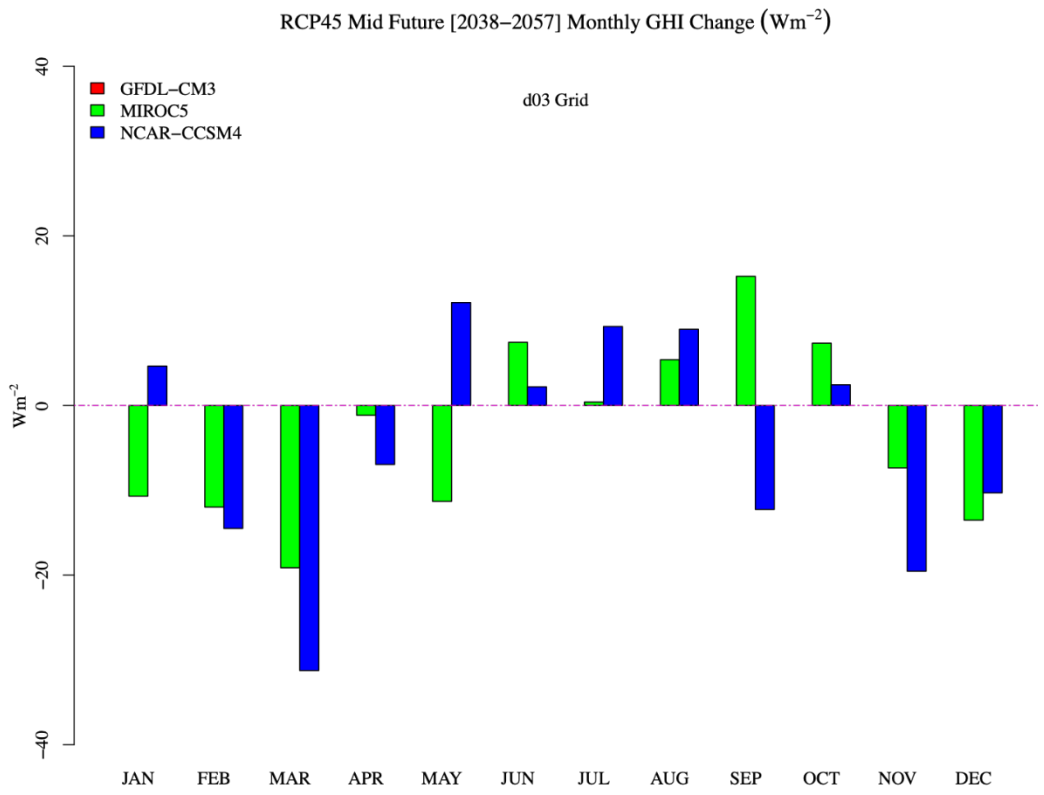

Figure 71. Change in Monthly Irradiance: D03 Grid, RCP8.5, Near-Future Period

Monthly changes in GHI are shown in W/m² for the d03 grid. Outputs are provided for GFDL-CM3 (red bars), MIROC5 (green bars), and NCAR-CCSM4 (blue bars).

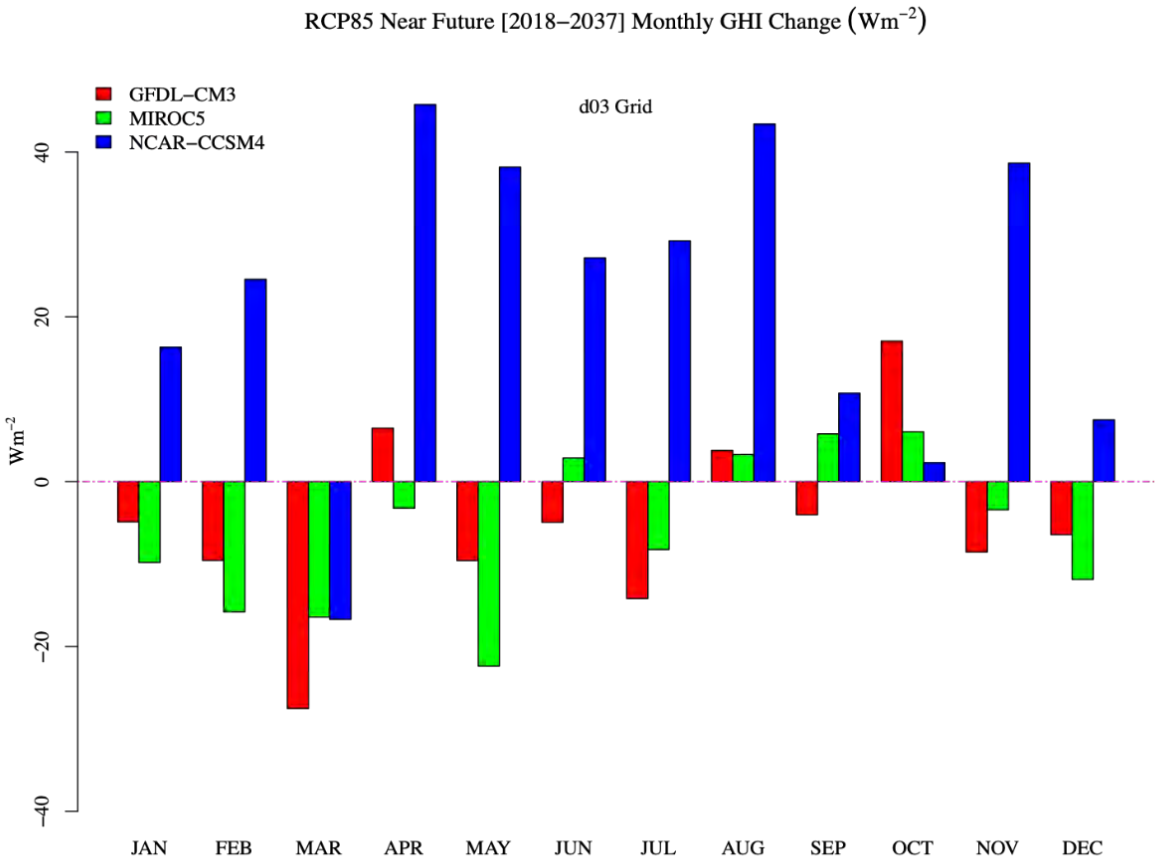

Figure 72. Change in Monthly Irradiance: D03 Grid, RCP8.5, Mid-Future Period

Monthly changes in GHI (W/m²) for the d03 grid. Outputs are shown for GFDL-CM3 (red bars), MIROC5 (green bars), and NCAR-CCSM4 (blue bars).

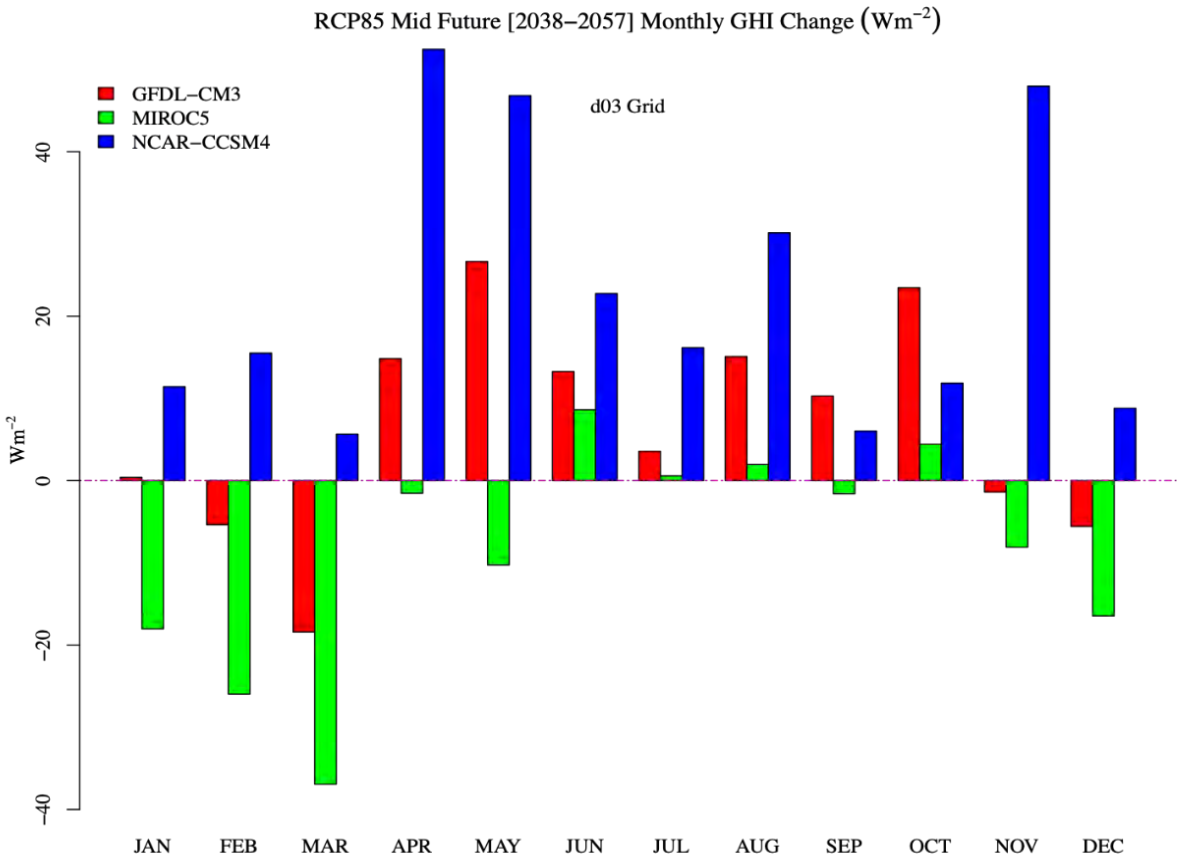

6 Conclusions

We used the WRF model (version 3.9.1) system to dynamically downscale climate projections from three models in the CMIP5 ensemble for two climate change scenarios, RCP4.5 and RCP8.5, for near-future (2018–2037) and mid-future (2038–2057) periods. We compared these future scenarios with historical climate (1998–2017) simulations of the CMIP5 models, all bias-corrected using ERA-I reanalysis. Two inner nests covering the State and adjacent offshore waters were run at 6 km resolution to capture terrain effects and land-lake and land-sea circulations, providing insight into how future climate change may influence New York State's weather regimes, which control the distribution of the renewable energy resources. This report summarizes results from the downscaling efforts, including domain, statewide, and regional quantitative future estimates of changes in the potential temporal and spatial redistribution of wind, solar, and hydropower resources.

6.1 Future Trends in Precipitation

For the near future (2018–2037) RCP4.5 scenario, all three models show a consistent precipitation increase across the d03 grid (13–52 mm/yr, or 0.4–1.9 in/yr) during the near-future period, with an acceleration of the increase during the mid-future period (37–95 mm/yr, 1.2–3.1 in/yr) in annual precipitation over the domain (~5%–10% increase). In contrast, for the near-future RCP8.5 scenario, two of the three models (GFDL and NCAR) show a decrease in precipitation during the near-future period (18 to 67 mm/yr, 0.6 to 2.2 in/yr) in annual precipitation over the domain (~2%–7% decrease). At the same time, the MIROC5 run shows a 57 mm/yr increase in annual precipitation. For the mid-future RCP8.5 scenario, only the NCAR model projects a decrease in annual precipitation (-5.1 mm/yr trend or a decrease of 4.0 inches in annual precipitation); the GFDL and MIROC5 models show positive trends (2.2 and 6.2 mm/yr, respectively). When considering the model ensemble average (both scenarios), regional changes show an overall increase in mean annual precipitation for both periods (15–37 mm/yr), about 2%–5% of the yearly average, or well within the interannual variability of about 175–194 mm/yr (±15% of the annual average).

6.2 Future Trends in Wind

For the d03 domain, a very slight decrease (0 to 0.16 m/s) appears for both scenarios during the near-future and mid-future periods for the GFDL and MIROC5 runs (Table S-2). The same trend appears for the d04 (mostly offshore) domain (+0.01 to -0.21 m/s). The NCAR runs, however, show a more robust increase in wind speeds, 0.46 m/s (near-future) and 0.35 m/s (mid-future) for the d03 domain,

and 0.19–0.20 m/s for the d04 domain for both future periods. As with precipitation, these values are within the historical (and projected future) interannual variability experienced in the region (0.20–0.40 m/s offshore and onshore). We note, however, that the NCAR d03 near-future increase could result in a 10% increase in capacity factor (depending on the turbine and the mean local wind speed, given the 100-m annual mean wind speed of 7.8–8.8 m/s in the d03, d04, and d04 offshore regions); the largest decrease indicated by an individual model (the GFDL-CM3: 0.21 m/s for d04, mid-future period), could result in approximately a 5% decrease in the regional capacity factor. When considering the model ensemble average (both scenarios), regional changes in wind speed are quite small (<0.05 m/s), or less than 1% of the domain-averaged 100-m wind speeds, and well within the mean interannual variability of up to 0.34 m/s (±4%) for the d03 domain and 0.4 m/s (±5%) for the offshore region of the d04 domain.

6.3 Future Trends in Surface Irradiance

For the near-future period, the GFDL and MIROC5 models generally show a slight decrease in surface irradiance for both scenarios, both periods, and both domains (the exception being the GFDL RCP8.5 mid-future period, which predicts a slight increase of about 7 W/m^2). However, the NCAR-CCSM4 RCP8.5 model runs indicate an increase (~22 W/m^2) in GHI for both periods, roughly 10% of available solar energy. However, the ensemble average of all models for both scenarios shows little change in the near-future period, with slight or modest increases for the mid-future period (+5.48 W/m^2 for the d04 domain, or <2%, and +14.69 W/m^2 for the d03 domain, or about 5% of the available resource, and within the interannual variability of ±10–15 W/m^2).

7 References

Baker, N.C., and H.-P. Huang. 2014. “A Comparative Study of Precipitation and Evaporation Between CMIP3 and CMIP5 Climate Model Ensembles in Semiarid Regions.” *Journal of Climate* 27: 3731–49.

Brower, M. 2012. “The Climate Adjustment Process.” In *Wind Resource Assessment: A Practical Guide to Developing a Wind Project*, 155–77. Wiley.

Bruyère, C.L., J.M. Done, G.J. Holland, and S. Fredrick. 2014. “Bias Corrections of Global Models for Regional Climate Simulations of High Impact Weather.” *Climate Dynamics* 43: 1847–56.

Chen, L. 2020. “Impacts of Climate Change on Wind Resources Over North America Based on NA-CORDEX.” *Renewable Energy* 135: 1428–38.

Clean Power Research. 2013. SolarAnywhere data. https://www.solaranywhere.com/

Dai, A. et al. 2017. “A new approach to construct representative future forcing data for dynamic downscaling.” Published online 2017. *Climate Dynamics* 55: 315–323 (2020).

Daly, C., R.P. Neilson, and D.L. Phillips. 1994. “A Statistical-Topographic Model for Mapping Climatological Precipitation Over Mountainous Terrain.” *Journal of Applied Meteorology* 33: 140–58.

Decker, M., M.A. Brunke, Z. Wang, K. Sakaguchi, X. Zeng, and M.G. Bosilovich. 2012. “Evaluation of the Reanalysis Products from GSFC, NCEP, and ECMWF Using Flux Tower Observations.” *Journal of Climate* 25: 1916-44.

EIA (U.S. Energy Information Administration). 2021. *State Electricity Profiles*. Washington, DC: EIA. https://www.eia.gov/electricity/state/unitedstates/index.php

Fréchet, M. 1927. “Sur la loi de probabilité de l'écart maximum.” *Annales de la Société Polonaise de Mathématique*, Cracovie 6: 93–116.

Hayhoe, K., et al. 2006. “Past and Future Changes in Climate and Hydrological Indicators in the U.S. Northeast.” *Climate* Dynamics 28: 381–407.

Hong, S-Y., and J-O.J. Lim. 2006. “The WRF Single-Moment 6-Class Microphysics Scheme (WSM6).” *Journal of the Korean Meteorological Society* 42: 129–51.

Kulkarni, S., and H.-P. Huang. 2014. “Changes in Surface Wind Speed Over North America From CMIP5 Model Projections and Implications for Wind Energy.” *Advances in Meteorology* 2014, Article ID 292768. doi:10.1155/2014/292768

Lileo, S., and O. Petrik. 2011. “Investigation on the Use of NCEP/NCAR, MERRA and NCEP/CFSR Reanalysis Data in Wind Resource Analysis.” Presentation at the EWEA Conference, Brussels, Belgium.

Lin, J.L., and T.T. Qian. 2014. “Solar Energy and Global Climate Change.” *Advanced Materials Research* 875–77, 1767–70. https://doi.org/10.4028/www.scientific.net/amr.875-877.1767

Mearns, L.O., R. Arritt, S. Biner, M. Bukovsky, S. Stain, D. Caya, J. Correia Jr., D. Flory, W. Gutowski, E.S. Takle, R. Jones, R. Leung, W. Moufouma-Okia, L. McDaniel, A.M.B. Nunes, Y. Qian, J. Roads, L. Sloan, and M. Snyder. 2012. “The North American Regional Climate Change Assessment Program: Overview of Phase I Results.” *Bulletin of the American Meteorological Society* 93: 1337–62. doi:10.1175/BAMS-D-11-00223.1

Meehl, G., C. Covey, T. Delworth, M. Latif, B. McAvaney, J. Mitchell, R. Stouffer, and K. Taylor. 2007. “The WCRP CMIP3 Multimodel Dataset: A New Era in Climate Change Research.” *Bulletin of the American Meteorological Society* 88: 1383–94.

Northeast Regional Climate Center. 2021. “Monthly State-wide Precipitation Maps.” Available at http://www.nrcc.cornell.edu/regional/climatenorms/climatenorms.html

NYISO (New York Independent System Operator). 2021. *The New York ISO Annual Grid & Markets Report, The Vision for a Greener Future. Power Trends 2020*. https://www.nyiso.com/power-trends

NYSERDA (New York State Energy Research and Development Authority). 2021. “Toward a Clean Energy Future: A Strategic Outlook 2021–2024.” Albany, NY: NYSERDA. Available at https://www.nyserda.ny.gov/About/Publications/Program-Planning-Status-and-Evaluation-Reports/Strategic-Outlook

NYSDEC (New York State Department of Environmental Conservation). https://dec.ny.gov/nature/waterbodies/watersheds

PRISM Climate Group. NYS Mean Annual Precipitation 1981–2010, created 2014. Oregon State University. https://prism.oregonstate.edu/

Pryor, S. C., R.J. Barthelmie, and J.T. Schoof. 2012. “Past and Future Wind Climates Over the Contiguous USA Based on the NARCCAP Model Suite.” *Journal of Geophysical Research* 117: D24102.

R Core Team. 2018. *R: A Language and Environment for Statistical Computing.* Vienna, Austria: R Foundation for Statistical Computing. http://www.R-project.org/

Rosenzweig, C., W. Solecki, A. DeGaetano, M. O'Grady, S. Hassol, P. Grabhorn (Eds.). 2011. *Responding to Climate Change in New York State: The ClimAID Integrated Assessment for Effective Climate Change Adaptation*. Technical Report. New York State Energy Research and Development Authority (NYSERDA), Albany, New York. www.nyserda.ny.gov

Solecki, W. and Rosenzweig, C. 2019. “New York City Panel on Climate Change 2019 Report Chapter 9: Perspectives on a City in a Changing Climate 2008–2018.” *Annals of the New York Academy of Sciences*, 1439: 280-305. https://doi.org/10.1111/nyas.14017

Taylor, K.E, R.J. Stouffer, and Gerald A. Meehl. 2012. “An Overview of CMIP5 and the Experiment Design.” *Bulletin of the American Meteorological Society* 93: 485–98.

Thompson, G., and T.A. Eidhammer. 2014. “Study of Aerosol Impacts on Clouds and Precipitation Development in a Large Winter Cyclone.” *Journal of the Atmospheric Sciences* 71: 3636–58.

Torralba, V., F.J. Doblas-Reyes, and N. Gonzalez-Reviriego. 2017. “Uncertainty in Recent Near-Surface Wind Speed Trends: A Global Reanalysis Intercomparison. *Environmental Research Letters* 12: 114019.

Van Rossum, G., and F.L. Drake. 2009. “The Python Language Reference Manual.” Network Theory Ltd.

Appendix A. Model monthly changes in wind speed: d03 domain

Figure A-1. Domain d03 monthly changes in 100 m wind speed (ms^{-1}) under RCP4.5 scenario for near-future period

Upper left: January; upper right: February; middle left: March; middle right: April; lower left: May; lower right: June.

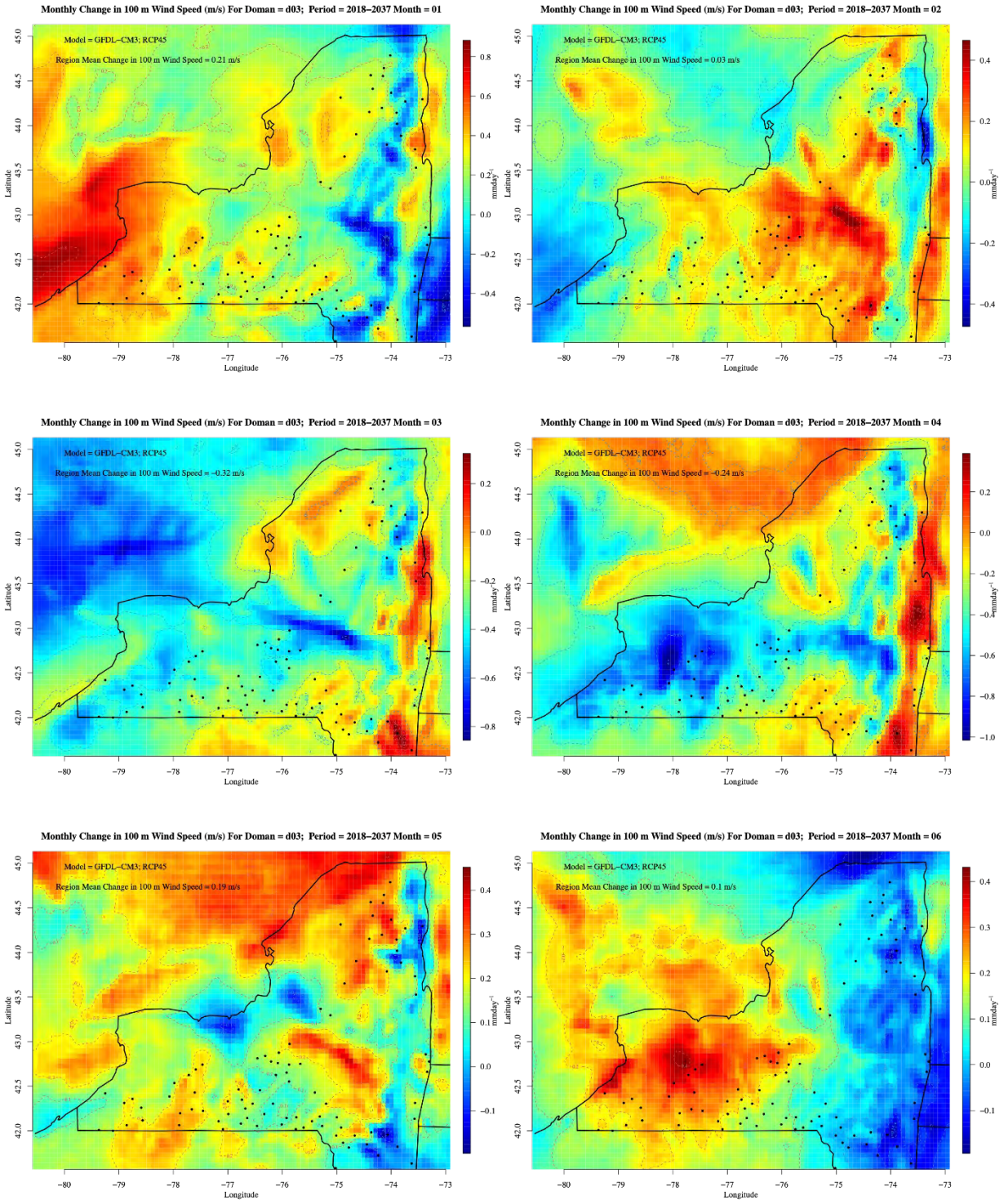

Figure A-2. Same as Figure A-1 except Upper left: July; upper right: August; middle left: September; middle right: October; lower left: November; lower right: December

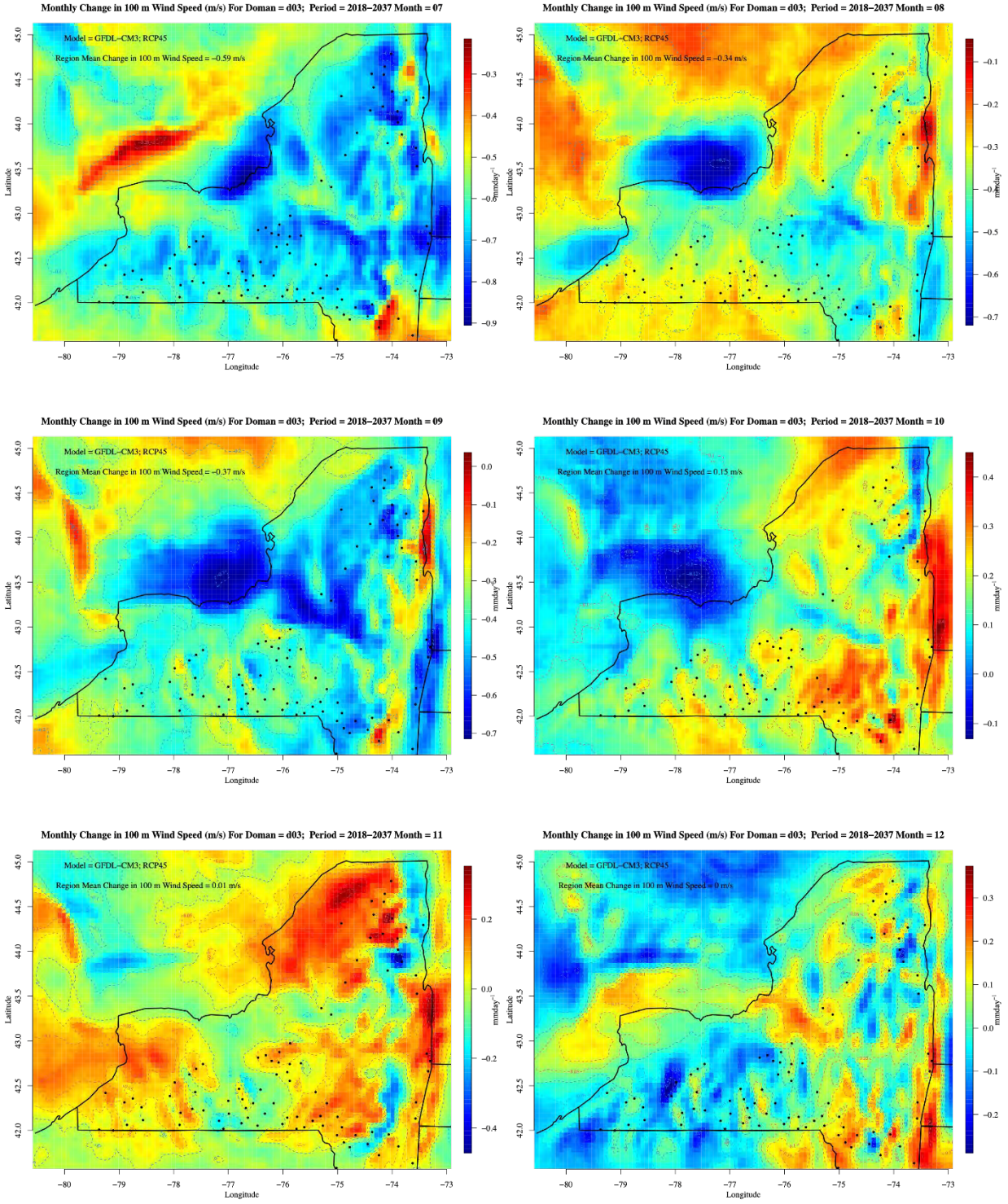

Figure A-3. Same as Figure A-1 except for mid-future period

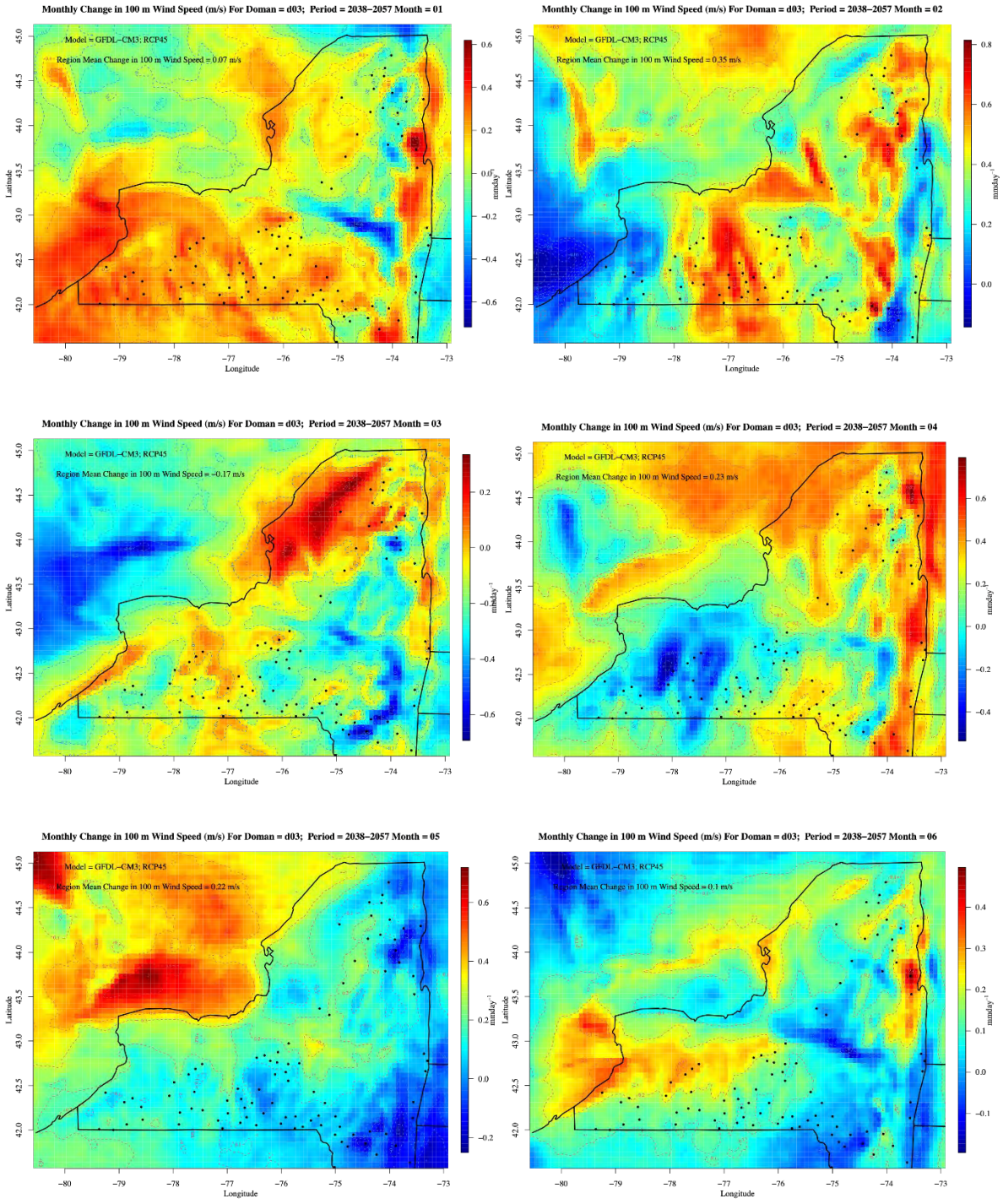

Figure A-4. Same as Figure A-2 except for mid-future period

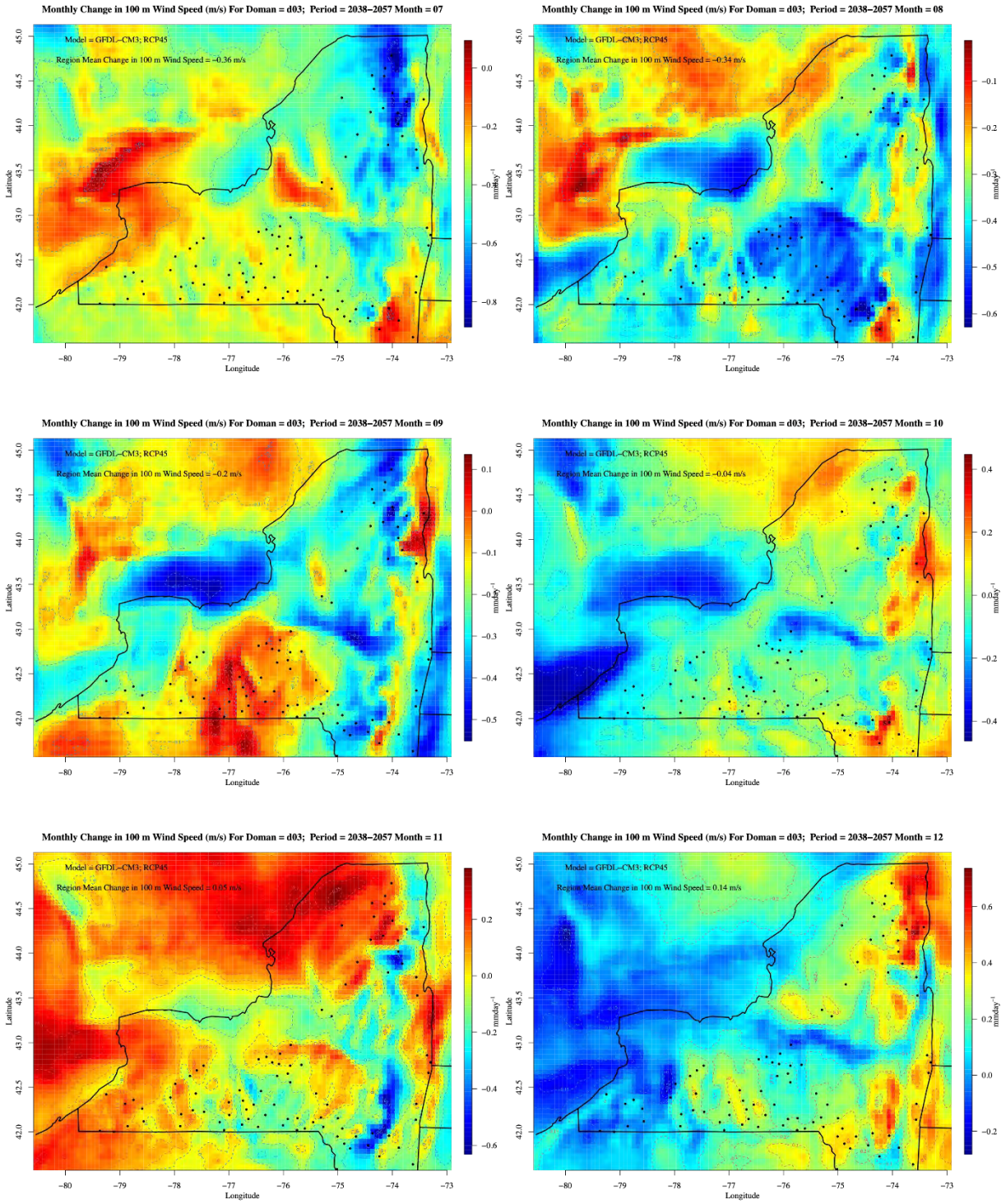

Figure A-5. Same as Figure A-1 except for RCP8.5

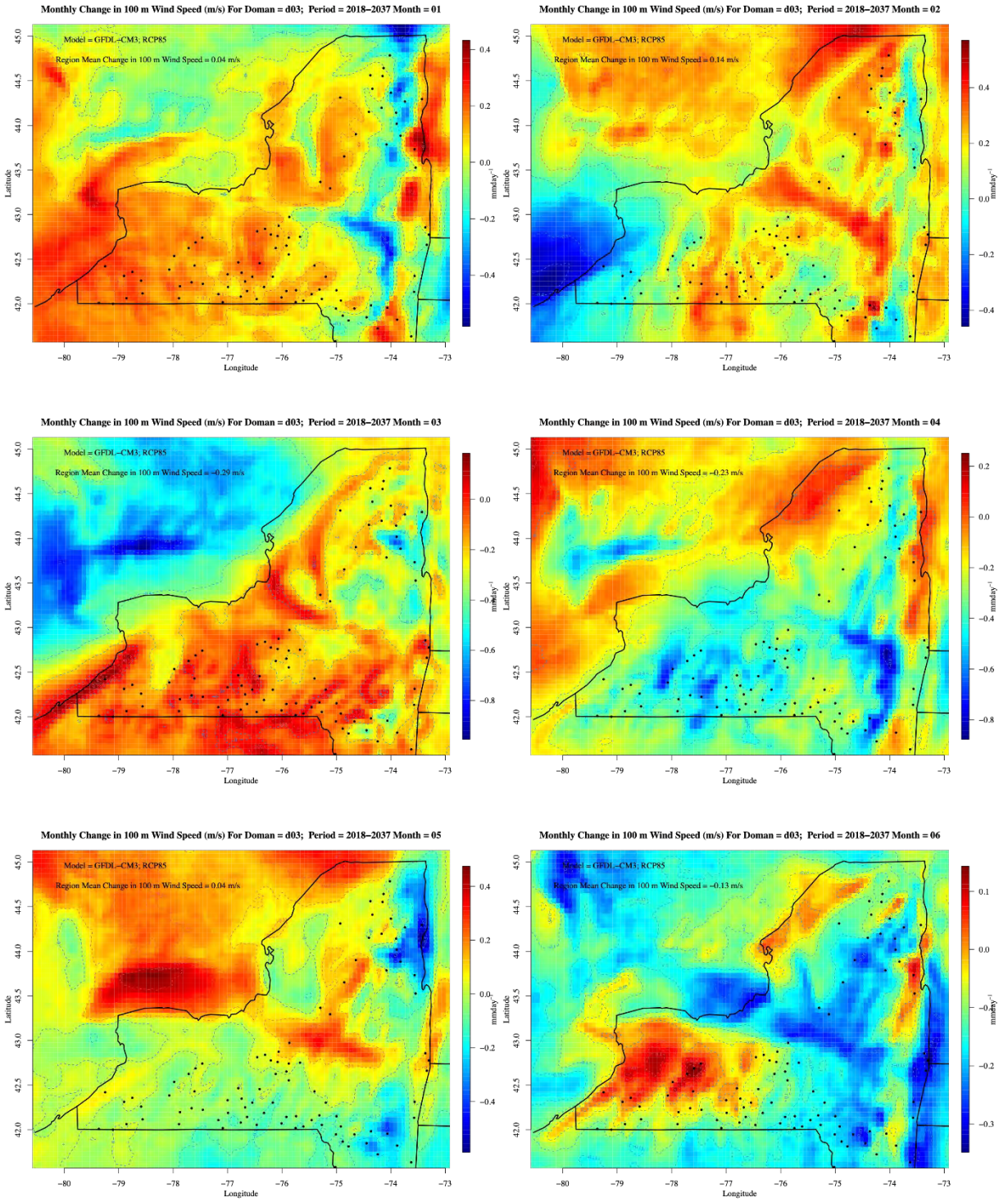

Figure A-6. Same as Figure A-2 except for RCP8.5

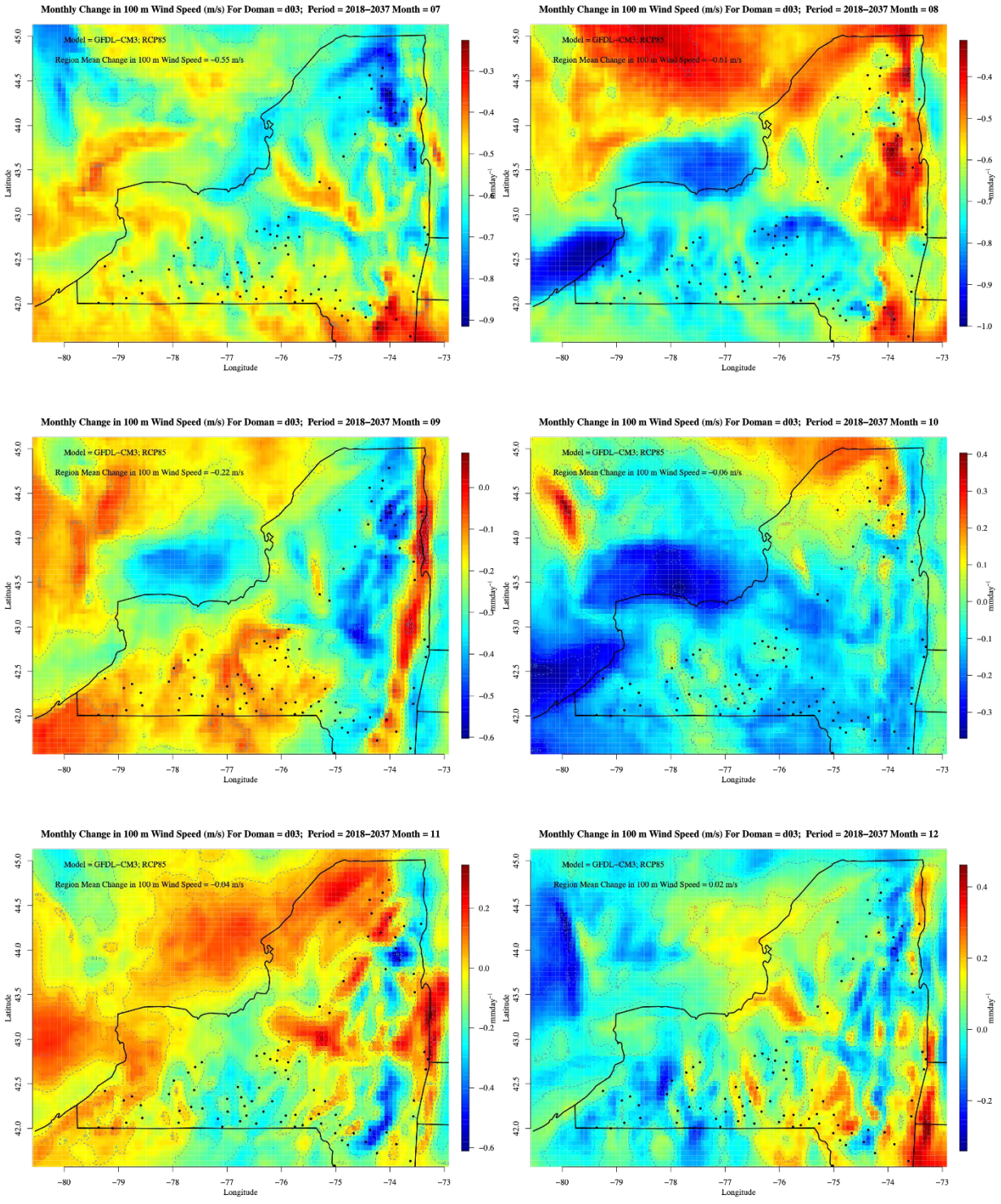

Figure A-7. Same as Figure A-5 except for the mid-future period

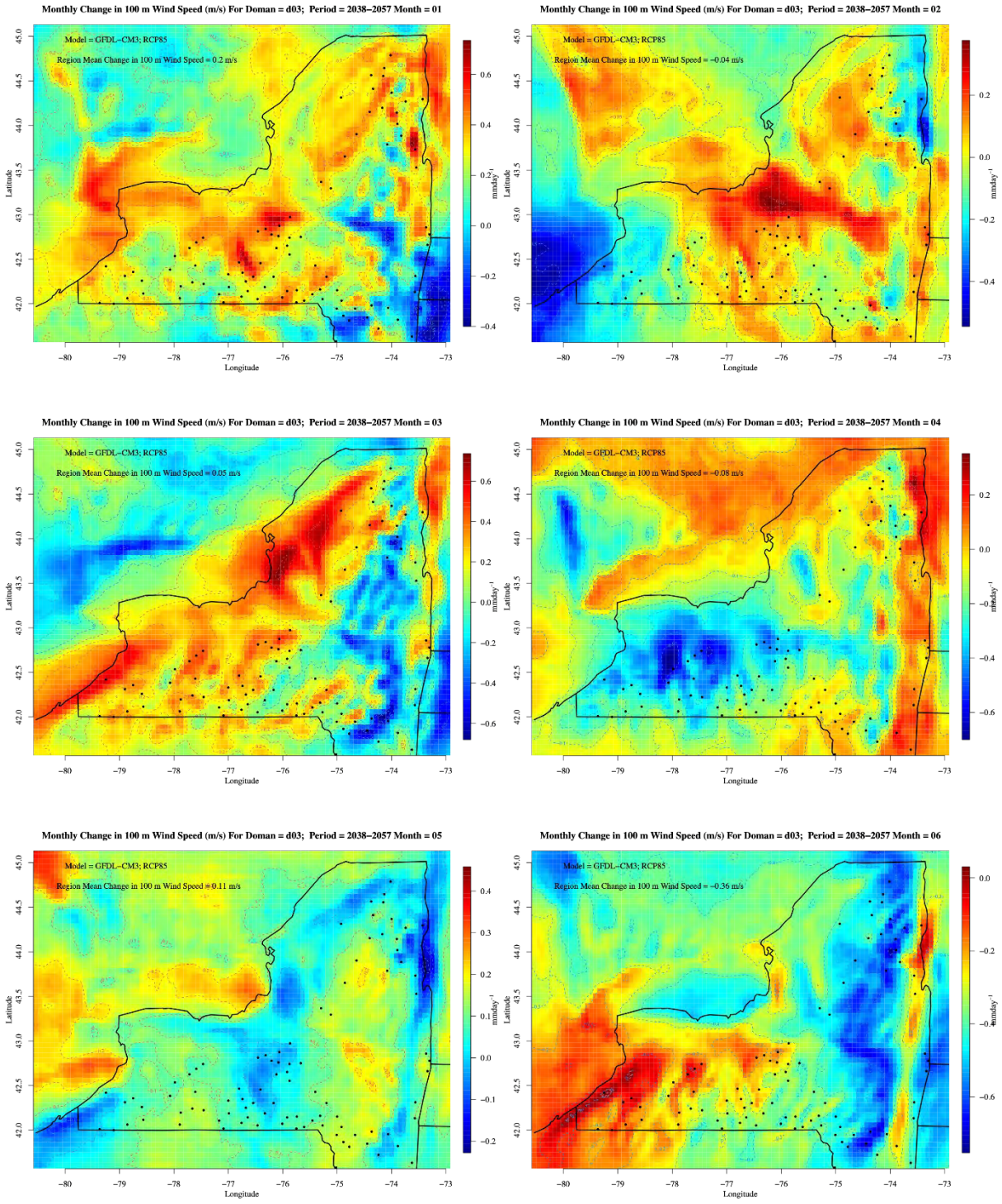

Figure A-8. Same as Figure A-6 except for the mid-future period

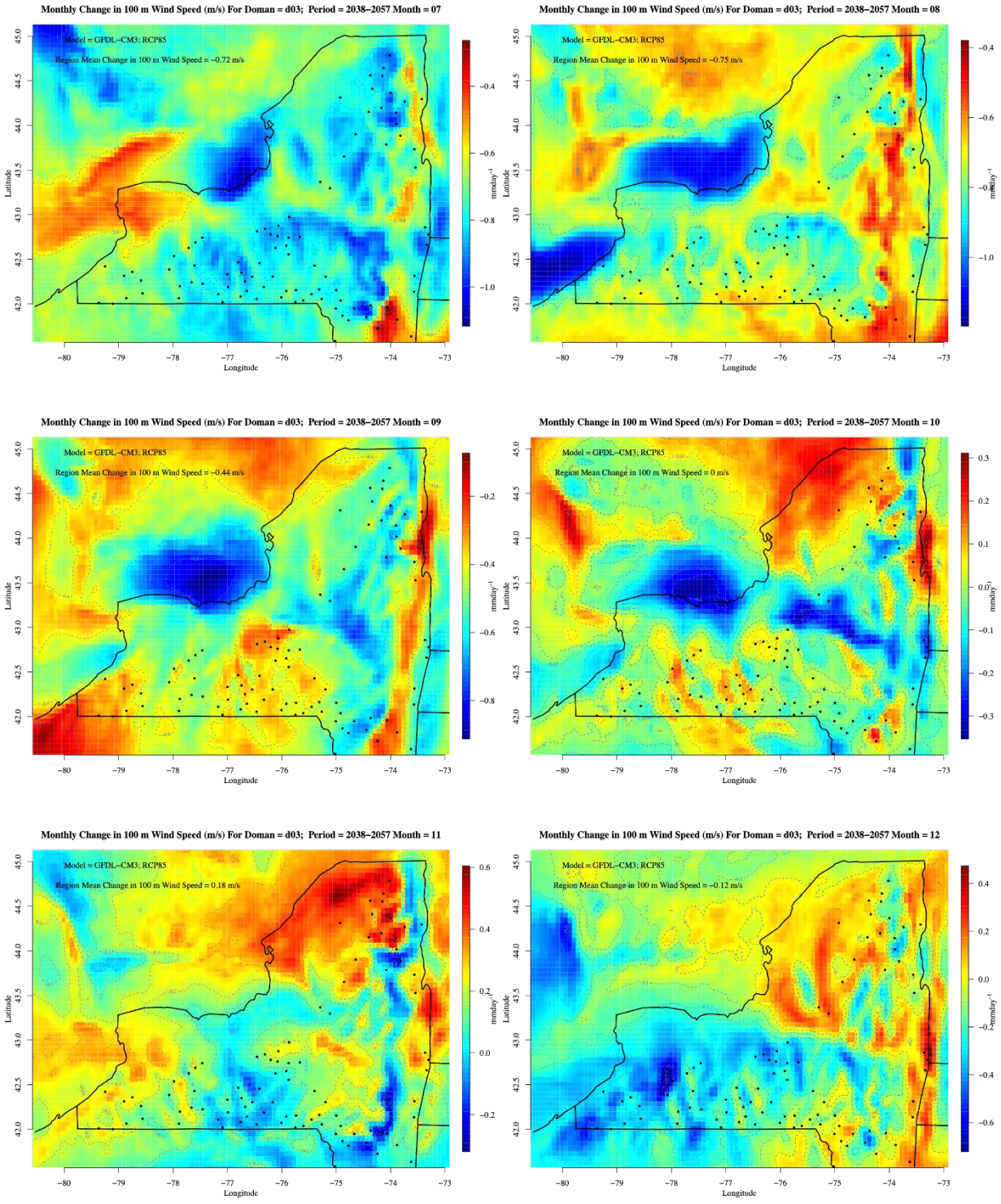

Figure A-9. Same as Figure A-1 except for MIROC5

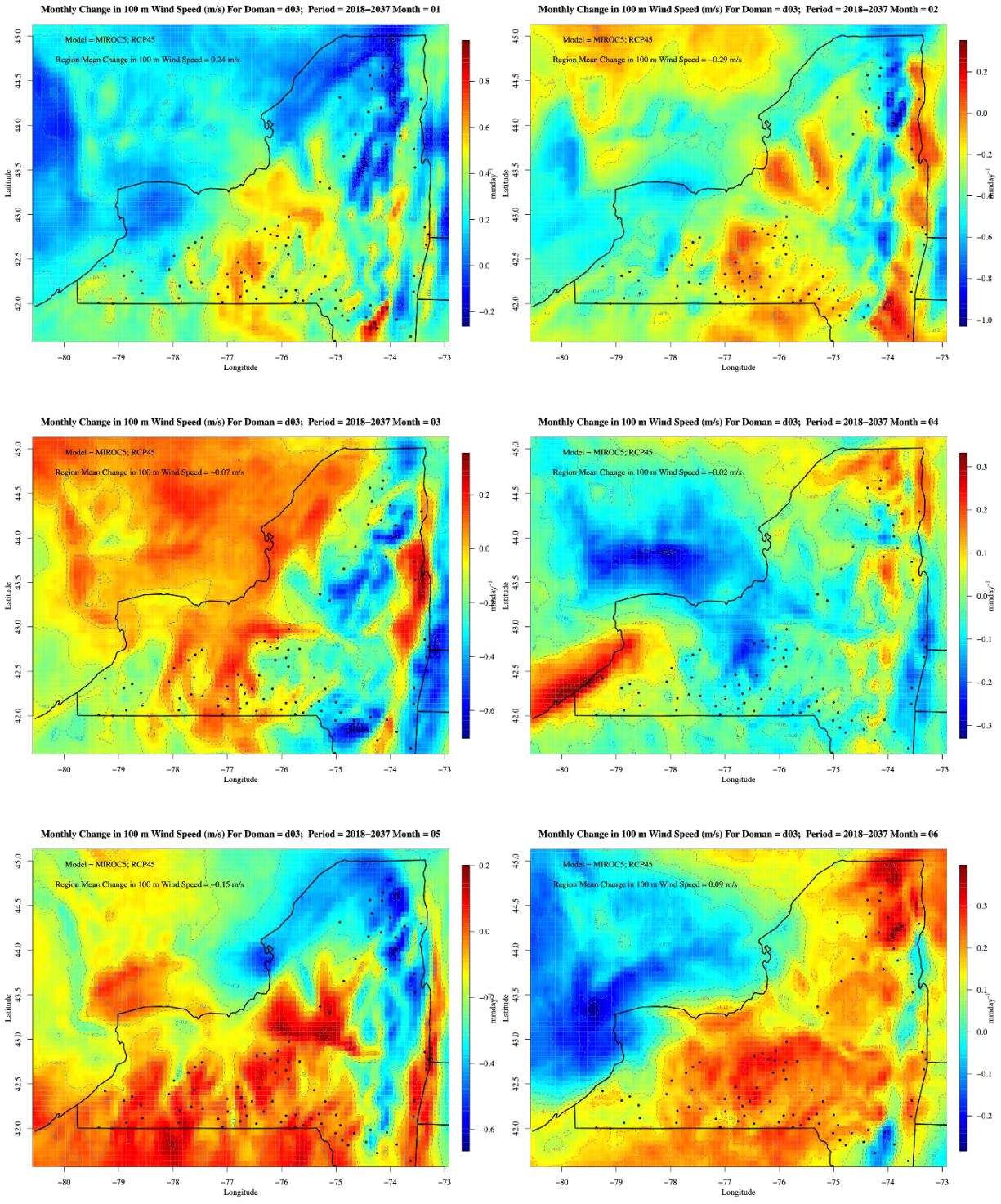

Figure A-10. Same as Figure A-2 except for MIROC5

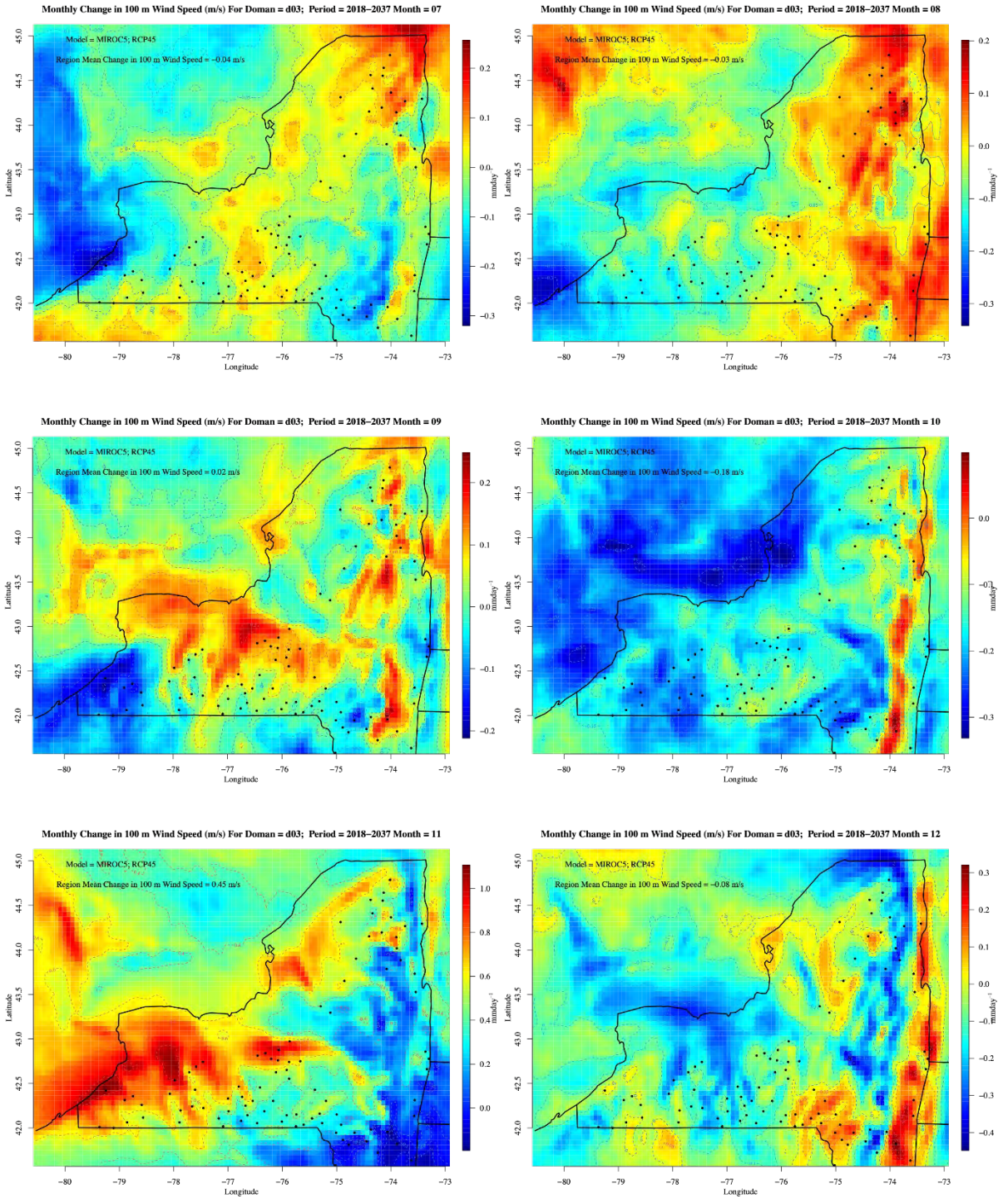

Figure A-11. Same as Figure A-3 except for MIROC5

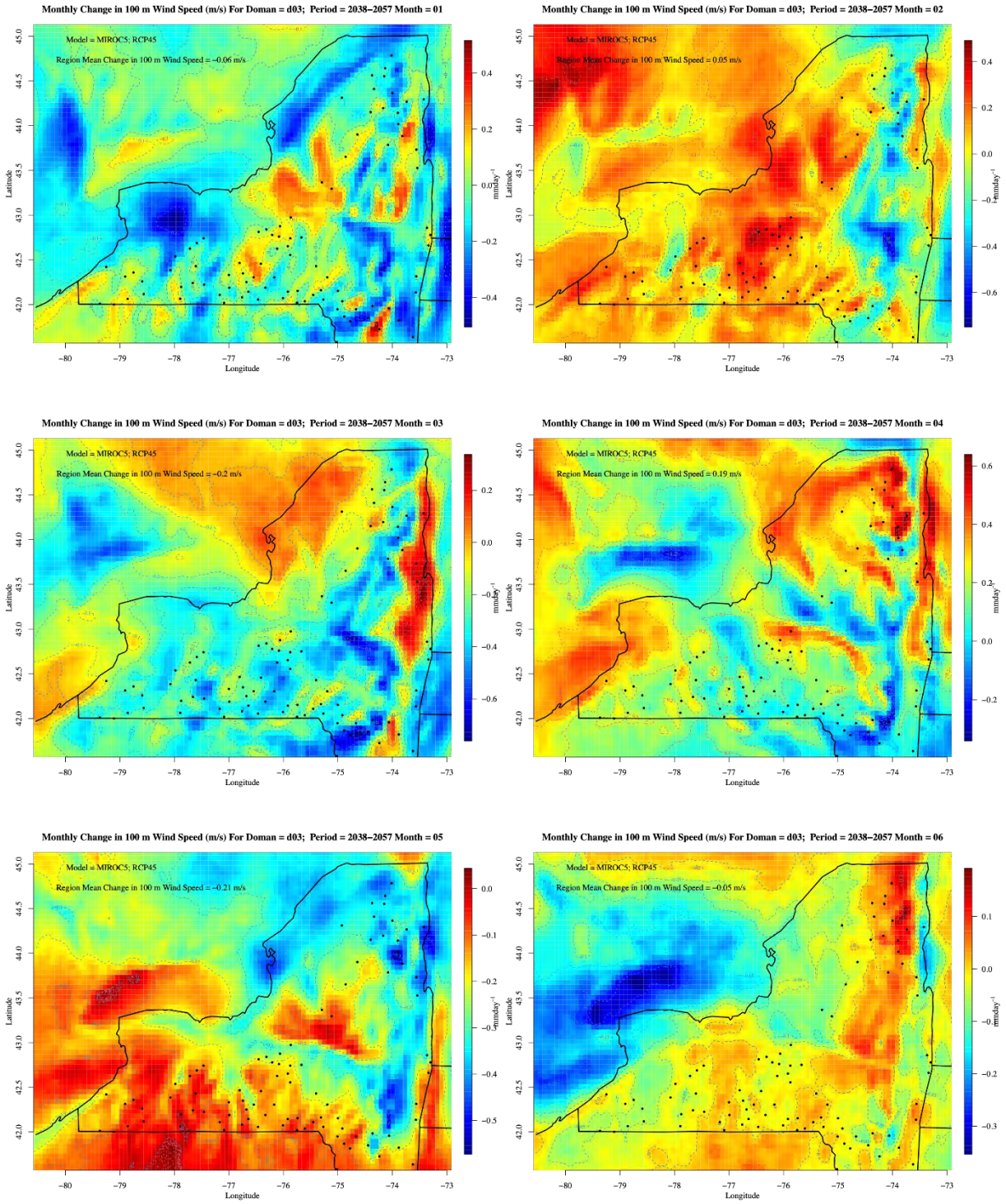

Figure A-12. Same as Figure A-4 except for MIROC5

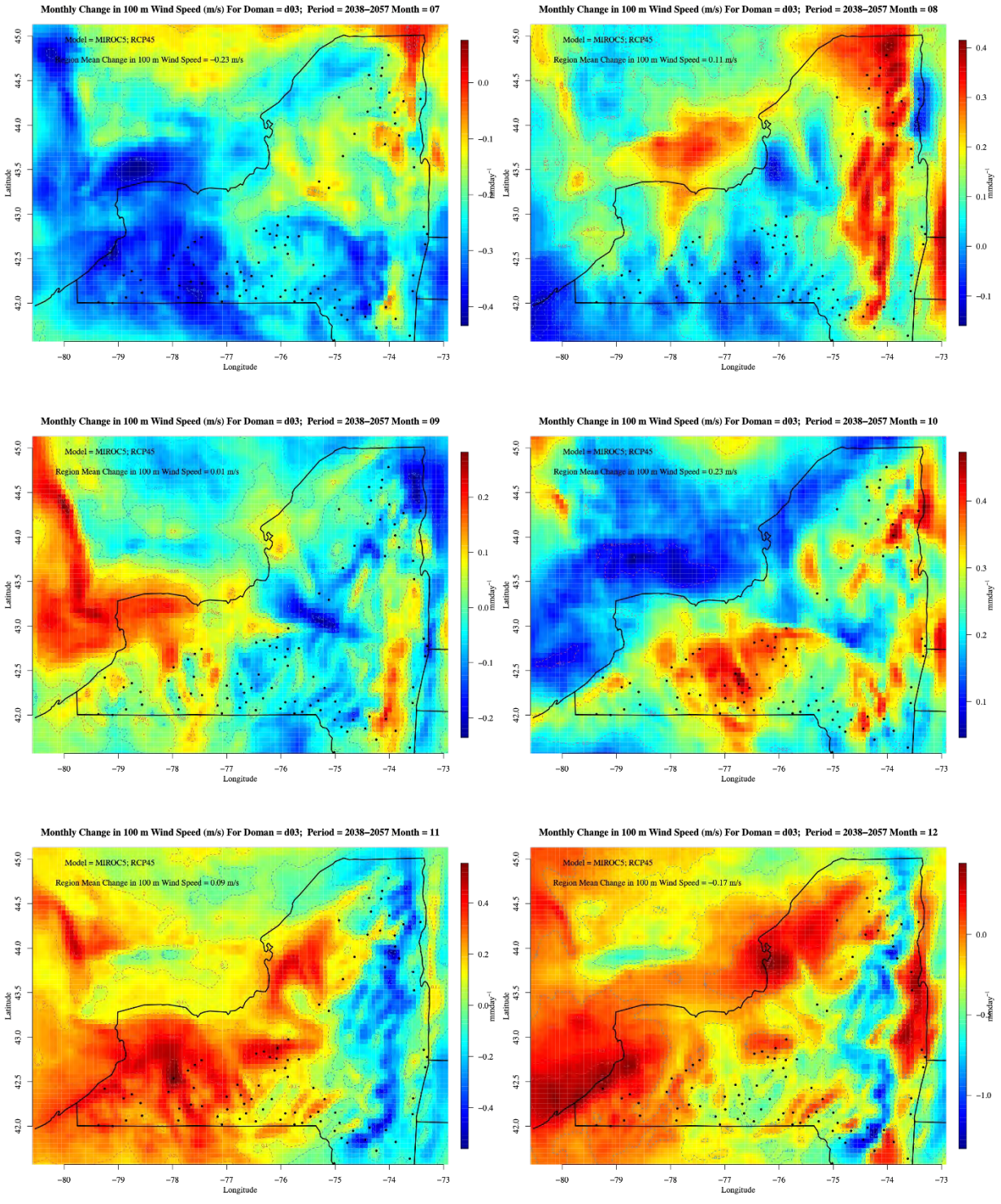

Figure A-13. Same as Figure A-5 except for MIROC5

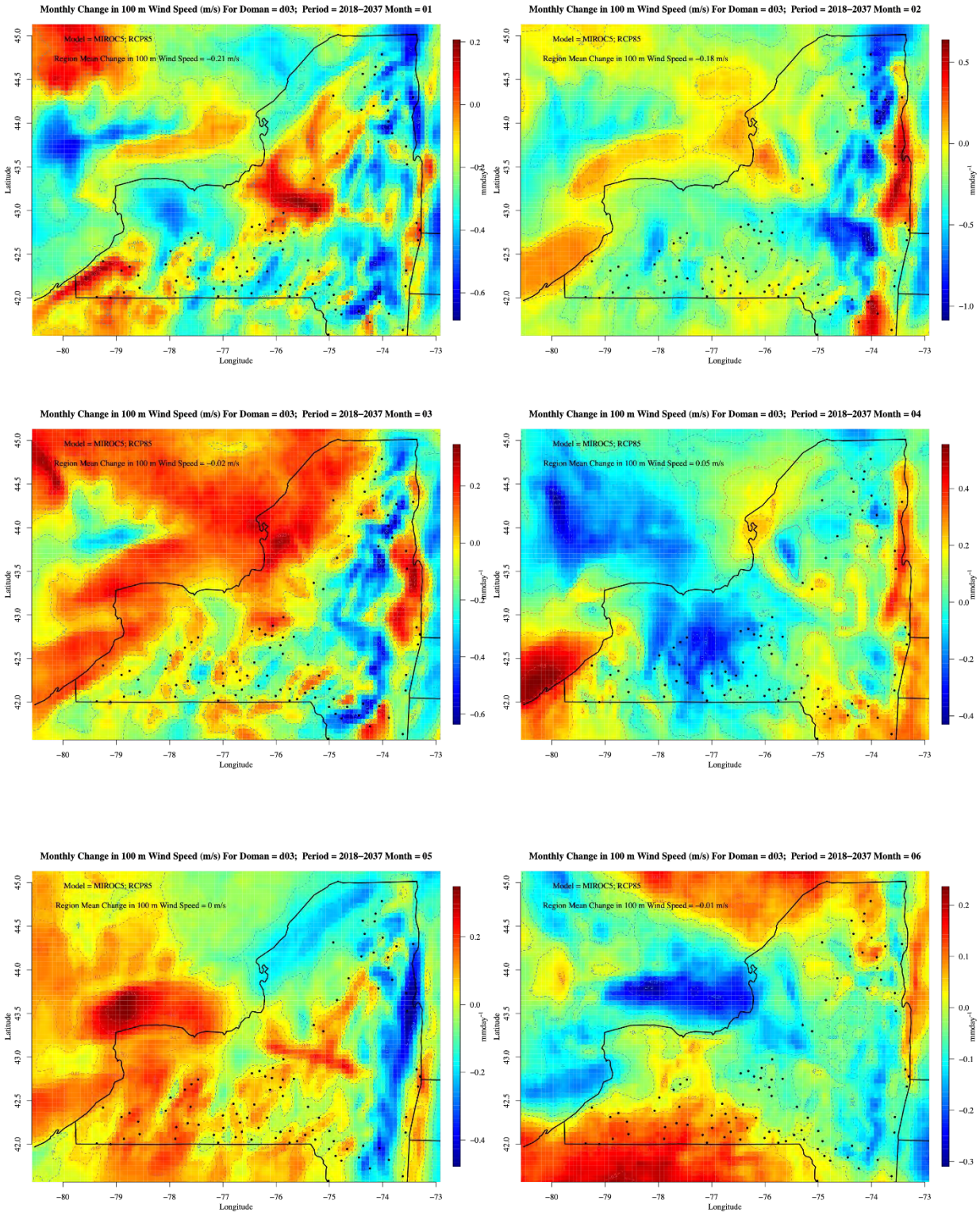

Figure A-14. Same as Figure A-6 except for MIROC5

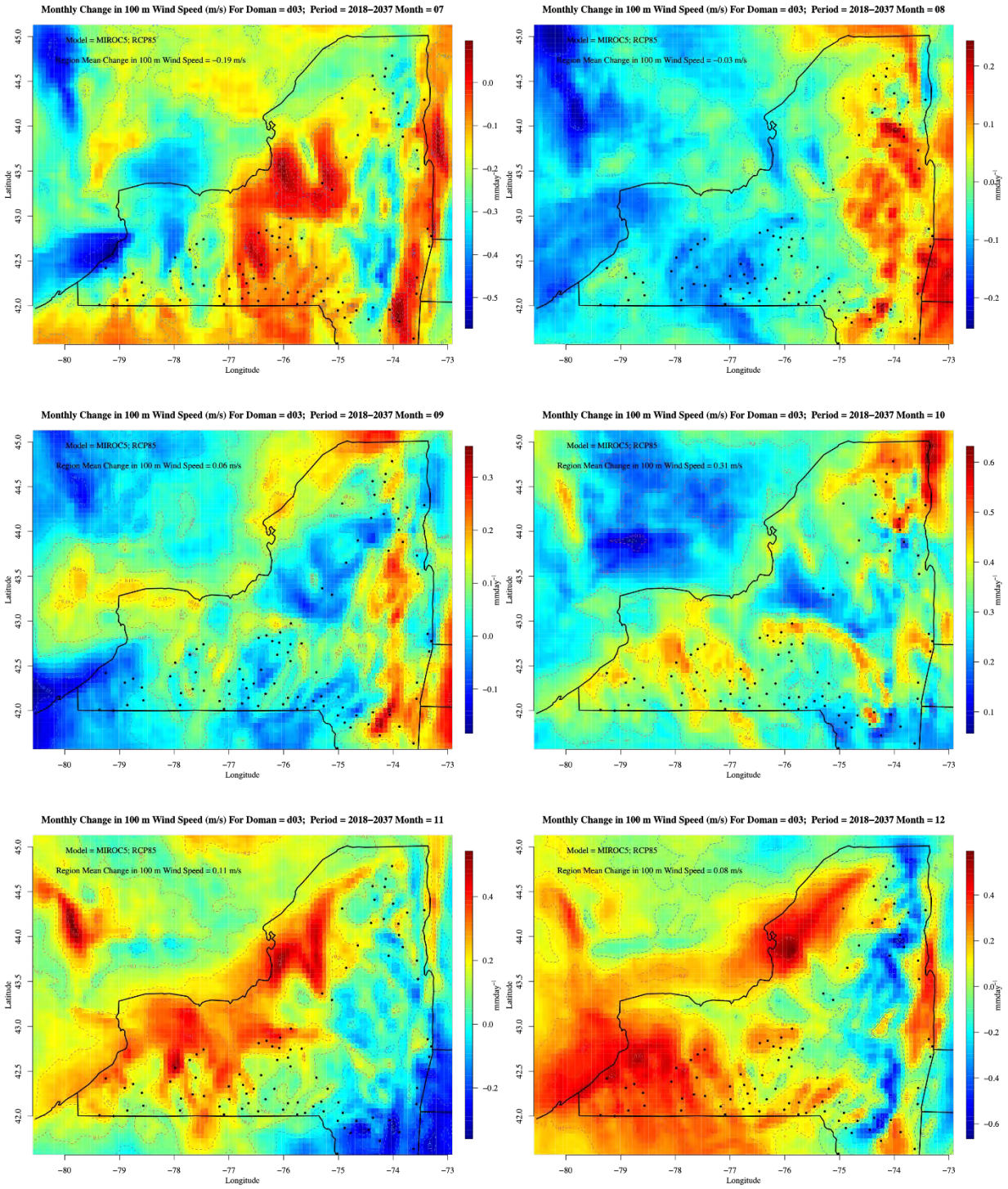

Figure A-15. Same as Figure A-7 except for MIROC5

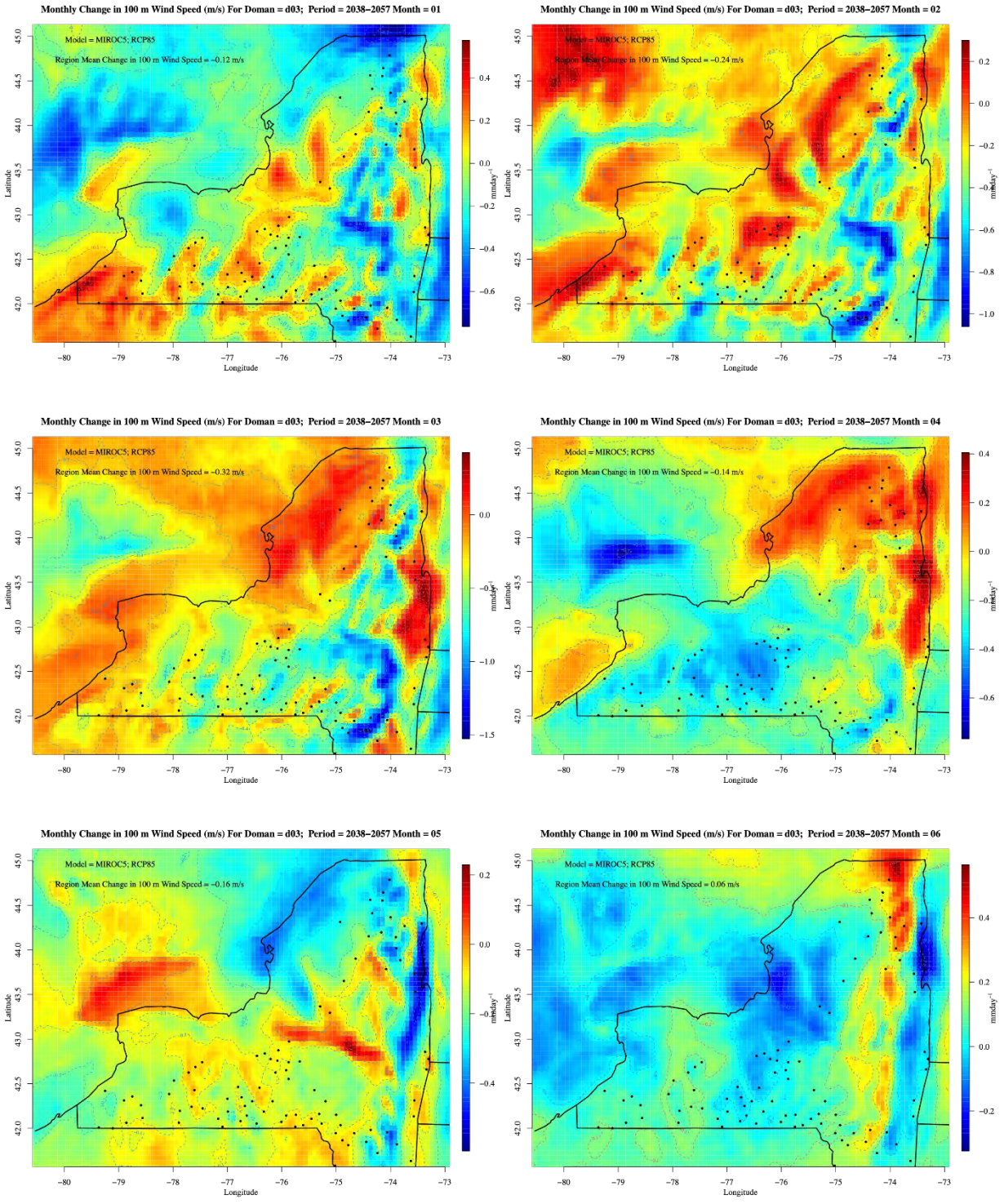

Figure A-16. Same as Figure A-8 except for MIROC5

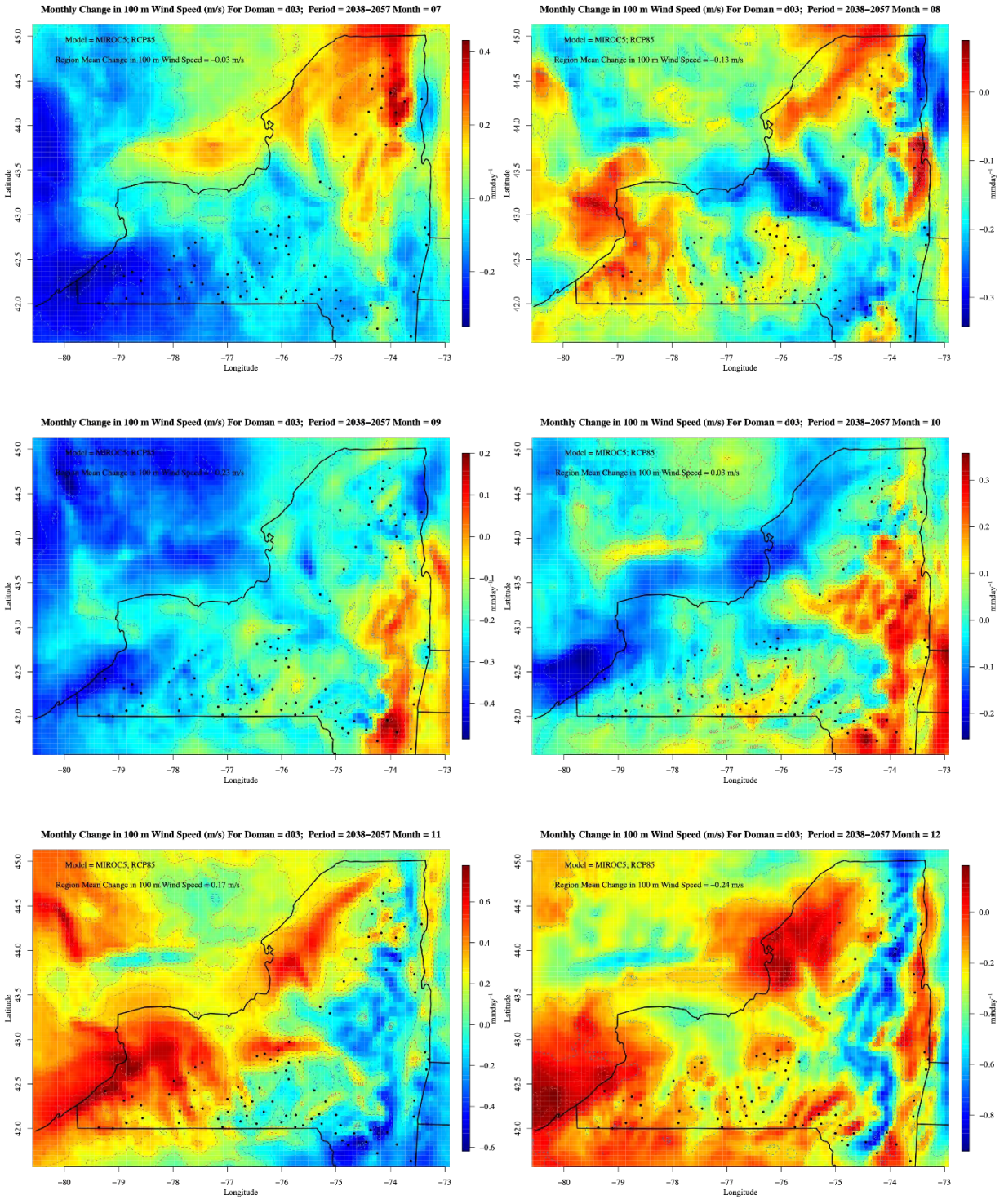

Figure A-17. Same as Figure A-1 except for NCAR-CCSM4

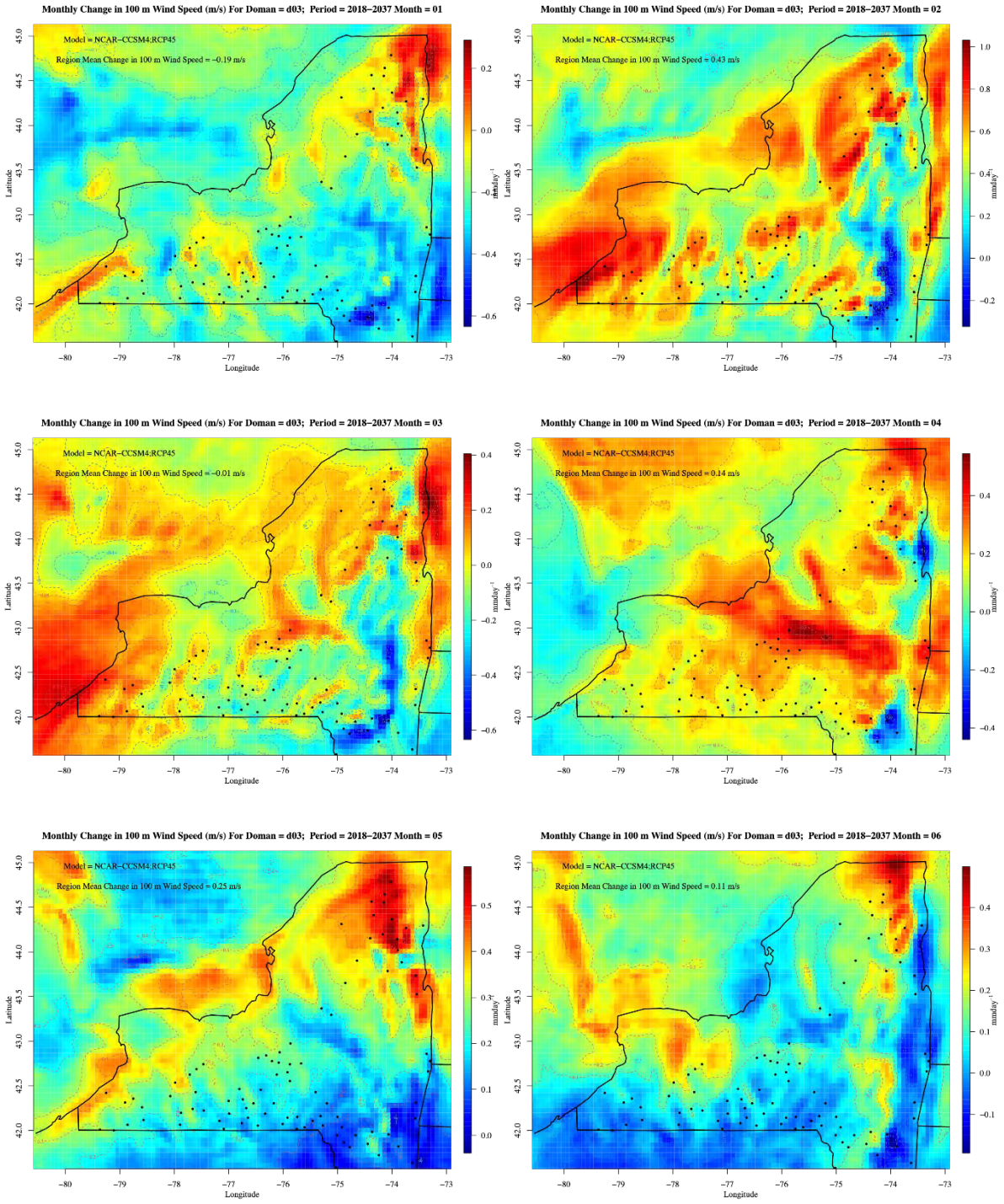

Figure A-18. Same as Figure A-2 except for NCAR-CCSM4

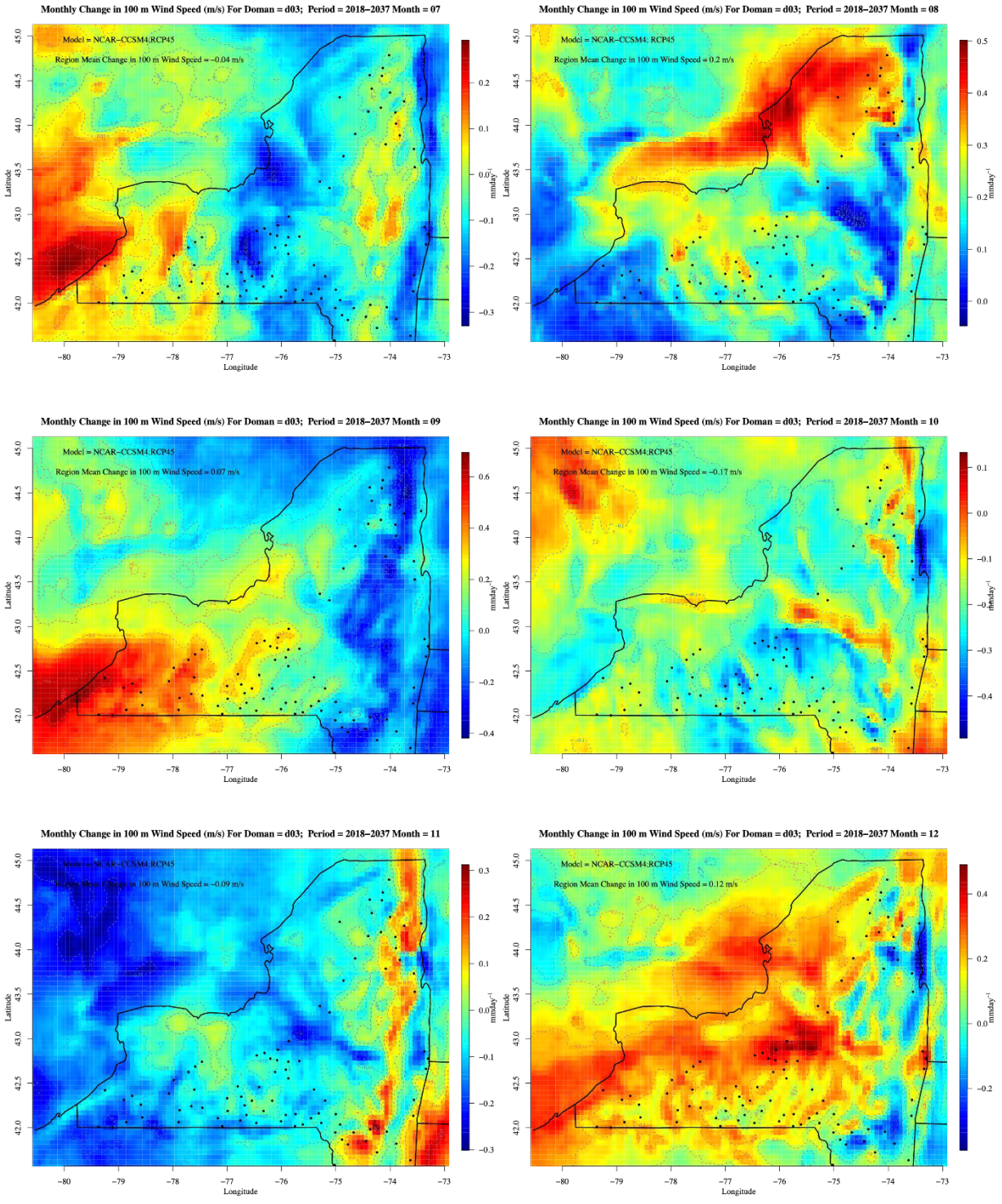

Figure A-19. Same as Figure A-3 except for NCAR-CCSM4

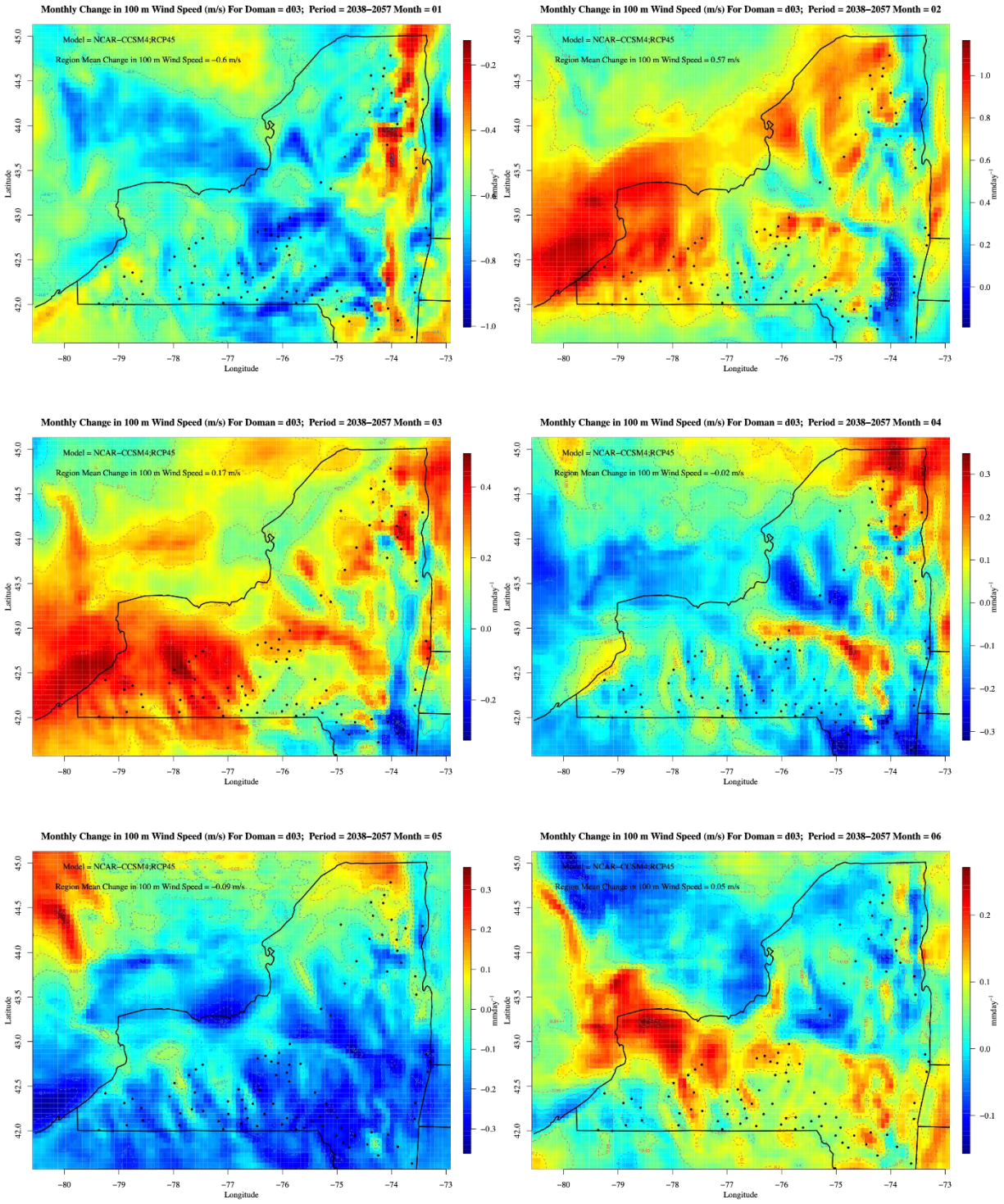

Figure A-20. Same as Figure A-4 except for NCAR-CCSM4

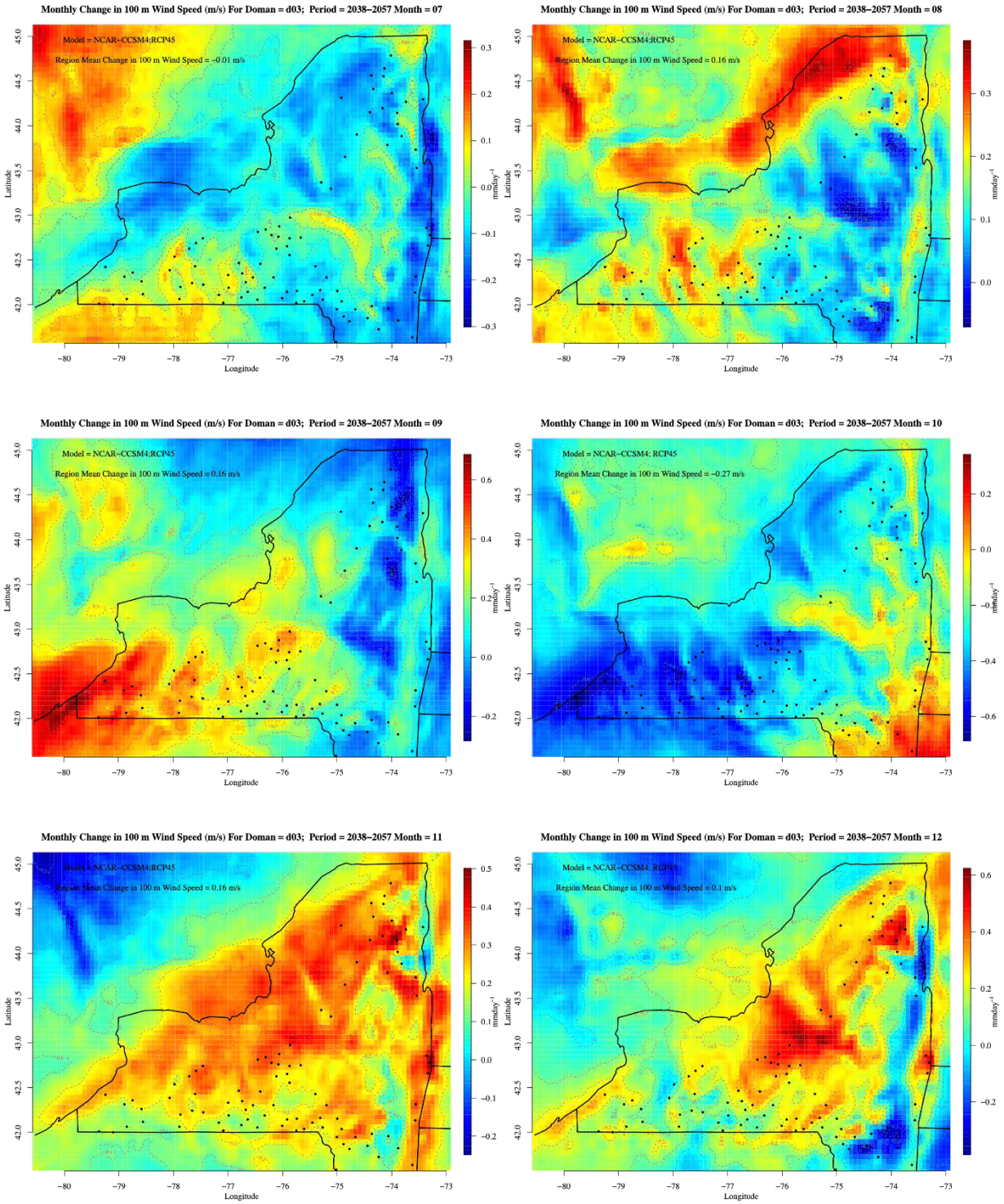

Figure A-21. Same as Figure A-5 except for NCAR-CCSM4

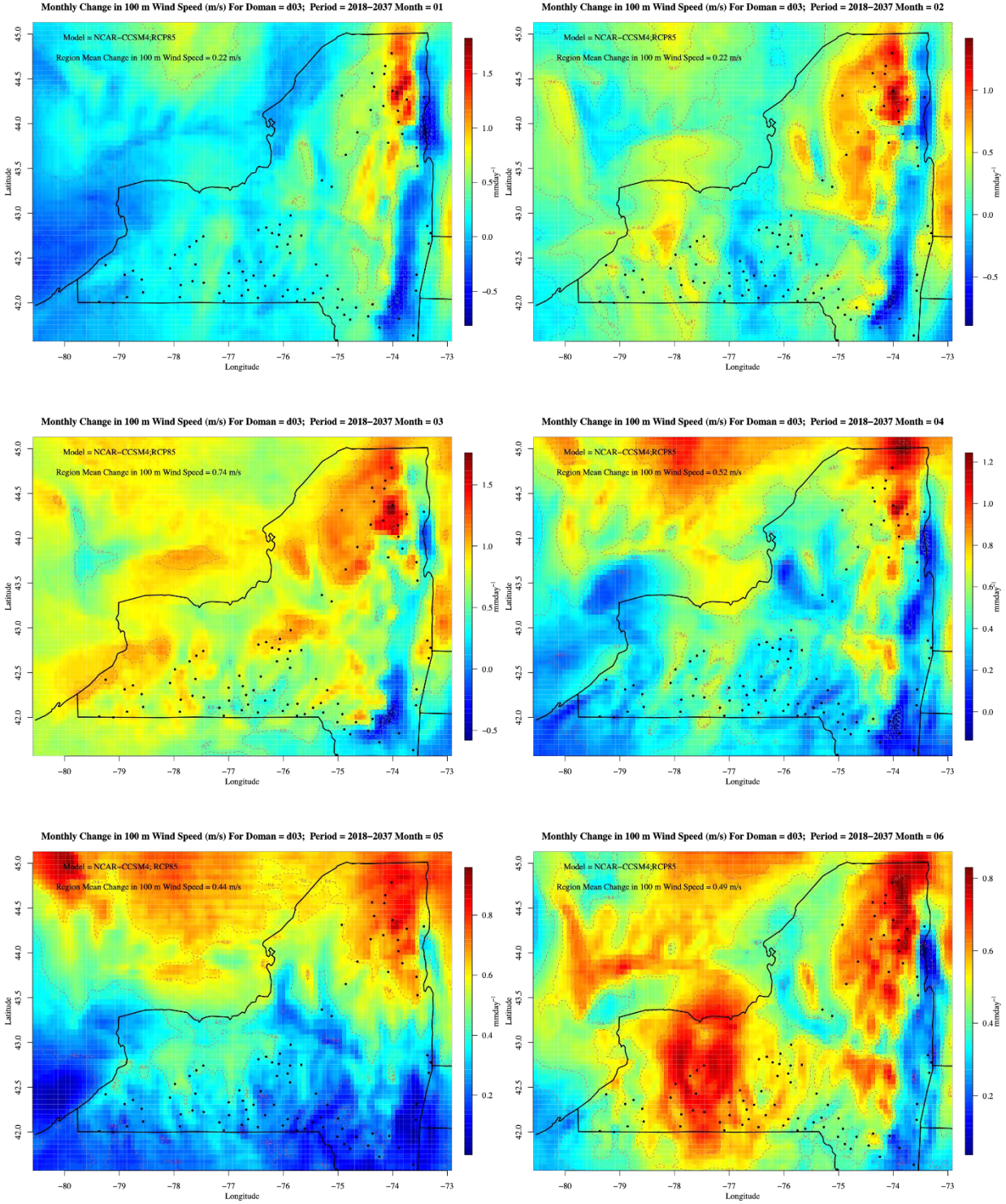

Figure A-22. Same as Figure A-6 except for NCAR-CCSM4

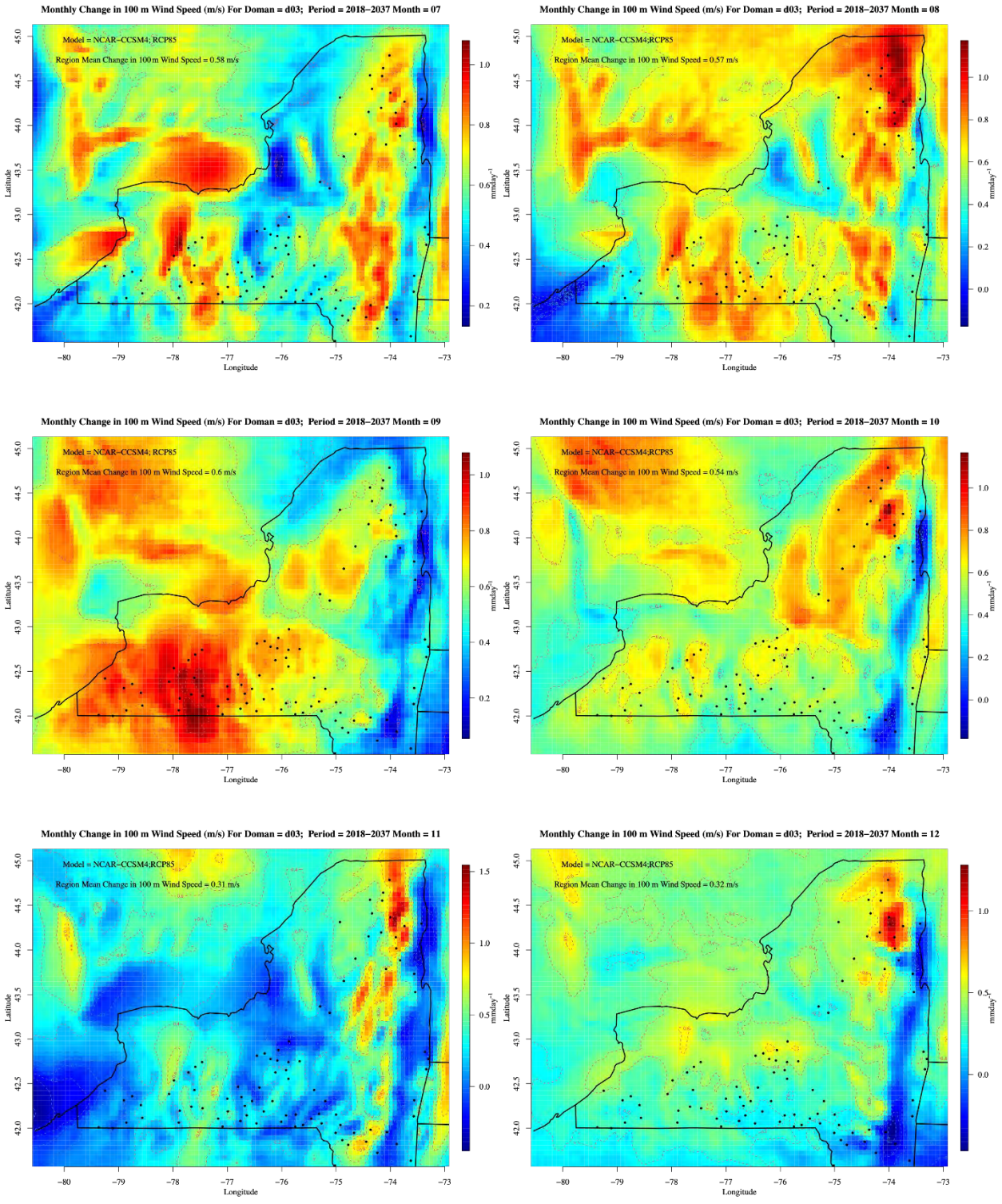

Figure A-23. Same as Figure A-7 except for NCAR-CCSM4

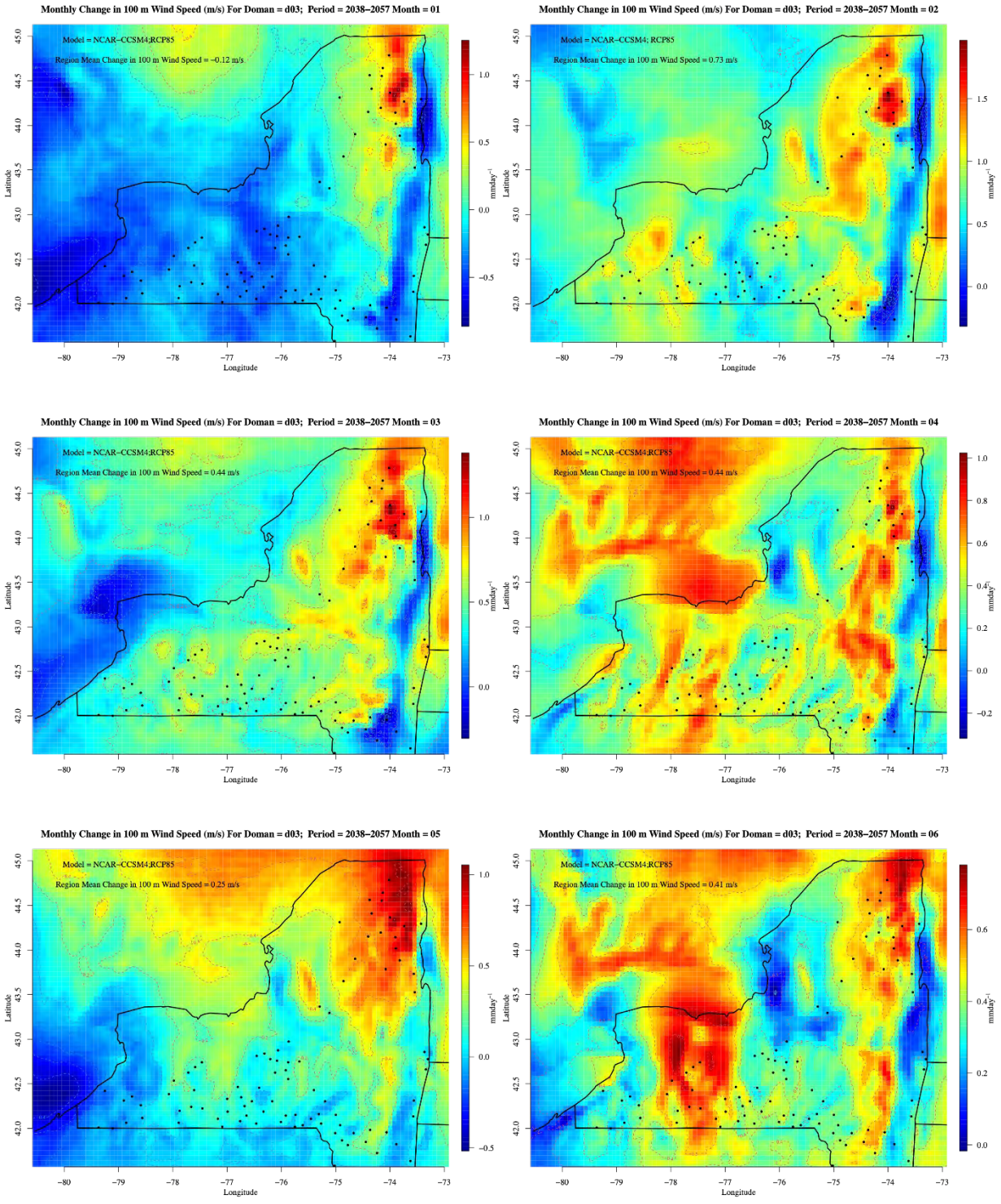

Figure A-24. Same as Figure A-8 except for NCAR-CCSM4

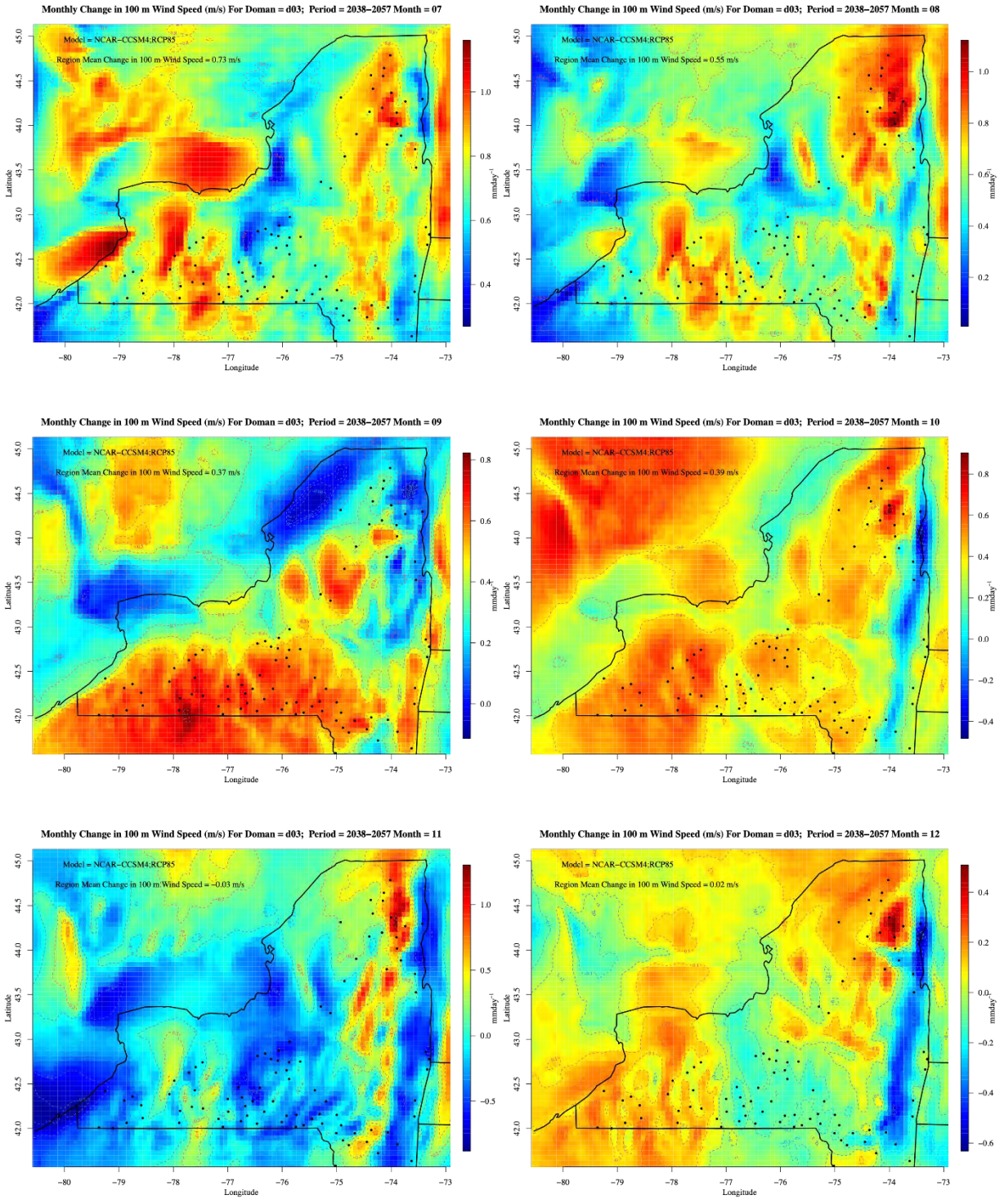

Appendix B. Model monthly changes in wind speed: d04 domain

Figure B-1. Domain d04 monthly changes in 100 m wind speed (ms^{-1}) under RCP4.5 scenario for near-future period

Upper left: January; upper right: February; middle left: March; middle right: April; lower left: May; lower right: June.

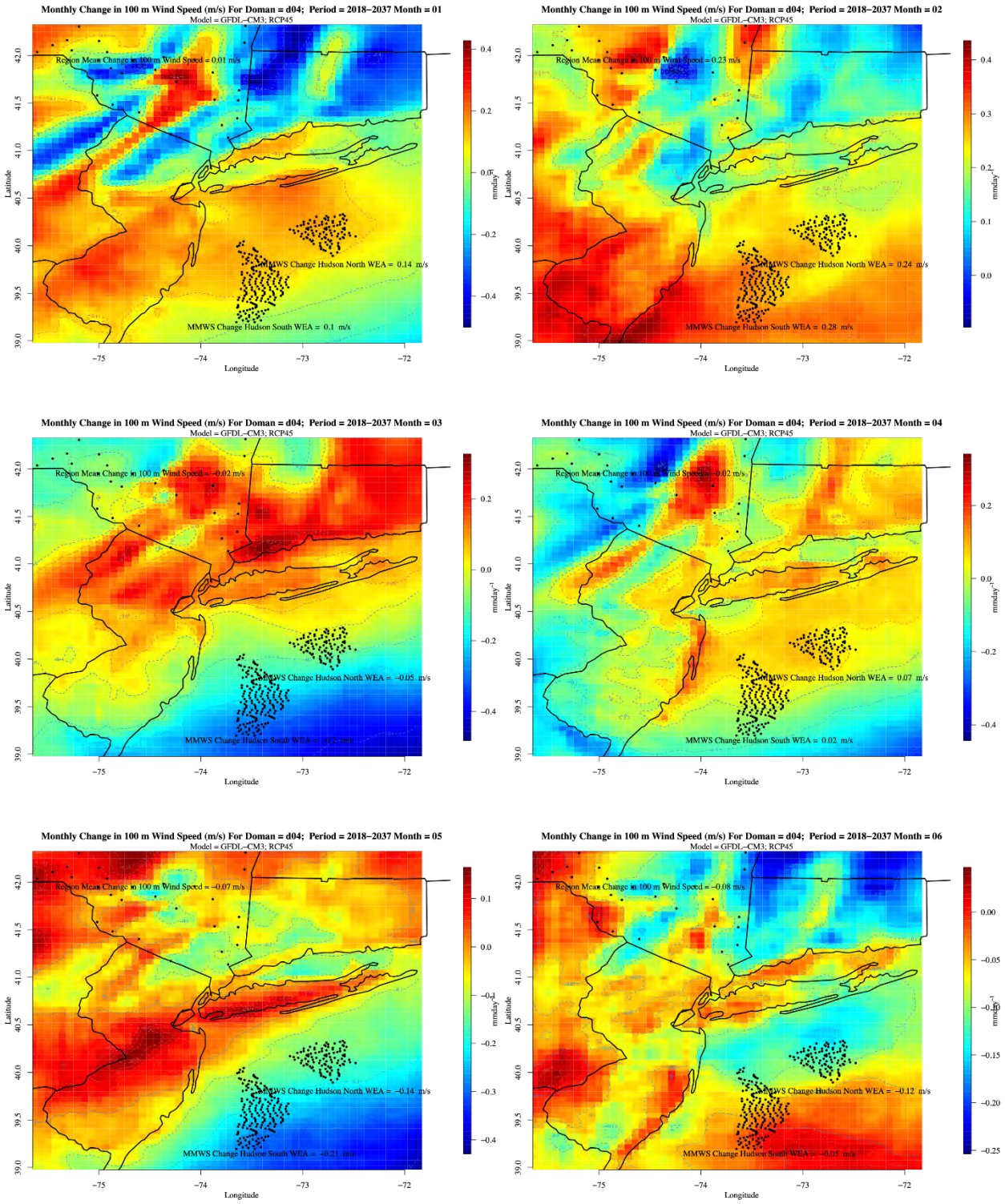

Figure B-2. Same as Figure B-1 except Upper left: July; upper right: August; middle left: September; middle right: October; lower left: November; lower right: December

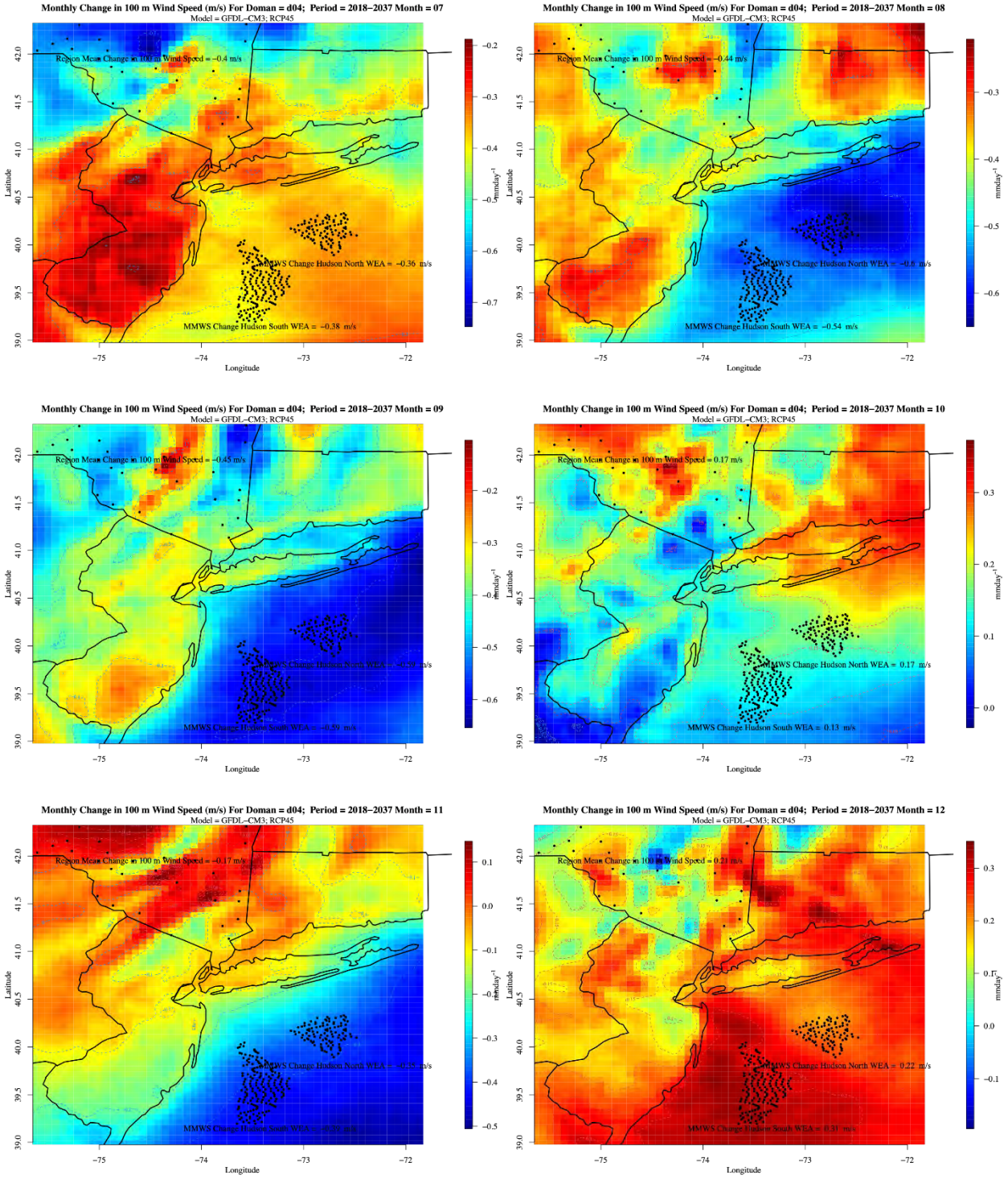

Figure B-3. Same as Figure B-1 except for mid-future period

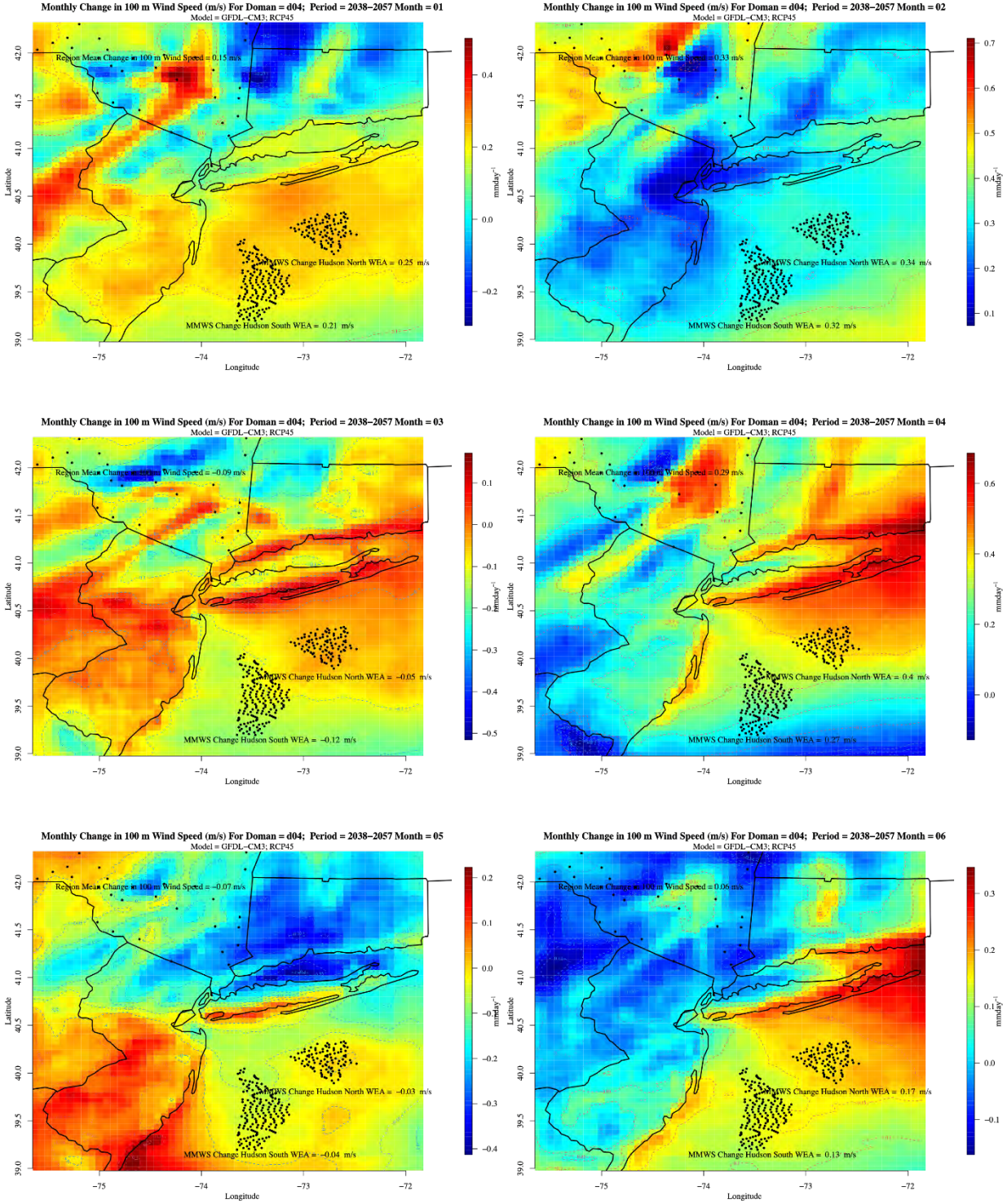

Figure B-4. Same as Figure B-2 except for mid-future period

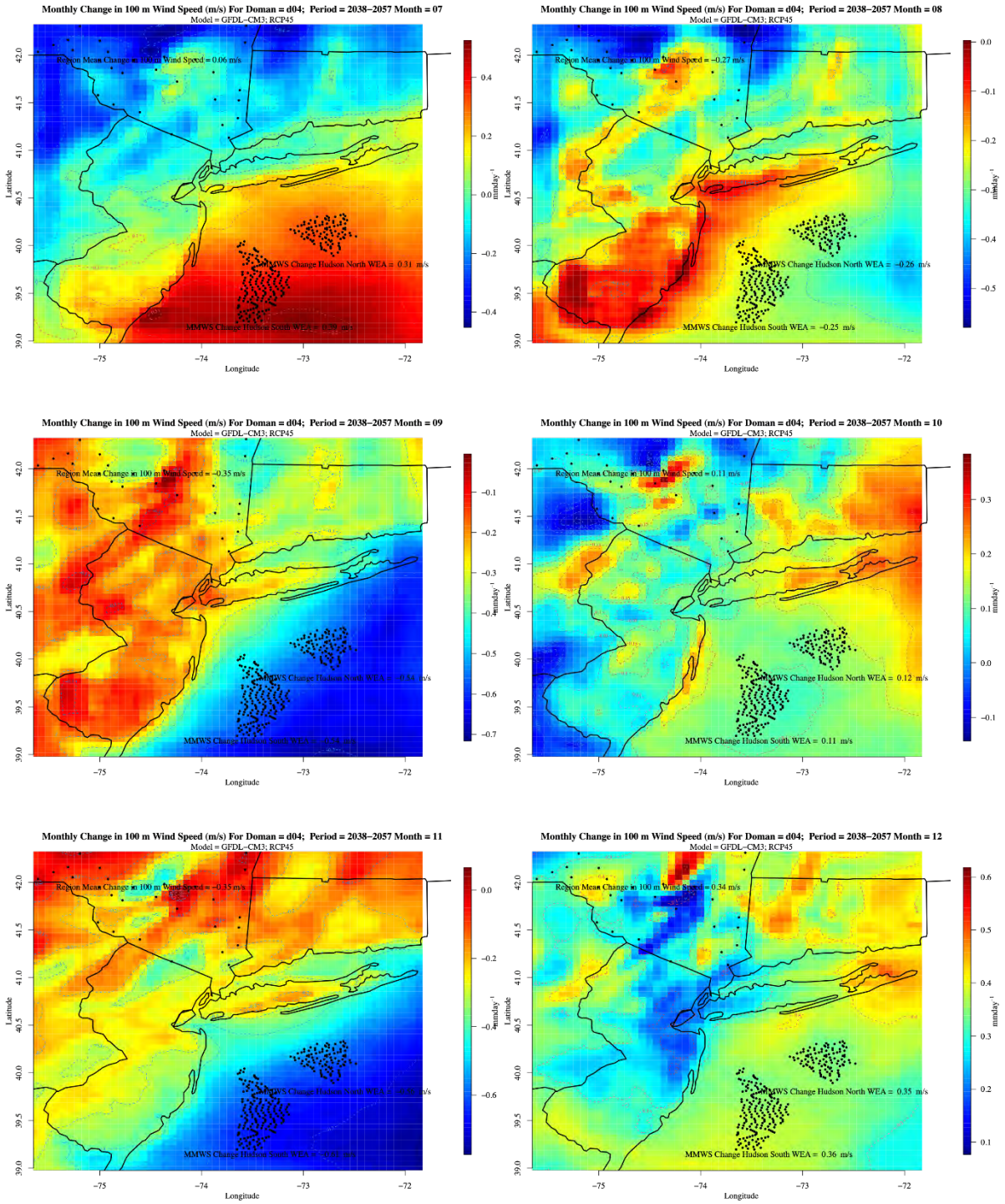

Figure B-5. Same as Figure B-1 except for RCP8.5

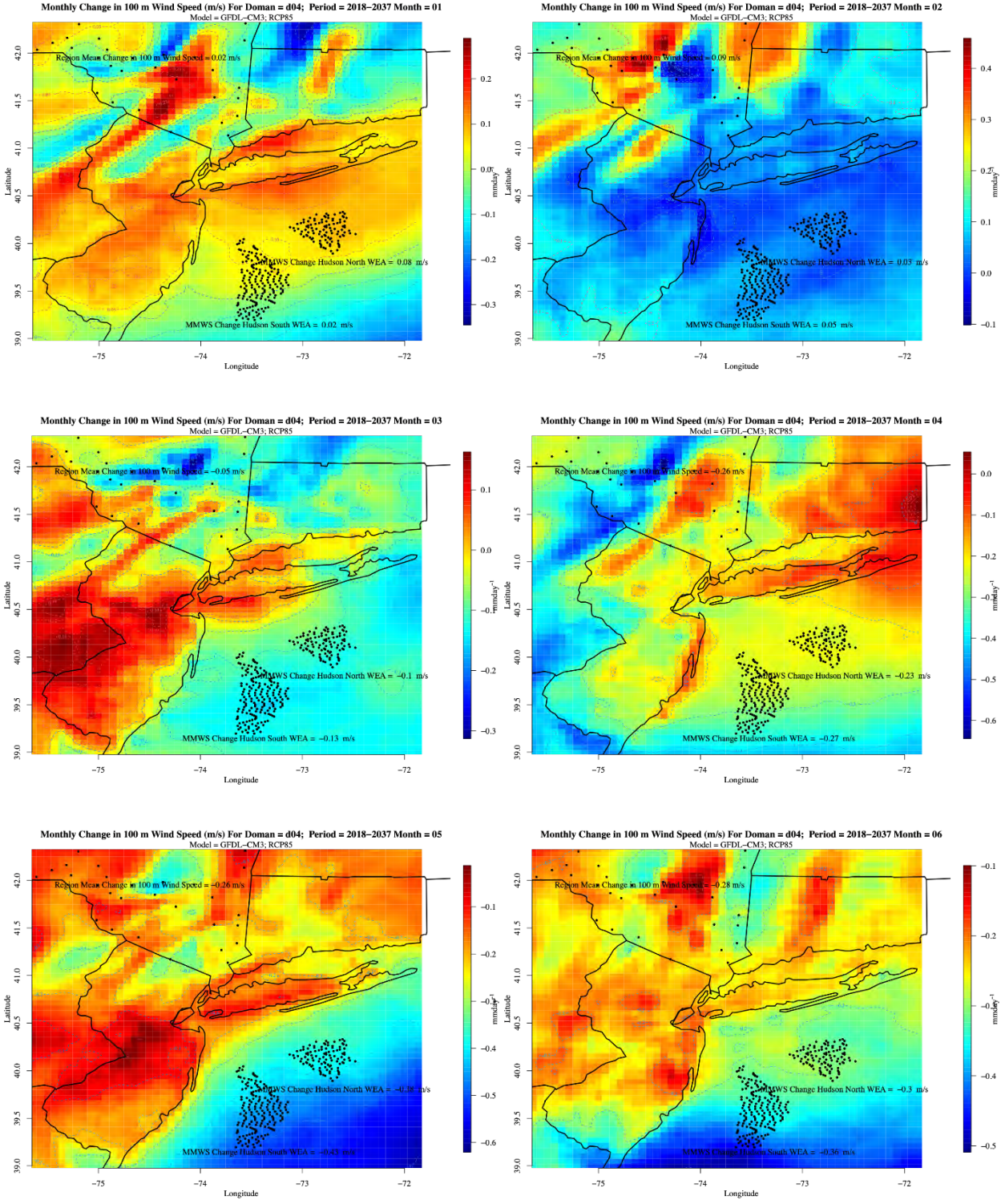

Figure B-6. Same as Figure B-2 except for RCP8.5

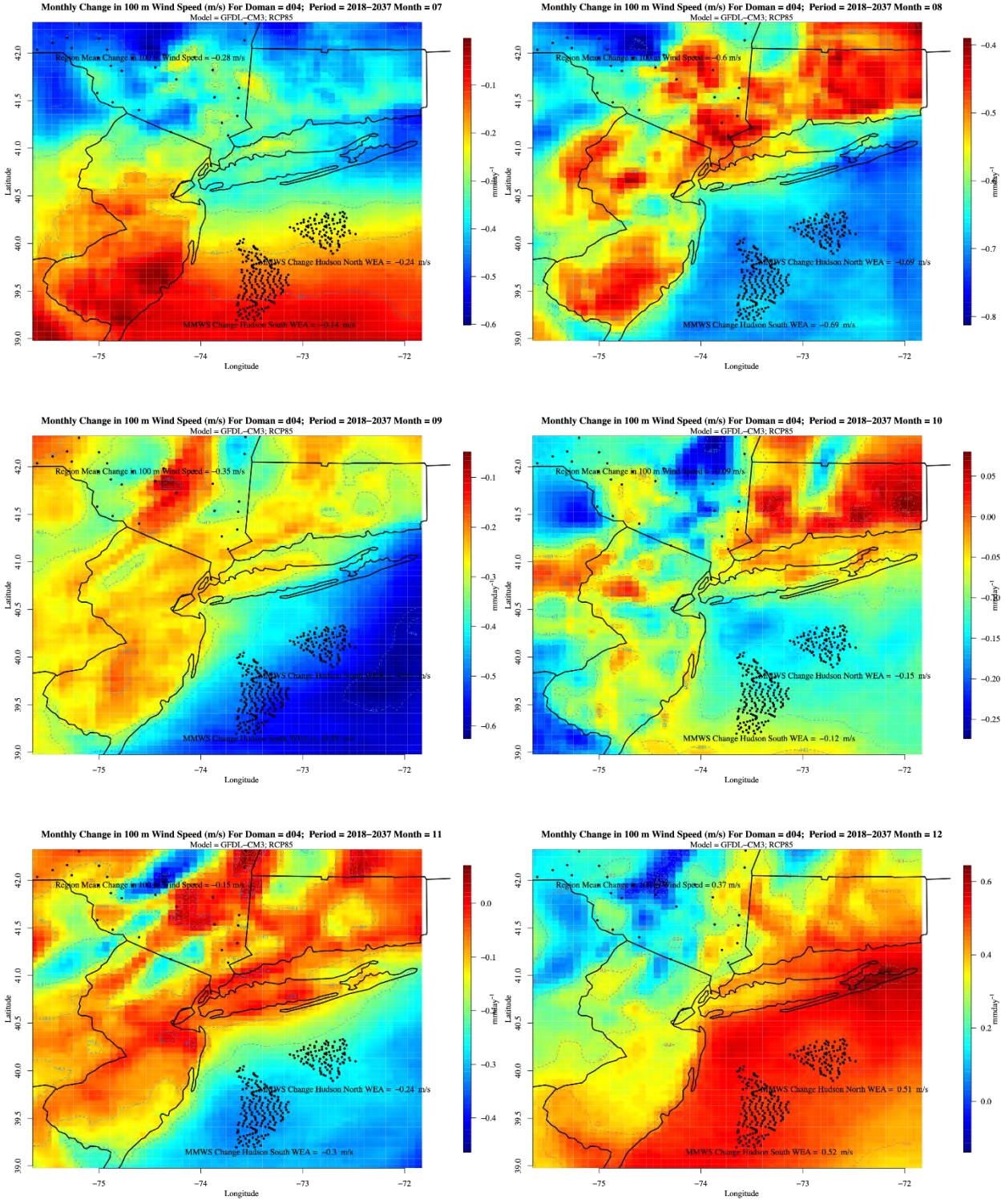

Figure B-7. Same as Figure B-5 except for the mid-future period

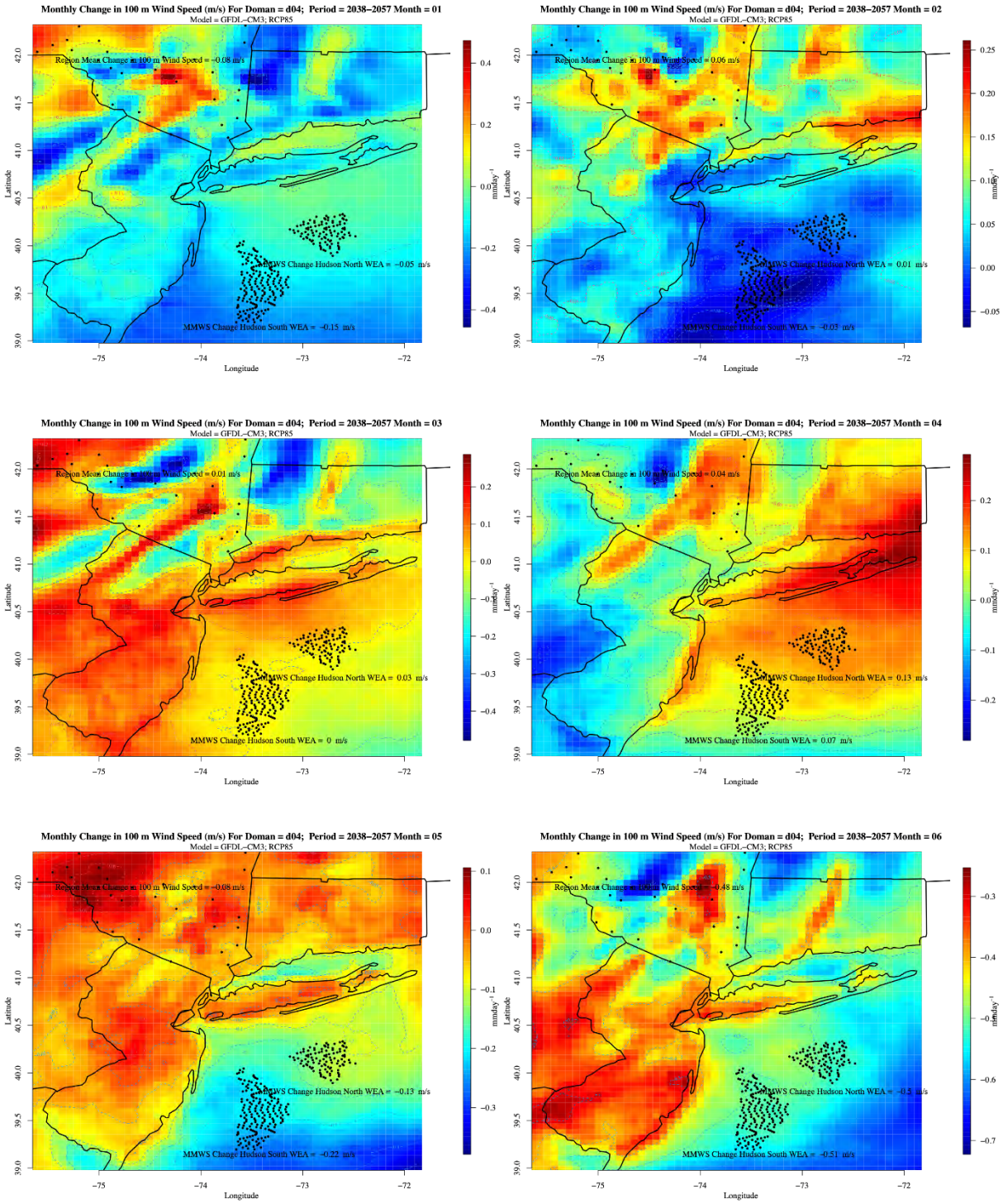

Figure B-8. Same as Figure B-6 except for the mid-future period

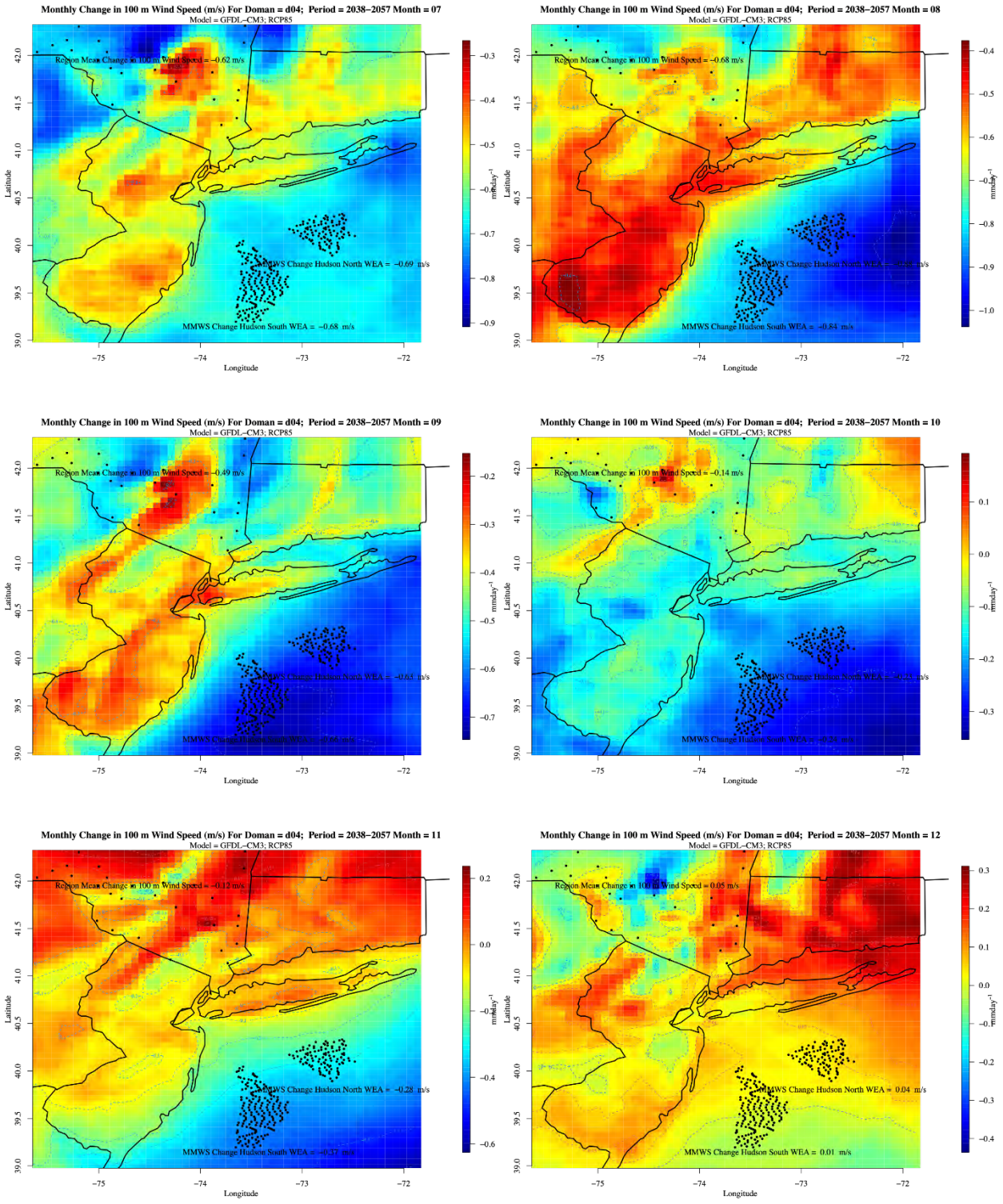

Figure B-9. Same as Figure B-1 except for MIROC5

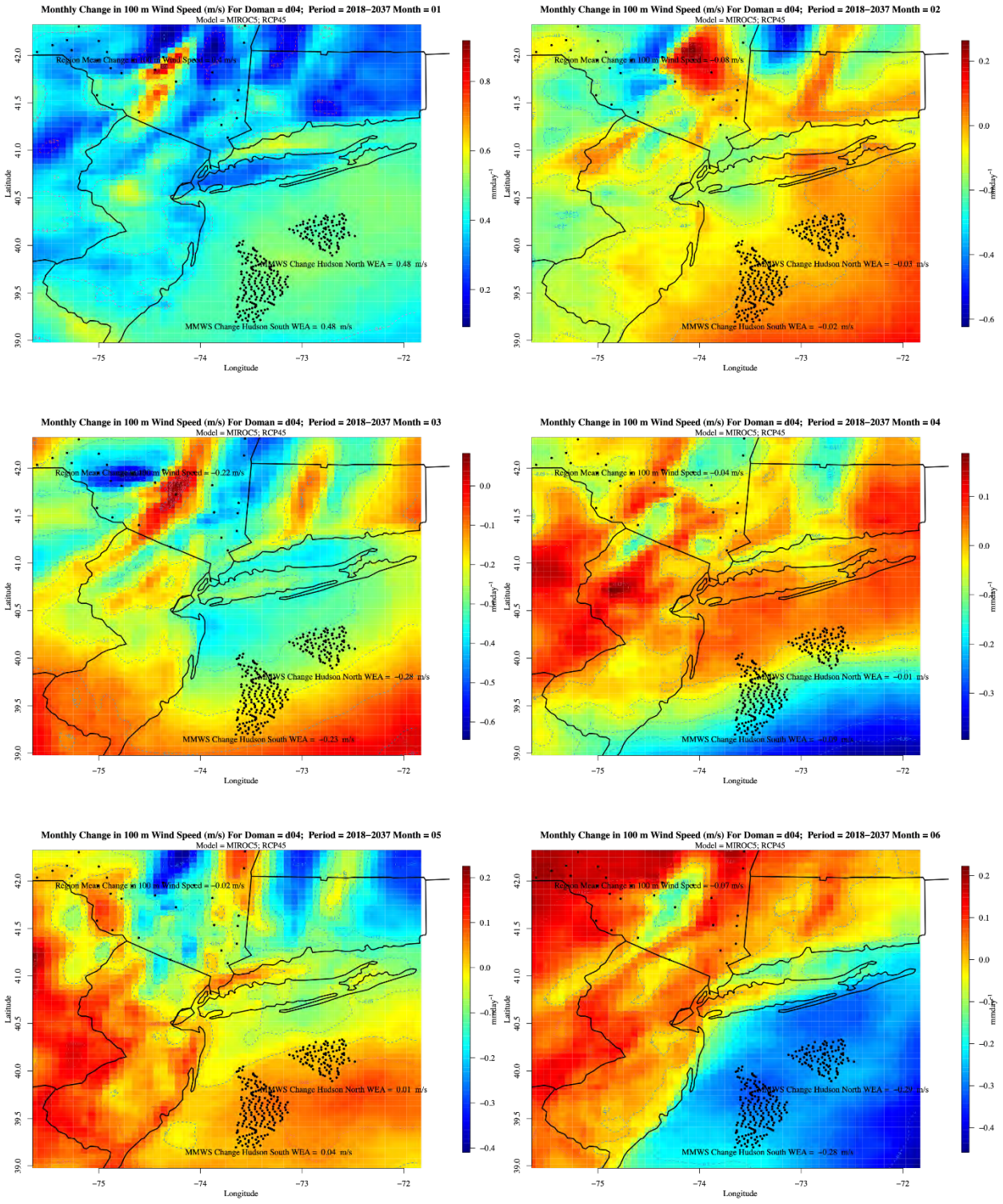

Figure B-10. Same as Figure B-2 except for MIROC5

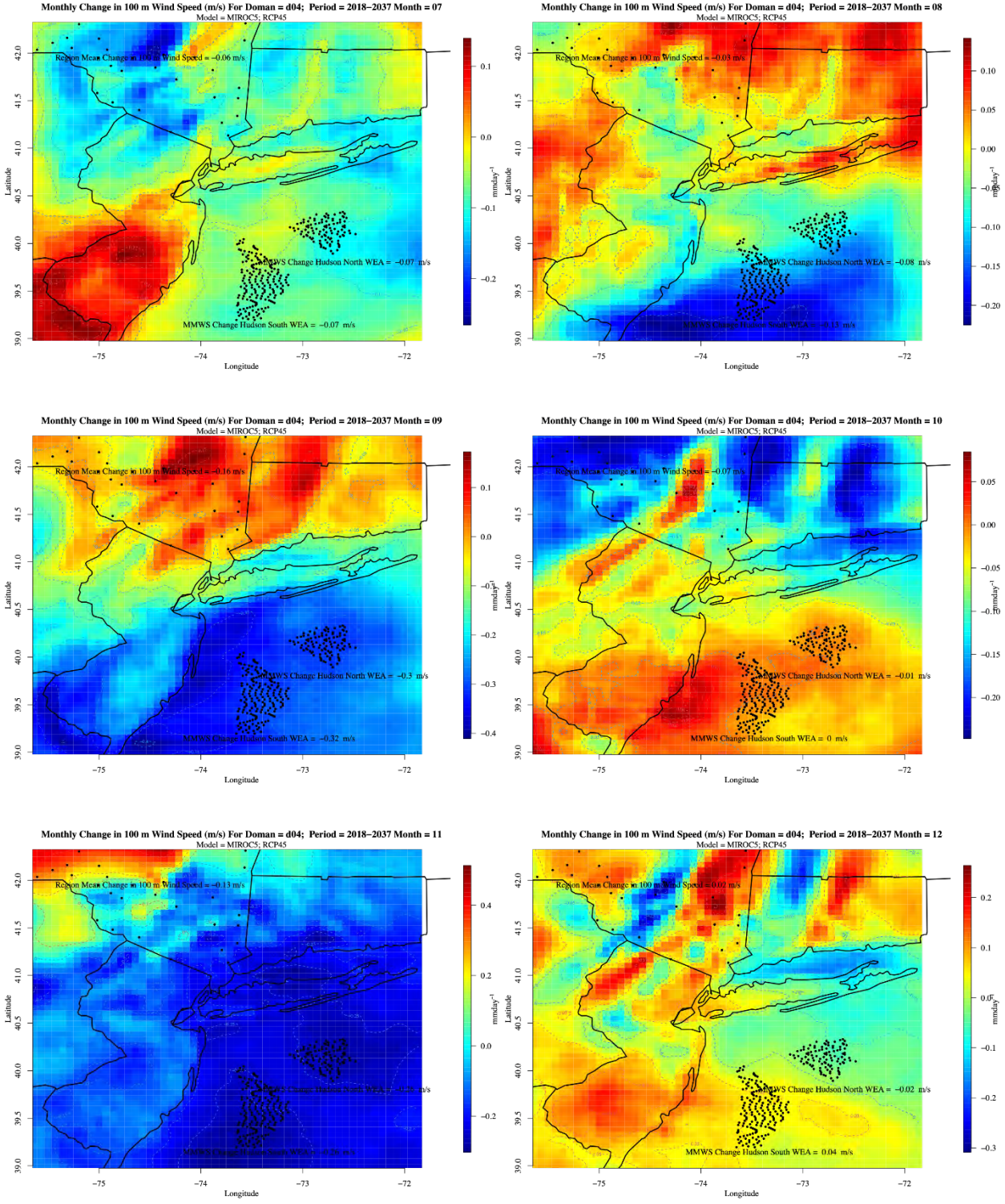

Figure B-11. Same as Figure B-3 except for MIROC5

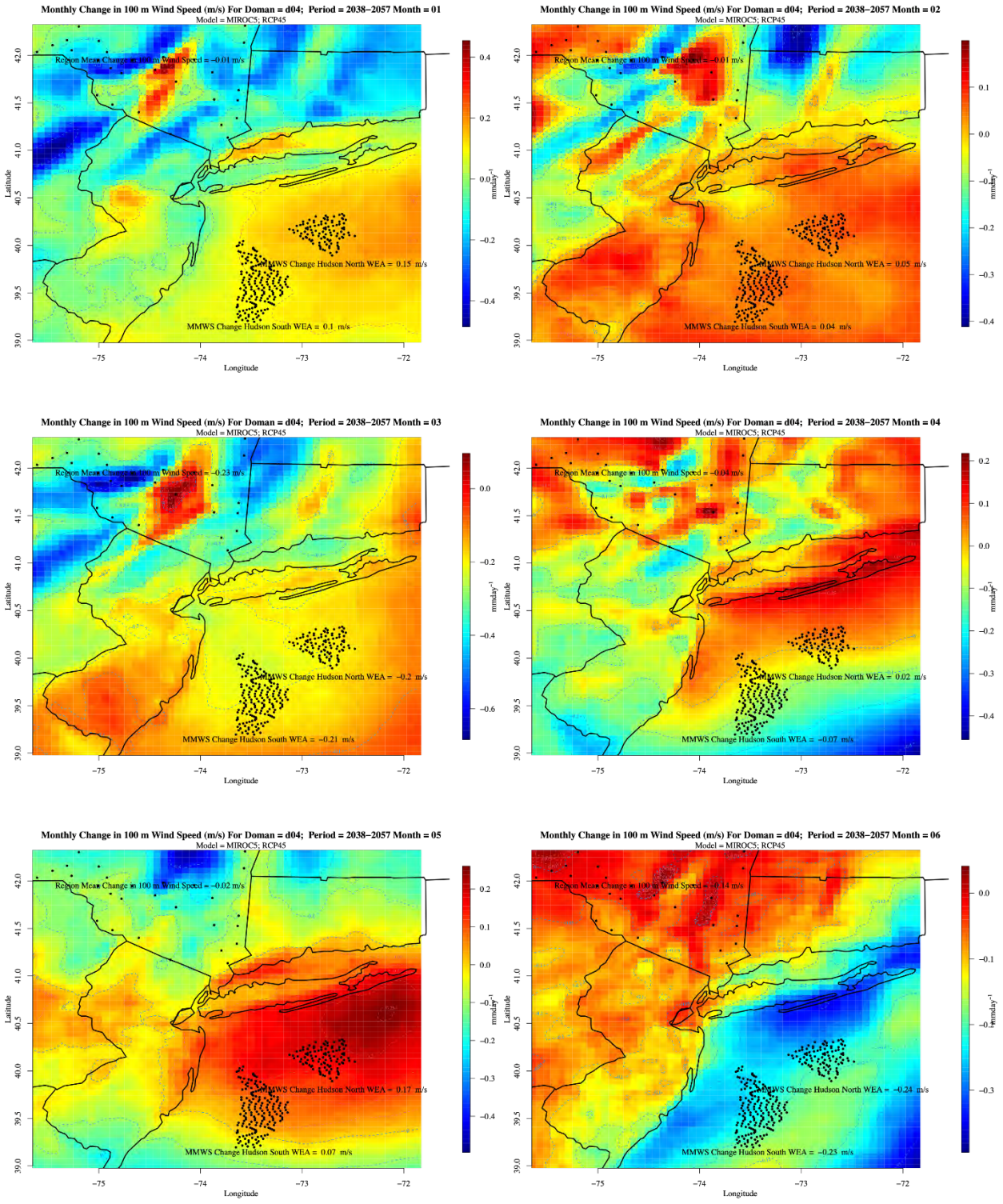

Figure B-12. Same as Figure B-4 except for MIROC5

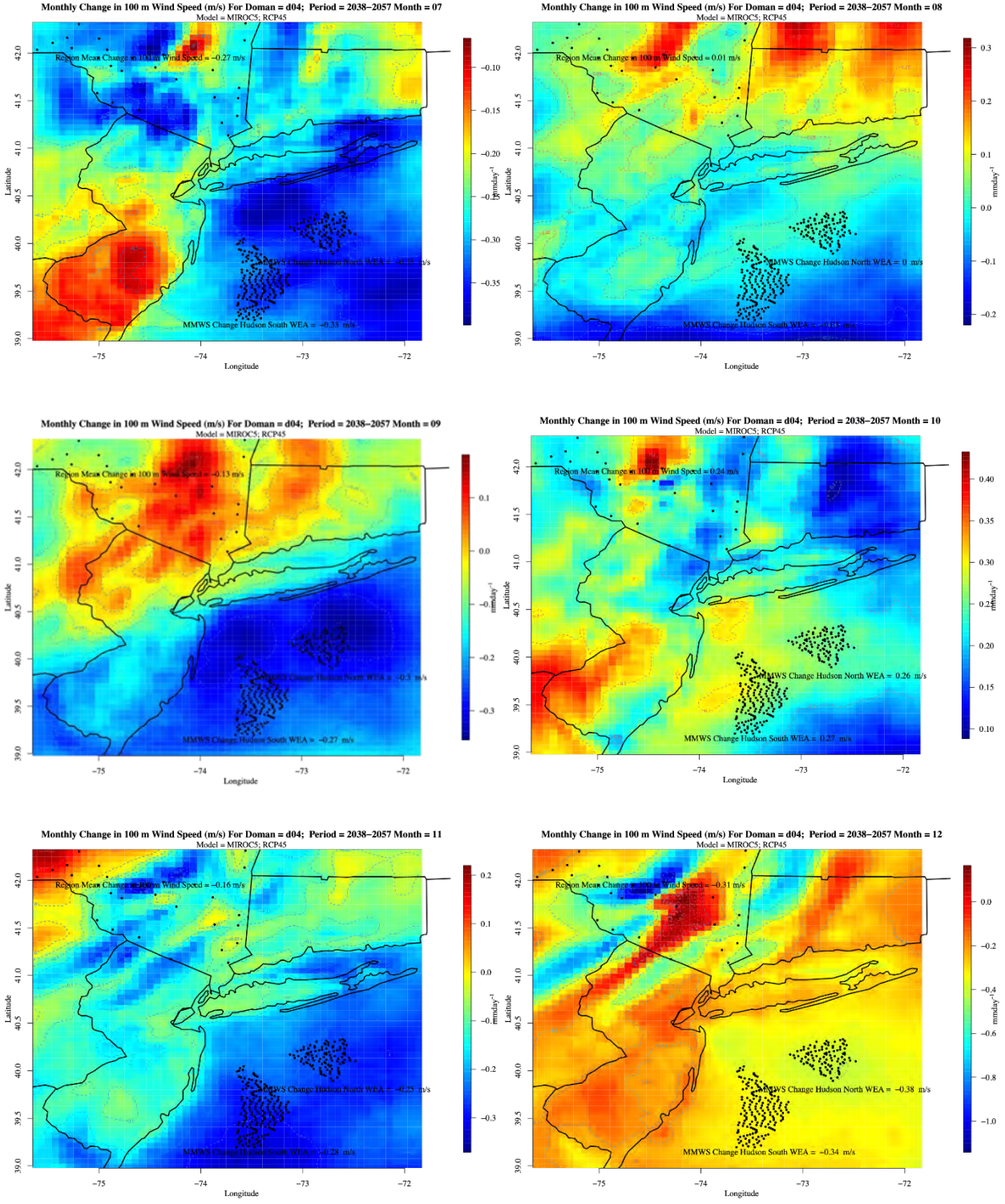

Figure B-13. Same as Figure B-5 except for MIROC5

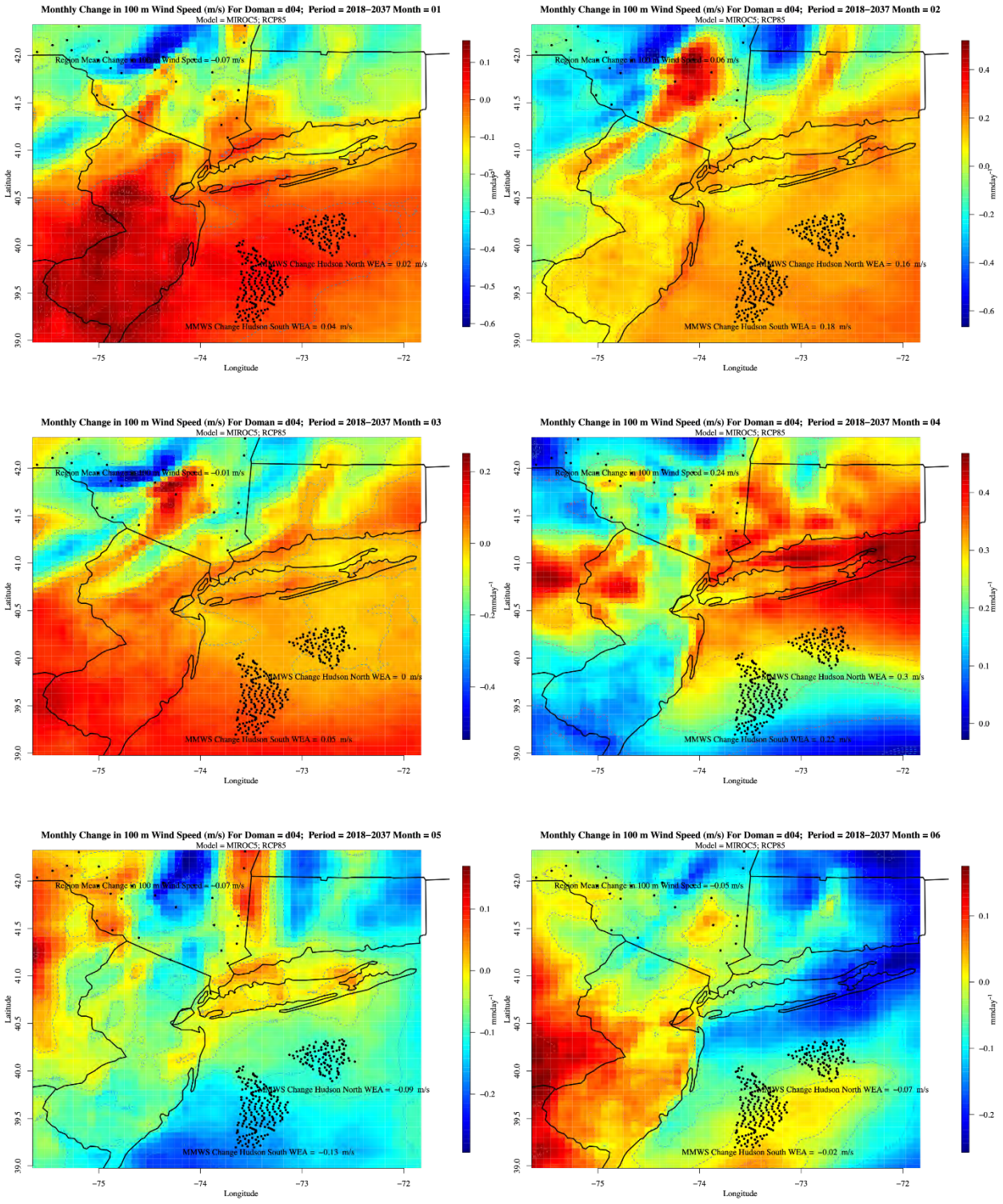

Figure B-14. Same as Figure B-6 except for MIROC5

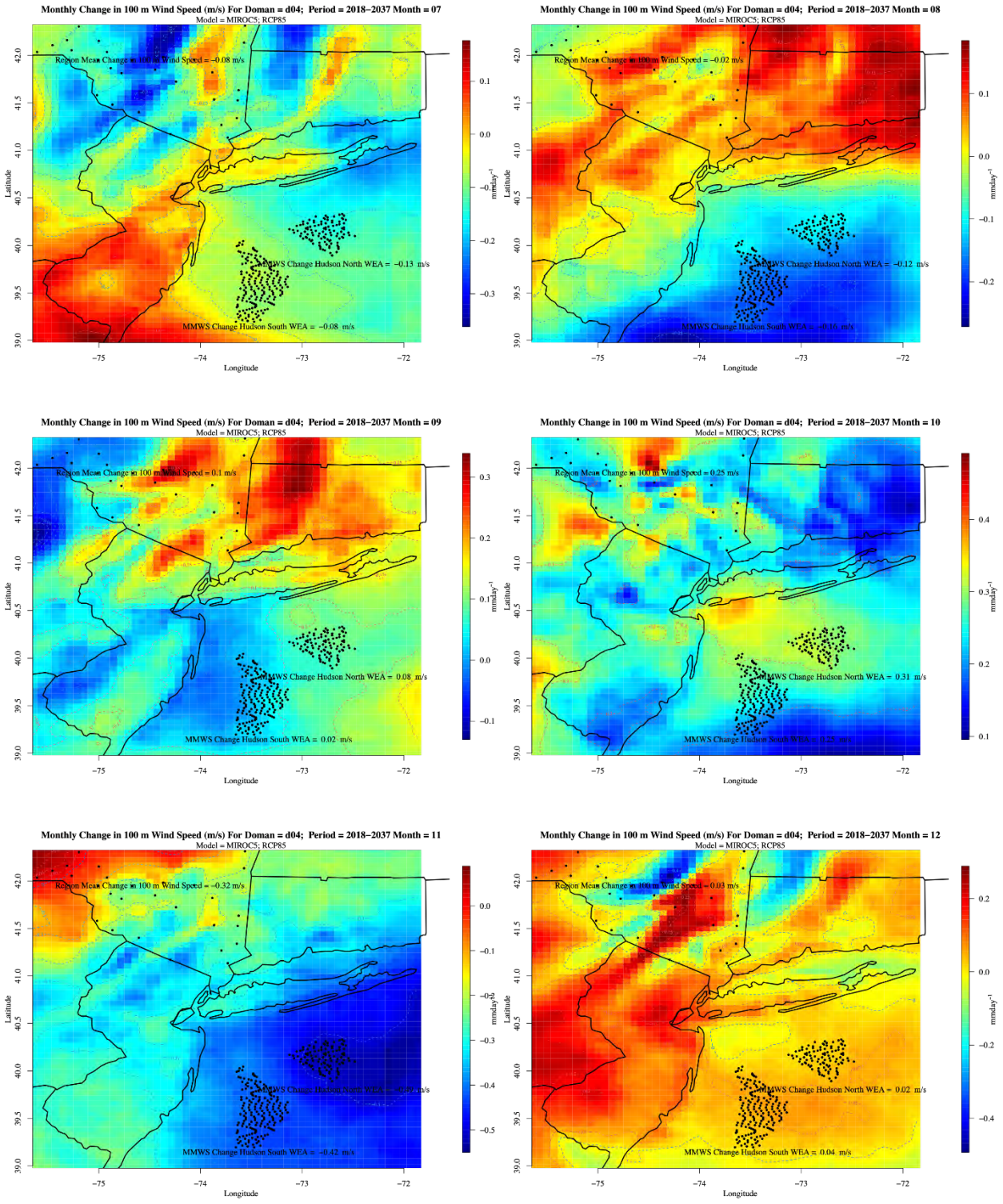

Figure B-15. Same as Figure B-7 except for MIROC5

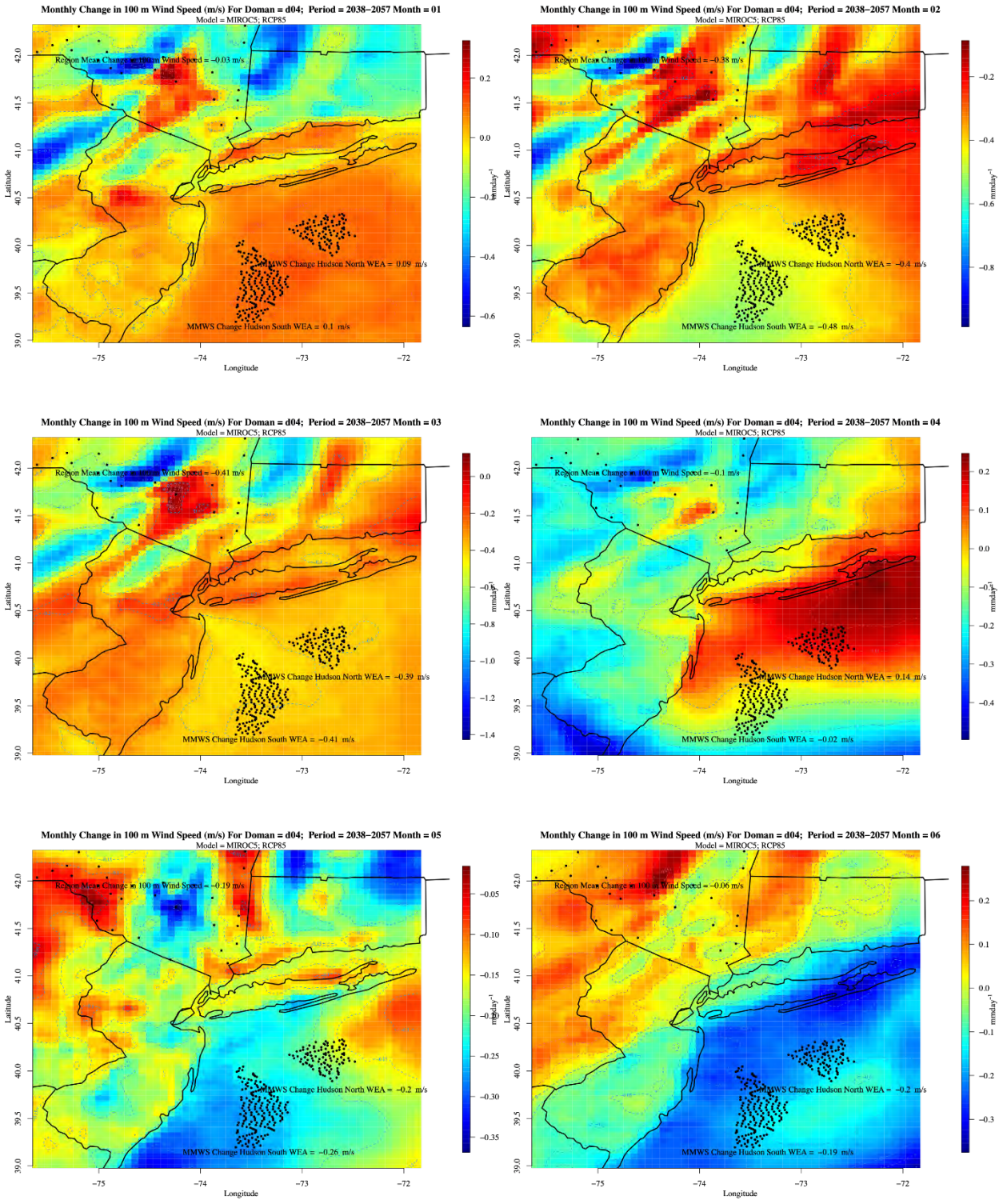

Figure B-16. Same as Figure B-8 except for MIROC5

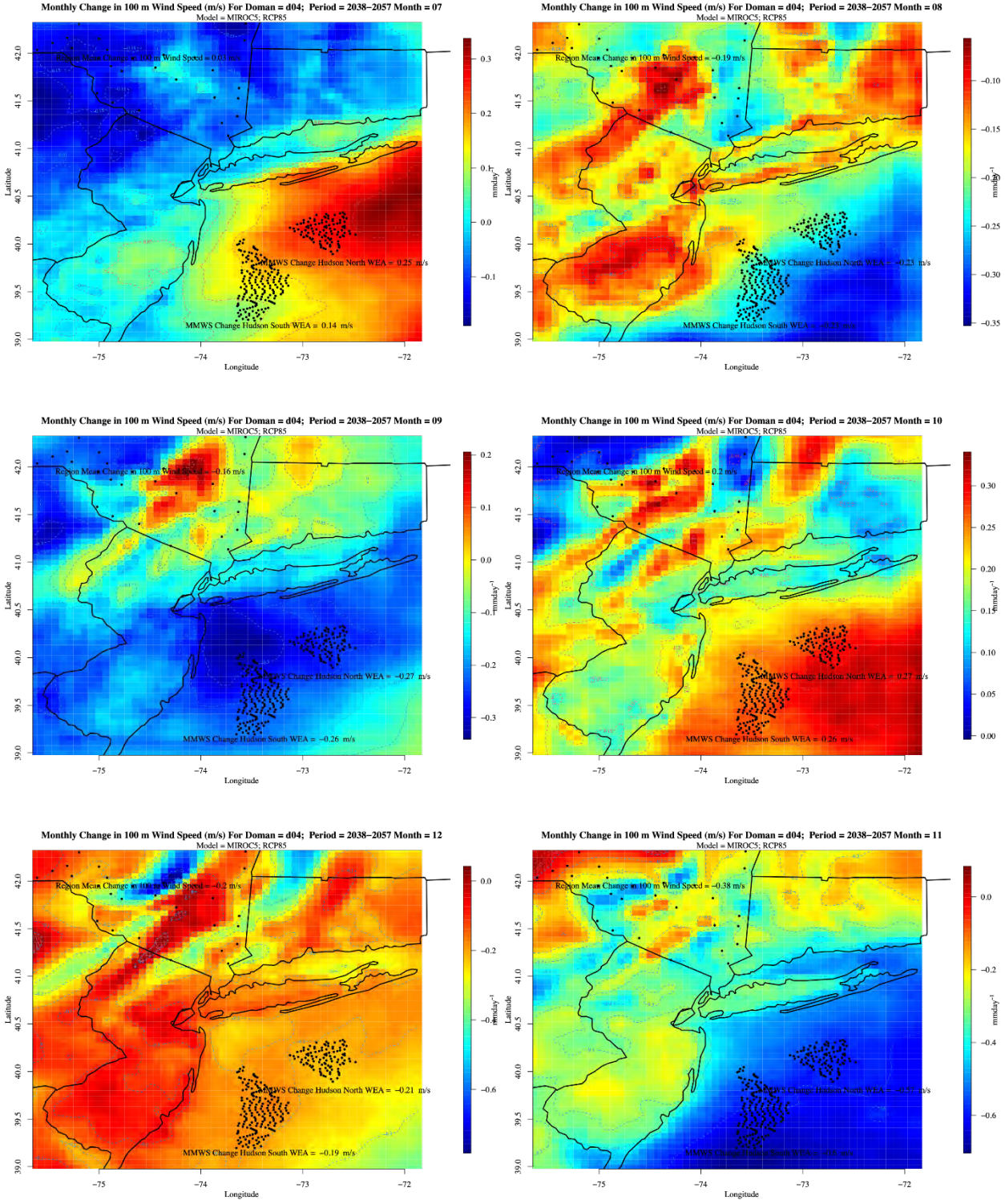

Figure B-17. Same as Figure B-1 except for NCAR-CCSM4

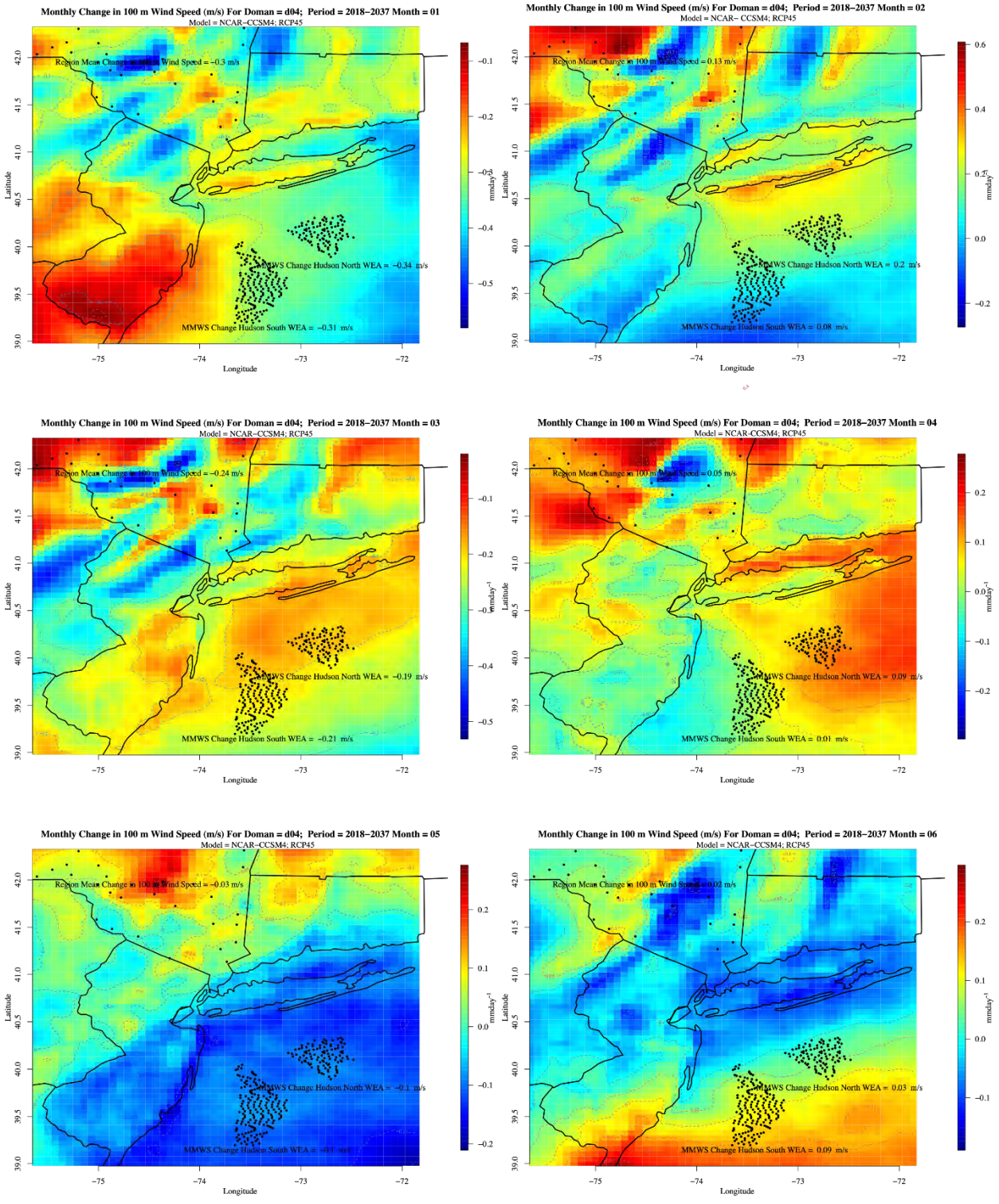

Figure B-18. Same as Figure B-2 except for NCAR-CCSM4

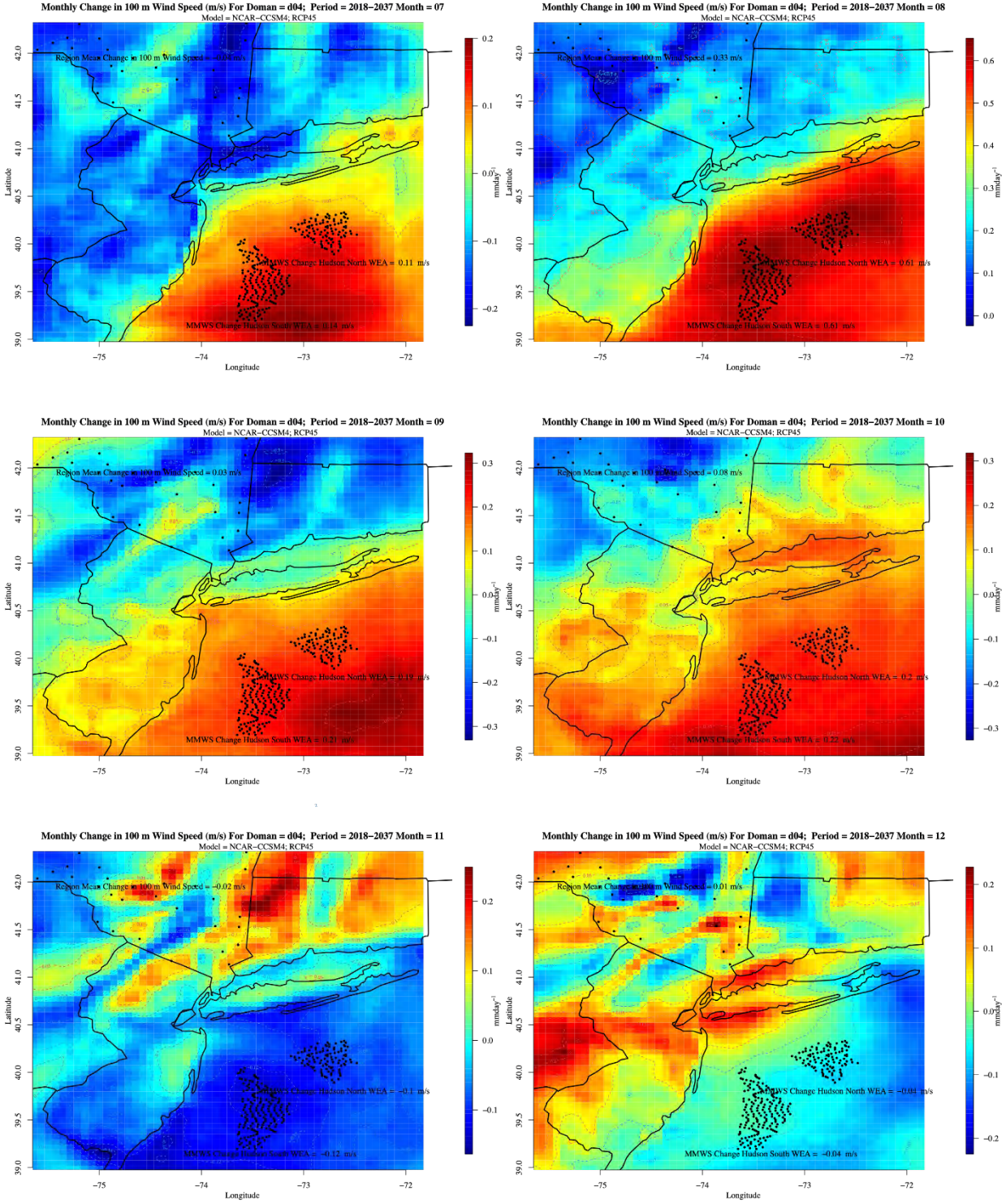

Figure B-19. Same as Figure B-3 except for NCAR-CCSM4

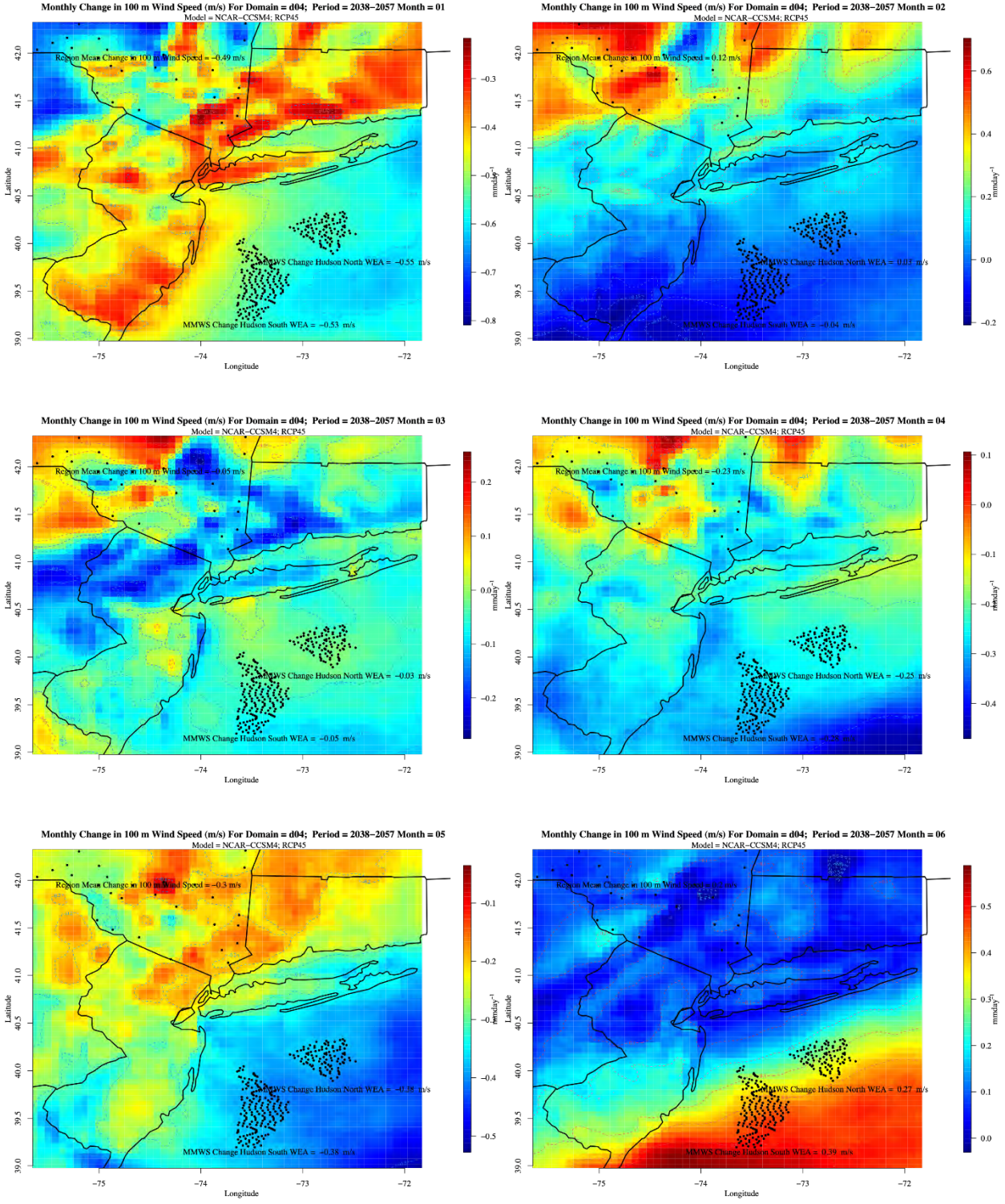

Figure B-20. Same as Figure B-4 except for NCAR-CCSM4

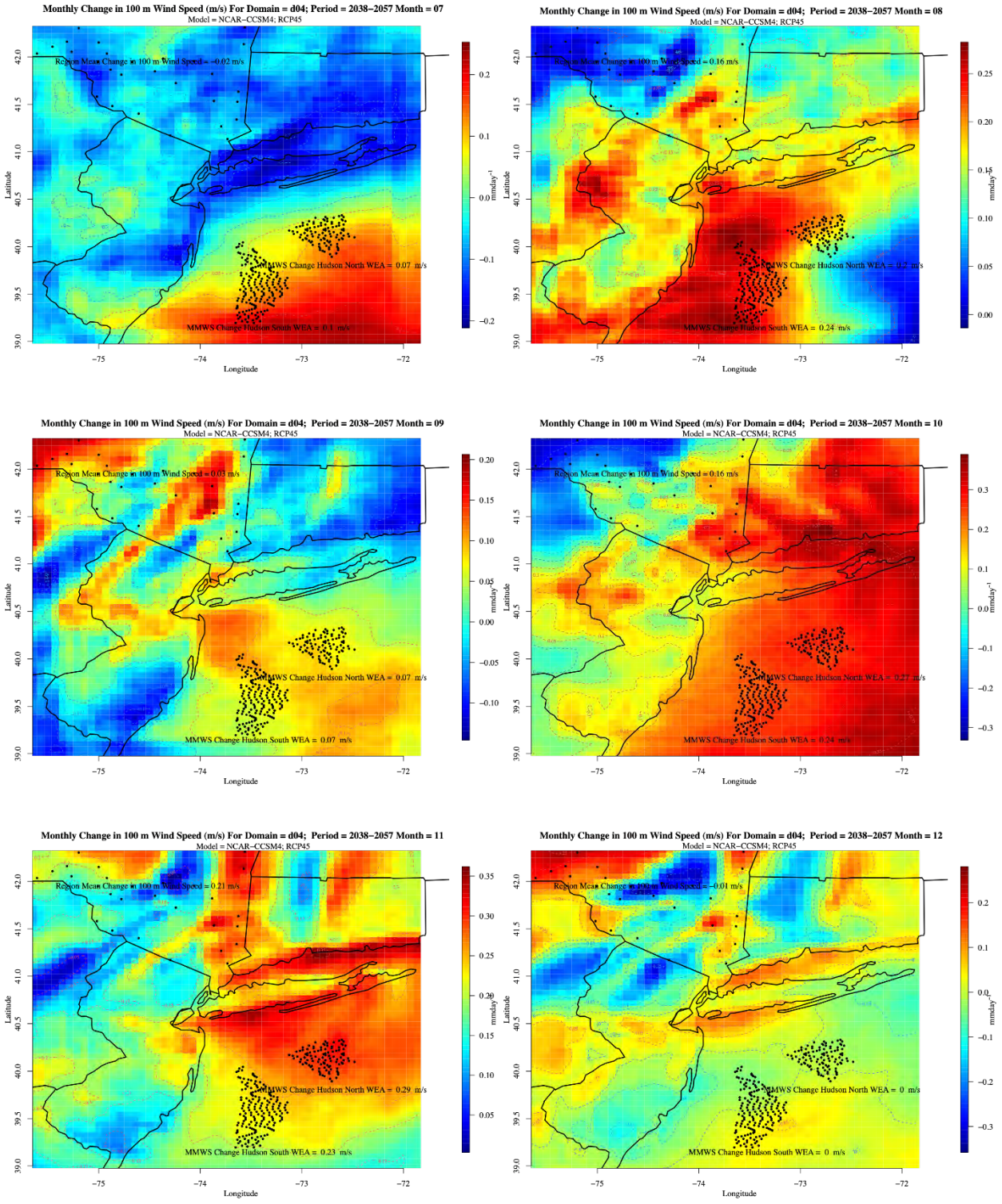

Figure B-21. Same as Figure B-5 except for NCAR-CCSM4

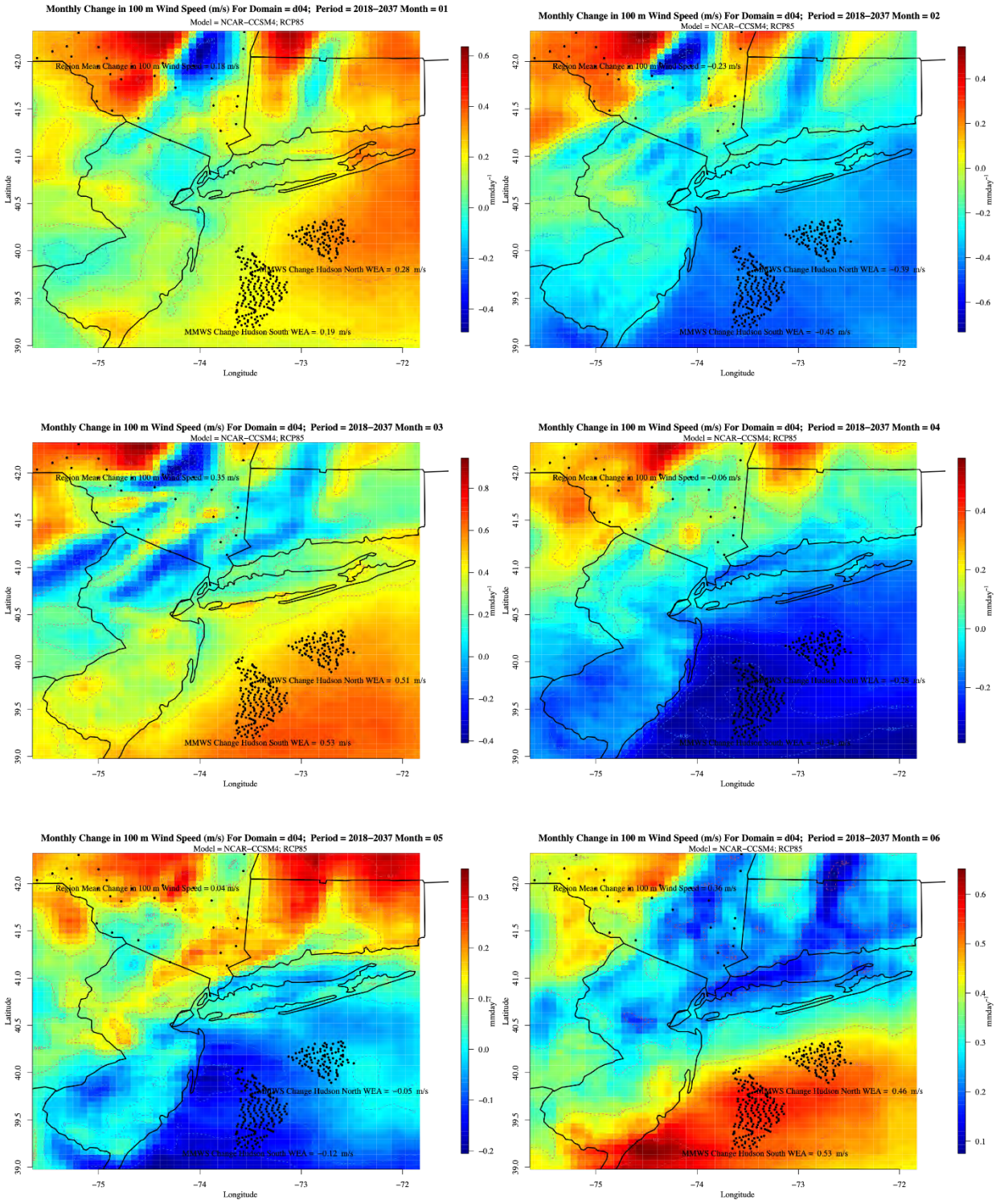

Figure B-22. Same as Figure B-6 except for NCAR-CCSM4

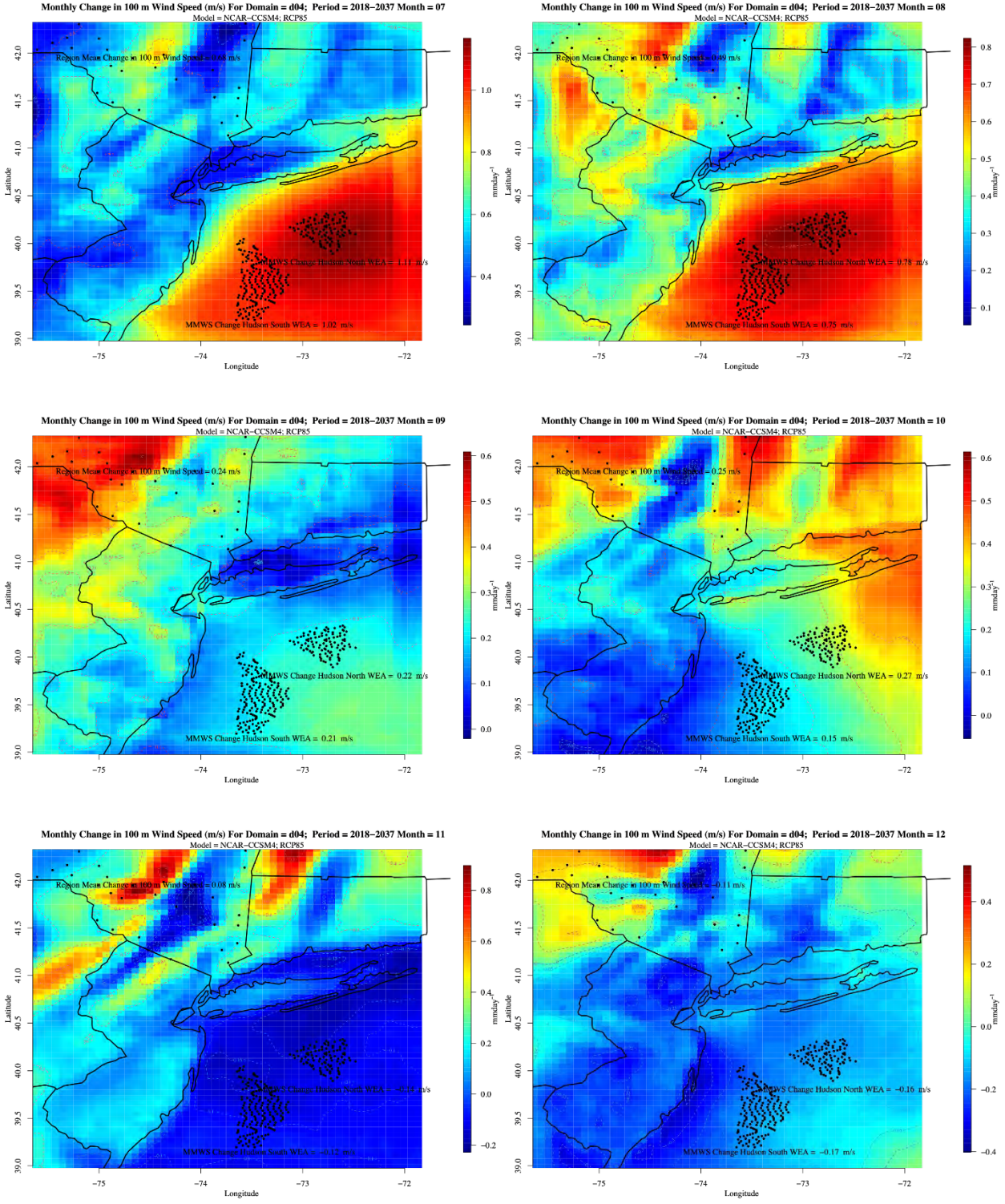

Figure B-23. Same as Figure B-7 except for NCAR-CCSM4

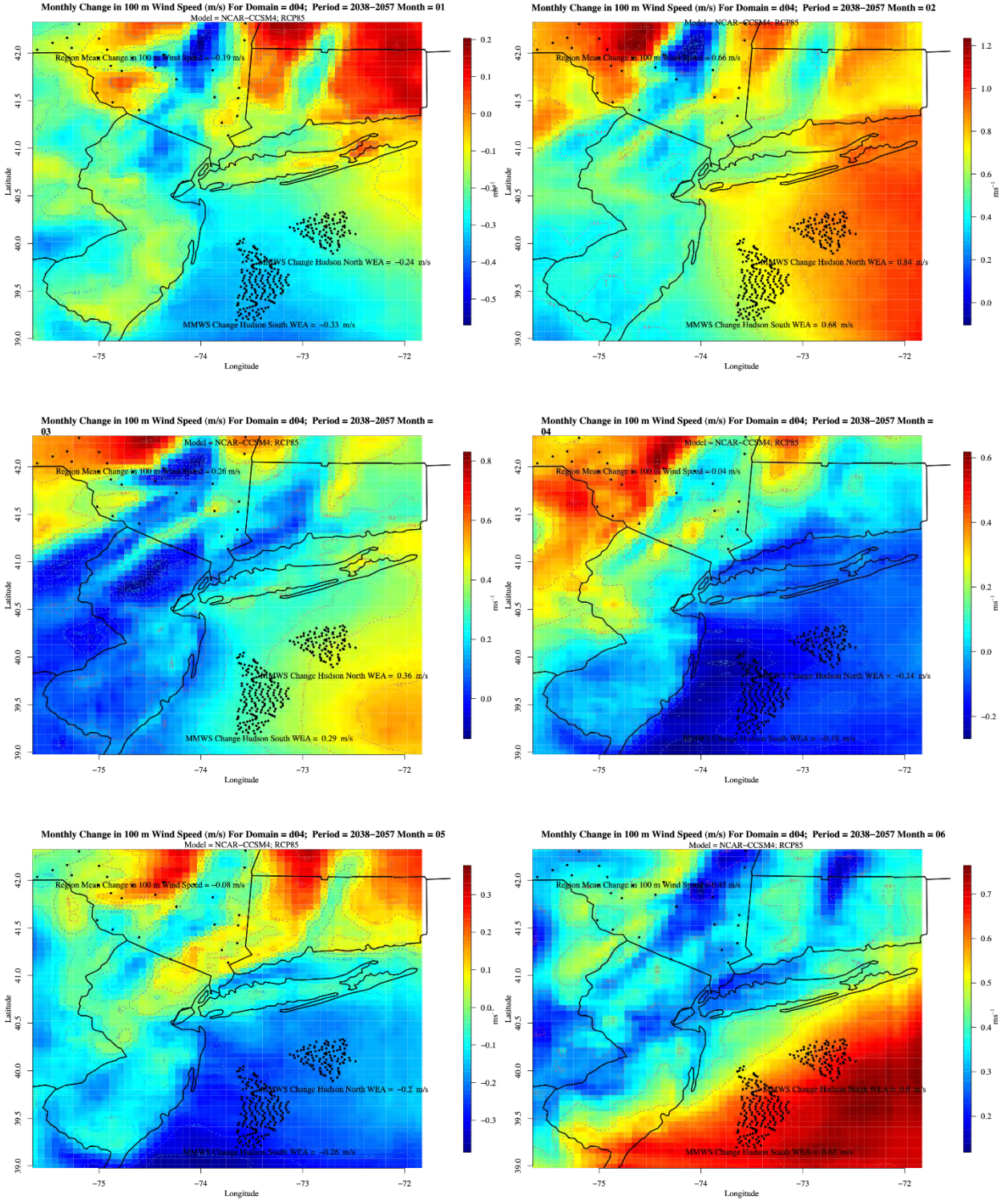

Figure B-24. Same as Figure B-8 except for NCAR-CCSM4

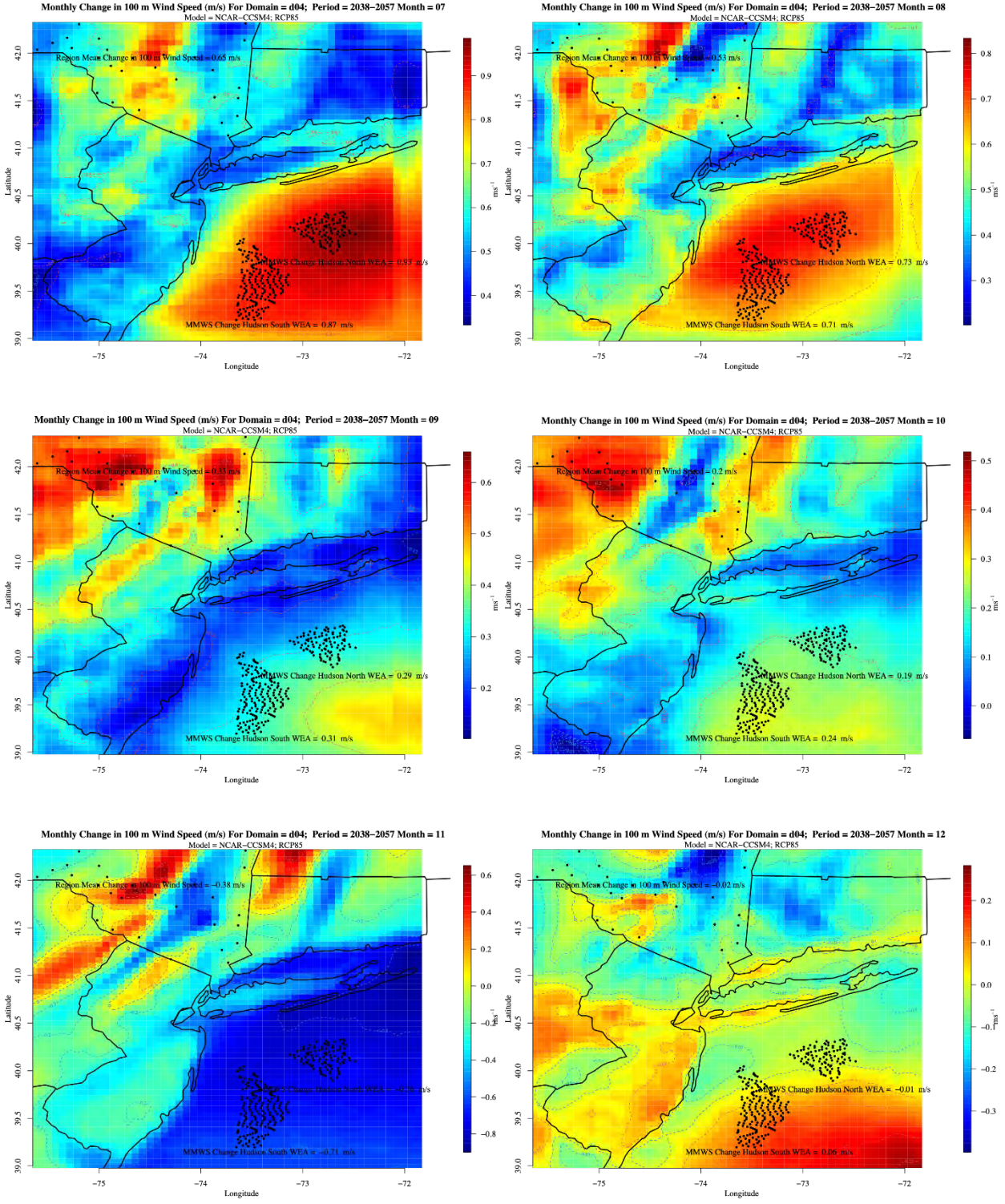

Appendix C. Model monthly changes in surface irradiance: d03 domain

Figure C-1. Domain d03 monthly changes in surface irradiance (Wm^{-2}) under RCP4.5 scenario for near-future period

Upper left: January; upper right: February; middle left: March; middle right: April; lower left: May; lower right: June.

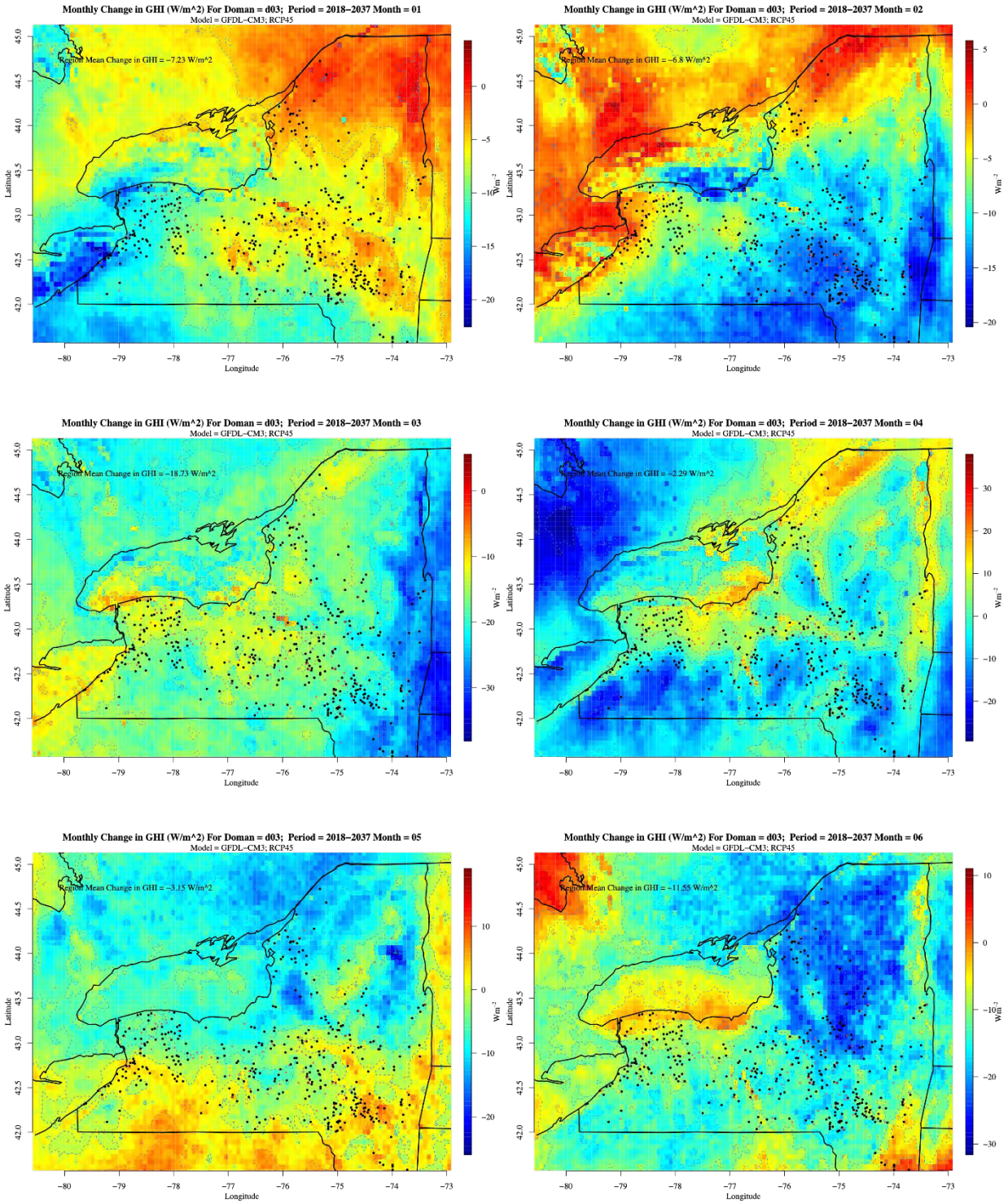

Figure C-2. Same as Figure C-1 except Upper left: July; upper right: August; middle left: September; middle right: October; lower left: November; lower right: December

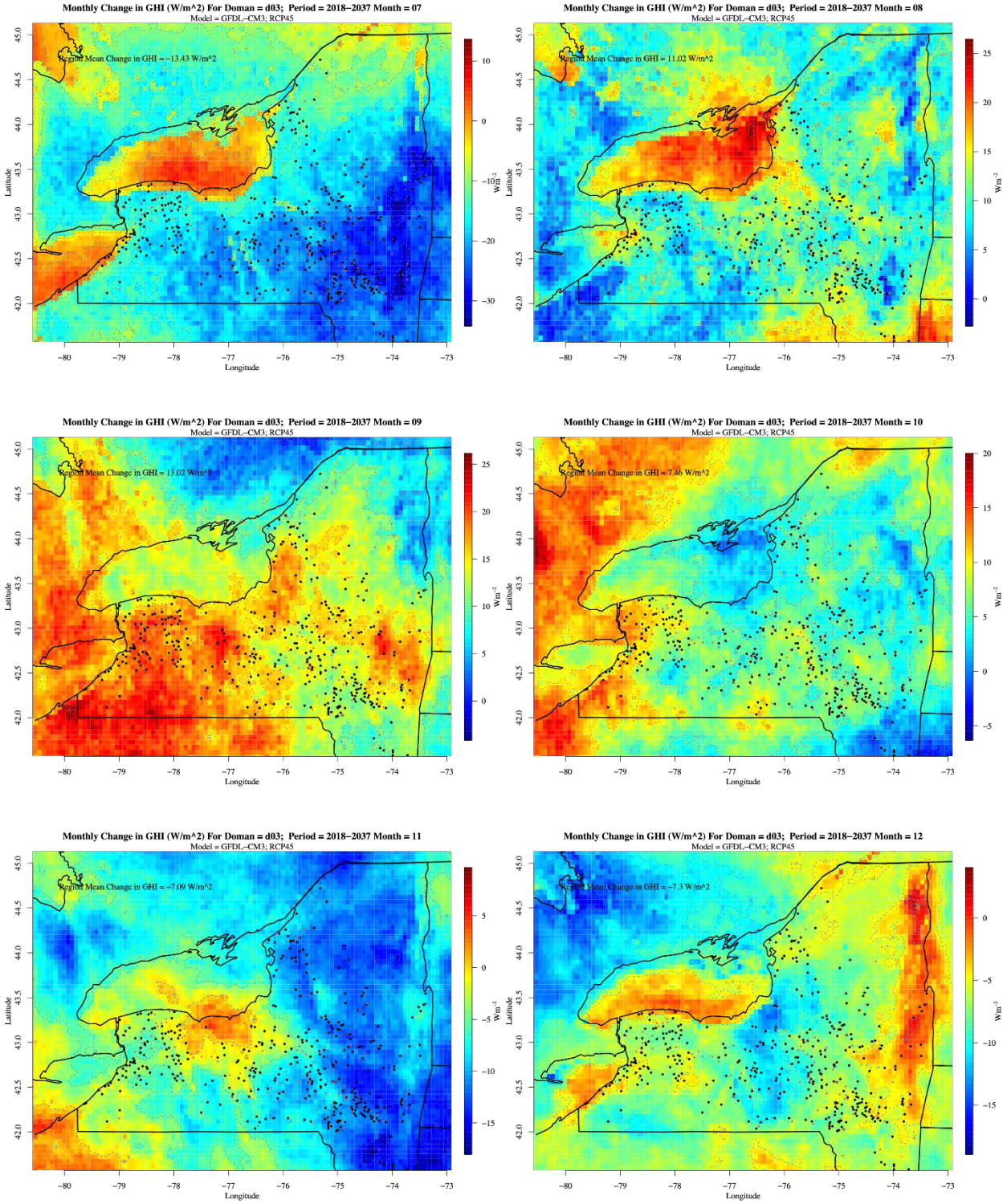

Figure C-3. Same as Figure C-1 except for RCP8.5

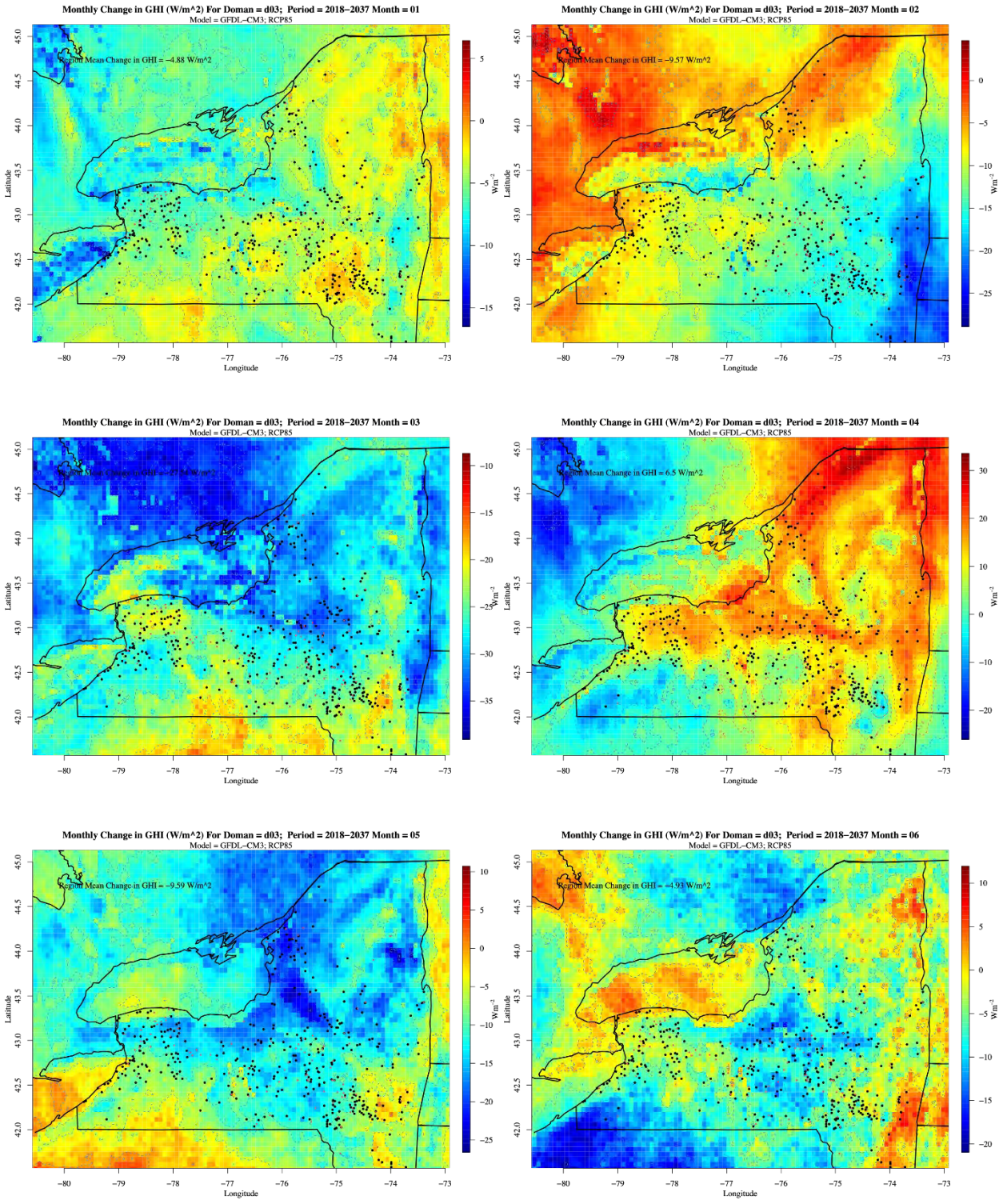

Figure C-4. Same as Figure C-2 except for RCP8.5

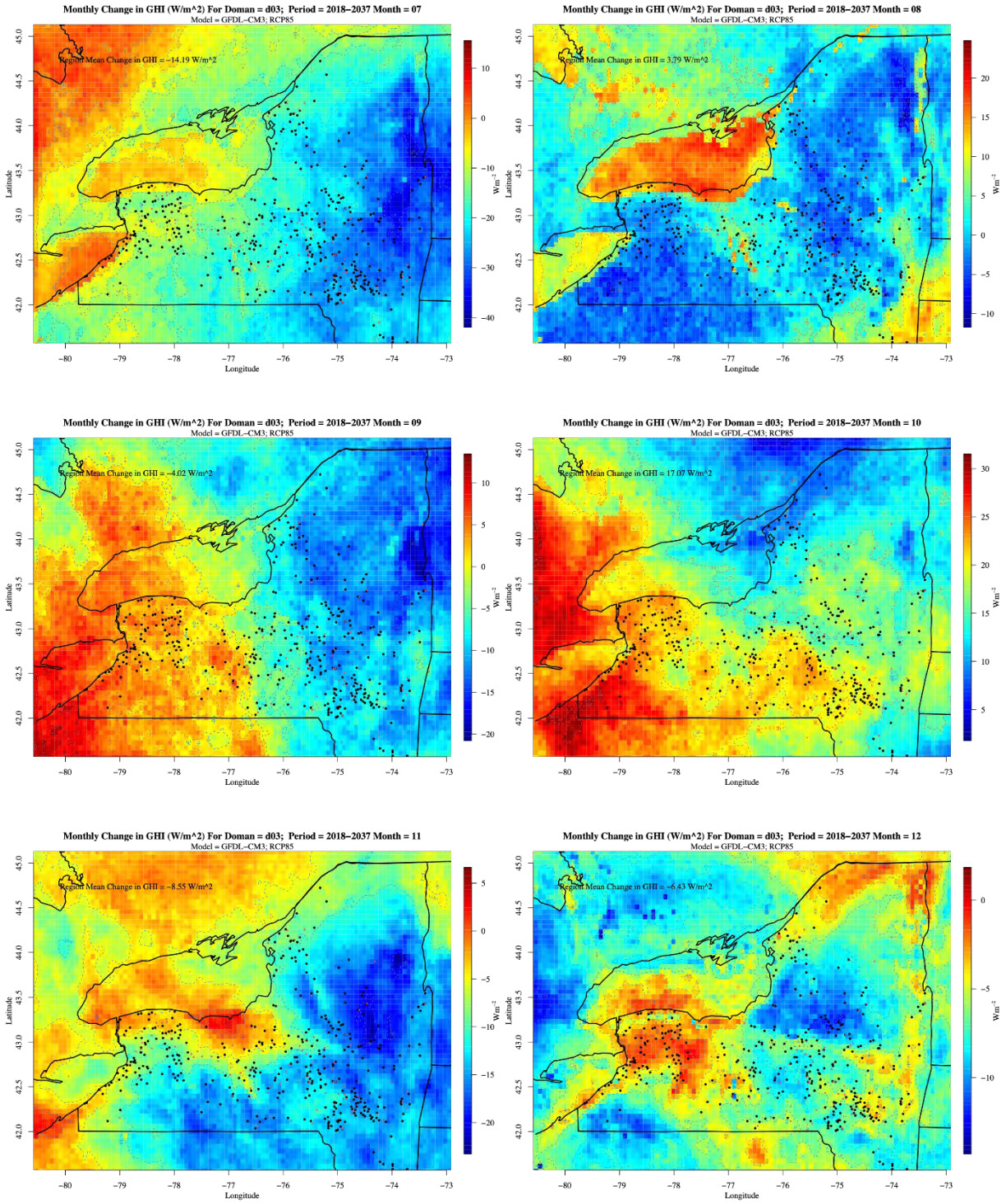

Figure C-5. Same as Figure C-3 except for the mid-future period

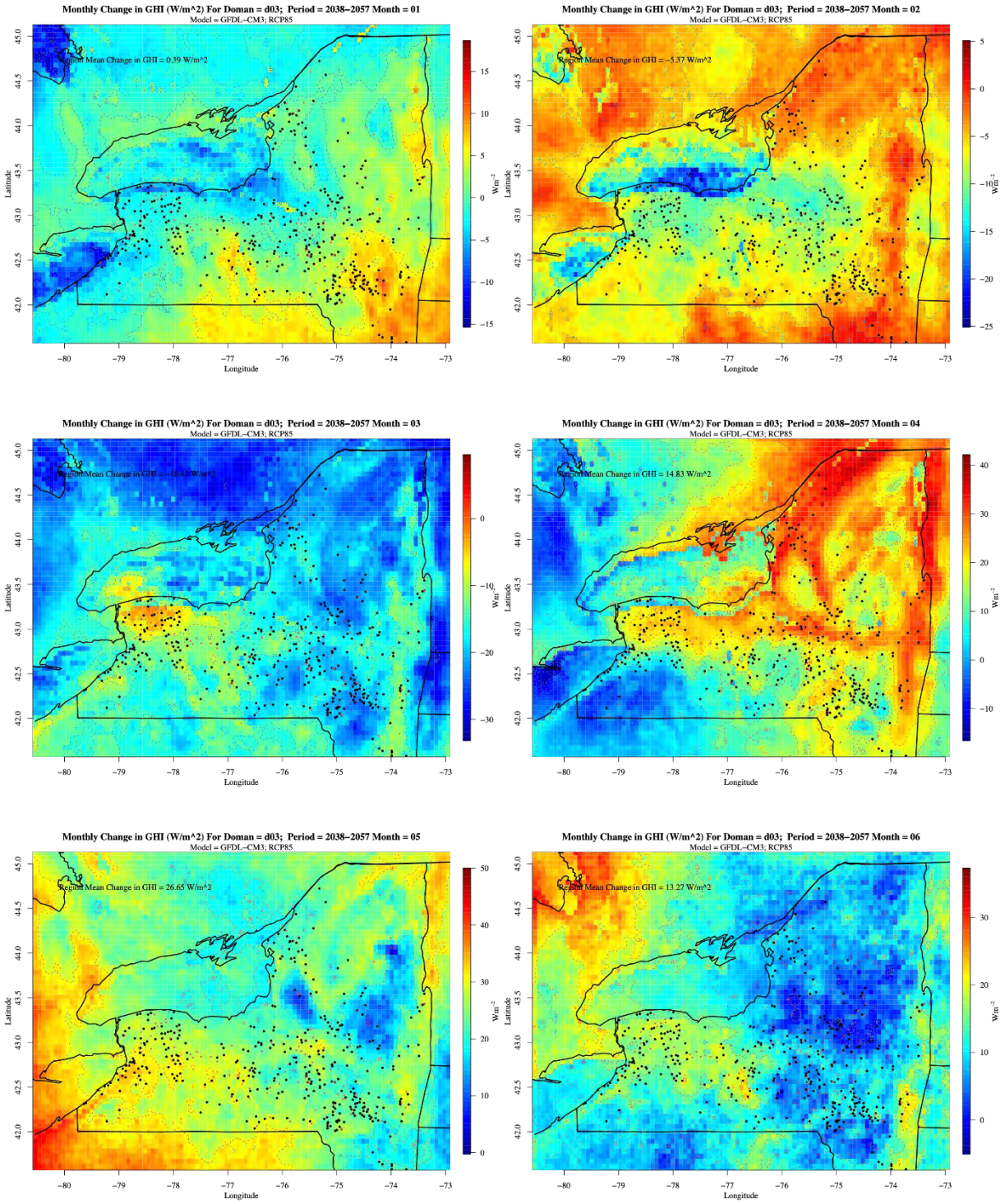

Figure C-6. Same as Figure C-4 except for the mid-future period

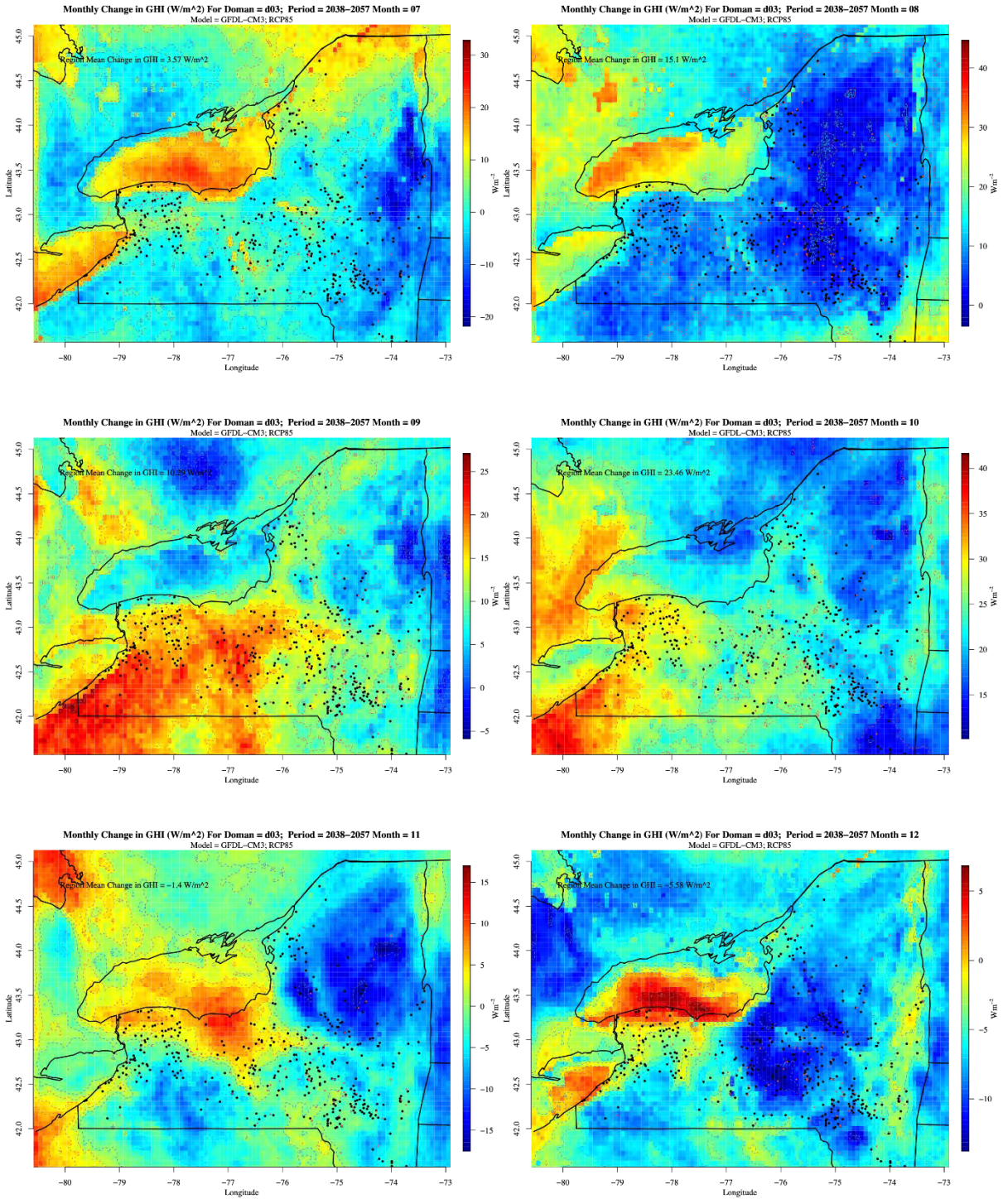

Figure C-7. Same as Figure C-1 except for MIROC5

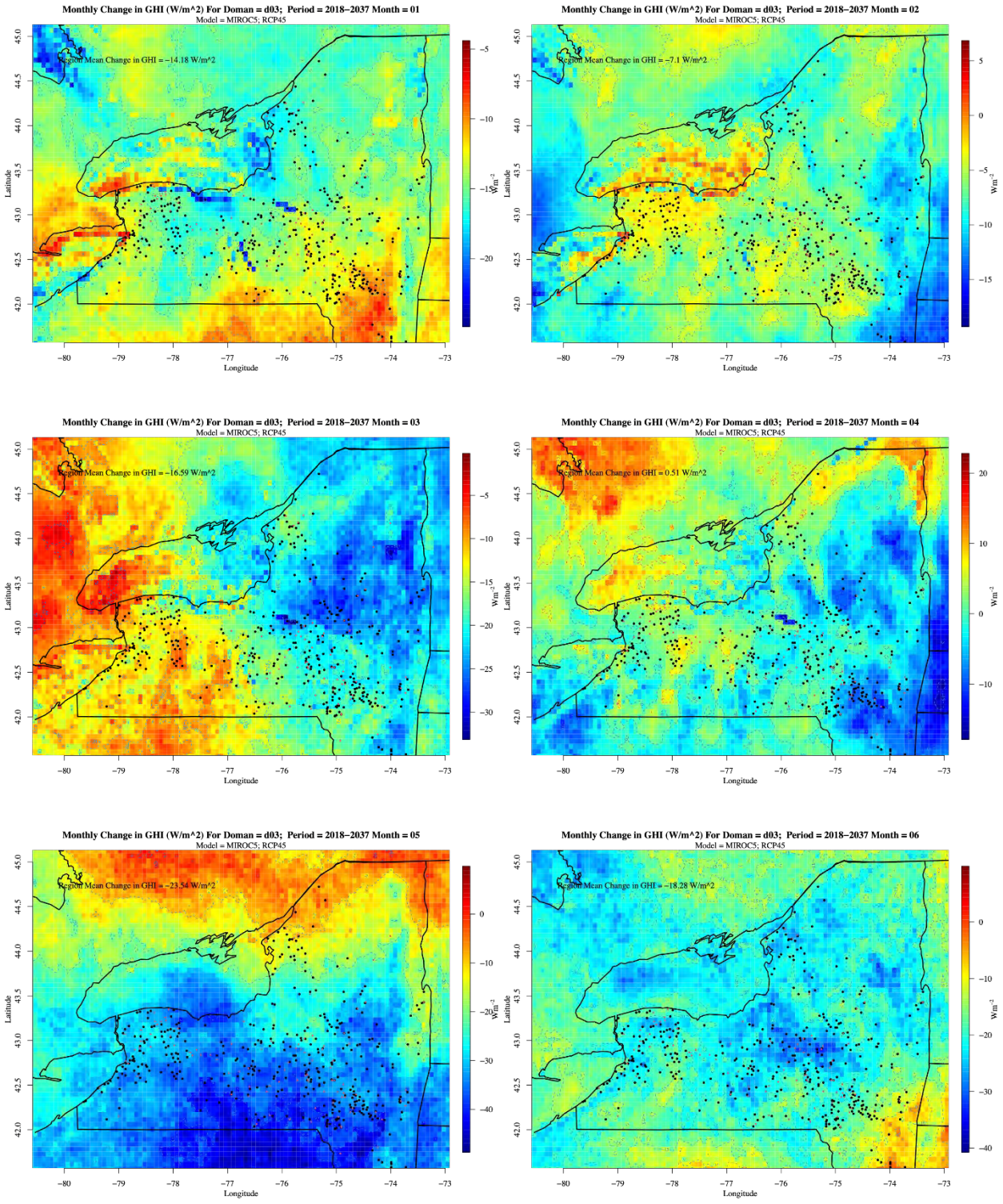

Figure C-8. Same as Figure C-2 except for MIROC5

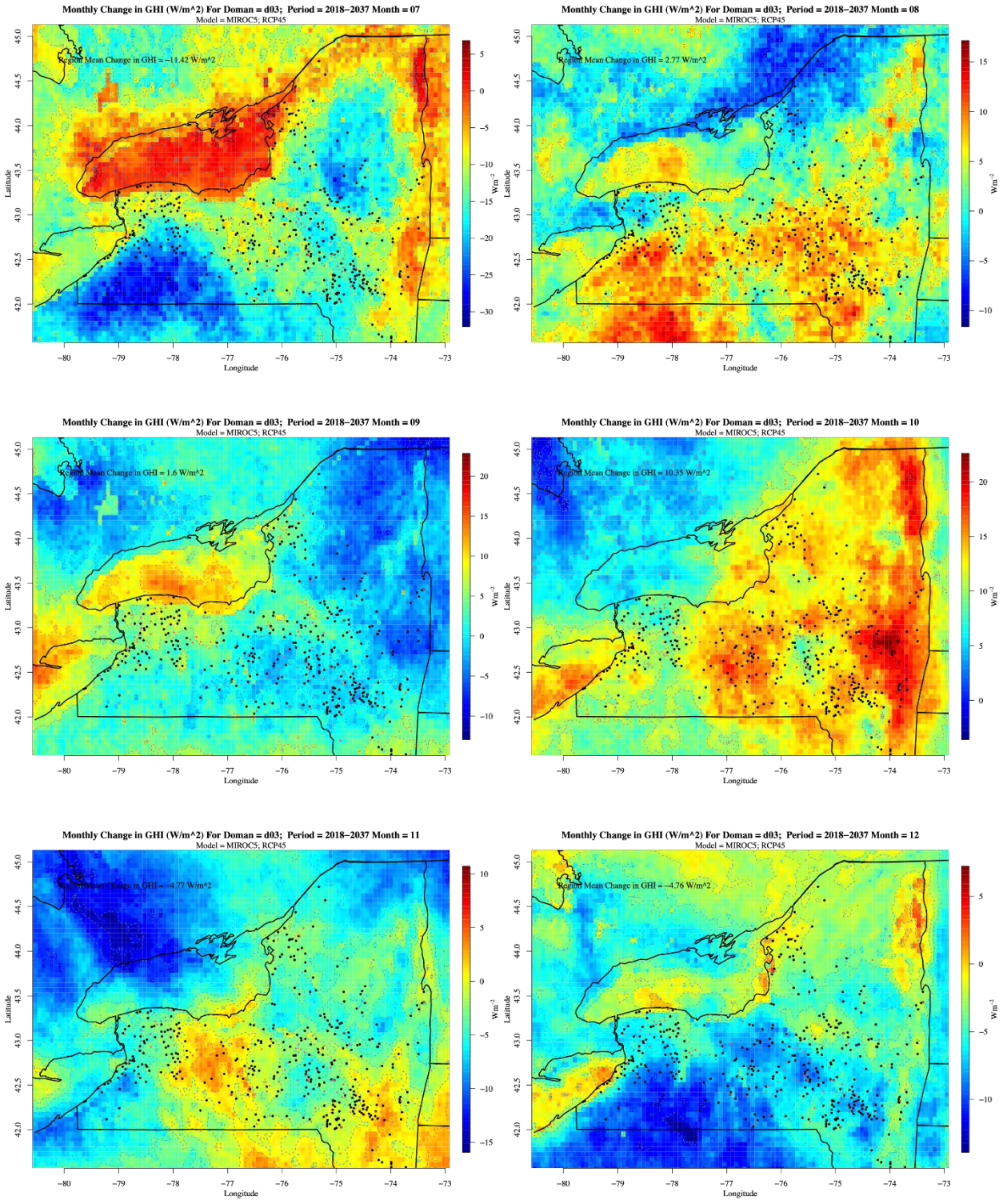

Figure C-9. Same as Figure C-1 except for MIROC5 and mid-future period

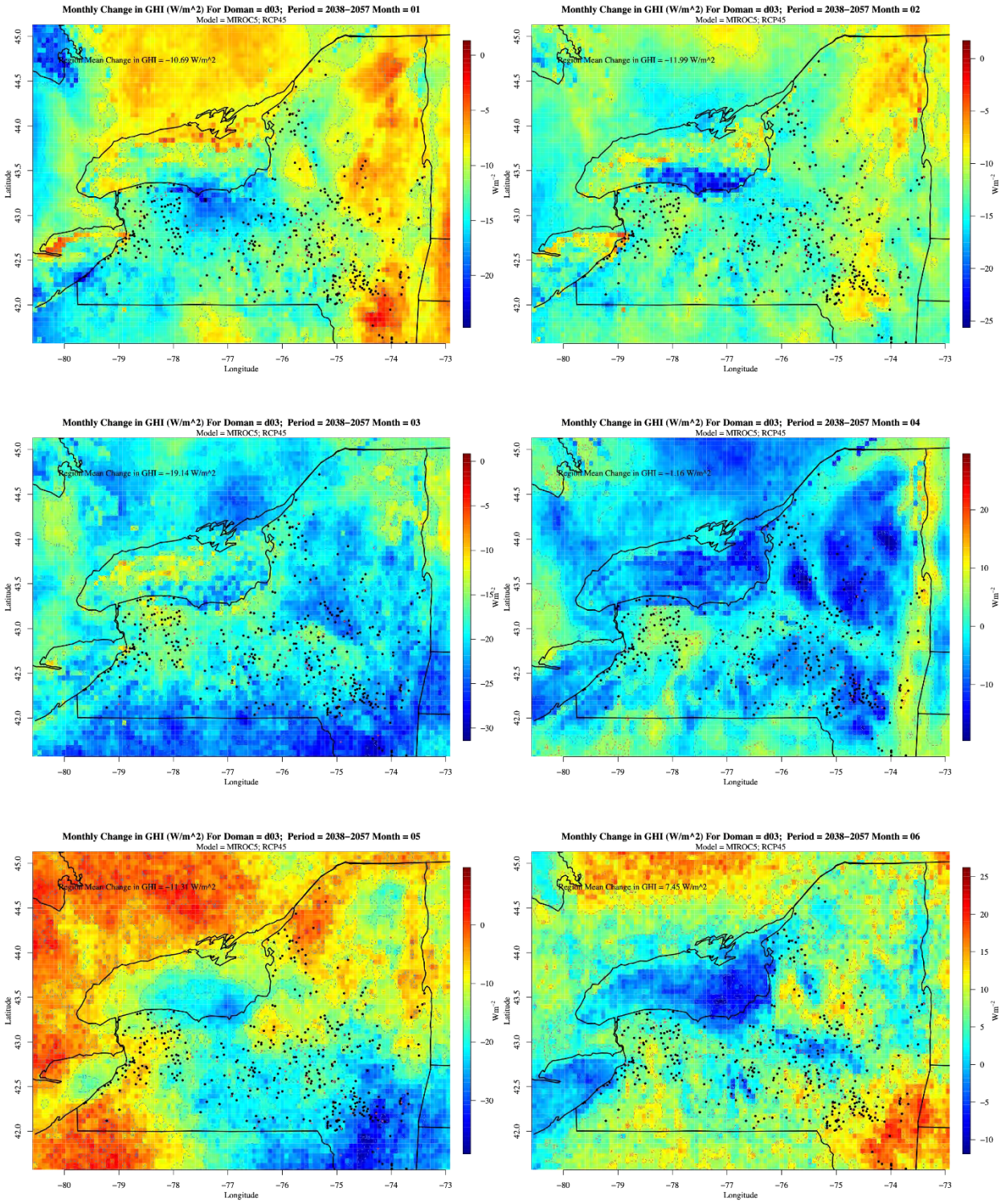

Figure C-10. Same as Figure C-2 except for MIROC5 and mid-future period

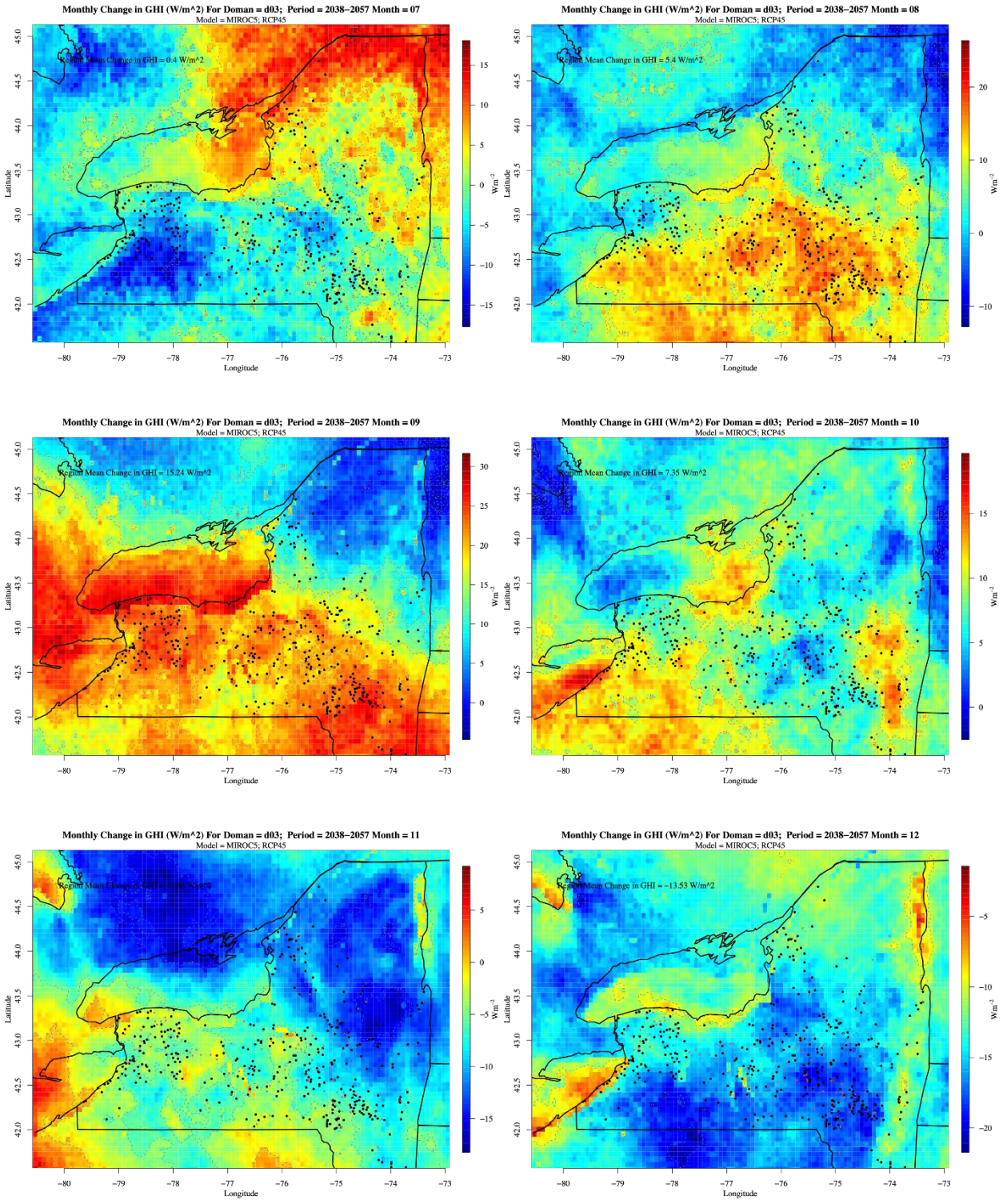

Figure C-11. Same as Figure C-7 except for RCP8.5

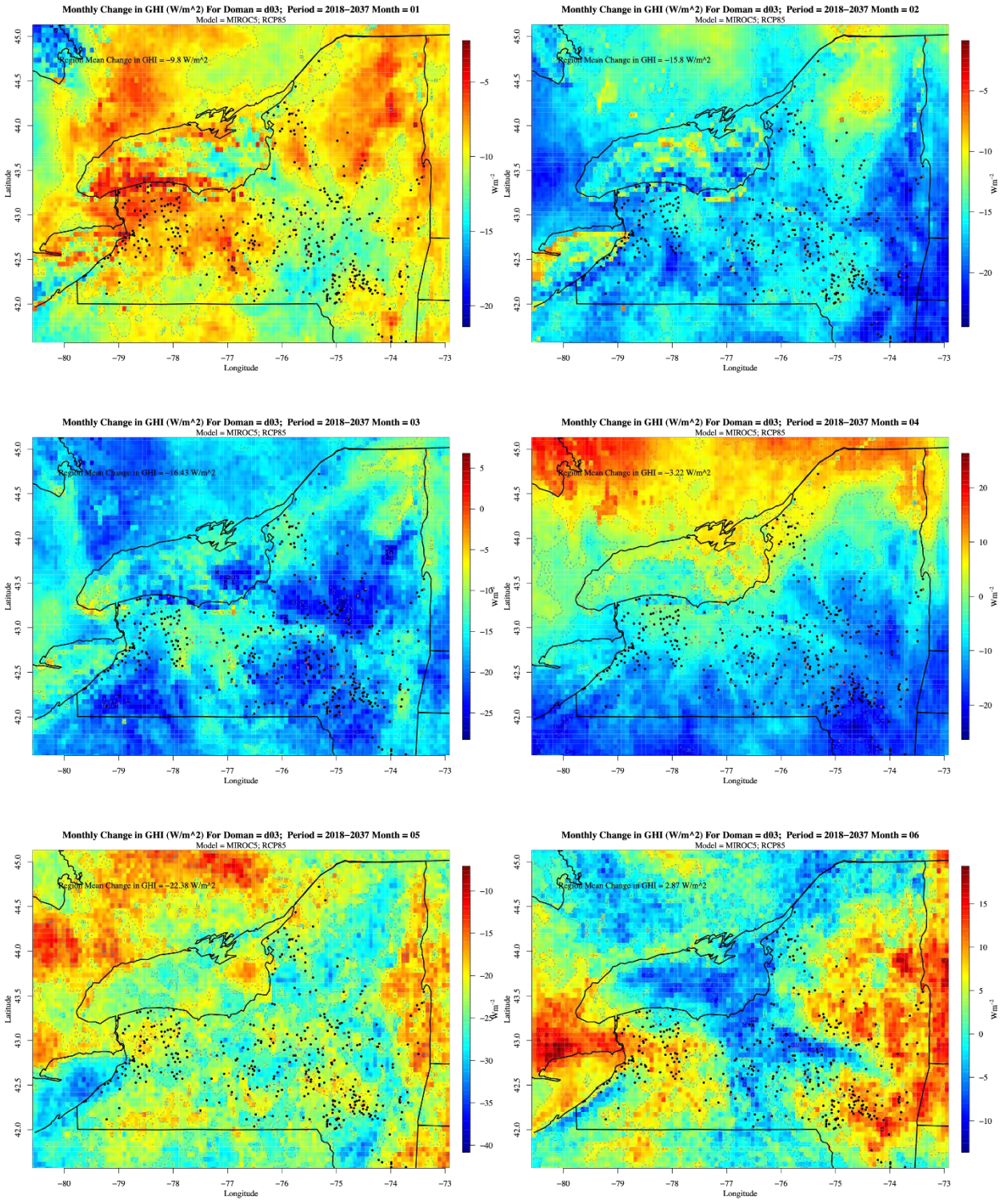

Figure C-12. Same as Figure C-8 except for RCP8.5

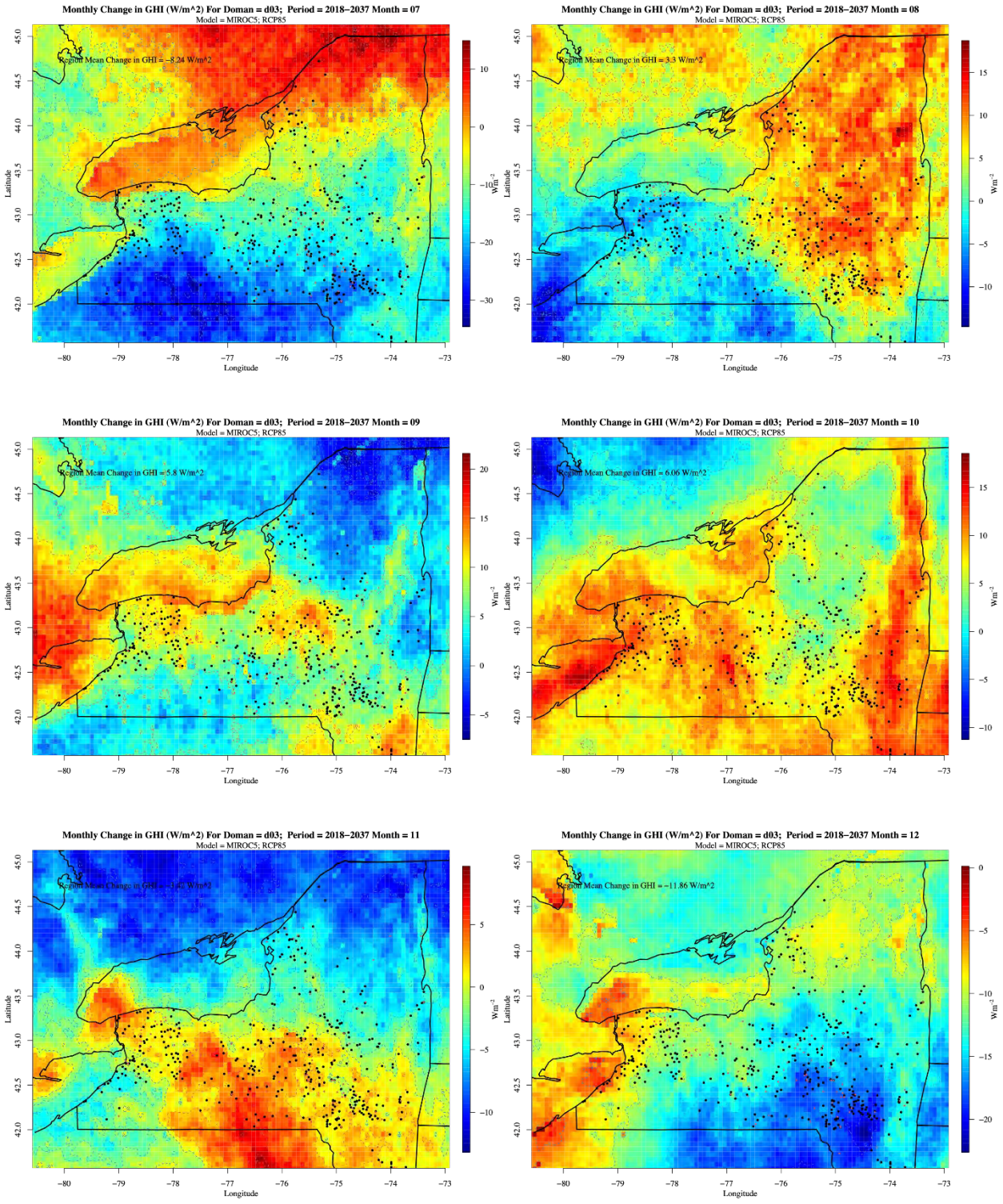

Figure C-13. Same as Figure C-9 except for RCP8.5

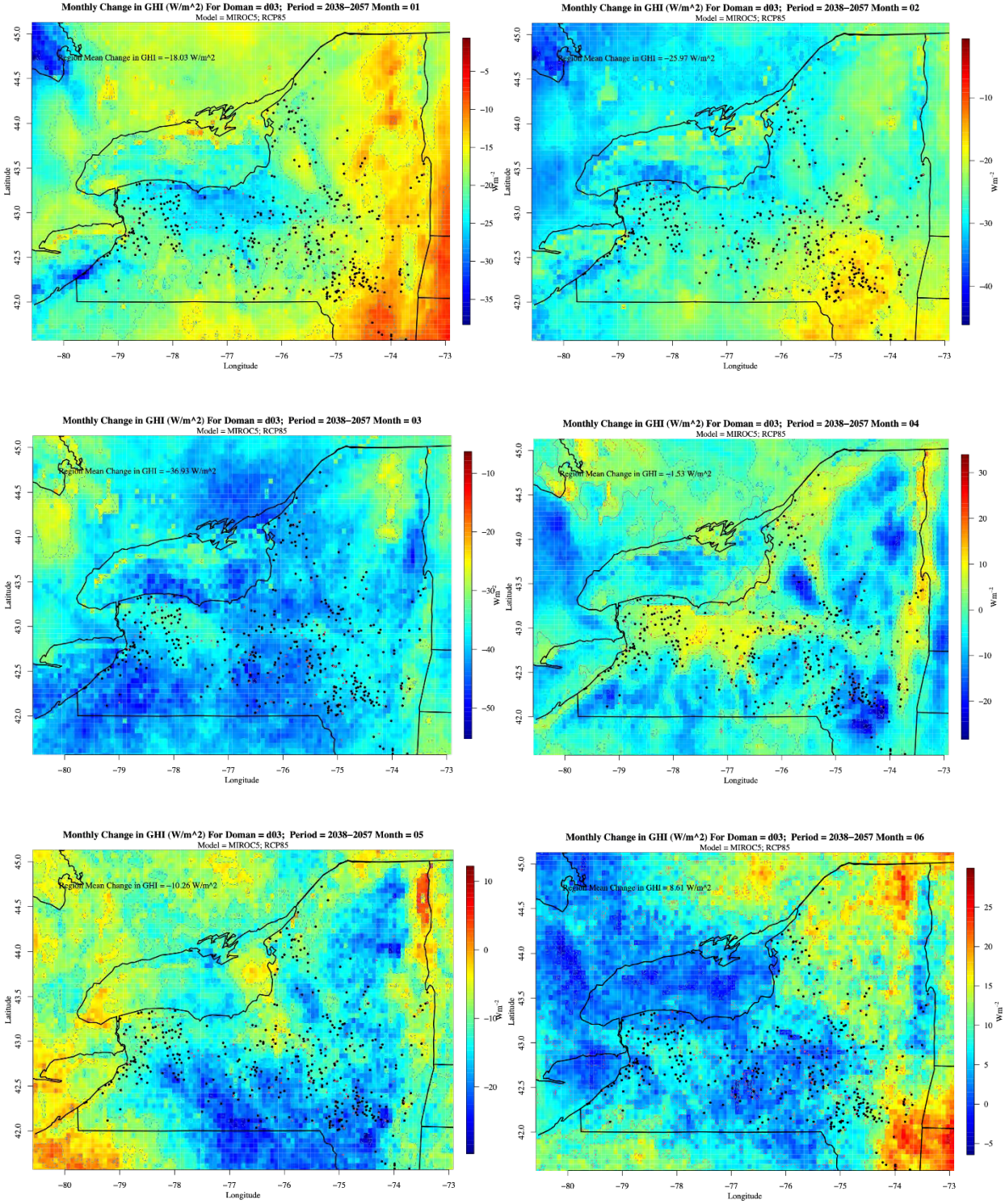

Figure C-14. Same as Figure C-10 except for RCP8.5

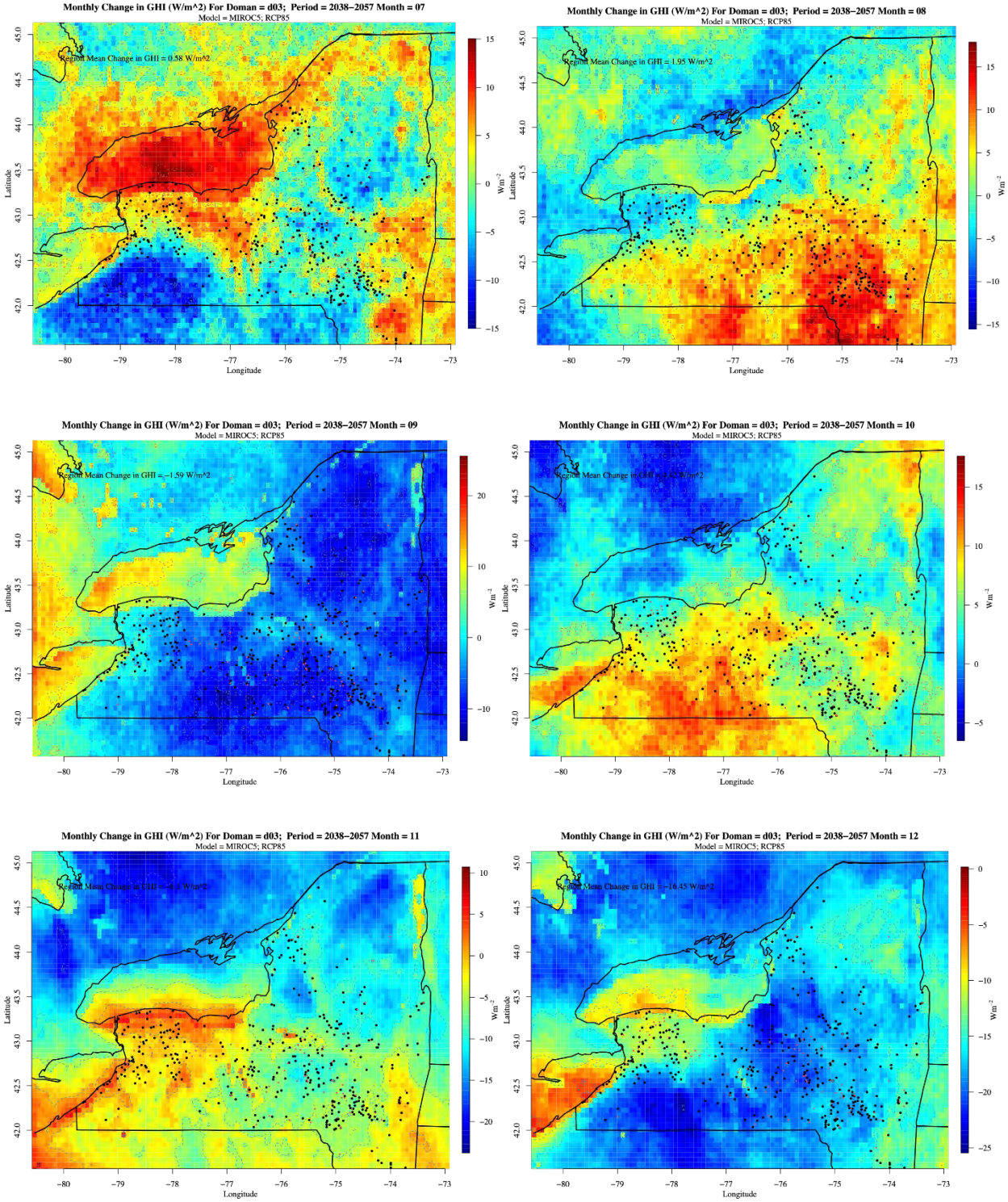

Figure C-15. Same as Figure C-7 except for NCAR-CCSM4

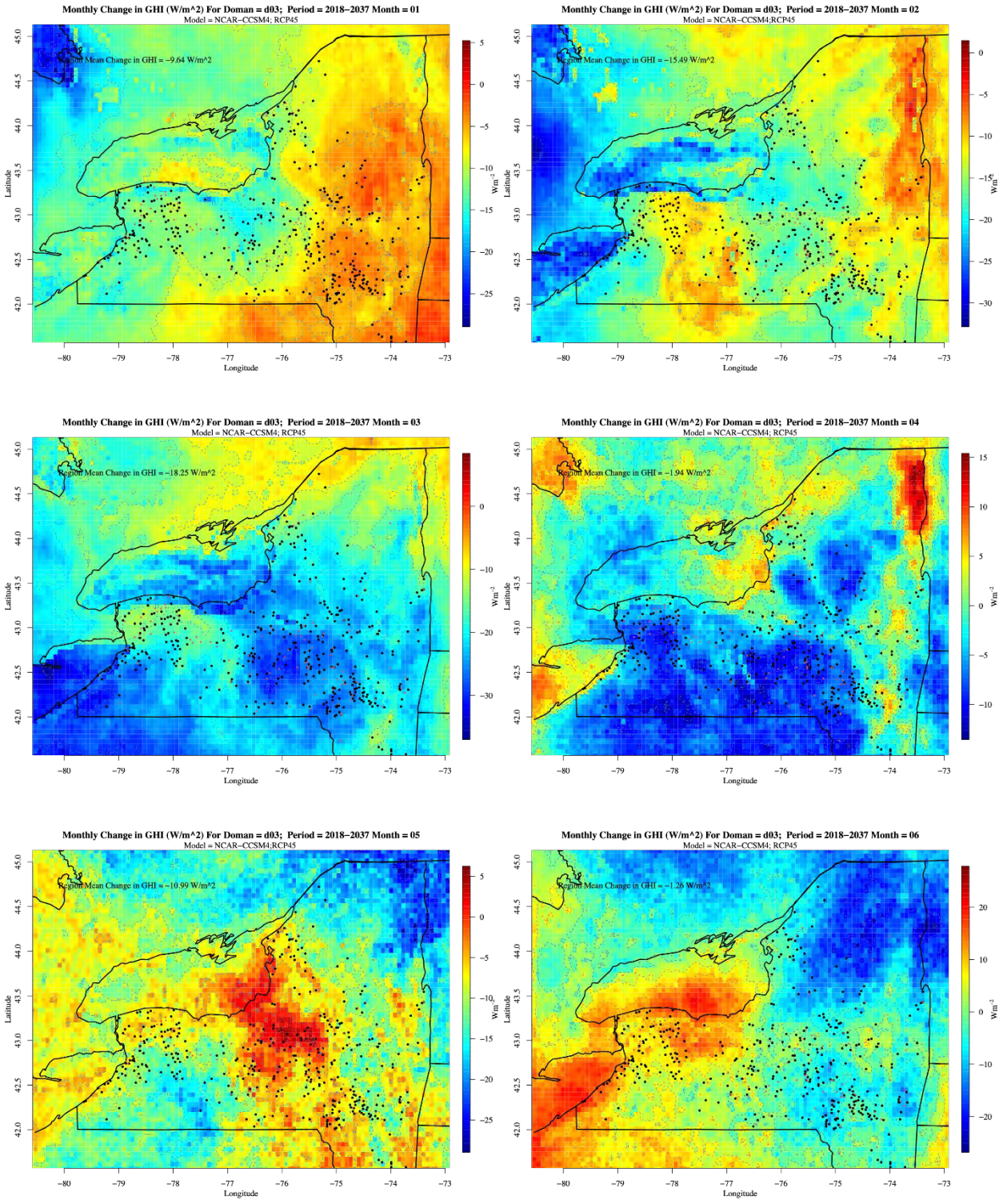

Figure C-16. Same as Figure C-8 except for NCAR-CCSM4

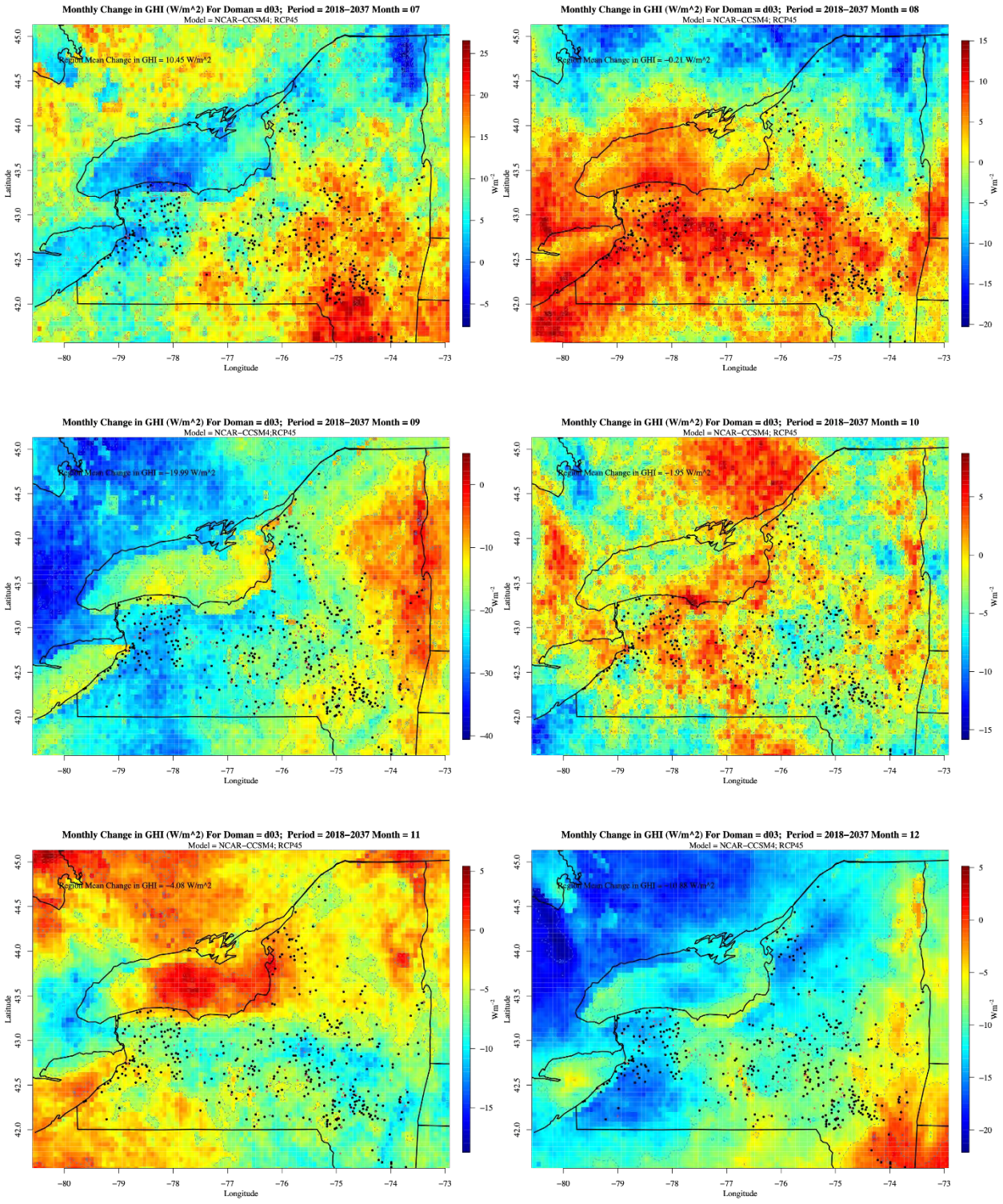

Figure C-17. Same as Figure C-9 except for NCAR-CCSM4

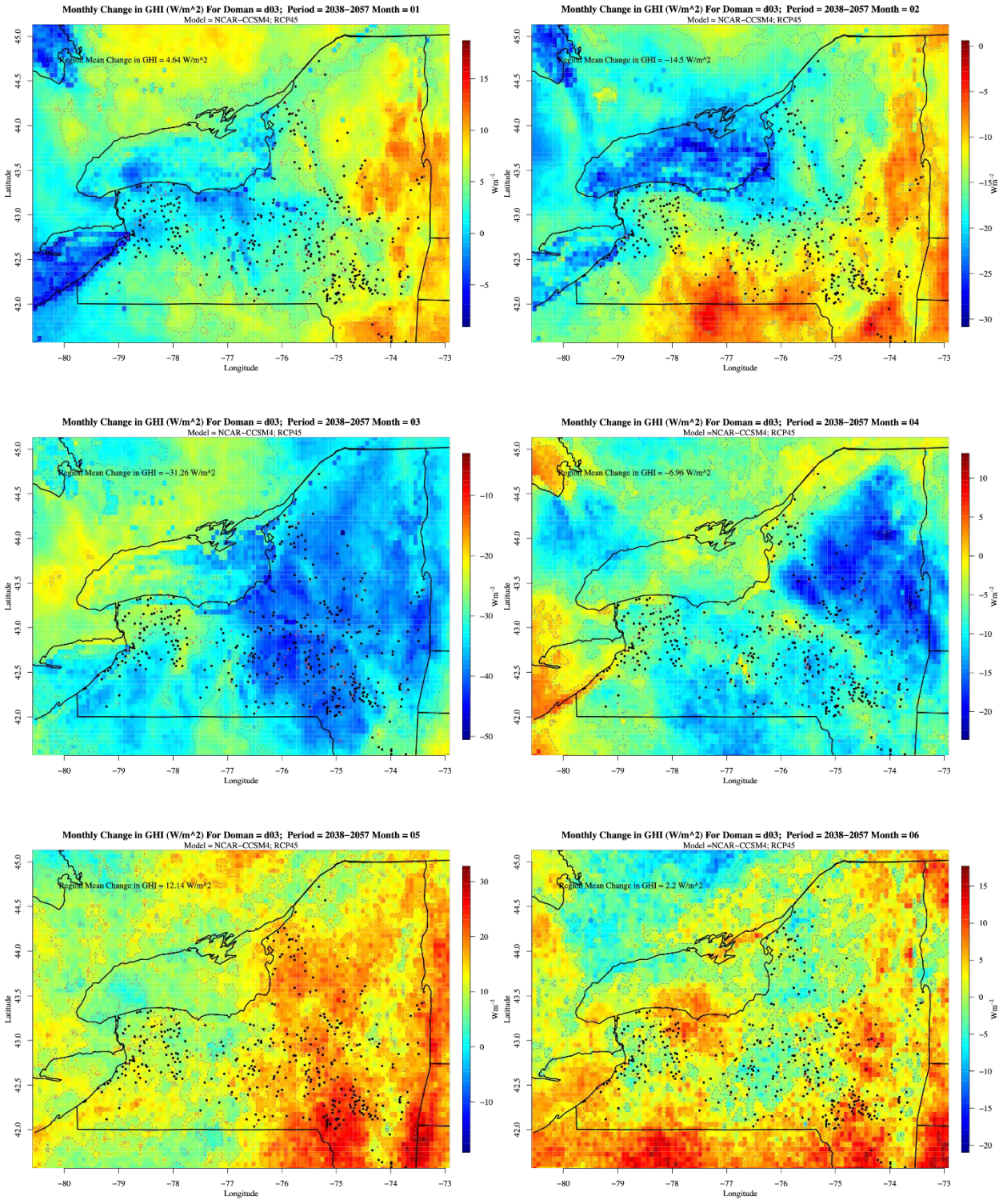

Figure C-18. Same as Figure C-10 except for NCAR-CCSM4

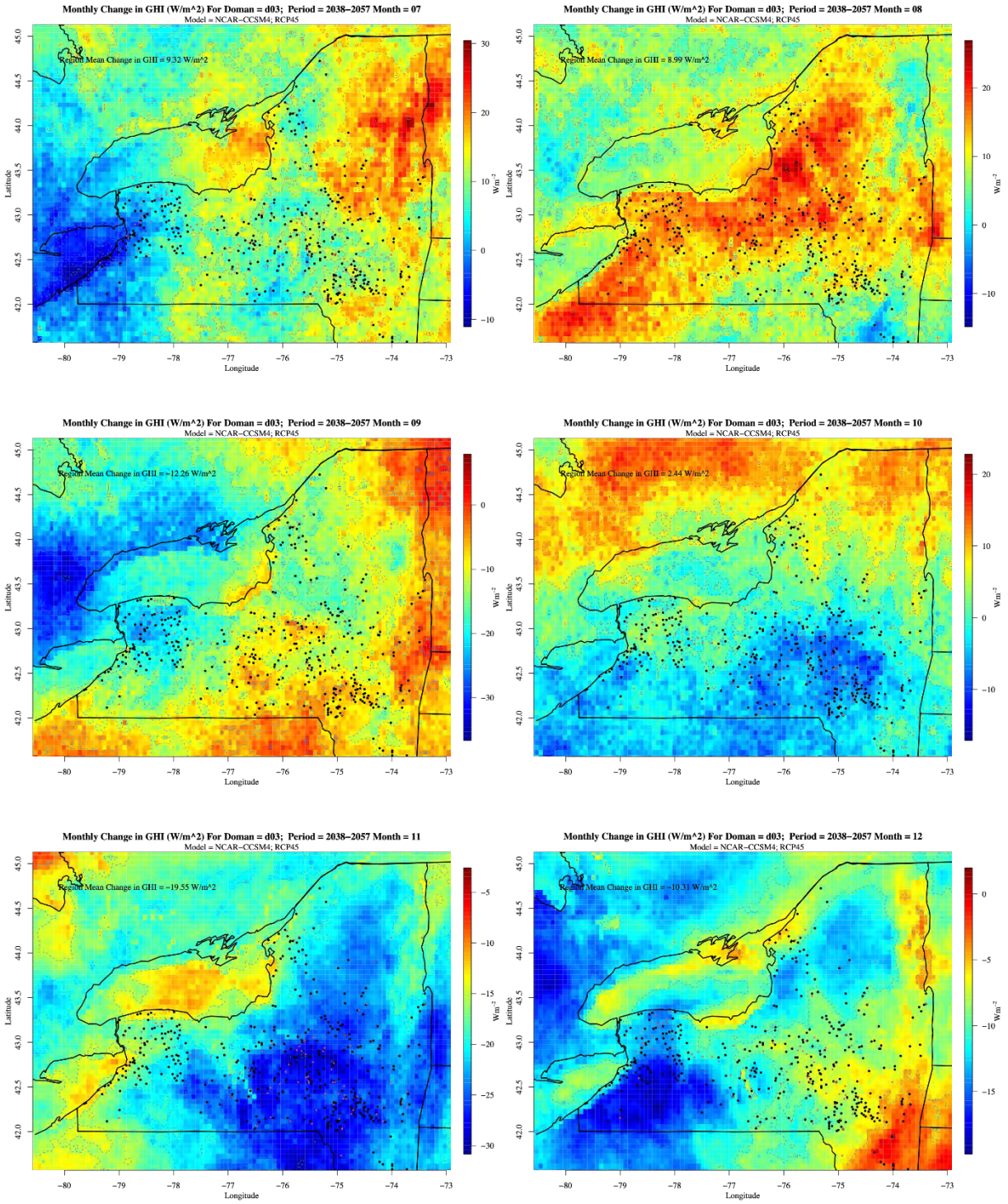

Figure C-19. Same as Figure C-11 except for NCAR-CCSM4

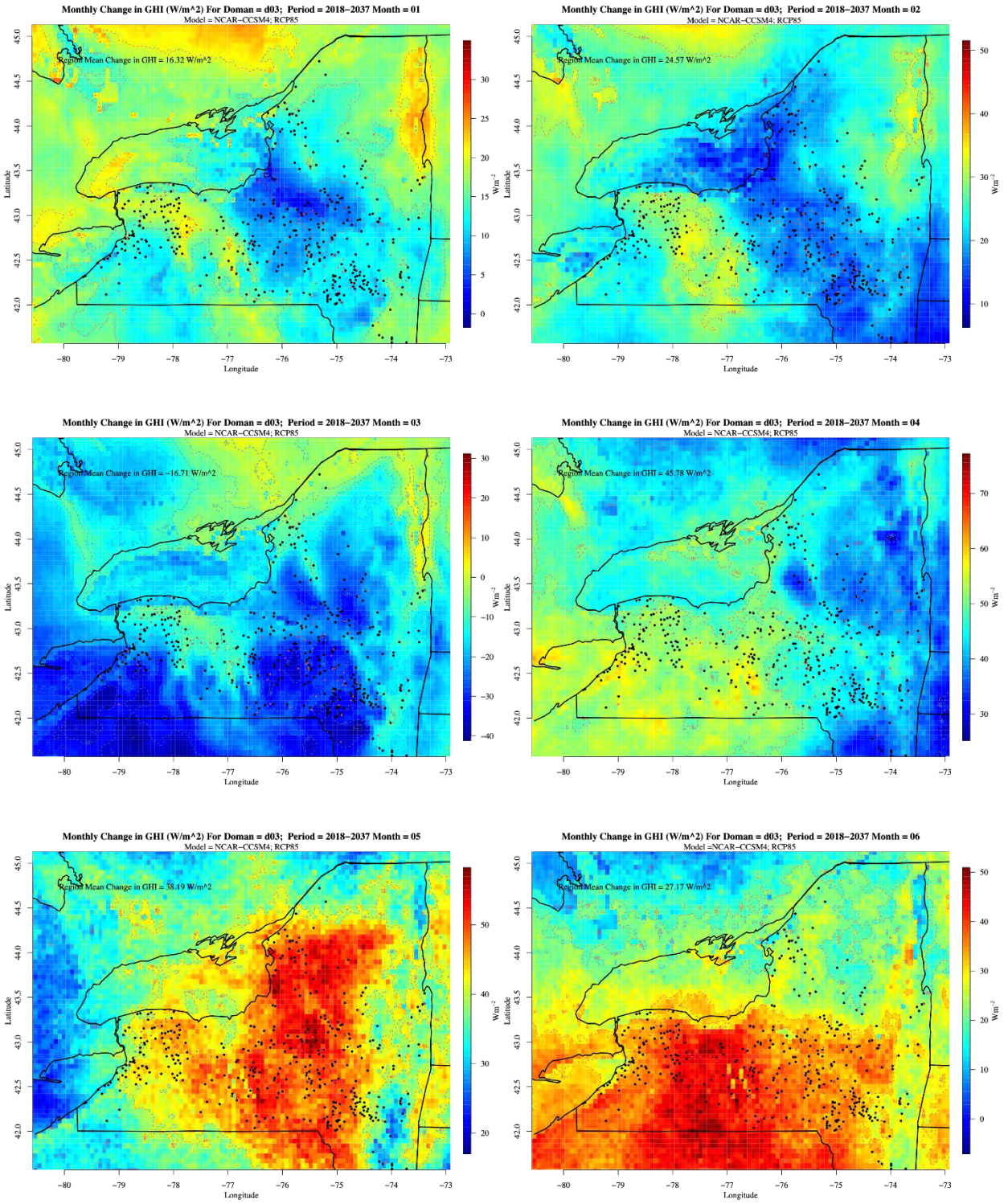

Figure C-20. Same as Figure C-12 except for NCAR-CCSM4

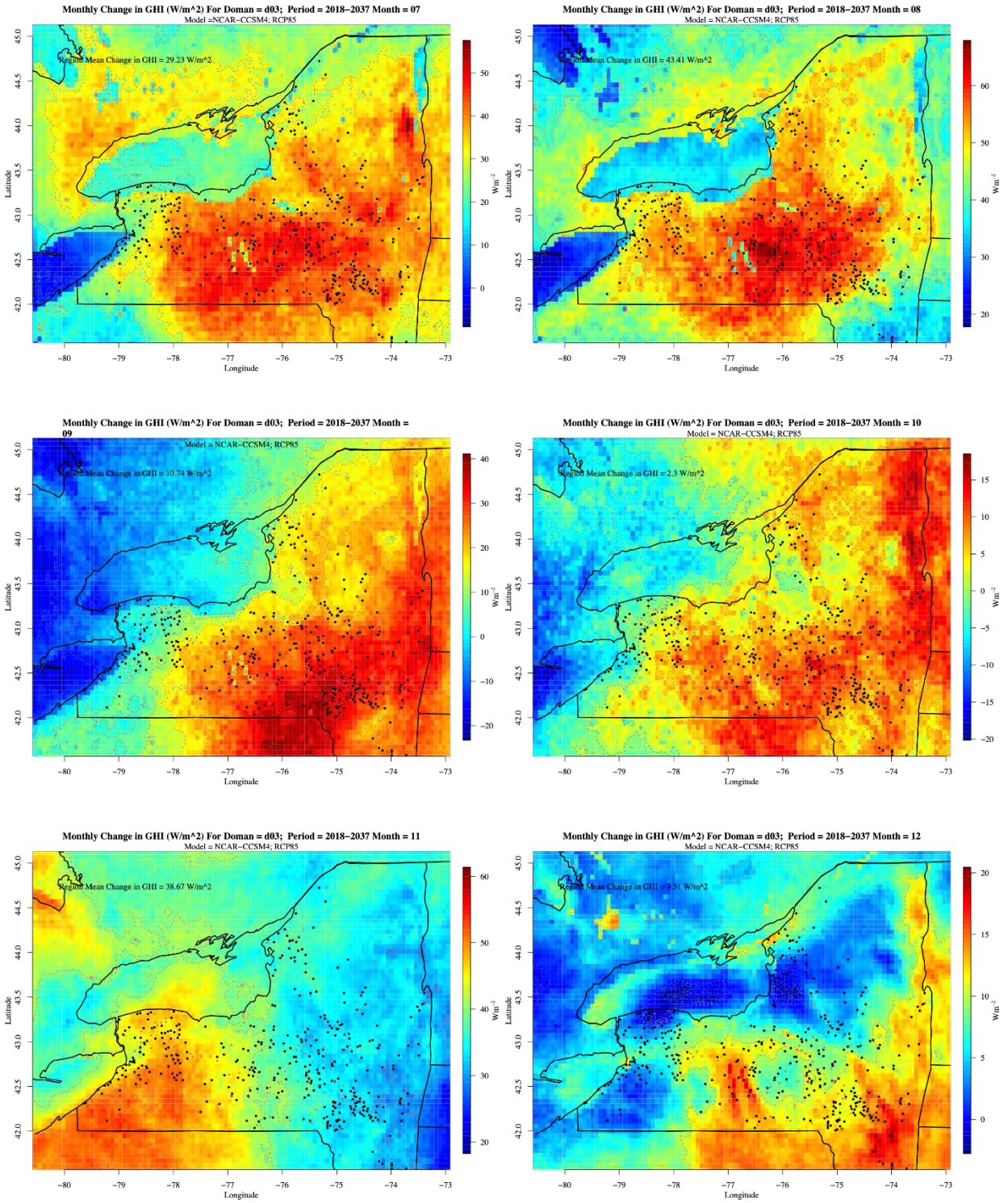

Appendix D. Model monthly changes in precipitation: d03 domain

Figure D-1. Domain d03 monthly changes in precipitation (mm day^{-1}) under RCP4.5 scenario for near-future period

Upper left: January; upper right: February; middle left: March; middle right: April; lower left: May; lower right: June.

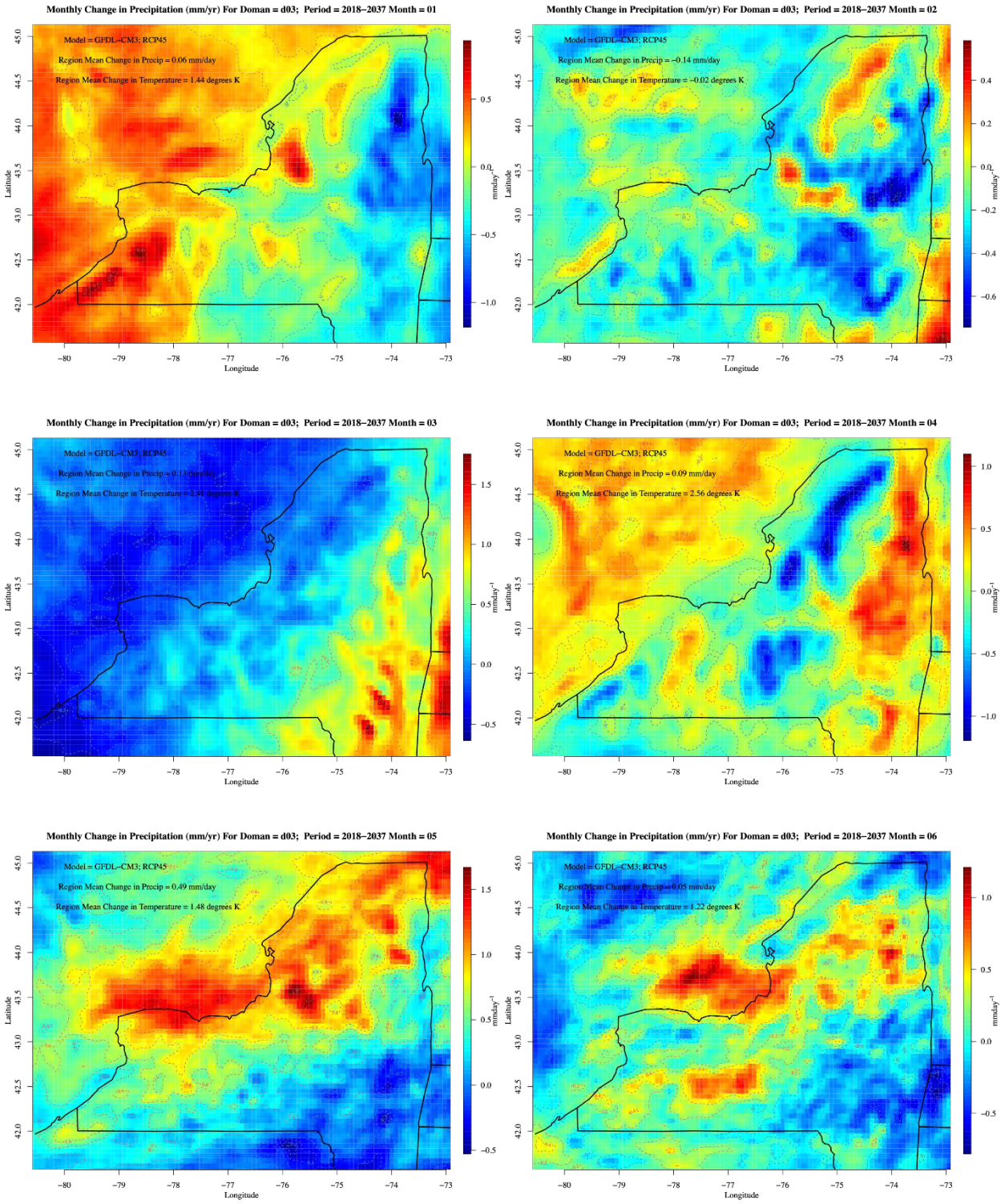

Figure D-2. Same as Figure D-1 except Upper left: July; upper right: August; middle left: September; middle right: October; lower left: November; lower right: December

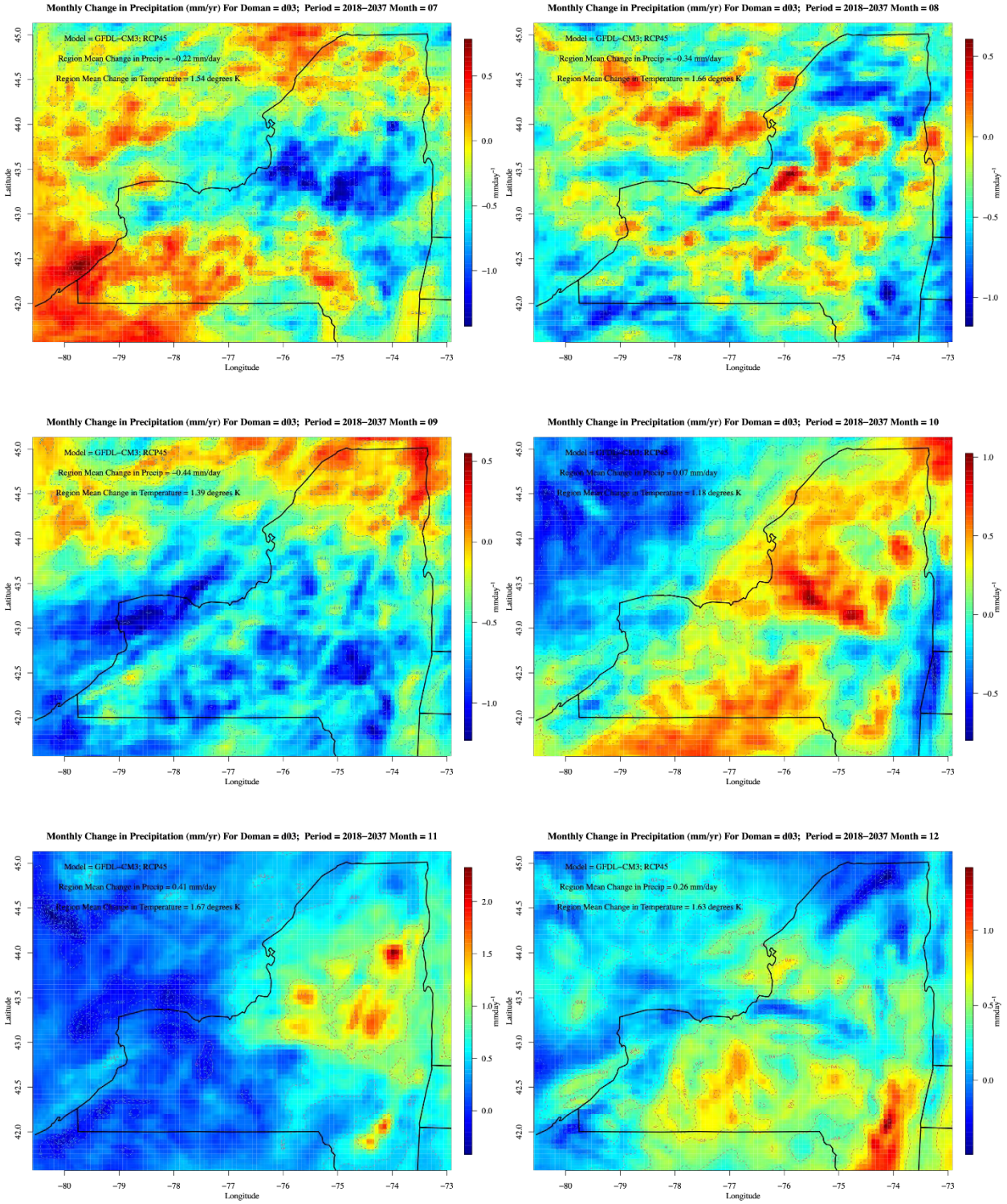

Figure D-3. Same as Figure D-1 except for mid-future period

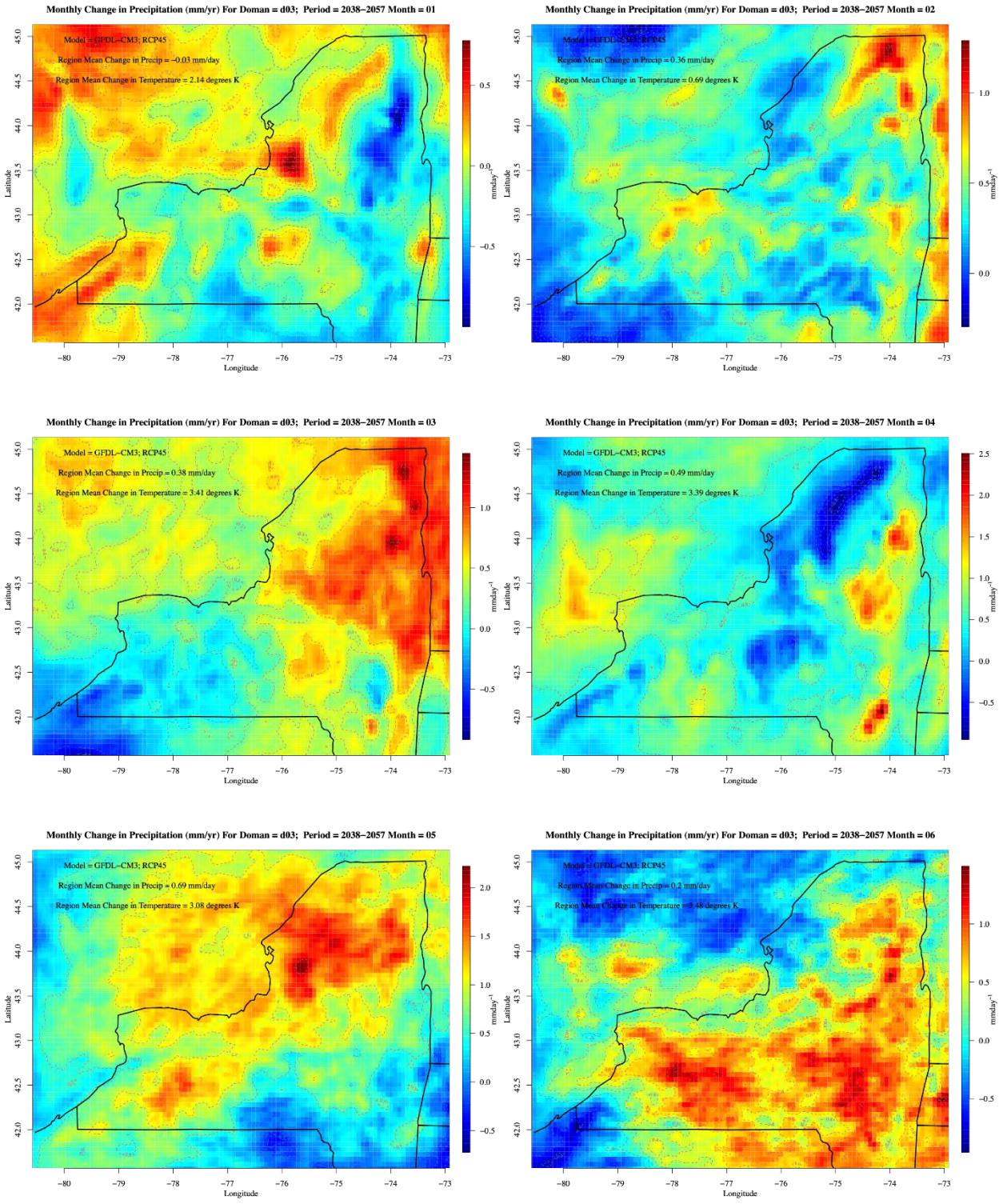

Figure D-4. Same as Figure D-2 except for mid-future period

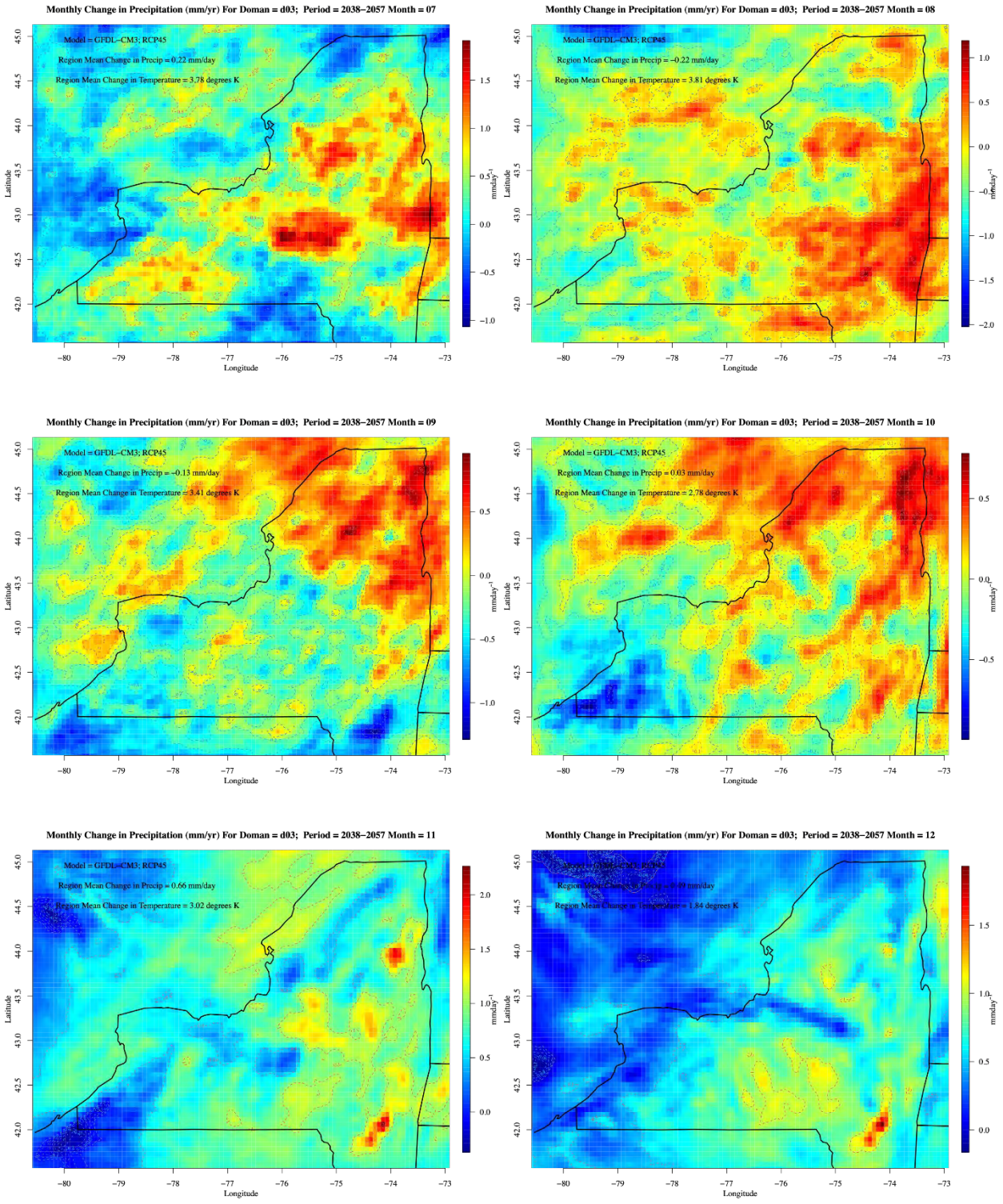

Figure D-5. Same as Figure D-1 except for RCP8.5

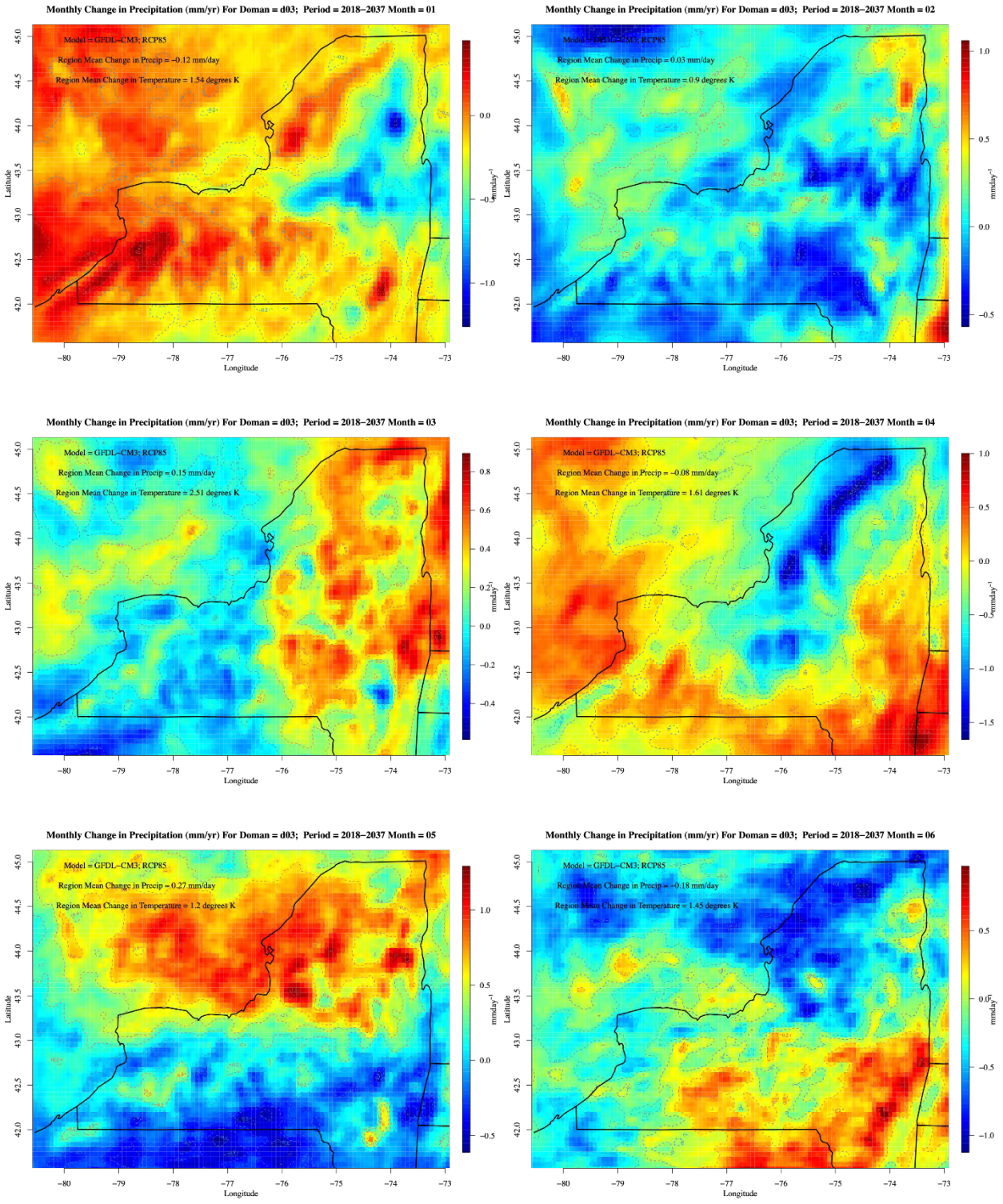

Figure D-6. Same as Figure D-2 except for RCP8.5

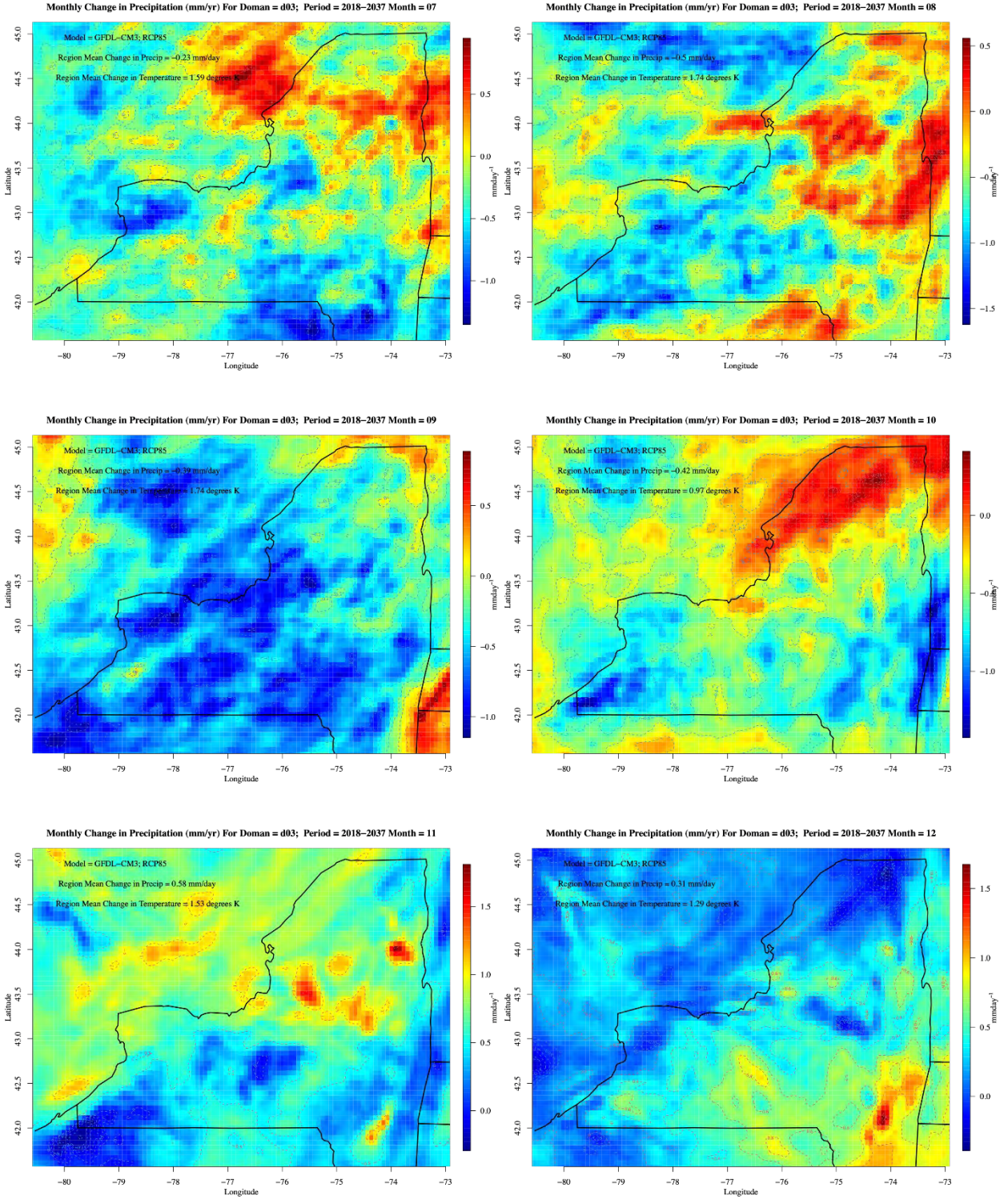

Figure D-7. Same as Figure D-3 except for RCP8.5

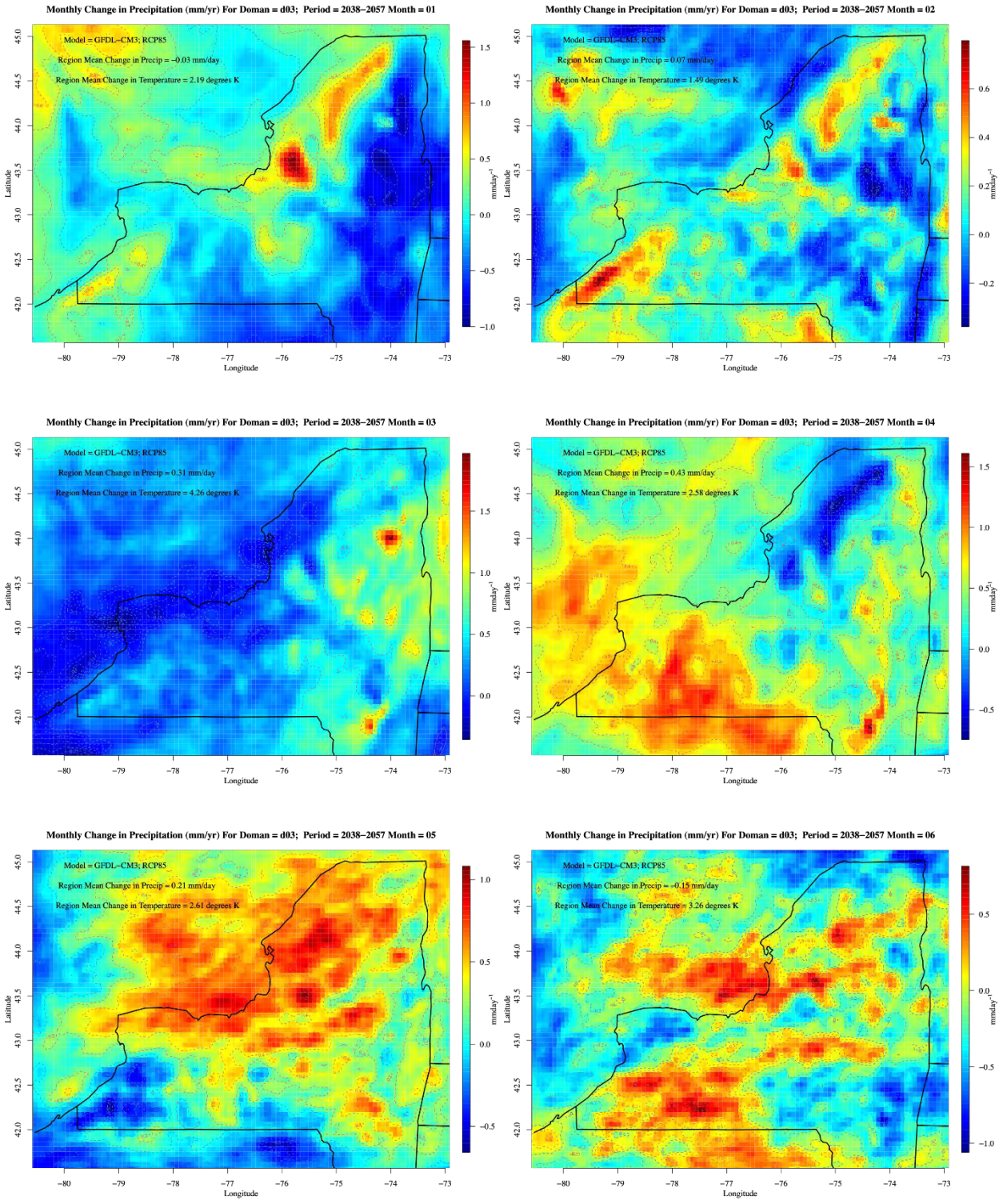

Figure D-8. Same as Figure D-4 except for RCP8.5

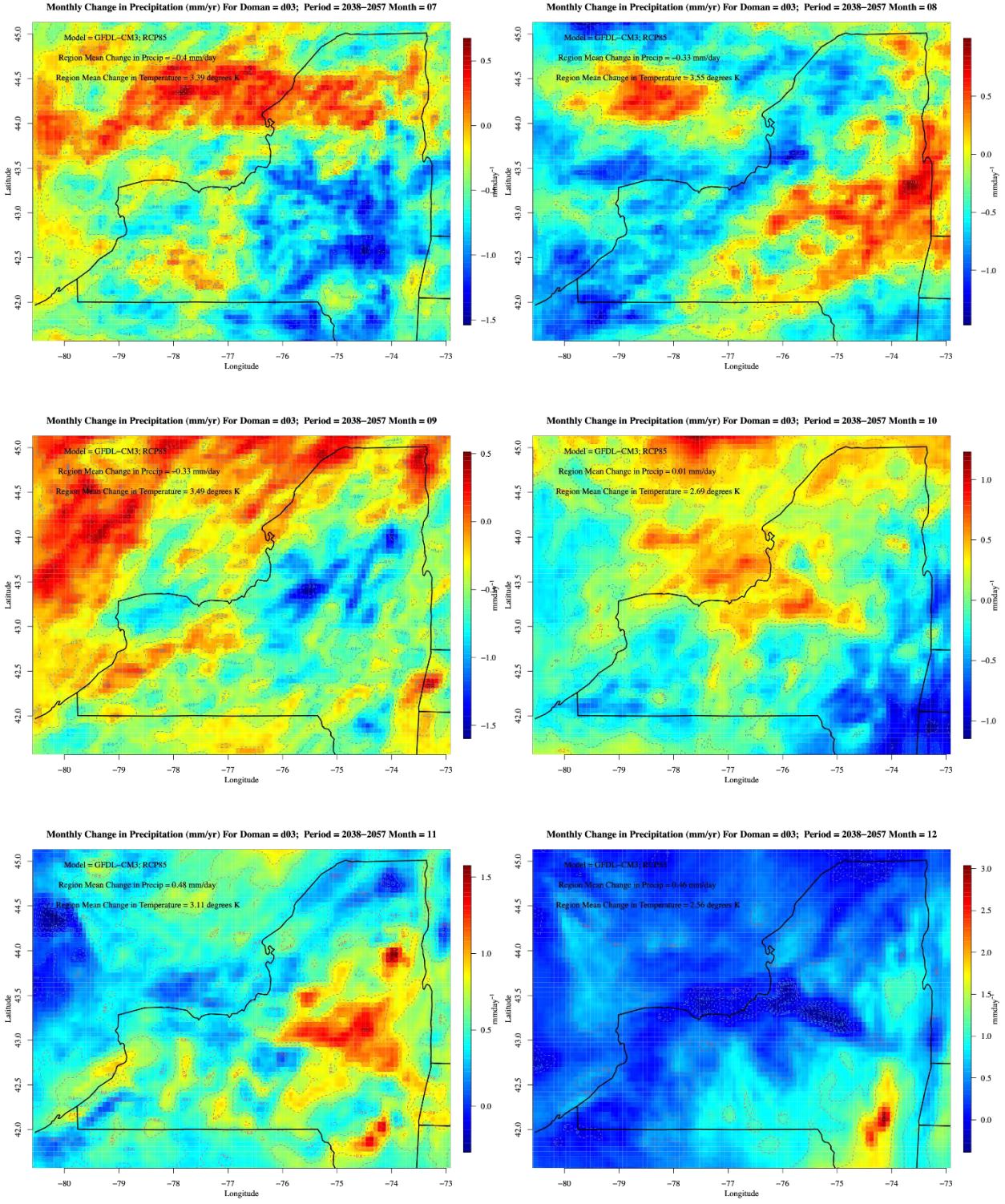

Figure D-9. Same as Figure D-1 except for MIROC5

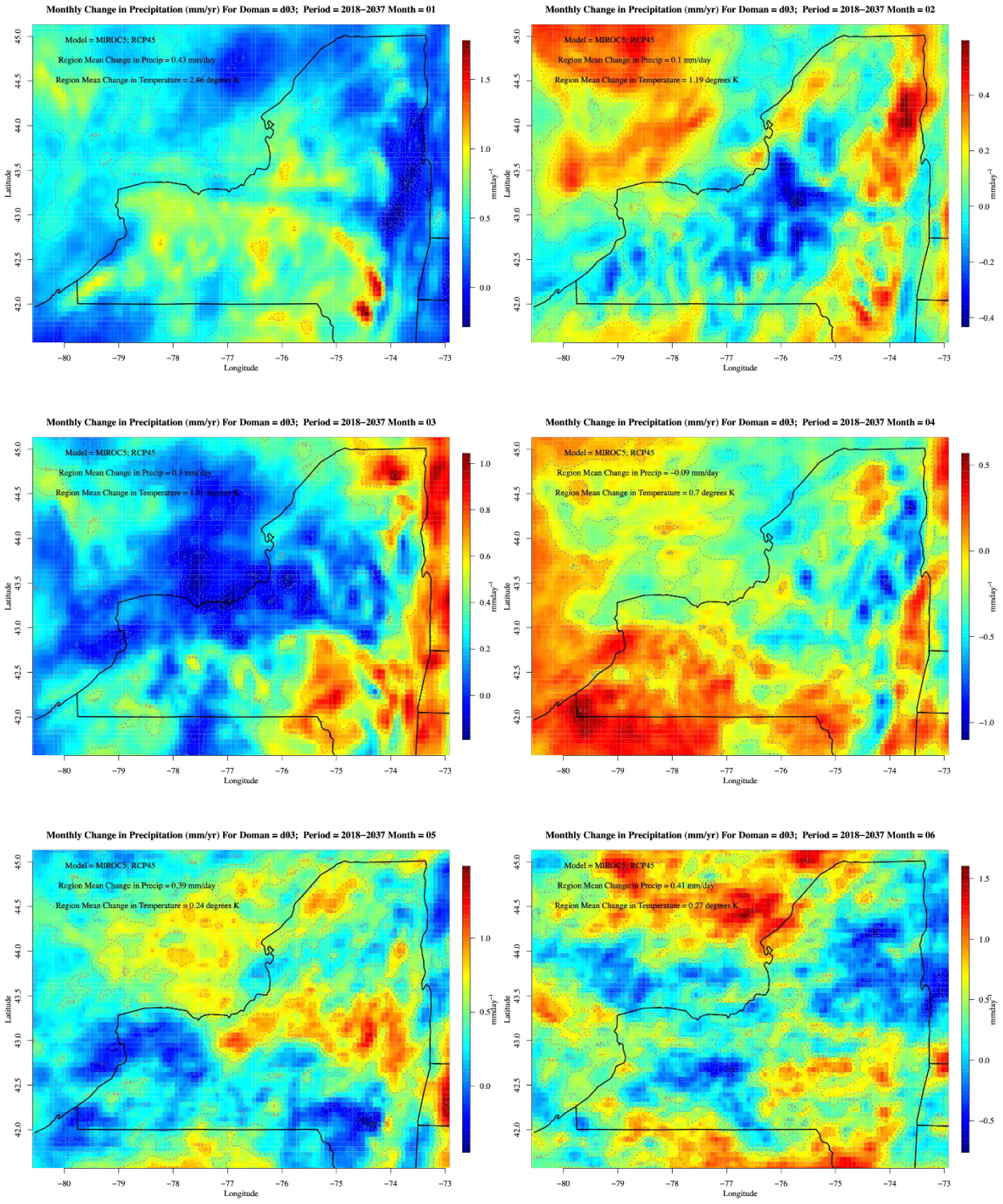

Figure D-10. Same as Figure D-2 except for MIROC5

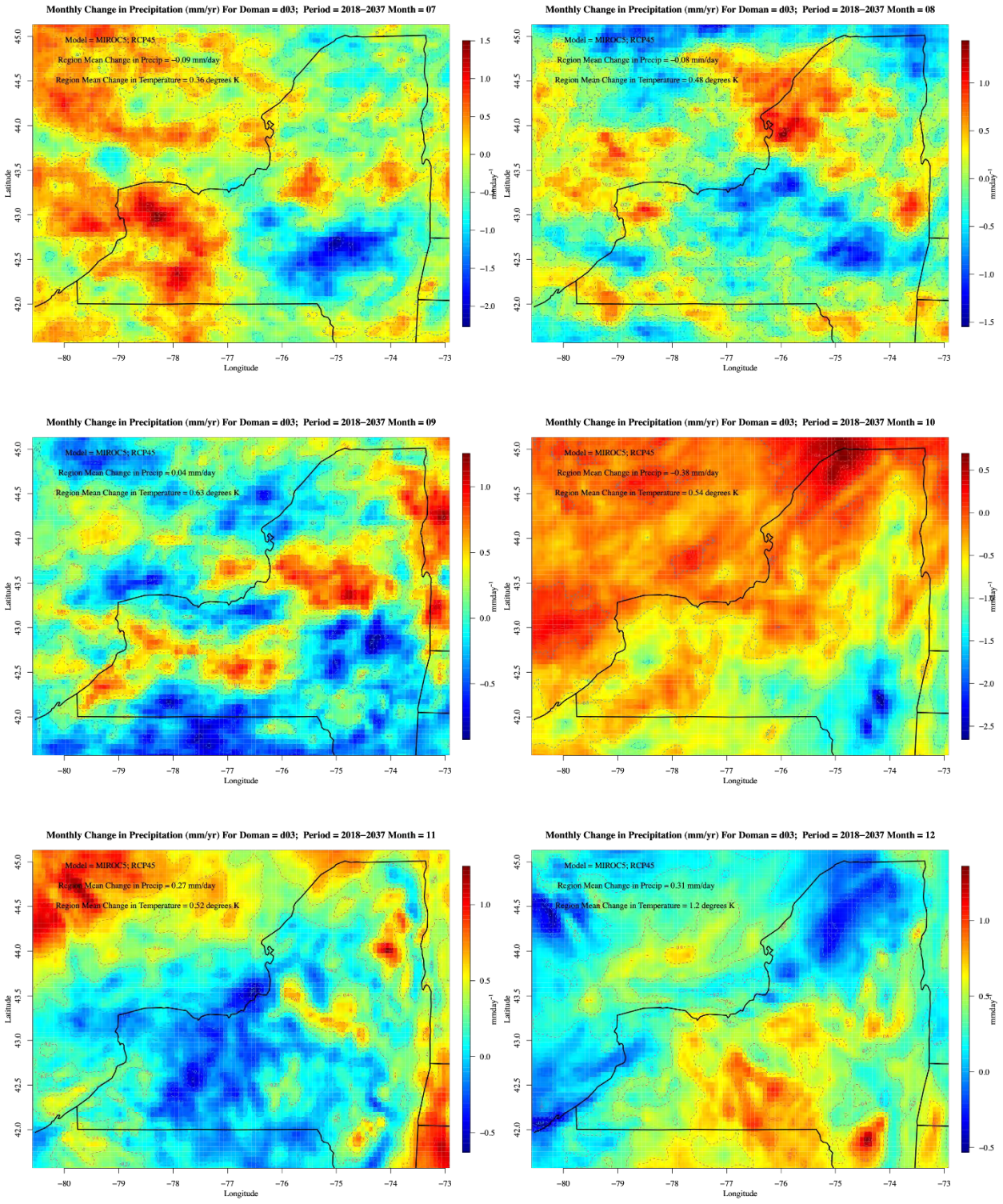

Figure D-11. Same as Figure D-3 except for MIROC5

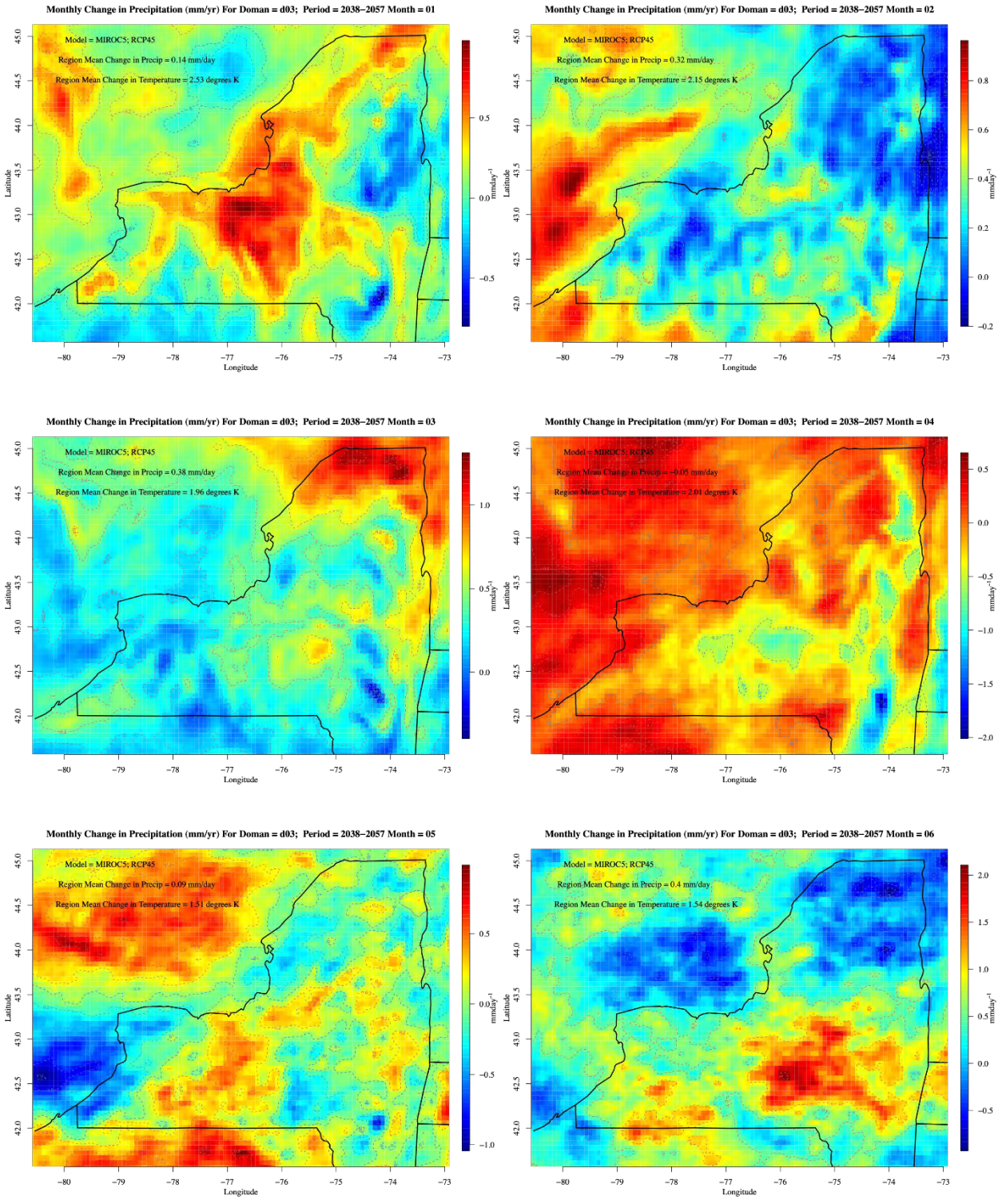

Figure D-12. Same as Figure D-4 except for MIROC5

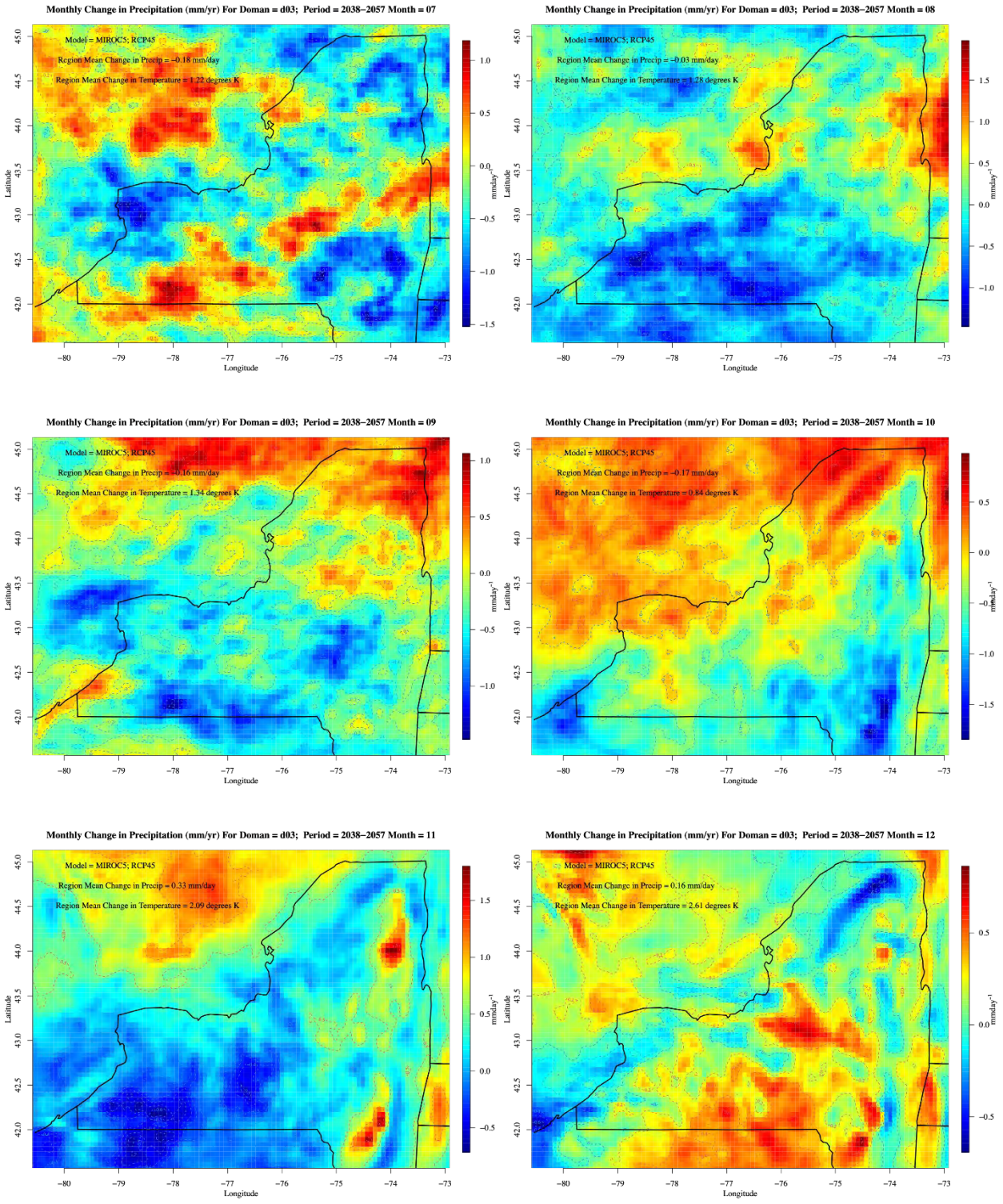

Figure D-13. Same as Figure D-5 except for MIROC5

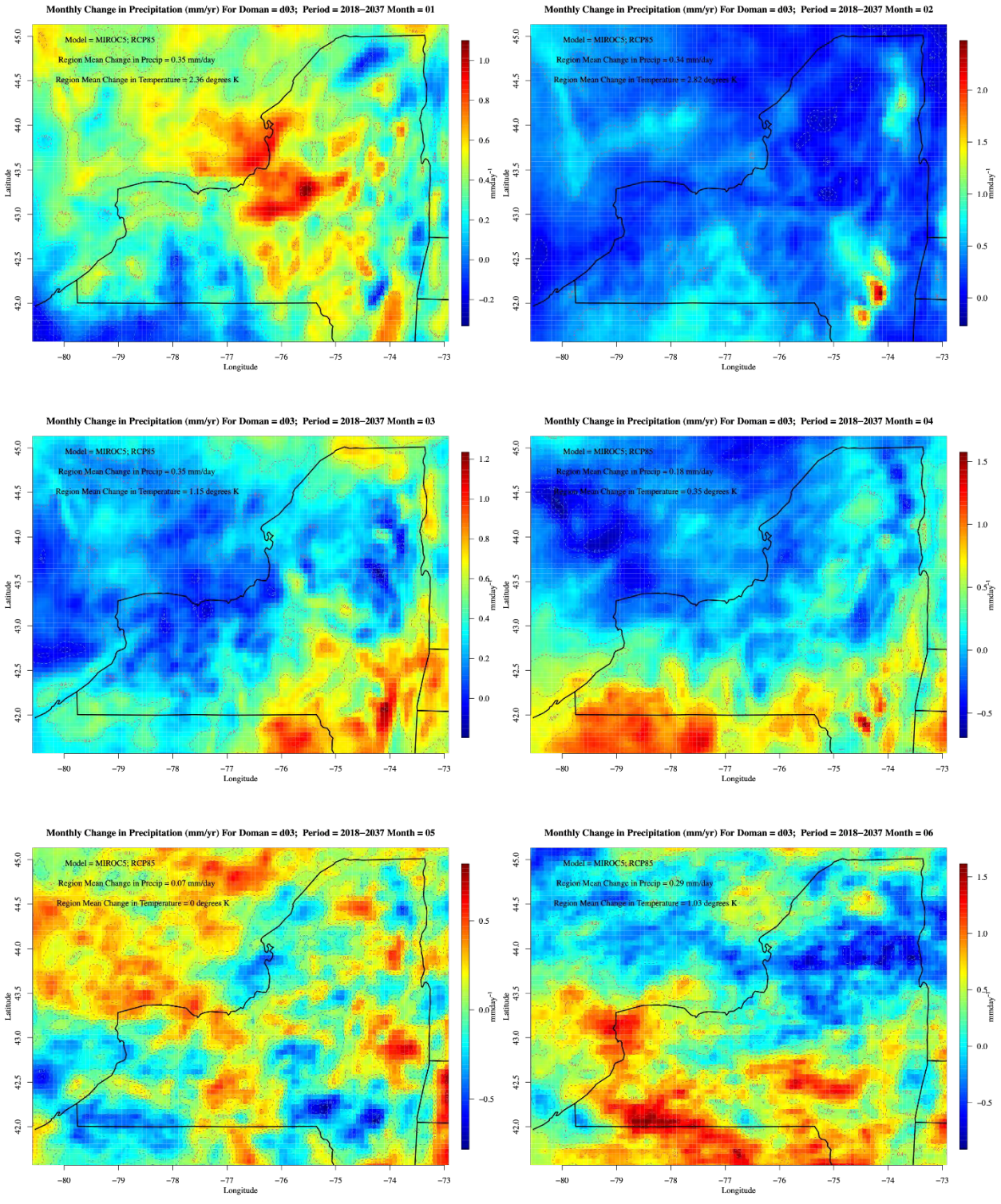

Figure D-14. Same as Figure D-6 except for MIROC5

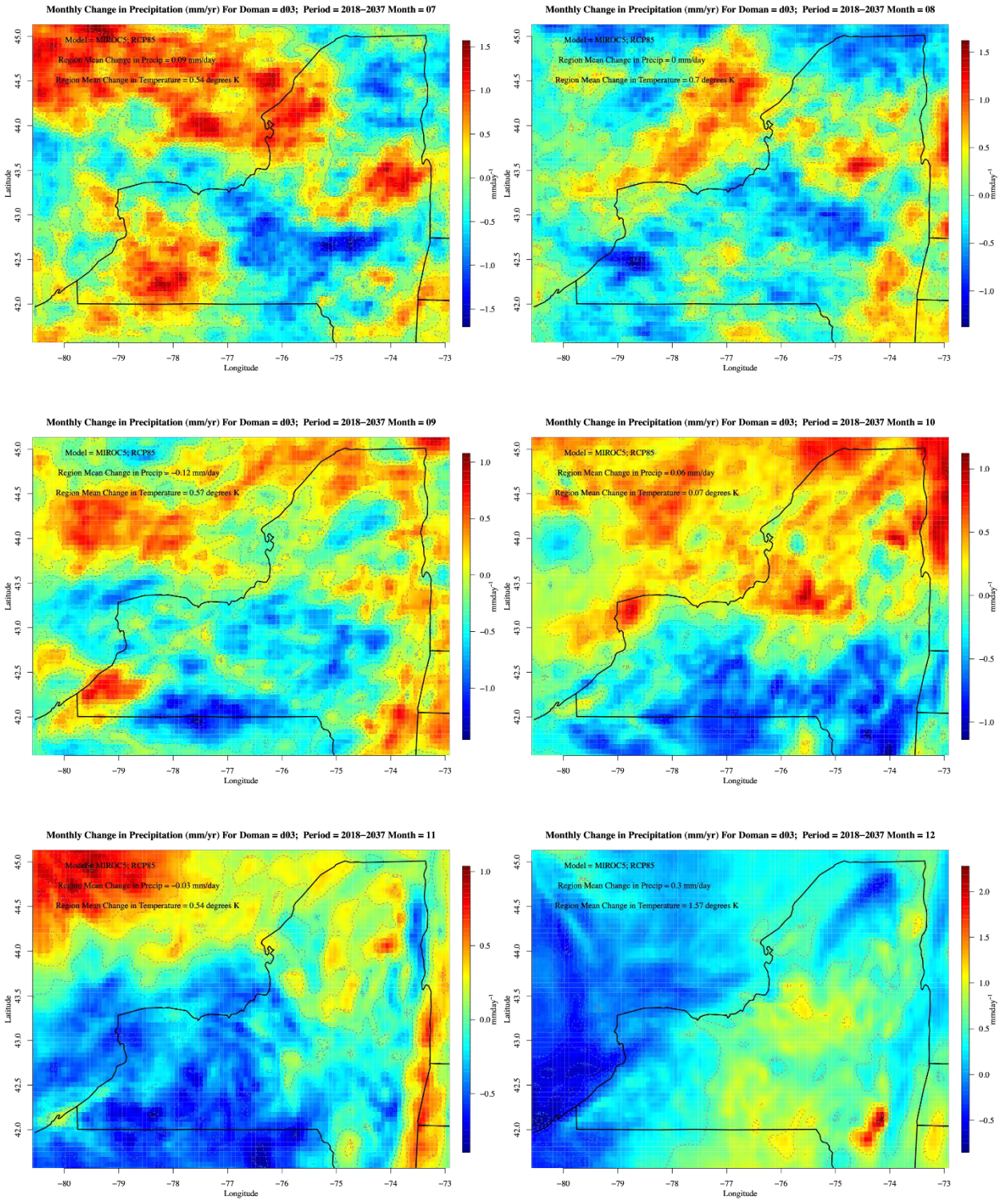

Figure D-15. Same as Figure D-7 except for MIROC5

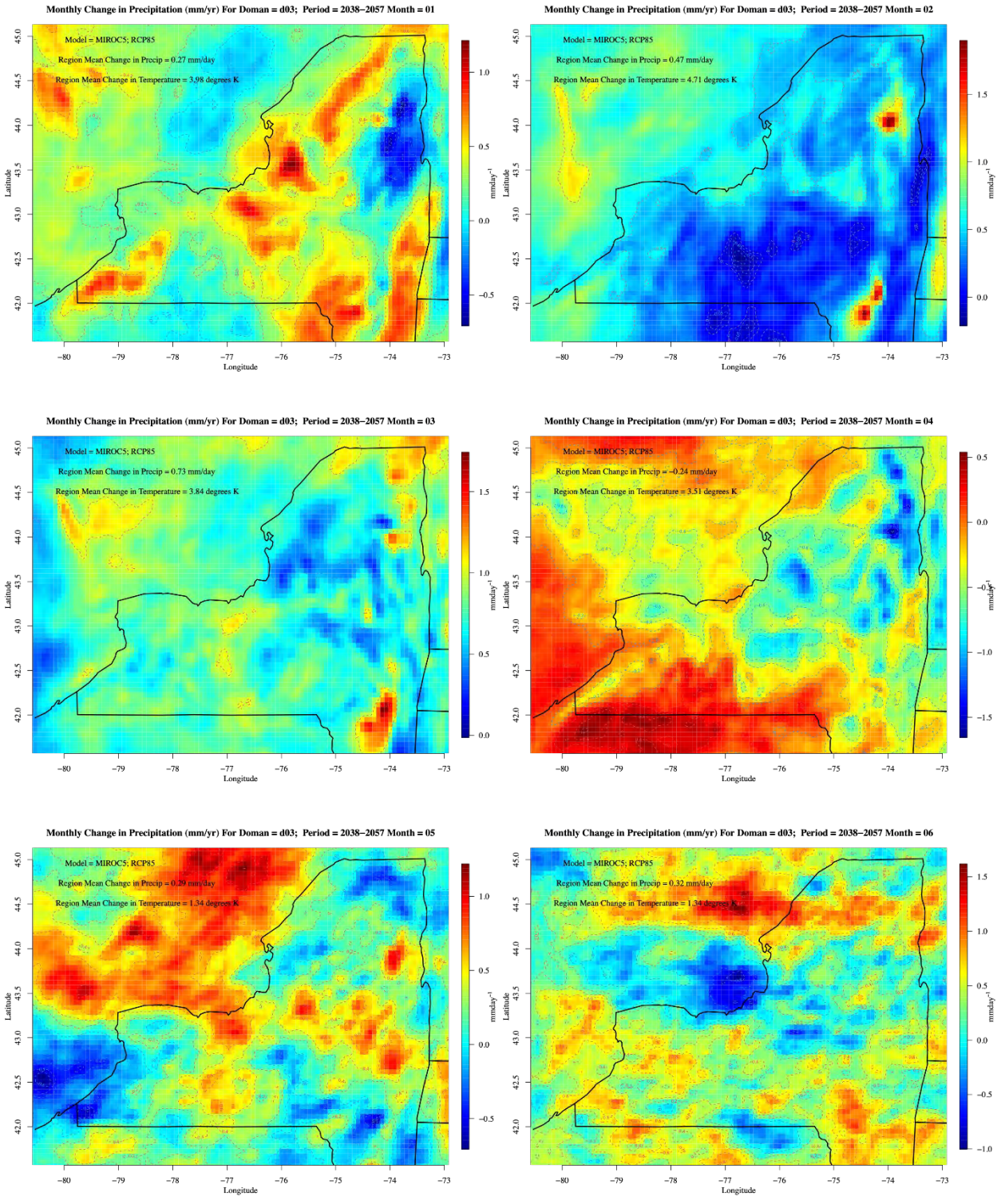

Figure D-16. Same as Figure D-8 except for MIROC5

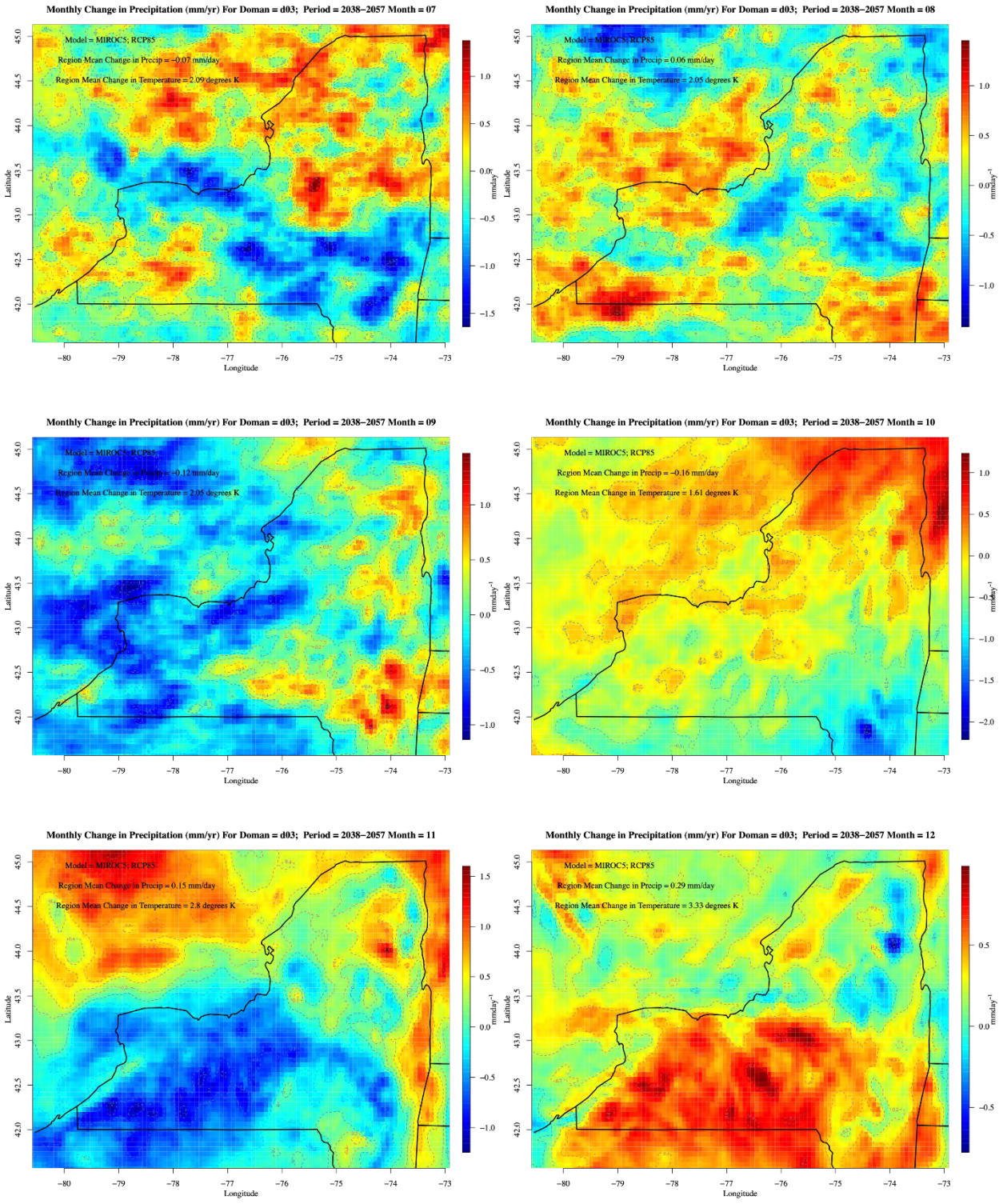

Figure D-17. Same as Figure D-1 except for NCAR-CCSM4

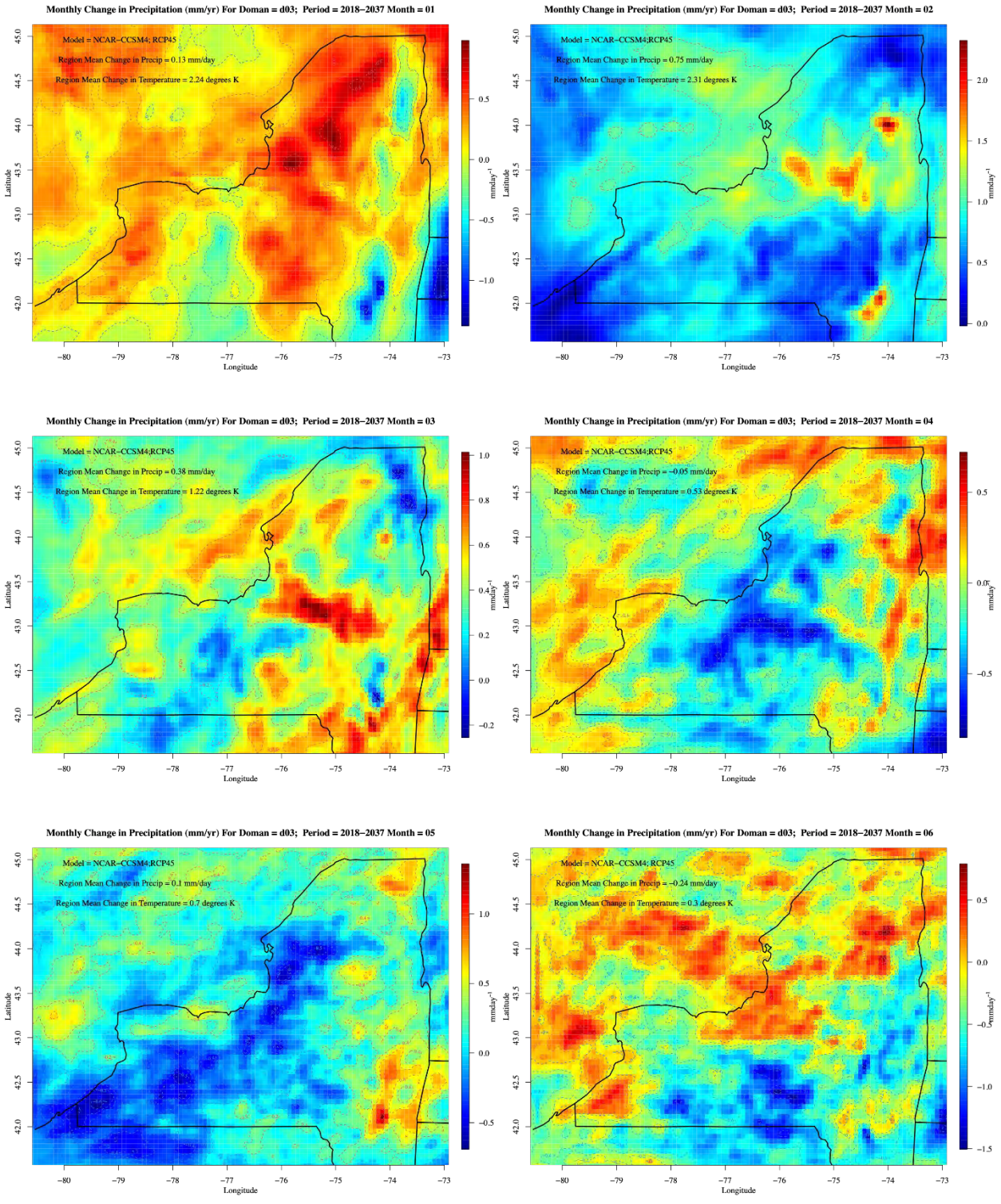

Figure D-18. Same as Figure D-2 except for NCAR-CCSM4

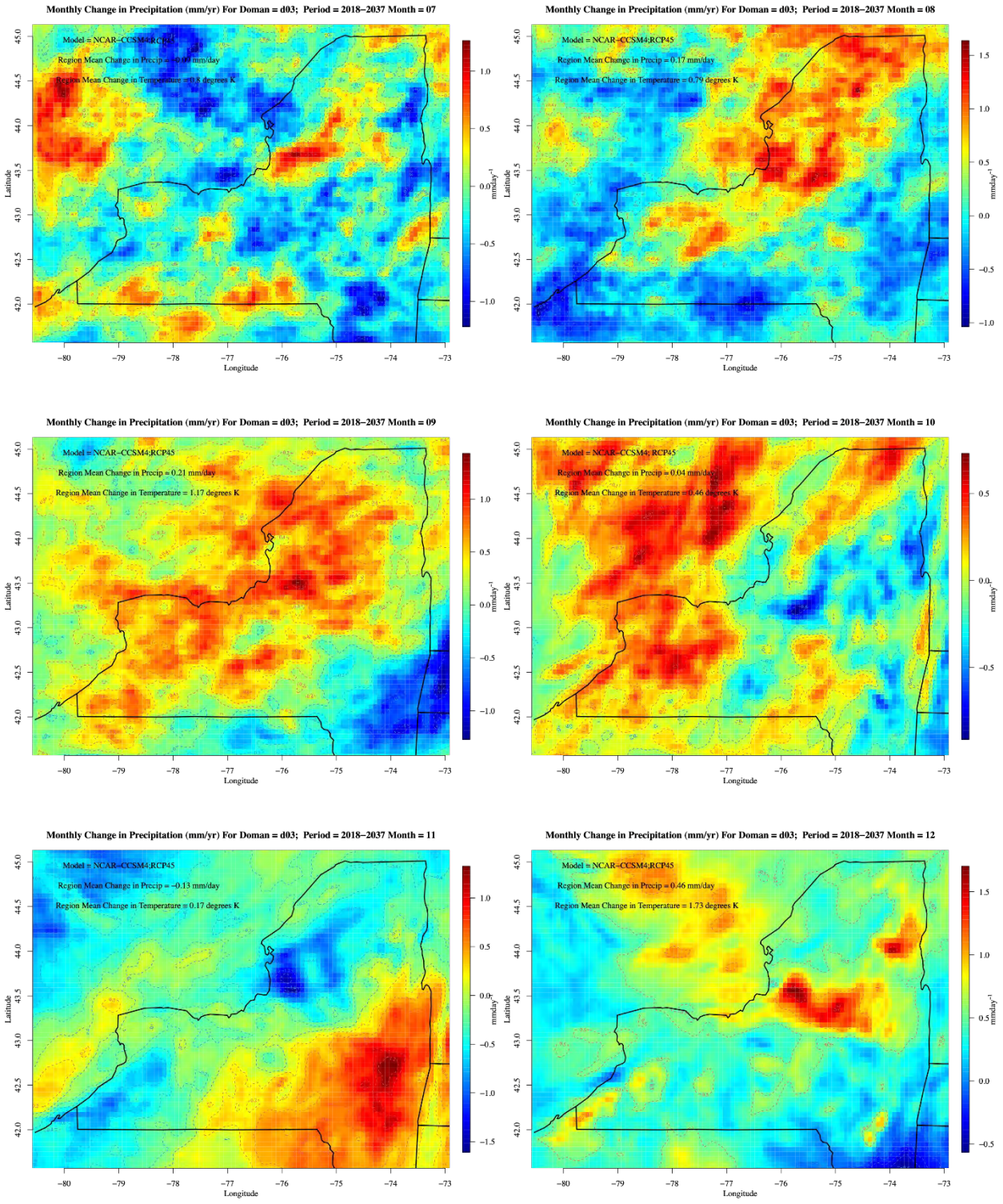

Figure D-19. Same as Figure D-3 except for NCAR-CCSM4

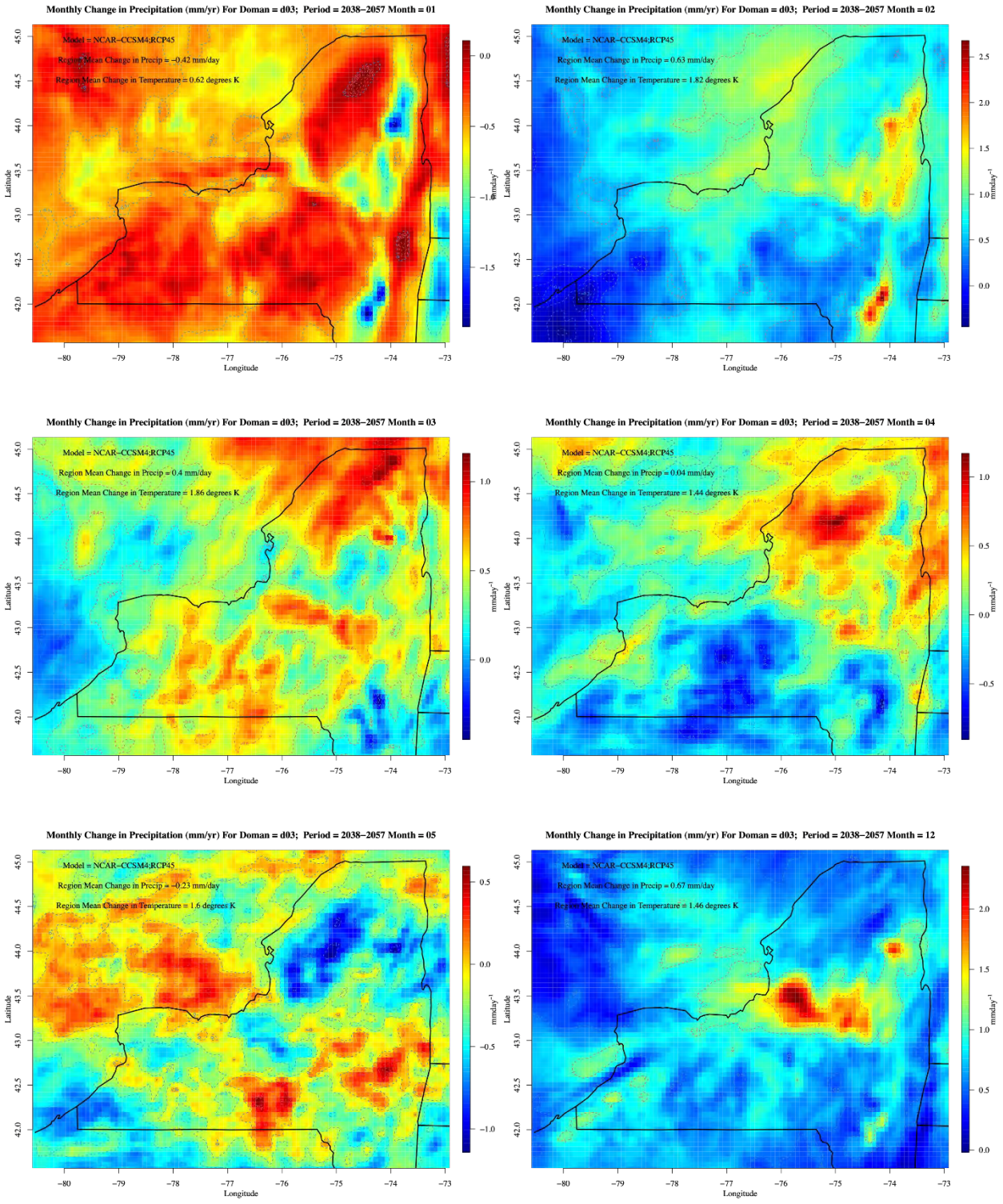

Figure D-20. Same as Figure D-4 except for NCAR-CCSM4

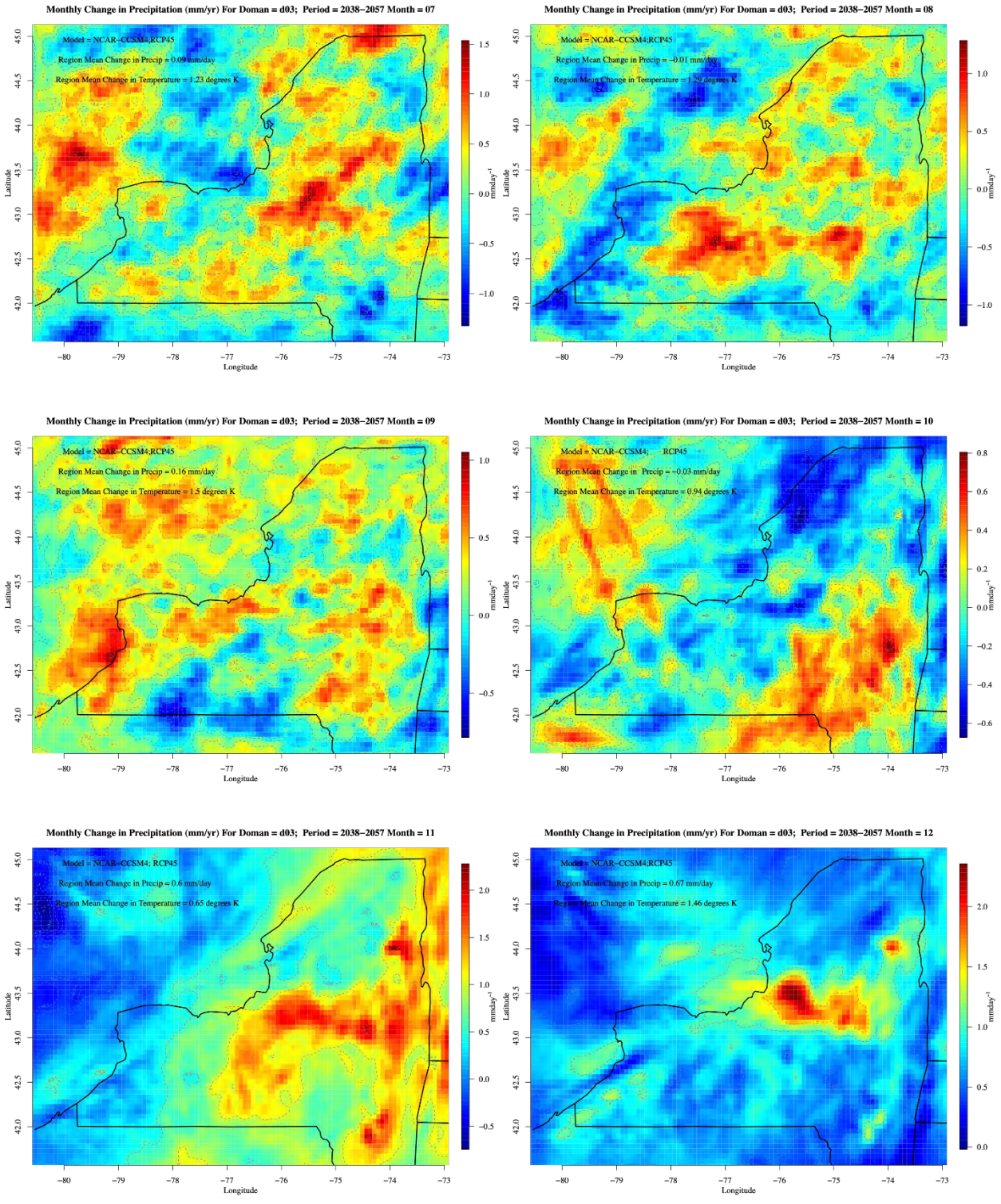

Figure D-21. Same as Figure D-5 except for NCAR-CCSM4

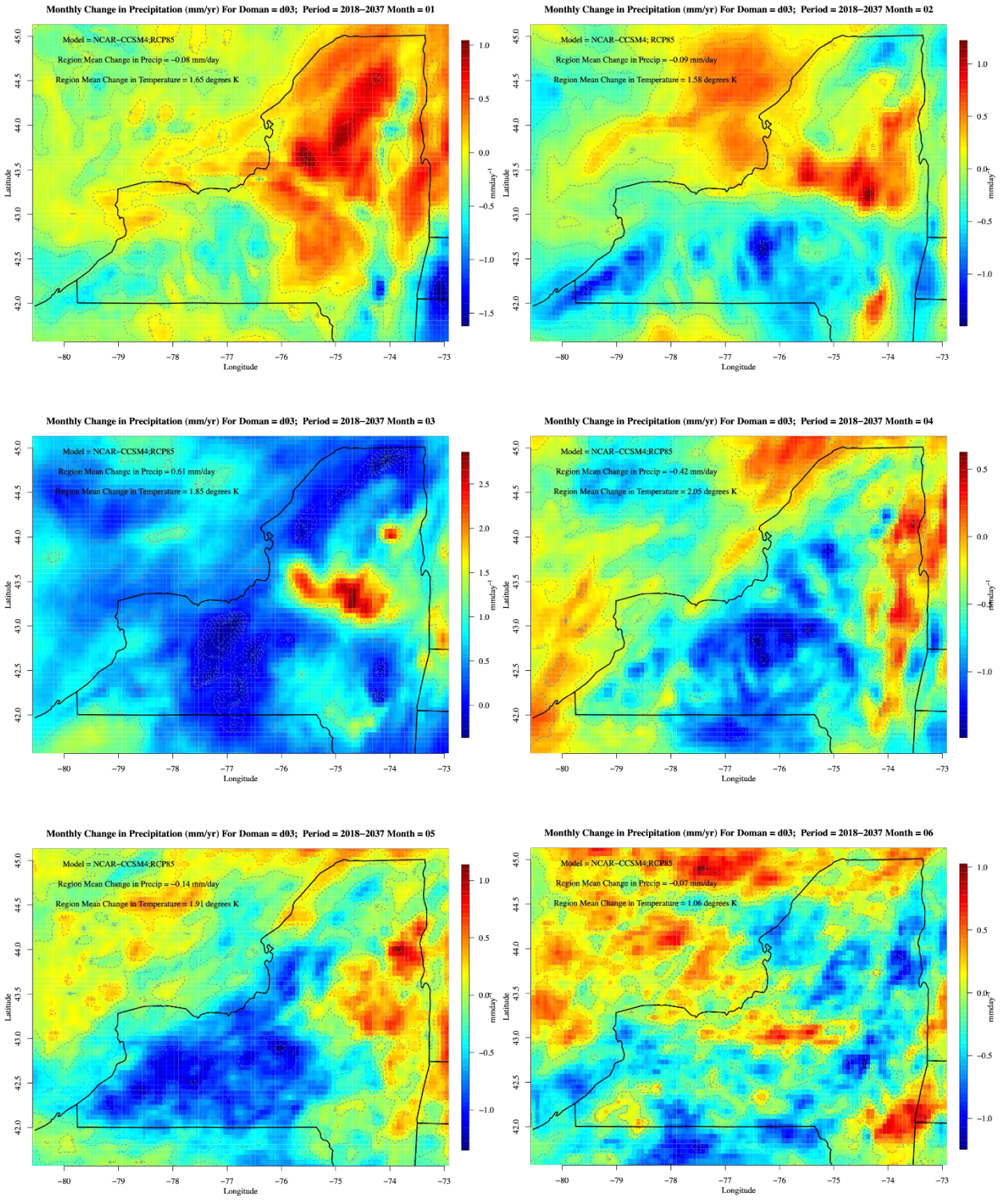

Figure D-22. Same as Figure D-6 except for NCAR-CCSM4

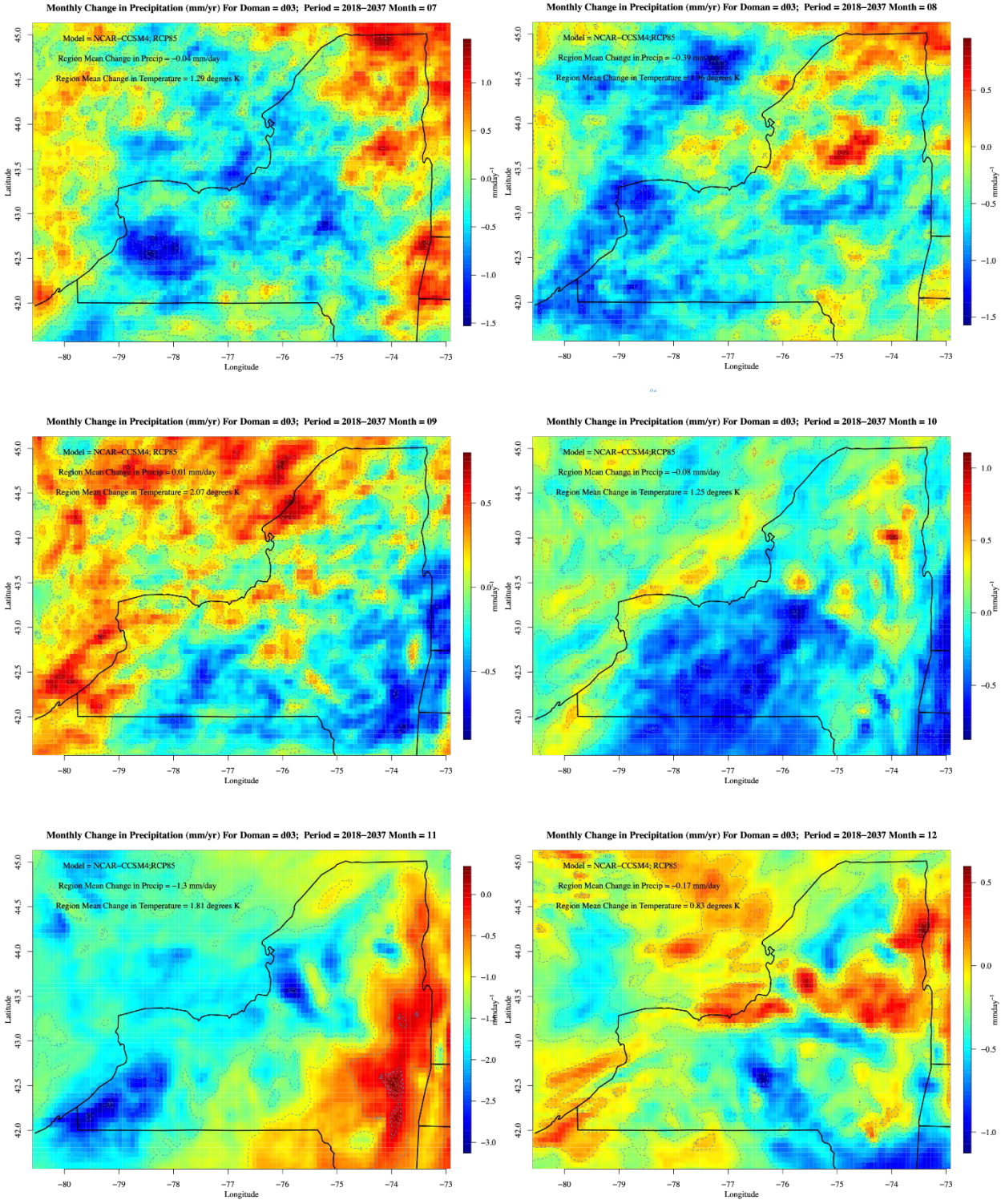

Figure D-23. Same as Figure D-7 except for NCAR-CCSM4

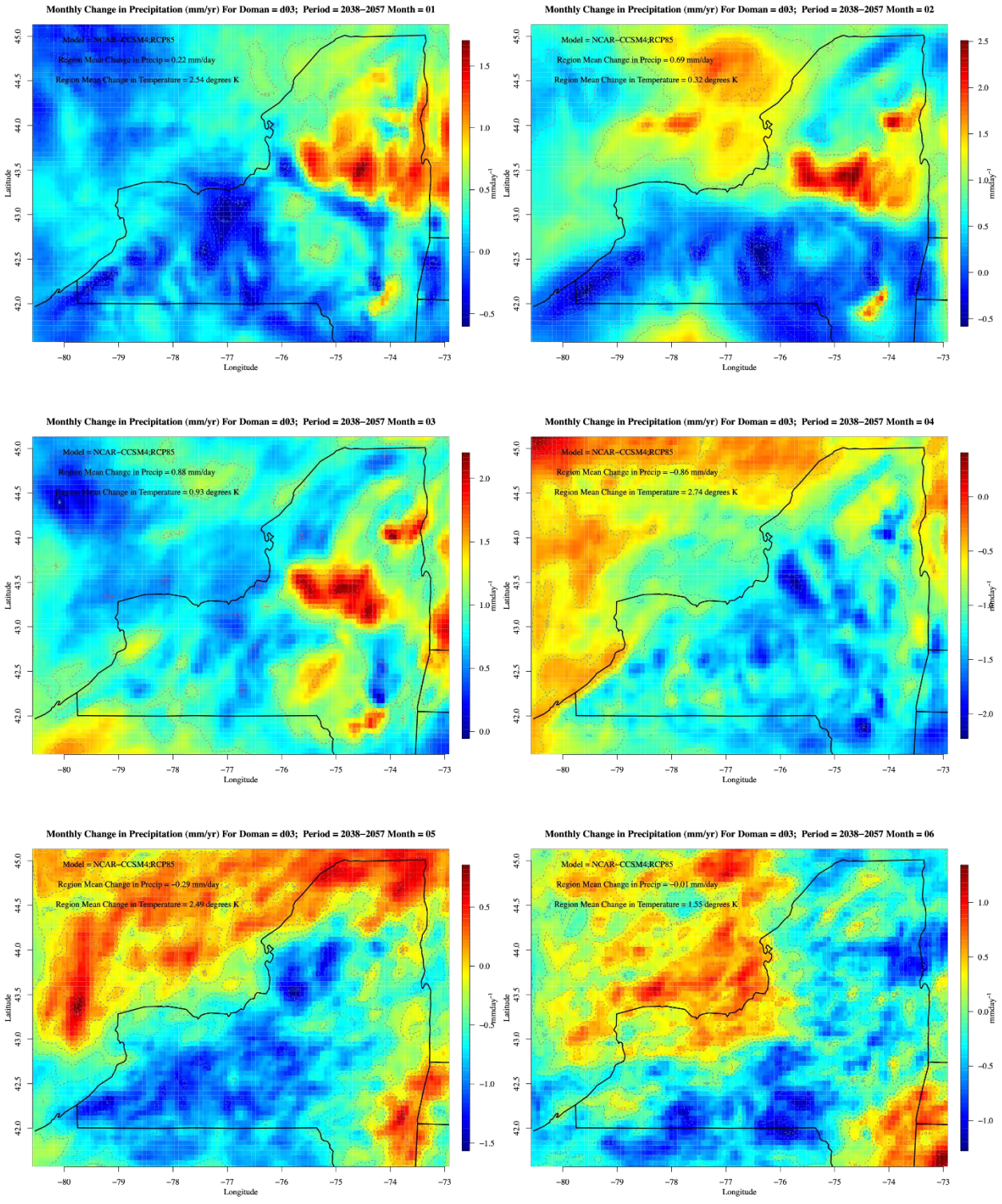

Figure D-24. Same as Figure D-8 except for NCAR-CCSM4

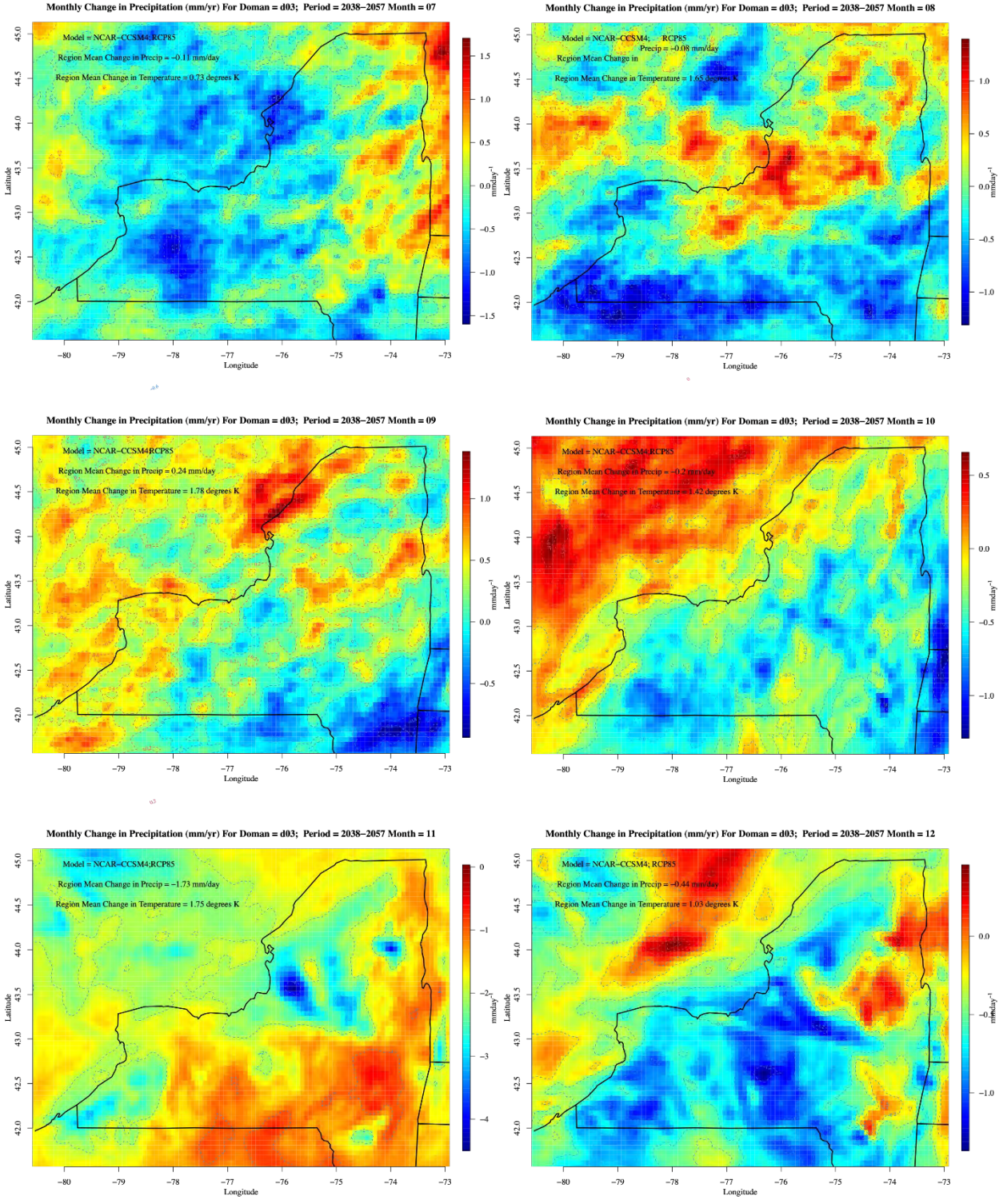

Endnotes

[1] On June 19, 2019, the New York State Legislature passed the Climate Act, and the Governor signed it into law. See ECL §§75-0101–75-0119.

[2] As of September 2016, AWS Truepower (AWST) became UL Renewables/AWS Truepower.

[3] Although the SOW mentions that six models were to be used, three for each RCP scenario to perform a true intercomparison and ensure consistency across historical and future scenario runs, the same three-model subgroup must be used.

[4] Two additional nodes were subsequently added during the model runs.

[5] "Wall clock time" refers to the elapsed time needed to run a simulation.

[6] We did not change the number of vertical levels in the PBL because this is where the fields relevant to this study (precipitation, hub-height wind speeds, surface irradiance) were extracted. Sensitivity testing indicated no changes in time series or spatial representation of standard meteorological fields driving the weather (e.g., pressure).

[7] This is the integration time required to calculate all fields necessary for capturing the phenomena represented by the modeling effort.

[8] As mentioned earlier, the BNU model was replaced with MIROC5. See discussion in section 4.2.2.

[9] Note that the above results are consistent with the analysis presented in section 5.

[10] The areas downwind of the Great Lakes tend to be noted for abundant cloudiness, often associated with lake-effect snow. However, the areas adjacent to Lake Ontario and Lake Erie are more cloud-free during the warm season, when potential irradiance is at a maximum due to the relatively cool waters of the lakes suppressing cloud formation.

NYSERDA, a public benefit corporation, offers objective information and analysis, innovative programs, technical expertise, and support to help New Yorkers increase energy efficiency, save money, use renewable energy, and reduce reliance on fossil fuels. NYSERDA professionals work to protect the environment and create clean-energy jobs. NYSERDA has been developing partnerships to advance innovative energy solutions in New York State since 1975.

To learn more about NYSERDA's programs and funding opportunities, visit nyserda.ny.gov or follow us on X, Facebook, YouTube, or Instagram.

New York State Energy Research and Development Authority

17 Columbia Circle
Albany, NY 12203-6399

toll free: 866-NYSERDA
local: 518-862-1090
fax: 518-862-1091

info@nyserda.ny.gov
nyserda.ny.gov

NYSERDA
New York State Energy Research and Development Authority